

DOTTORATO DI RICERCA IN ASTROFISICA

Ciclo XXXI

**SHOCK WAVES AND
NON-THERMAL PHENOMENA
IN MERGING GALAXY CLUSTERS**

Tesi di Dottorato in Astrofisica

Presentata da: **Andrea BOTTEON**

Supervisore:
Chiar.mo Prof.

Daniele DALLACASA

Coordinatore Dottorato:
Chiar.mo Prof.

Francesco R. FERRARO

Co-Supervisori:

Dr. **Gianfranco BRUNETTI**

Dr. **Fabio GASTALDELLO**

Esame finale anno 2019

**THIS THESIS WORK WAS DONE AS
PART OF THE RESEARCH ACTIVITY OF THE
ISTITUTO DI RADIOASTRONOMIA -
ISTITUTO NAZIONALE DI ASTROFISICA
(BOLOGNA)**

ABSTRACT

In this Thesis, we used state of the art radio and X-ray datasets and techniques to derive constraints on the formation mechanisms of diffuse radio emission in merging galaxy clusters. In particular, turbulence is believed to be responsible for the formation of the central and likely spherical sources called radio halos, while shocks are the origin of the elongated and polarized emissions found in cluster outskirts known as radio relics. Although this scenario seems supported by current observations, the processes that originate these synchrotron sources are still poorly constrained.

An important goal achieved during the Thesis is a progress on the relic–shock connection and on the origin of radio relics. This was obtained thanks to the detection in the X-rays of new shocks in merging galaxy clusters. In combination with the analysis of radio observations, this allowed us to derive efficient constraints on the mechanisms of particle (re)acceleration and on the magnetic fields in relics. Notably, we demonstrated for the first time, in an homogeneous way, that merger shocks can not reproduce the luminosity of radio relics if particles are accelerated from the thermal pool. This strongly support that other mechanisms, such as shock re-acceleration, are involved in the formation of this kind of sources.

LOFAR is a new generation interferometer that is providing a revolutionary view of clusters at low frequencies. For this reason, the exploitation of LOFAR observations represented a central task of the Thesis. We used LOFAR observations in combination with X-ray and radio data coming from other facilities to study non-thermal phenomena in two dynamically complex cluster mergers providing also first hints of a radio bridge of emission connecting two clusters in a pre-merging phase. Our results proved the extraordinary potential of LOFAR in galaxy cluster science.



Contents

List of acronyms	xvii
Nomenclature	xxi
Thesis outline	xxv
1 Galaxy clusters: focus on mergers and non-thermal phenomena	1
1.1 Galaxy clusters	1
1.1.1 Mass determination	2
1.2 The intra-cluster medium	4
1.2.1 Microphysics	4
1.2.2 Thermal emission	4
1.2.3 The Sunyaev-Zel'dovich effect	6
1.2.4 Non-thermal components	7
1.3 Galaxy cluster mergers	10
1.3.1 Impact velocity	11
1.3.2 Shocks	12
1.3.3 Turbulence	15
1.4 Diffuse radio sources in merging galaxy clusters	16

1.4.1	Radio relics	17
1.4.2	Radio halos	19
1.5	Origin of radio relics	20
1.5.1	Adiabatic compression	20
1.5.2	Diffusive shock acceleration	23
1.5.3	Shock re-acceleration	25
1.6	Origin of radio halos	26
1.6.1	Hadronic models	27
1.6.2	Turbulent re-acceleration models	27
1.7	Non-thermal X-ray emission	28
2	A shock at the radio relic position in Abell 115	31
2.1	Introduction	31
2.2	Observations and data reduction	32
2.2.1	X-ray data reduction	32
2.2.2	Radio data reduction	33
2.3	Results	33
2.4	Discussion	36
2.4.1	Radio relic–shock connection	36
2.4.2	Acceleration efficiency	36
2.5	Conclusions	37
3	A $\mathcal{M} \gtrsim 3$ shock for El Gordo and the origin of the NW radio relic	39
3.1	Introduction	39
3.2	Observations and data reduction	40
3.2.1	X-ray data reduction	40
3.2.2	Radio data reduction	40
3.3	Results	42
3.3.1	X-ray/radio analysis	42
3.3.2	Relics and shocks	43

3.3.3	Constraints on the downstream magnetic field	47
3.3.4	Acceleration efficiency	48
3.3.5	Overall considerations on El Gordo	49
3.4	Conclusions	50
4	IC emission and magnetic fields in radio relics: the case of El Gordo	51
4.1	Introduction	51
4.2	The definitive approach to detect IC	52
4.3	El Gordo: the best target	53
4.4	Future steps toward the detection of IC emission	56
4.4.1	Feasibility study	56
4.4.2	Impact of the discovery	58
4.5	Conclusions	58
5	Shock acceleration efficiency in a sample of radio relics	61
5.1	Introduction	61
5.2	Relic sample	62
5.3	Methods and data reduction	62
5.3.1	<i>Chandra</i>	62
5.3.2	<i>XMM-Newton</i>	63
5.3.3	Surface brightness and density profiles	63
5.4	Computation of the acceleration efficiency	63
5.4.1	X-ray and DSA Mach numbers	66
5.5	Results	68
5.6	Discussion	82
5.7	Conclusions	84
6	Shocks and cold fronts in merging and massive galaxy clusters: new detections with <i>Chandra</i>	87
6.1	Introduction	87
6.2	Cluster sample	88

6.3	Methods and data analysis	90
6.3.1	X-ray data preparation	90
6.3.2	Edge detection filter	90
6.3.3	Surface brightness profiles	91
6.3.4	Spectra	92
6.4	Characterization of the edges	94
6.5	Results	94
6.5.1	Detections	95
6.5.2	Summary of the detected edges	111
6.5.3	Non-detections	114
6.6	Conclusions	119
7	Galaxy cluster science with LOFAR	121
7.1	The LOw Frequency ARray	121
7.1.1	System overview	122
7.1.2	Antennas	124
7.2	LOFAR 2.0 and LOFAR-IT	127
7.3	The impact of LOFAR in the study of merging galaxy clusters	128
7.4	The LOFAR Two-meter Sky Survey	129
7.5	LOFAR HBA data calibration	131
8	LOFAR, GMRT, and <i>XMM-Newton</i> observations of the cluster chain Abell 781	135
8.1	Introduction	135
8.2	Observations and data reduction	136
8.2.1	LOFAR	136
8.2.2	GMRT	138
8.2.3	<i>XMM-Newton</i>	138
8.3	Results	139
8.3.1	The peripheral emission in A781	139
8.3.2	X-ray discontinuities in the ICM	143

8.3.3	Constraints on the radio halo emission	145
8.4	Discussion	146
8.4.1	On the nature of the peripheral radio emission	146
8.4.2	A triple merger in A781	148
8.5	Conclusions	149
9	LOFAR discovery of a double radio halo system in Abell 1758 and radio/X-ray study of the cluster pair	151
9.1	Introduction	151
9.2	Observations and data reduction	152
9.2.1	LOFAR	152
9.2.2	GMRT	153
9.2.3	VLA	154
9.2.4	Integrated synchrotron spectra and source subtraction	154
9.2.5	<i>Chandra</i>	155
9.3	Results	156
9.3.1	A1758N radio halo	156
9.3.2	A1758S radio halo	159
9.3.3	A1758S candidate radio relic	160
9.3.4	X-ray properties of A1758N and A1758S	160
9.3.5	The bridge between A1758N and A1758S	161
9.4	Discussion	163
9.4.1	The radio halos in the A1758 complex	163
9.4.2	Merger scenario between A1758N and A1758S	164
9.5	Conclusions	165
	Thesis conclusions	169
I.	Relic–shock connection and particle acceleration mechanisms	169
II.	Non-thermal phenomena in dynamically complex mergers	170
III.	Magnetic field in cluster outskirts	172

A	A SB jump across the Sausage?	175
B	Galactic absorption	177
C	NXB modeling	179
D	Statistical precision of the fits	181
E	Null results	185
F	Error maps	187
G	Temperature map	189
H	X-ray channel spectra	191
	References	195
	Acknowledgments	221

MISCELLANEOUS

AGN	Active Galactic Nucleus
CC	Cool-Core
CCD	Charge-Coupled Device
CEP	CEntral Processing
CR	Cosmic Ray
CR_e	Cosmic Ray electron
CR_p	Cosmic Ray proton
CMB	Cosmic Microwave Background
CXB	Cosmic X-ray Background
DSA	Diffusive Shock Acceleration
FoV	Field of View
GGM	Gaussian Gradient Magnitude
GH	Galactic Halo
HBA	High Band Antenna
HETDEX	Hobby-Eberly Telescope Dark Energy Experiment
KSP	Key Science Project
IC	Inverse Compton
ICM	Intra-Cluster Medium
INAF	Istituto di AstroFisica

IRA	Istituto di RadioAstronomia
LBA	Low Band Antenna
LHB	Local Hot Bubble
NCC	Non Cool-Core
NXB	Non-X-ray Background
RFI	Radio Frequency Interference
PSF	Point Spread Function
SB	Surface Brightness
S/N	Signal-to-Noise ratio
SNR	SuperNova Remnant
SZ	Sunyaev Zel'dovich
USSRH	Ultra Steep Spectrum Radio Halo
X-COP	XMM-Newton Cluster Outskirts Project

INSTRUMENTS

ACIS	Advanced CCD Imaging Spectrometer
ASCA	Advanced Satellite for Cosmology and Astrophysics
ATCA	Australia Telescope Compact Array
EPIC	European Photon Imaging Camera
GMRT	Giant Metrewave Radio Telescope
JVLA	Jansky Very Large Array
LOFAR	LOw Frequency ARray
MWA	Murchison Widefield Array
NuSTAR	Nuclear Spectroscopic Telescope ARray
ROSAT	RÖentgen SATellite
SKA	Square Kilometre Array
VLA	Very Large Array
WEAVE	William Herschel Telescope Enhanced Area Velocity Explorer

SURVEYS & CATALOGS

BCS	Brightest Cluster Sample
eBCS	extended Brightest Cluster Sample
FIRST	Faint Images of the Radio Sky at Twenty-centimeter
GLEAM	GaLactic and Extragalactic All-sky MWA
MSSS	Multifrequency Snapshot Sky Survey
LoLSS	LOFAR LBA Sky Survey
LoTSS	LOFAR Two-meter Sky Survey
PSZ	Planck Sunyaev Zel'dovich
MACS	MAssive Cluster Survey
NORAS	NOrthern ROSAT All-Sky
NVSS	NRAO VLA Sky Survey
REFLEX	ROSAT-ESO Flux Limited X-ray
SDSS	Sloan Digital Sky Survey
TGSS ADR	TIFR GMRT Sky Survey Alternative Data Release
VLSSr	VLA Low-frequency Sky Survey redux
WENSS	WEsterbork Northern Sky Survey

SOFTWARE & PACKAGES

AIPS	Astronomical Image Processing System
CALDB	CALibration DataBase
CASA	Common Astronomy Software Applications
CIAO	Chandra Interactive Analysis of Observations
ESAS	Extended Source Analysis Software
SAS	Scientific Analysis System
SPAM	Source Peeling and Atmospheric Modeling
WSCLEAN	W-Stacking Clean

PHYSICAL CONSTANTS

σ_T	Thomson cross-section
c	Speed of light
G	Gravitational constant
h	Planck constant
k	Boltzmann constant
M_\odot	Solar mass
m_e	Electron mass
m_p	Proton mass
Z_\odot	Solar metallicity

GREEK SYMBOLS

α	Spectral index of the synchrotron radiation
δ	Index of the power-law electron spectrum
ε_B	Magnetic field energy density
ε_{ph}	Photon field energy density
η_e	Electron acceleration efficiency
Γ	Photon index

γ	Lorentz factor
γ_{ad}	Adiabatic index
μ	Mean molecular mass
ν	Radiation frequency
ρ	Volumetric mass density

ROMAN SYMBOLS

B	Magnetic field
B_{cmb}	Equivalent magnetic field strength of the CMB
K	Entropy
K_0	Core entropy
$K_{e/p}$	Electron-to-proton ratio
M_{500}	Mass within r_{500}
n	Number density
N_H	Hydrogen column density
P	Pressure
p	Particle momentum
$P_{1.4}$	Power at 1.4 GHz
p_{min}	Minimum momentum of accelerated particles
r_{500}	Radius of a sphere whose density is 500 times the critical density of the Universe
S	Flux density
T	Temperature
V_{sh}	Shock velocity
z	Redshift

OTHER SYMBOLS

C	Compression factor
\mathcal{M}	Mach number

\mathcal{P}	Pressure ratio
\mathcal{R}	Temperature ratio

SUBSCRIPTS

d	Downstream
e	Electron
inj	Injection
p	Proton
u	Upstream

GALAXY CLUSTERS are the largest virialized structures in the Universe and form via aggregation of less massive systems. The most massive clusters in the Universe exceed $10^{15} M_{\odot}$ and cover linear sizes of a few Mpc. Dark matter is the main constituent of clusters ($\sim 80\%$) while baryons represent a small fraction of the cluster mass ($\sim 20\%$). The majority of baryons ($\sim 85\%$) resides in the form of a hot ($T \sim 10^7 - 10^8$ K) and diluted ($n_e \sim 10^{-3} - 10^{-4} \text{ cm}^{-3}$) plasma, called intra-cluster medium (ICM), which emits in the X-rays mostly via thermal bremsstrahlung. Stars in galaxies comprise the rest of the cluster baryonic mass.

In the process of cluster formation, the kinetic energy associated with two colliding sub-structures reaches $10^{63} - 10^{64}$ erg, making cluster mergers the most energetic events in the Universe since the Big Bang. During a merger, a major fraction of this energy dissipates into the heating of the ICM via shocks and turbulence and generates non-thermal components. Non-thermal components can be revealed by radio observations of diffuse synchrotron sources in clusters, such as radio relics and halos, that prove the existence of magnetic fields and relativistic particles mixed with the thermal ICM. A strong association between these diffuse cluster-scale sources and mergers is indeed demonstrated by observations. In this respect, studying the interplay between thermal and non-thermal components in merging galaxy clusters is fundamental to understand the origin of diffuse synchrotron sources in the ICM and to probe the complex mechanisms that drain energy into non-thermal components and their impact on the microphysics of the ICM.

Radio relics are Mpc-scale elongated and arc-shaped polarized structures typically located in the periphery of clusters. According to the current leading scenario, relics trace cosmological shock waves that cross the ICM where particles are (re)accelerated and the magnetic field amplified. Whilst the connection between radio relics and shocks is supported by several observational facts, including the coincidence between relics and shocks identified in the X-rays, the details of the mechanisms leading their formation are still unclear.

Radio halos are giant radio sources located in the central regions of clusters. Their emission is extended on the cluster-scale with a morphology similar to the X-ray thermal emission. Halos are thought to be generated by electrons re-accelerated by turbulent-driven mechanisms during mergers, although many aspects of these processes remain poorly understood.

This Thesis is focused on shocks and non-thermal phenomena in merging galaxy clusters. The broad aim of the Thesis is to investigate the origin of cluster-scale radio sources using radio data (obtained from the most innovative facilities) combined with X-ray observations. More specifically, the PhD program was based on two main goals, as outlined below.

The first goal achieved in the Thesis is **a progress on the relic–shock connection and on the origin of radio relics**. This was obtained mainly with X-ray observations performed with the *Chandra* and *XMM-Newton* satellites that allowed us to discover new shocks in merging galaxy clusters. This is a relevant result on its own because it increased the modest number of shocks detected in the ICM with the clear detection of new X-ray discontinuities. In combination with the (re)analysis of radio observations of merger shocks, we derived also important constraints on the mechanisms of particle (re)acceleration and on the magnetic fields in radio relics. In particular, we presented the first attempt for a study on the acceleration efficiency in a sample of radio relics.

Due to their steep spectrum, the study of radio relics and, in general, of cluster-scale diffuse radio emission is one of the key science projects of the new generation of radio interferometers, such as the LOFAR and MWA and, in the future, of the SKA. In this respect, **the exploitation of LOFAR observations of merging galaxy clusters** has been identified as a central task of the PhD project due to the impact of this instrument in the field of non-thermal emission from the ICM. The analyses of two LOFAR pointings, containing the clusters Abell 781 and Abell 1758, were carried out as important steps of the Thesis. The outcome proved the extraordinary potential of LOFAR. Among the other results obtained during the LOFAR analysis, the following are worth to be mentioned: the revision of the nature of a peripheral radio emission formerly classified as a radio relic in Abell 781, the discovery of a new radio halo, and the detection of a faint bridge of radio emission connecting two galaxy clusters in a pre-merger phase in Abell 1758. The latest result triggered the search for similar signals from other binary clusters.

This Thesis is organized in the following structure:

- In **Chapter 1** we provide an introduction on the processes taking place in merging galaxy clusters important for this Thesis with particular emphasis on the non-thermal phenomena. The jargon and main formulas used along the Thesis are outlined in this Chapter.
- In **Chapter 2** we report on the discovery of a shock co-spatially located with the radio relic in Abell 115. This clear detection of a shock allowed us to give constraints on the mechanisms of formation of the radio source. We suggested that the relic is generated by shock re-acceleration.
- In **Chapter 3** we discuss the discovery of the most distant (and among the strongest) shock ever detected in a galaxy cluster, i.e. in “El Gordo” cluster at $z = 0.87$. The shock is co-located with a radio relic and from the study of the shock acceleration efficiency we found that this shock, in principle, is powerful enough to accelerate electron directly from the thermal pool. The presence of inverse Compton emission from the relic is also discussed.
- In **Chapter 4** we show how the detection of X-ray emission from inverse Compton from a relic would impact our understanding of cluster shock physics. We compared the 9 most powerful radio relic known so far and took El Gordo cluster, i.e. the best candidate for this search, as a test case to determine the feasibility of such an observation.
- In **Chapter 5** we extend the study of shock acceleration efficiency in galaxy cluster mergers to a sample of well studied relics with detected underlying shocks. We demonstrated that supra-thermal seed electrons are required to explain the formation of these radio sources.
- In **Chapter 6** we present the results of the search for new merger induced shocks and cold fronts in a sample of 15 clusters observed with *Chandra*. We made use of different techniques of X-ray data analysis confirming the presence of 6 shocks, 8 cold fronts and other 8 discontinuities with uncertain nature.

- In **Chapter 7** we provide an overview of the LOFAR focusing on its potential in the galaxy cluster science. We introduce one of the most important LOFAR survey from which the observations used in the next two Chapters have been retrieved.
- In **Chapter 8** we report on the results on the cluster chain Abell 781 from LOFAR, GMRT and *XMM-Newton* observations. In particular, we focused on the main cluster of the system, putting limits on the radio halo emission and discussing the peculiar peripheral radio source. We speculated that this emission is due to the interaction of a radio galaxy crossed by a shock wave and provided the tentative dynamics of the merger.
- In **Chapter 9** we present a combined radio/X-ray study of the double galaxy cluster Abell 1758. The new LOFAR data confirmed the presence of a radio halo in the northern cluster component and allowed us to discover a radio halo even in the southern system, making Abell 1758 the second double radio halo known so far. A faint bridge of radio emission connecting the two halos is also observed. We suggested that the clusters are in pre-merger phase.
- In the **Thesis conclusions** an overview of this Thesis is presented.

Throughout this Thesis, a Λ CDM cosmology with $\Omega_{\Lambda} = 0.7$, $\Omega_m = 0.3$ and $H_0 = 70$ km s⁻¹ Mpc⁻¹ is assumed. The convention used for radio synchrotron spectrum is $S_{\nu} \propto \nu^{-\alpha}$, where S_{ν} is the flux density at frequency ν and α is the spectral index.

* * *

Part of the results carried out during the PhD project have been published in the following papers:

1. *Relic–shock connection in Abell 115*
Botteon et al. 2016, *Galaxies*, 4, 4, 68
2. *A shock at the radio relic position in Abell 115*
Botteon et al. 2016, *MNRAS*, 460, L84-88
3. *A $\mathcal{M} \gtrsim 3$ shock in ‘El Gordo’ cluster and the origin of the radio relic*
Botteon et al. 2016, *MNRAS*, 463, 1534-1542
4. *Shocks and cold fronts in merging galaxy clusters: new detections with Chandra*
Botteon et al. 2018, *MNRAS*, 476, 5591-5620
5. *LOFAR discovery of a double radio halo system in Abell 1758 and radio-X-ray study of the cluster pair*
Botteon et al. 2018, *MNRAS*, 478, 885-898
6. *The spectacular cluster chain Abell 781 as observed with LOFAR, GMRT, and XMM-Newton*
Botteon et al. 2019, *A&A*, accepted (arXiv:1811.07930)

The following publications are the result of work conducted in collaborative projects during the PhD, but not presented in this Thesis:

7. *Studying the late evolution of a radio-loud AGN in a galaxy group with LOFAR*
Savini et al. 2018, *MNRAS*, 474, 5023-5035

8. *Search for low-frequency diffuse radio emission around a shock in the massive galaxy cluster MACS J0744.9+3927*
Wilber et al. 2018, MNRAS, 476, 3415-3424
9. *Radio observations of the double-relic galaxy cluster Abell 1240*
Hoang et al. 2018, MNRAS, 478, 2218-2233
10. *First evidence of diffuse ultra-steep-spectrum radio emission surrounding the cool core of a cluster*
Savini et al. 2018, MNRAS, 478, 2234-2242
11. *LOFAR discovery of radio emission in MACS J0717.5+3745*
Bonafede et al. 2018, MNRAS, 478, 2927-2938
12. *The LOFAR Two-metre Sky Survey - II. First Data Release*
Shimwell et al. 2019, A&A, accepted (arXiv:1811.07926)
13. *The evolutionary phases of merging clusters as seen by LOFAR*
Wilber et al. 2019, A&A, accepted (arXiv:1811.07929)
14. *Characterizing the radio emission from the binary galaxy cluster merger Abell 2146*
Hoang et al. 2019, A&A, accepted (arXiv:1811.09708)
15. *A LOFAR study of non-merging massive galaxy clusters*
Savini et al. 2019, A&A, accepted (arXiv:1811.08410)
16. *Radio observations of the merging galaxy cluster Abell 520*
Hoang et al. 2019, A&A, accepted (arXiv:1811.09713)
17. *Ultra-steep spectrum emission in the merging galaxy cluster Abell 1914*
Mandal et al. 2019, A&A, accepted (arXiv:1811.08430)
18. *A massive cluster at $z = 0.288$ caught in the process of formation: the case of Abell 959*
Bîrzan et al., MNRAS, submitted
19. *A joint XMM-Newton and NuSTAR observation of the galaxy cluster Abell 523*
Cova et al., A&A, submitted

Galaxy clusters: focus on mergers and non-thermal phenomena

ABSTRACT

Galaxy clusters hierarchically form by the aggregation of smaller structures. During cluster mergers, shocks and turbulence are produced in the intra-cluster medium and dissipate part of their energy into non-thermal components, such as magnetic fields and relativistic particles. These may eventually generate large scale diffuse synchrotron emission in the form of radio relics and radio halos. The processes originating these sources are still poorly understood and suggest a complex hierarchy of mechanisms that transport energy from cluster Mpc-scales into particle micro-scales.

1.1 Galaxy clusters

Galaxy clusters are the most massive gravitationally bound systems in the Universe, reaching masses up to $10^{15} M_{\odot}$ within linear sizes of a few Mpc. The largest amount ($\sim 80\%$) of the cluster mass is in dark matter, that shapes deep potential wells where baryons ($\sim 20\%$) virialize. Roughly 15% of the baryons in clusters are locked up into stars in galaxies (Lin et al. 2003), while the rest is in the form of hot and rarefied gas, referred to as intra-cluster medium (ICM), which fills the entire cluster volume.

According to the current picture of structure formation in the Universe, galaxy clusters form by gravitational collapse starting from small density fluctuations. The existence of such density perturbations can be inferred from the temperature perturbations of the cosmic microwave background (CMB), firstly observed with the COsmic Background Explorer (COBE) mission (Bennett et al. 1996). The *Planck* satellite (Planck Collaboration I 2011) provided the clearest view of such tiny fluctuations which represent the seeds of the cosmic structures observed in the present Universe. Once that the collapse started, matter is accumulated and grows via a hierarchical sequence of accretion of smaller systems (e.g. Press & Schechter 1974; Blumenthal et al. 1984; Kaiser 1984, 1986). These structures grow over cosmic time with the endpoint of their evolution being today massive clusters of galaxies (e.g. Voit 2005; Kravtsov & Borgani 2012, for reviews). This scenario is supported by both observations and numerical simulations (e.g. Springel et al. 2006, for a review).

There are two different regimes of growth of the perturbations: linear and non-linear. The two regimes can be distinguished defining the density fluctuation (or overdensity)

$$\delta_c = \frac{\rho - \langle \rho \rangle}{\langle \rho \rangle} \quad (1.1)$$

where $\langle \rho \rangle$ is the mean mass density of the Universe. The linear regime acts as long as $\delta_c \ll 1$ and can be easily treated (see Peebles 1980, 1993; Coles & Lucchin 1995, 2002). Nevertheless, galaxy clusters are highly non-linear ($\delta_c \gg 1$) objects, and this requires more complex approaches for studying the evolution of perturbations in this particular regime.

Nowadays, numerical methods constitute the frontier in the study of cosmic structure formation, being the only instruments available to follow the non-linear evolution of perturbations. The increasing computational power made possible to develop large N -body simulations that allow to trace the dark matter evolution in a cosmological context. Among the largest runs, we mention the Millenium simulation (Springel et al. 2005) and its updates (Millennium-II, Boylan-Kolchin et al. 2009; Millennium-XXL Angulo et al. 2012), and the Illustris simulation (Vogelsberger et al. 2014), which complements the N -body simulation with hydrodynamic simulations, required to model radiative processes such as cooling and feedback (Fig. 1.1).

1.1.1 Mass determination

In the present Universe, clusters may contain hundreds to thousands of galaxies that move with typical velocity dispersion of $\sigma_V \sim 1000 \text{ km s}^{-1}$. The crossing time of a cluster of size r can be estimated as

$$\begin{aligned} t_{cr} &= \frac{\sigma_V}{r} \\ &\simeq \left(\frac{r}{1 \text{ Mpc}} \right) \left(\frac{10^3 \text{ km s}^{-1}}{\sigma_V} \right) \quad [\text{Gyr}] \end{aligned} \quad (1.2)$$

thus, in a Hubble time ($\sim 13.7 \text{ Gyr}$), the system has enough time to dynamically relax in its center while its outskirts are still affected by the accretion physics (e.g. Walker et al. 2019, for a review). Therefore, under the assumption of virial equilibrium, it is possible to estimate the cluster virial mass via

$$\begin{aligned} M_{vir} &\simeq \frac{\sigma_V^2 r_{vir}}{G} \\ &\simeq 10^{15} \left(\frac{r_{vir}}{1 \text{ Mpc}} \right) \left(\frac{\sigma_V}{10^3 \text{ km s}^{-1}} \right)^2 \quad [M_\odot] \end{aligned} \quad (1.3)$$

where G is the gravitational constant, σ_V^2 can be inferred from the measurement of the radial velocity dispersion of a number of cluster galaxies ($\sigma_V^2 = 3\sigma_r^2$), and r_{vir} takes the name of virial radius.

Another simple method to estimate the mass of a galaxy cluster is based, again, on the assumption that the cluster is relaxed and relies on measurements of ICM quantities (see Section below). Under the hypotheses of spherical symmetry and hydrostatic equilibrium of the ICM in the cluster gravitational potential, is it possible to derive the mass inside a given radius via

$$M(< r) = -\frac{kTr}{\mu m_p G} \left(\frac{d \ln \rho}{d \ln r} + \frac{d \ln T}{d \ln r} \right) \quad (1.4)$$

where k is the Boltzmann constant, μ is the mean molecular mass of the considered gas (hereafter $\mu = 0.6$, which is a typical value for the ICM), m_p is the proton mass, and the density ρ and temperature T profiles can be inferred from X-ray observations (e.g. Ettori et al. 2013, for a review). Clearly, Eq. 1.4 may fail in the case of dynamically disturbed clusters such as merging systems,

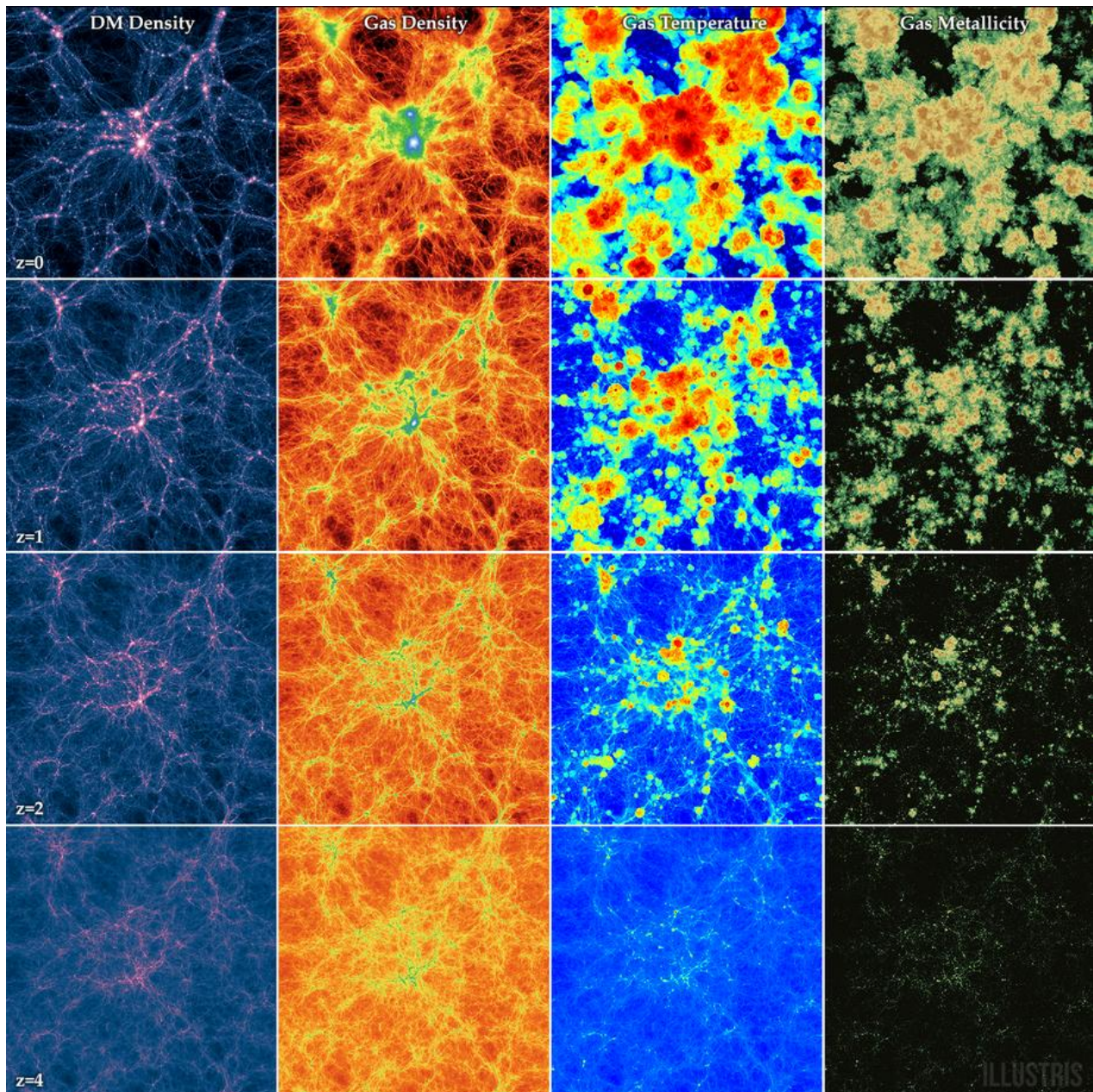


Figure 1.1: Time evolution of the the most massive cluster at $z = 0$ in the Illustris simulation. The panels display the evolution of a box slice that covers the entire simulation volume (106.5 Mpc width) from $z = 4$ to $z = 0$, showing four projections: dark matter density, gas density, gas temperature, and gas metallicity. From Vogelsberger et al. (2014).

where the merger introduces substantial deviations from hydrostatic equilibrium and spherical symmetry, leading to large errors in the determination of the mass (e.g. Evrard et al. 1996; Roettiger et al. 1996; Schindler 1996; Rasia et al. 2006, 2012; Meneghetti et al. 2010).

A third, independent, method to estimate the cluster mass is based on gravitational lensing, i.e. on the images of distant objects that result distorted by the gravitational potential of the cluster (e.g. Bartelmann & Schneider 2001; Refregier 2003; Schneider 2005; Bartelmann 2010; Treu 2010, for reviews). Lensing effects are generally divided into strong and weak lensing events. The former occur in the cores of some massive galaxy clusters, leading to the formation of “gravitational arcs” and/or to the formation of systems of multiple images of the same source. The latter, which can only be measured statistically, are impressed on the shape of distant galaxies that lie on the sky at large

angular distances from the cluster centers. Gravitational lensing analysis can be used to map the mass distribution in galaxy clusters and, in contrast with the other two methods mentioned above, it is independent of the equilibrium state. However, lensing measures the mass along the line of sight, thus it is sensitive to projection effects. To infer the true mass, lensing maps must be deprojected assuming a cluster shape, and this possibly introduces biases in the mass and concentration measurement (e.g. Gavazzi 2005; Oguri et al. 2005; Sereno & Zitrin 2012).

Obviously, multi-probe approaches can determine in a more accurate way the distribution and the physical properties of matter in galaxy clusters from the inner regions out to the peripheries (e.g. Zaroubi et al. 1998; Reblinsky 2000; Doré et al. 2001; Fox & Pen 2002; Puchwein & Bartelmann 2006; Mahdavi & Chang 2011; Morandi et al. 2012; Tchernin et al. 2018). In this spirit, the CLUster Multi-Probes in Three Dimensions (CLUMP-3D) project aims to get the unbiased intrinsic properties of galaxy clusters by exploiting rich datasets ranging from X-ray, to optical, to radio wavelengths (Sereno et al. 2017; Chiu et al. 2018; Umetsu et al. 2018).

1.2 The intra-cluster medium

1.2.1 Microphysics

During the cluster formation process, the primordial cosmic gas collapses into dark matter halos and undergoes shocks and adiabatic compression, settling down at densities of $n_e \sim 10^{-3} - 10^{-4} \text{ cm}^{-3}$ and temperatures of $T \sim 10^7 - 10^8 \text{ K}$ (i.e. $kT \sim 1 - 10 \text{ keV}$). The mean free path in a fully ionized plasma without a magnetic field is determined by Coulomb collisions (Spitzer 1956) via

$$l_{mfp} \simeq 15 \left(\frac{n_e}{10^{-3} \text{ cm}^{-3}} \right)^{-1} \left(\frac{kT}{8 \text{ keV}} \right)^2 \left(\frac{40}{\ln \Lambda} \right) \quad [\text{kpc}] \quad (1.5)$$

where $\ln \Lambda$ is the Coulomb logarithm. Compared to the Larmor gyroradius-scale (Braginskii 1965)

$$r_L \simeq 3 \times 10^{-12} \left(\frac{kT}{10 \text{ keV}} \right) \left(\frac{B}{\mu\text{G}} \right)^{-1} \quad [\text{kpc}] \quad (1.6)$$

this implies $l_{mfp} \gg r_L$. In this regime, the plasma is called *weakly collisional* and plasma instabilities and kinetic effects play important roles in regulating microphysical properties (e.g. Levinson & Eichler 1992; Pistinner et al. 1996; Schekochihin et al. 2010; Brunetti & Lazarian 2011a; Yan & Lazarian 2011; Santos-Lima et al. 2014, 2017). In fact, the collisional parameter in the ICM (namely the ratio of the Coulomb collision frequency and plasma frequency) is $R_C \sim 10^{-16}$ and for $R_C \ll 1$ wave-particle interactions become more important than Coulomb collisions. On the one hand, the possibility that wave-particle interactions can mediate momentum exchange at a rate faster than Coulomb particle-particle interactions provides a motivation for a fluid treatment of the ICM (e.g. Santos-Lima et al. 2017, and references therein). On the other hand, the importance of micro-instabilities and collisionless kinetic processes in the ICM open to the possibility to a fraction of the energy of the large-scale motions that are generated by the process of cluster formation into electromagnetic fluctuations and collisionless particle acceleration mechanisms on much smaller scales (e.g. Brunetti & Jones 2014, for a review). This is fundamental to understand the processes leading to the formation of diffuse radio sources in merging galaxy clusters (Section 1.2.4).

1.2.2 Thermal emission

At temperatures $T \gtrsim 3 \times 10^7$ (i.e. $kT \gtrsim 2 \text{ keV}$) and typical ICM metallicities ($0.1 - 1 Z_\odot$), thermal bremsstrahlung in the X-rays is the dominant cooling process in the ICM (e.g. Sarazin 1986; Böhringer & Werner 2010, for reviews). In this case, the specific emissivity per unit frequency ν is

$$\varepsilon_{\nu} \propto n_e^2 T_e^{-1/2} \exp(-h\nu/kT_e) \quad (1.7)$$

and the ICM temperature and density can be determined from the X-ray spectral analysis (h is Planck constant). At lower temperatures ($kT \lesssim 2$ keV), line emission becomes a more important or, eventually, the dominant cooling process and it can be used to measure abundances of heavy elements and the cluster redshift as well as an additional temperature discriminator.

The cluster X-ray surface brightness (SB) is easier to characterize than the temperature as it requires less net counts. The SB analysis is usually performed in a soft X-ray band (e.g. 0.5 – 2.0 keV), i.e. where the performances of the present X-ray mirrors and detectors are maximized and the bolometric emissivity $\varepsilon = \int_{\nu} \varepsilon_{\nu} d\nu \propto n_e^2 T_e^{1/2}$ does not depend very much from the gas temperature, and can be used to determine the distribution (hence, the mass) of the cluster gas (e.g. Etori 2000; Etori & Molendi 2011; Etori et al. 2013).

The general morphology of the ICM can be approximated by the hydrostatic isothermal model (Cavaliere & Fusco-Femiano 1976, 1978), leading to a density profile described by

$$n(r) = n(0) \left[1 + \left(\frac{r}{r_c} \right)^2 \right]^{-\frac{3}{2}\beta} \quad (1.8)$$

where $n(0)$ is the central density, r_c is the core radius, and β is the slope parameter, originating from the ratio between kinetic energy in the galaxies and thermal energy of the gas. This distribution for the gas density results in the well known β -model SB profile

$$\text{SB}(r) = \text{SB}(0) \left[1 + \left(\frac{r}{r_c} \right)^2 \right]^{\frac{1}{2} - 3\beta} \quad (1.9)$$

that is routinely applied to fit the ICM emission (e.g. Jones & Forman 1984; Vikhlinin et al. 1999) proving a good description of the data. Nevertheless, new empirical parametric models of increasing complexity have been introduced to overcome the overestimation of the true profiles by the β -model at $r \gg r_c$ (e.g. Vikhlinin et al. 2006). The β -model also underestimates the centrally peaked density profile of cooling clusters (see below) as a consequence of the cusped nature of the dark matter profile (Pratt & Arnaud 2002; Arnaud 2009).

A dichotomy exists between cool-core (CC) and non cool-core (NCC) clusters (e.g. Molendi & Pizzolato 2001), depending whether their core region shows a drop in the temperature profile or not. The reason of this drop is a natural consequence of the strongly peaked X-ray emissivity of relaxed systems (Fig. 1.2) that leads to efficient cooling of the gas in this denser environment. To date, the active galactic nucleus (AGN) feedback represents the most promising scenario to counter-balance this process and to reconcile the low cooling flow rates observed (e.g. Peterson & Fabian 2006, for a review). Conversely, disturbed systems exhibit shallower X-ray emissivity (Fig. 1.2), hence lower cooling rates. For this reason there is a connection between the properties of the cluster core to its dynamical state: relaxed (i.e. in equilibrium) systems naturally form a CC while NCCs are typically found in unrelaxed objects (e.g. Leccardi et al. 2010), where the effects of energetic events such as mergers have tremendous impact on their core, leading either to its direct disruption (e.g. Russell et al. 2012; Rossetti et al. 2013; Wang et al. 2016) or to its mixing with the surrounding hot gas (ZuHone et al. 2010).

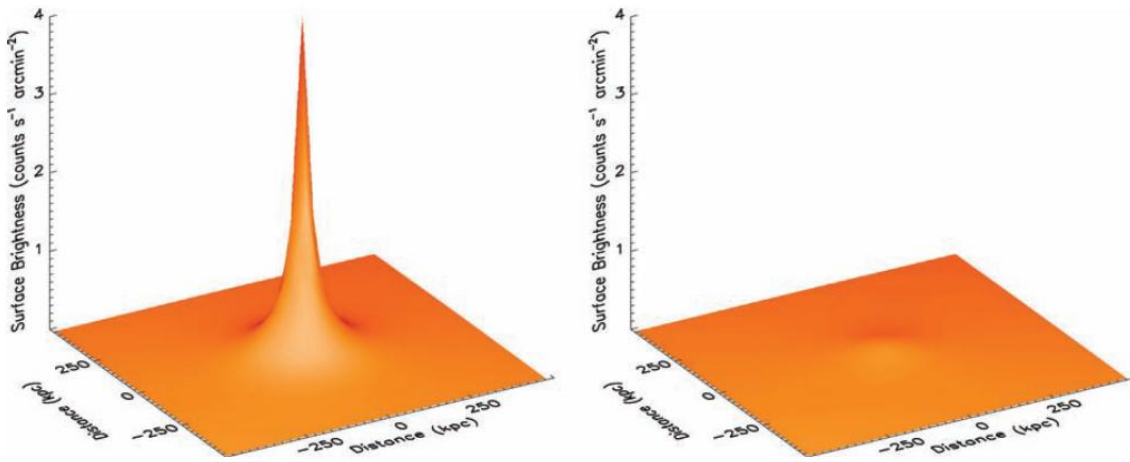


Figure 1.2: The three-dimensional representation of the projected SB for the CC cluster Abell 2029 (*left*) and the NCC cluster Abell 2319 (*right*) scaled to appear as they would appear if observed at the same redshift. From Million & Allen (2009).

1.2.3 The Sunyaev-Zel'dovich effect

The presence of hot electrons in the ICM can lead to a small distortion of the CMB spectrum via inverse Compton (IC) scattering. This physical process, known as Sunyaev-Zel'dovich (SZ) effect¹ (Sunyaev & Zel'dovich 1972), provides a complementary tool to study the thermodynamical properties of the ICM. In particular, thanks to the new state of the art high angular resolution instruments working in the millimeter waves, such as the New IRAM KIDs Array 2 (NIKA2; Adam et al. 2018a) and the MULTiplexed Squid Tes Array at Ninety Gigahertz 2 (MUSTANG2; Dicker et al. 2014), the study of sub-structures in the ICM through SZ effect is entering in a new era (e.g. Korngut et al. 2011; Young et al. 2015; Adam et al. 2016, 2017a,b, 2018b).

Assuming a thermal distribution for the electrons in the ICM, the change in the background CMB intensity is $\Delta I_{cmb}/I_{cmb} = f(\nu)y_e$, where $f(\nu)$ is the spectral shape function that gives the dependence of the SZ effect from the frequency (e.g. Birkinshaw 1999; Carlstrom et al. 2002), and y_e is the Comptonization parameter. The latter provides the integrated electron pressure of the ICM along the line of sight and is defined as

$$y_e = \frac{\sigma_T}{m_e c^2} \int n_e T_e dl \quad (1.10)$$

where σ_T is the Thomson cross-section, m_e is the electron mass, and c is the speed of light. For typical ICM temperatures and densities, the relative change in CMB intensity is small, i.e. $\Delta I_{cmb}/I_{cmb} \sim 10^{-4} - 10^{-5}$. This effect results in a distortion in the black body shape of the CMB (Fig. 1.3, left panel) and now it represents one of the most effective tools to search galaxy clusters. In fact, this effect is independent of the redshift of the (spatially resolved) source responsible for the up-scattering of the CMB photons, and it can be detected in maps like those made out of *Planck* data (Planck Collaboration I 2011), where a cluster appears as a decrement or an increment of emission in the microwave sky below or above 218 GHz, respectively (Fig. 1.3, right panel). Currently, three large-scale experiments in operation are providing many more SZ selected clusters up to $z = 1$ and beyond: the South Pole Telescope (SPT; Vanderlinde et al. 2010), the Atacama Cosmology Telescope (ACT; Marriage et al. 2011) and the *Planck* satellite (Planck Collaboration VIII 2011).

¹Formally, this should be referred to as thermal SZ effect (tSZ) to distinguish it from the kinematic SZ effect (kSZ, Sunyaev & Zeldovich 1980), which is the scattering signal caused by the bulk motion of the cluster gas. The latter has an amplitude more than an order of magnitude lower than the thermal effect.

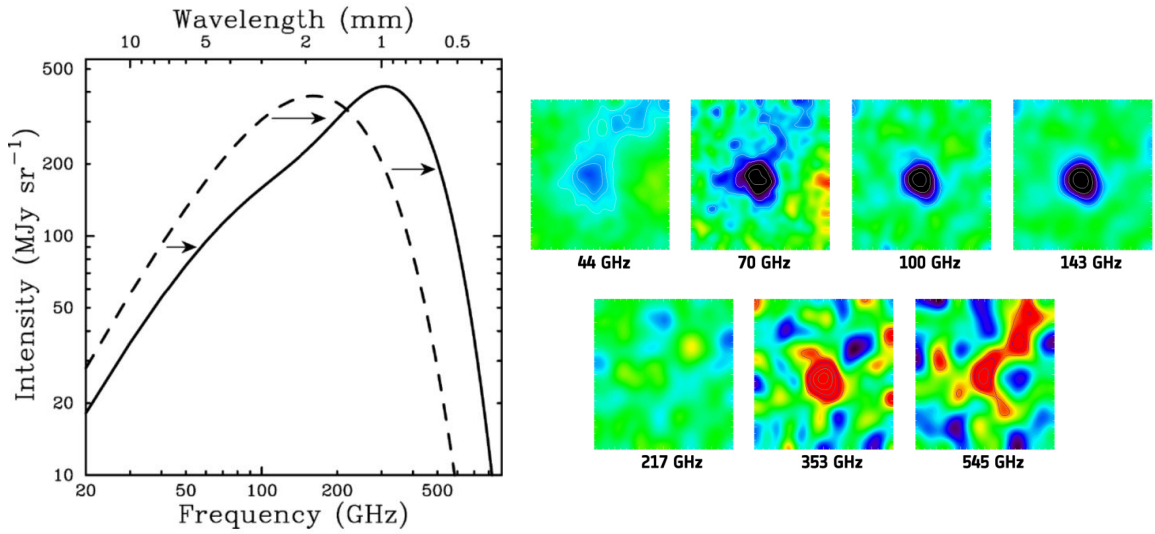


Figure 1.3: *Left:* CMB spectrum, undistorted (*dashed line*) and distorted by the SZ effect (*solid line*). To emphasize the effect, the SZ distortion shown is for a fictional cluster 1000 times more massive than a typical massive galaxy cluster. From Carlstrom et al. (2002). *Right:* *Planck* view on the cluster Abell 2319 at various frequencies (see panels) demonstrating that the cluster appears as a decrement on the photon number for $\nu < 218$ GHz and as an increment above 218 GHz as result of the SZ effect. Credit: ESA.

1.2.4 Non-thermal components

Radio observations of giant diffuse synchrotron emission in some galaxy clusters (e.g. Ferrari et al. 2008; Feretti et al. 2012; van Weeren et al. 2019, for reviews) probe the presence of non-thermal components, i.e. (\sim GeV) relativistic particles (or cosmic rays, CR) and ($\sim \mu$ G) magnetic fields, spread on Mpc-scales in the ICM. These radio sources represent one of the main topics of this Thesis, and will be thoroughly described in Section 1.4. Nowadays, there is a broad consensus that the hierarchical process of structure formation in the Universe plays an important role in the generation of non-thermal components in ICM (e.g. Dolag et al. 2008; Brunetti & Jones 2014, for reviews).

Shocks occurring during the cluster progressive assembly (Section 1.3.2) are believed to be the main injectors of cosmic ray electrons (CRE) and protons (CRp) in the ICM (e.g. Norman et al. 1995; Kang et al. 1996; Miniati et al. 2001; Ryu et al. 2003). The processes leading to the (re)acceleration of particles at shocks and turbulence will be discussed in Sections 1.5 and 1.6. Other possible generators of CRs in clusters are: individual galaxies, that can inject high-energy particles through relativistic AGN outflows (e.g. Miley 1980) and with phenomena related to star formation activity, such as stellar winds and supernova explosions (e.g. Völk et al. 1996; Bykov 2001), and magnetic reconnection regions (e.g. Lazarian & Brunetti 2011; Brunetti & Lazarian 2016).

Relativistic particles undergo energy losses that limit their life-time in the ICM and the maximum energy at which they can be accelerated by various mechanisms (e.g. Sarazin 1999; Brunetti & Jones 2014), as shown in Fig. 1.4.

For CRE, Coulomb losses are the dominant cooling process at low energies while radiative losses are dominant at high energies. The time evolution of a particle with Lorentz factor γ (typically $\gamma \sim 10^4$ for CRE) radiating via synchrotron and IC emission is

$$\frac{d\gamma}{dt} \propto - (B^2 + B_{cmb}^2) \gamma^2 \quad (1.11)$$

where B is the intensity of the magnetic field in the relativistic plasma and

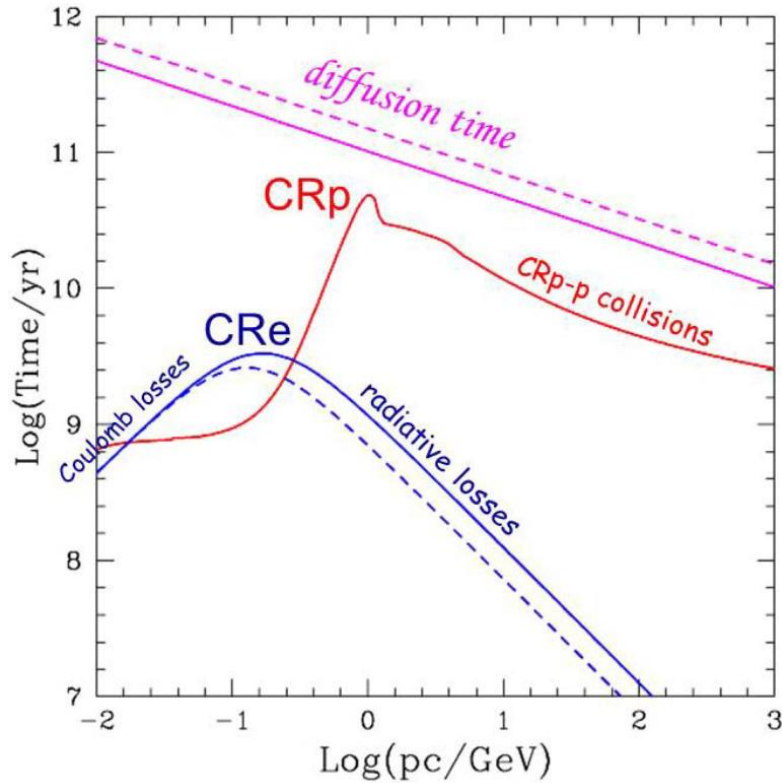


Figure 1.4: Life-time of CRp (red) and CRe (blue) in the ICM at $z = 0$, compared with the CR diffusion time on Mpc-scales (magenta). The most relevant channels of CR energy losses at different energies are highlighted in the panel. Adopted physical parameters are: $n_e = 10^{-3} \text{ cm}^{-3}$, $B = 1$ (solid) and $3 \mu\text{G}$ (dashed). Adapted from Blasi et al. (2007).

$$B_{cmb} = 3.25(1+z)^2 \quad [\mu\text{G}] \quad (1.12)$$

is the equivalent magnetic field due to IC with the CMB at redshift z . When $B > B_{cmb}$, synchrotron is the dominant radiative process, otherwise IC prevails. At a given emitting frequency, the particle life-time is maximized for $B = B_{cmb}/\sqrt{3}$. The maximum life-time of CRe (~ 1 Gyr) occurs at energies ~ 100 MeV, where radiative losses are roughly equivalent to Coulomb losses. The CRe that emit synchrotron radiation in the radio band (GHz) have higher energies (\sim several GeV), and their life-time is shorter (~ 0.1 Gyr).

For CRp, energy losses are dominated by ionization and Coulomb scattering at low energies and by inelastic proton-proton collisions at higher energies. The CRp are long-living particles in the ICM (Völk et al. 1996; Berezhinsky et al. 1997), and are confined for several Gyr within the cluster volume (Fig. 1.4).

Knowledge of the origin and evolution of magnetic fields in galaxy clusters is still very limited (e.g. Carilli & Taylor 2002; Govoni & Feretti 2004; Ryu et al. 2012, for reviews). The information on magnetic fields is directly provided from radio observations of cluster-wide diffuse sources and from studies of Faraday rotation of polarized radio sources embedded in clusters or behind them (e.g. Kim et al. 1990, 1991; Clarke et al. 2001; Bonafede et al. 2010, 2013). Further techniques adopted to infer the presence and give limits on the ICM magnetic field strengths are X-ray analysis of IC emission (e.g. Rephaeli et al. 2008, for a review) and physical considerations on the sharpness of cold fronts (e.g. Vikhlinin et al. 2001a). These methods established the presence of magnetic fields with strengths of the order of few μG at the center of NCC clusters, while CC systems show strengths that are typically higher, possibility due the dynamics of the central regions (e.g. Perley

& Taylor 1991; Taylor & Perley 1993; Allen et al. 2001). Observations suggest that the magnetic fields decline with cluster radius, with a profile similar to that of the thermal gas (e.g. Dolag et al. 2001; Govoni et al. 2001a; Murgia et al. 2004). The presence of diffuse radio emission in some cluster outskirts (Section 1.4.1) indicates that $\gtrsim \mu\text{G}$ fields can exist even at large distances ($\gtrsim \text{Mpc}$) from the cluster centers. However, these sources trace particular regions where the magnetic fields may be locally enhanced by the passage of shock waves.

To explain the field strengths of the order of few μG measured in clusters, some amplification processes are required (e.g. Dolag et al. 2008; Donnert et al. 2018, for reviews). Indeed, although the magnetic field strength is naturally increased by compression during the gravitational collapse, this is not enough to reach the observed values of magnetic field (Fig. 1.5). From early numerical magneto-hydro dynamical simulations of merging galaxy clusters (e.g. Roettiger et al. 1996, 1997, 1999b), it was clear that shocks, bulk flows and turbulence play an important role in the amplification of the magnetic fields. In particular, the turbulent dynamo is expected to be the main process for the (non-linear) amplification of the field seeds (e.g. Ryu et al. 2008; Iapichino & Brüggen 2012; Iapichino et al. 2017; Miniati 2014, 2015; Vazza et al. 2018b), while turbulent diffusion is expected to spread magnetic fields out to cluster outskirts (e.g. Xu et al. 2009). As a result, the final structure and strength of the fields are totally driven by the formation process and the information on the initial seeds is then lost. In this respect, it has been shown that observing magnetic fields in low-density environments such as filaments is more useful than observing cluster magnetic fields to infer their possible origin (e.g. Brüggen et al. 2005; Donnert et al. 2009; Vazza et al. 2014, 2015b, 2017a); however, this kind of measurement has not been possible so far.

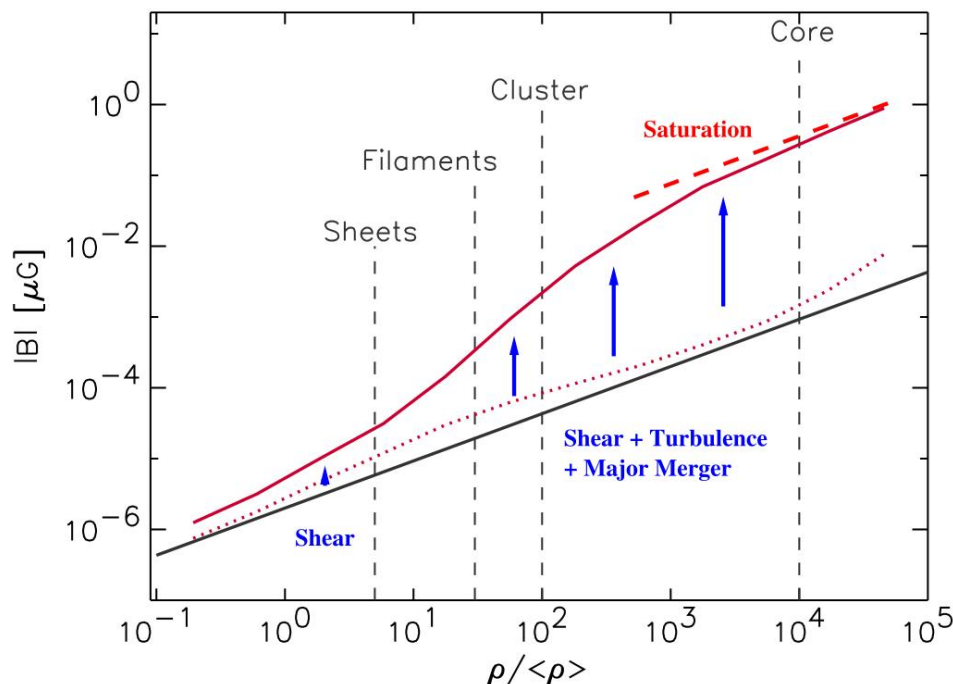


Figure 1.5: The strength of the magnetic field as a function of baryonic overdensity within a cosmological simulation. The *solid black line* shows the expectation for a purely adiabatic evolution, the *solid red line* gives the mean field strength at a given overdensity within a cosmological simulation (Dolag et al. 2005). While the latter is close to the adiabatic value in underdense regions, in clusters there is a significant inductive amplification due to shear flows and turbulence; this amplification however saturates in the cluster cores. At any given density, a large fraction of particles remains close to the adiabatic expectation, as shown by the *dotted line*, which gives the median of the distribution at each density. From Dolag et al. (2008).

At present, it is debated whether the seed fields to amplify have *primordial* or *galactic* origin. In the first case, magnetic fields are generated in the early Universe prior to recombination (e.g. Grasso & Rubinstein 2001; Widrow et al. 2012; Subramanian 2016, for reviews). A prediction of this class of models is that magnetic fields fill the entire volume of the Universe. In the second scenario, galactic winds (e.g. Völk & Atoyan 2000), AGN ejecta (e.g. Enßlin et al. 1997; Furlanetto & Loeb 2001) and supernova explosions in normal and starburst galaxies (e.g. Kronberg et al. 1999) contribute to deposit magnetic fields in the ICM. In this case, magnetic fields should be prevalently located around galaxies and within clusters.

1.3 Galaxy cluster mergers

Major mergers between galaxy clusters are the most energetic phenomena in the Universe after the Big Bang, with $10^{63} - 10^{64}$ erg of kinetic energy dissipated in a crossing time-scale (\sim Gyr) during the collision. At this stage shock waves, cold fronts, hydrodynamic instabilities, turbulence, and non-thermal components are generated in the ICM, making merging clusters unique probes to study several aspects of plasma astrophysics (e.g. Sarazin 2002; Markevitch & Vikhlinin 2007; Dolag et al. 2008; Feretti et al. 2012; Brunetti & Jones 2014; Molnar 2015; ZuHone & Roediger 2016; van Weeren et al. 2019, for reviews).

In the X-rays, ROSAT and ASCA observations revealed, for the first time, that many clusters show evidence of the accretion of smaller masses and others undergo major mergers of two nearly equal components (e.g. Briel et al. 1991; Henry & Briel 1991; Böhringer et al. 1994; Markevitch et al. 1999; Henriksen et al. 2000). Before the launch of the last generation of X-ray satellites, namely *Chandra* and *XMM-Newton*, the main information about mergers was based on morphology. With the spatially resolved spectroscopy and high-resolution imaging offered by the new instruments, the situation has radically changed, and sophisticated algorithms have been developed to achieve good and reliable temperature maps (e.g. Peterson et al. 2004; Bourdin et al. 2004; Diehl & Statler 2006; Sanders 2006), since the temperature is the more accurate tracer of the energy transfer from the collision to the X-ray gas itself. Strong signatures of the merging events such as shocks and cold fronts (see Section 1.3.2) have been detected in these maps and are now well established as common merger features (e.g. Markevitch & Vikhlinin 2007, for a review).

Optical data are also a powerful way to investigate the presence and the dynamics of cluster mergers (e.g. Girardi & Biviano 2002, for a review). The spatial distribution and kinematics of galaxy members allow to detect sub-structures and to analyze possible pre- and post-merging groups, and to distinguish between evolving mergers and remnants. Moreover, optical data are complementary to X-ray information because the ICM and galaxies react on different time-scales during a collision (e.g. Roettiger et al. 1997).

It has been shown that combining optical and X-ray data is the most effective approach to unveil the complex history of merging clusters (e.g. Arnaud et al. 2000; Maurogordato et al. 2000, 2011; Barrena et al. 2009, 2013, 2014; Boschin et al. 2009, 2012a,b, 2013; White et al. 2015; Girardi et al. 2016; Nascimento et al. 2016; Golovich et al. 2016, 2017, 2018; Benson et al. 2017; Caglar & Hudaverdi 2017; Boschin & Girardi 2018). These studies have revealed various peculiar properties of the galaxy distribution in the individual merging clusters, such as strong signatures in the density and velocity distribution, and alignments that can be used to infer the dynamics of the merger.

The full understanding of the complex processes at work in merging requires dedicated numerical simulations. Much progress has been made in this field, starting from the pioneering works of Schindler & Mueller (1993) and Roettiger et al. (1997). Ricker & Sarazin (2001) described the violent relaxation of gas in a dark matter potential well for a variety of idealized merging systems, paying special attention to the impact parameter and the mass ratio between units. Poole et al. (2006)

analyzed mergers of idealized relaxed clusters with sophisticated simulations including cooling and star formation, and detected the major transient signatures existing in observed temperature maps. Nowadays, tailored numerical simulations are customarily run attempting to reproduce the X-ray, optical, SZ and radio properties of the most complex merging galaxy clusters (e.g. Mastropietro & Burkert 2008; van Weeren et al. 2011a; Brüggén et al. 2012b; Machado & Lima Neto 2013, 2015; Molnar et al. 2013; Molnar & Broadhurst 2017, 2018; Donnert 2014; Machado et al. 2015; Ng et al. 2015; Zhang et al. 2015, 2018; Donnert et al. 2017).

1.3.1 Impact velocity

There are some simple analytical arguments which can be used to estimate the kinematics of an individual binary merger collision (see Ricker & Sarazin 2001; Sarazin 2002). The kinematic quantities describing the merger are defined in Fig. 1.6.

Following Sarazin (2002), we assume that two sub-clusters with mass M_1 and M_2 merge at time t_m and that have fallen together from a large distance d_0 with nonzero angular momentum. It can be assumed that the two sub-clusters are point masses initially expanding away from one another in the Hubble flow and that their radial velocity was zero at their largest separation d_0 . The collapse can be treated as the orbit of two point masses, and their largest separation will be given by the Kepler third law as

$$\begin{aligned} d_0 &\simeq [2G(M_1 + M_2)]^{1/3} \left(\frac{t_m}{\pi}\right)^{2/3} \\ &\simeq 4.5 \left(\frac{M_1 + M_2}{10^{15} M_\odot}\right)^{1/3} \left(\frac{t_m}{10^{10} \text{ yr}}\right)^{2/3} \quad [\text{Gyr}] \end{aligned} \quad (1.13)$$

where the exact value of d_0 does not significantly affect the collision velocity as long as d_0 is large and the infall velocity approaches free-fall from infinity. Conserving angular momentum and energy it is possible to derive the merger velocity at distance d , i.e.

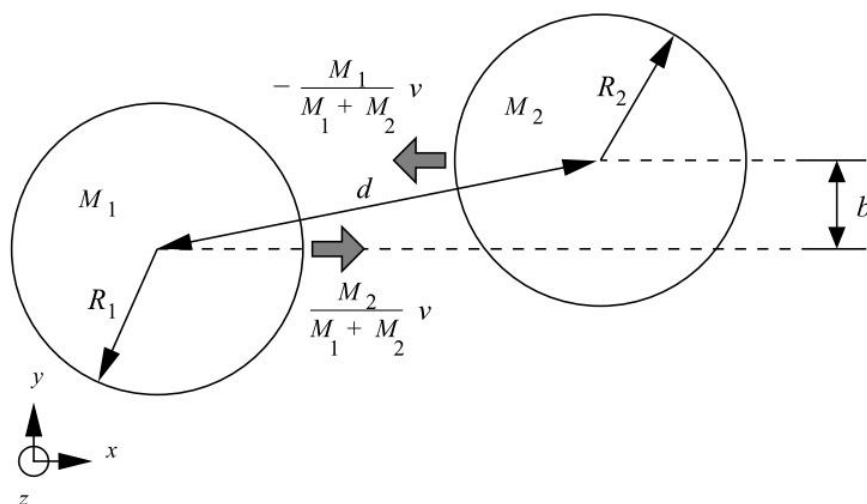


Figure 1.6: A schematic diagram of the kinematics for a merger between two sub-clusters of masses M_1 and M_2 and radii R_1 and R_2 . The separation of the cluster centers is d , and the impact parameter is b , and the initial relative velocity is v . From Ricker & Sarazin (2001).

$$v \simeq 2930 \left(\frac{M_1 + M_2}{10^{15} M_\odot} \right)^{1/2} \left(\frac{d}{1 \text{ Mpc}} \right)^{-1/2} \left[\frac{1 - \frac{d}{d_0}}{1 - \left(\frac{b}{d_0} \right)^2} \right]^{-1/2} \quad [\text{km s}^{-1}] \quad (1.14)$$

where b is the impact parameter (Fig. 1.6). Because of the high impact velocity, the motions involved in mergers between galaxy clusters are moderately supersonic. As a consequence, shock waves are driven in the ICM (see Section below).

1.3.2 Shocks

The shock strength can be characterized by its Mach number, that for a shock moving at speed V_{sh} is

$$\mathcal{M} = \frac{V_{sh}}{c_s} \quad (1.15)$$

where

$$\begin{aligned} c_s &= \sqrt{\frac{\gamma_{ad} k T}{\mu m_p}} \\ &\simeq 1150 \sqrt{\frac{k T}{5 \text{ keV}}} \quad [\text{km s}^{-1}] \end{aligned} \quad (1.16)$$

is the sound speed in the preshock medium, and γ_{ad} is the adiabatic index (assumed to be 5/3 in Eq. 1.16). Shocks generated in cluster mergers are weak ($\mathcal{M} \lesssim 3 - 5$) and dissipate a substantial fraction of the energy involved during a merger in gas heating (e.g. Schindler & Mueller 1993; Burns 1998; Roettiger et al. 1999a; Ricker & Sarazin 2001). Stronger shocks ($\mathcal{M} \sim 10 - 100$) associated with the accretion of cold gas onto gravitationally attracting nodes are expected in the tenuous intergalactic medium (e.g. Miniati et al. 2001). However, as shown in Fig. 1.7, these shocks are less important than merger shocks in terms of dissipated energy in the ICM because they propagate with lower velocities into low density environments (e.g. Ryu et al. 2003; Vazza et al. 2009a).

The Rankine-Hugoniot jump conditions are used to relate the quantities upstream and downstream (subscripts u and d) of the shock (e.g. Landau & Lifshitz 1959), as shown in Fig. 1.8. For a monatomic gas (i.e. $\gamma_{ad} = 5/3$) undergoing a shock with Mach number \mathcal{M} , the ratios in temperature T , density n , and pressure P are given by

$$\mathcal{R} \equiv \frac{T_d}{T_u} = \frac{5\mathcal{M}^4 + 14\mathcal{M}^2 - 3}{16\mathcal{M}^2} \quad (1.17)$$

$$\mathcal{C} \equiv \frac{n_d}{n_u} = \frac{4\mathcal{M}^2}{\mathcal{M}^2 + 3} \quad (1.18)$$

$$\mathcal{P} \equiv \frac{P_d}{P_u} = \frac{5\mathcal{M}^2 - 1}{4} \quad (1.19)$$

and the Mach number can be derived from the analysis of the emission profiles under some basic assumptions. The density ratio, also known as compression ratio, is related to the jump in temperature via

$$\frac{1}{\mathcal{C}} = [4(\mathcal{R} - 1)^2 + \mathcal{R}]^{1/2} - 2(\mathcal{R} - 1). \quad (1.20)$$

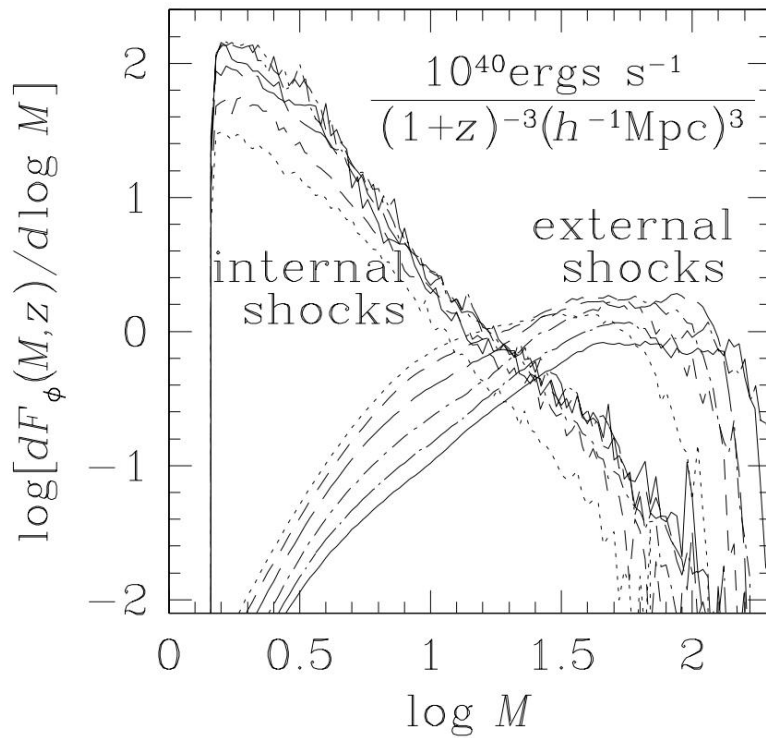


Figure 1.7: Distribution of the energy flux at shocks surfaces as a function of the shock Mach number from numerical (cosmological) simulations. Shocks are divided into internal and external categories. External shocks are defined as shocks forming when never-shocked, low-density, gas accreted onto non-linear structures, such as filaments, while internal shocks form within the regions bounded by external shocks. From Ryu et al. (2003).

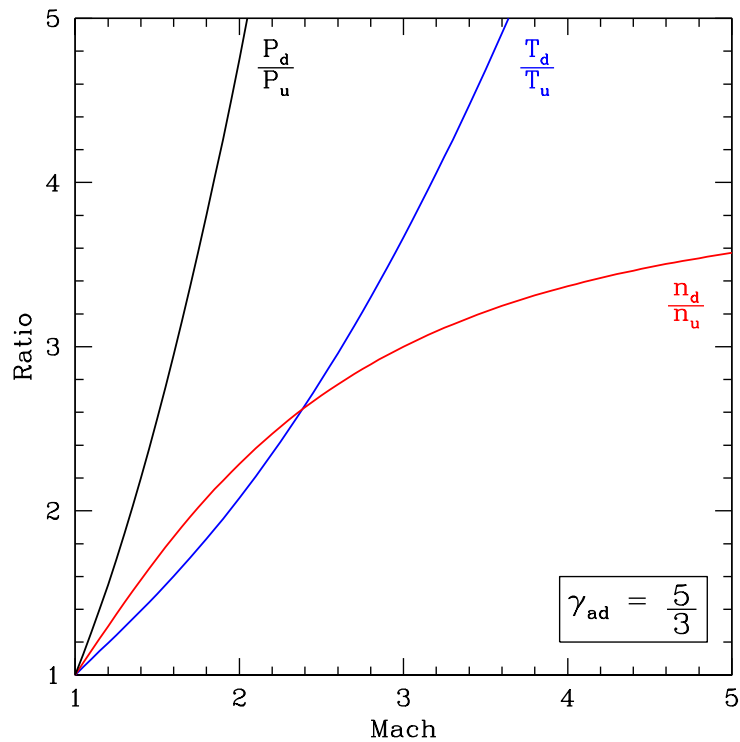


Figure 1.8: Temperature, density, and pressure ratios versus the shock Mach number (assuming $\gamma_{ad} = 5/3$). Note that when the Mach number is $\mathcal{M} \rightarrow \infty$, the compression factor is $\mathcal{C} \rightarrow 4$.

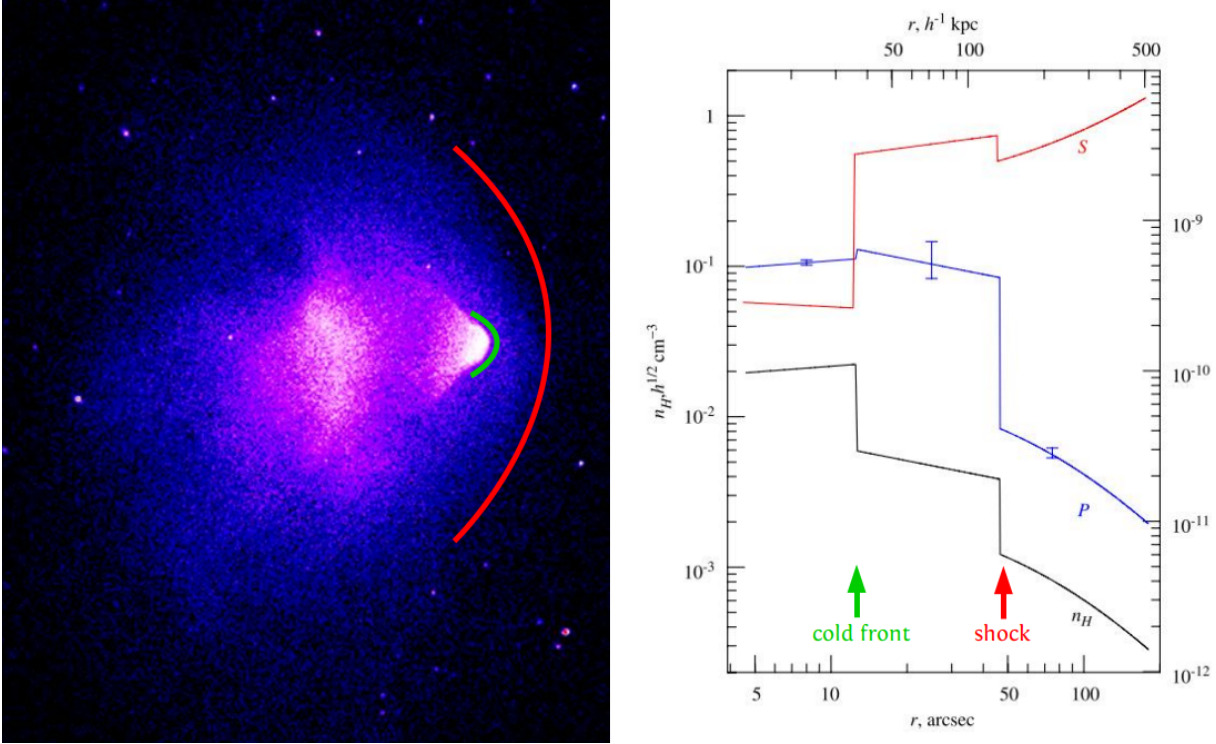


Figure 1.9: *Left:* *Chandra* X-ray image of 1E 0657-56, i.e. the Bullet Cluster (Markevitch et al. 2002; Markevitch 2006). *Right:* radial profiles for the gas density (n), pressure (P) and specific entropy (S) in a sector crossing the cold front (green) and shock front (red). From Markevitch & Vikhlinin (2007).

Observations in the X-rays have been customarily used to search for and characterize shocks in galaxy clusters (e.g. Markevitch & Vikhlinin 2007, for a review). Indeed, the temperature jump (Eq. 1.17) can be determined by spectral analysis in regions upstream and downstream the front, while the density jump (Eq. 1.18) can be inferred from the SB analysis across the discontinuity due to the dependencies of the bremsstrahlung emission on the density (Eq. 1.7). Generally, spherical symmetry and an underlying broken power-law density profile in the form

$$\begin{aligned}
 n_d(r) &= C n_0 \left(\frac{r}{r_j} \right)^{a_1}, & \text{if } r \leq r_j \\
 n_u(r) &= n_0 \left(\frac{r}{r_j} \right)^{a_2}, & \text{if } r > r_j
 \end{aligned}
 \tag{1.21}$$

is assumed to describe the discontinuity, where n_0 is the normalization factor, a_1 and a_2 are the power-law indexes, and r_j is the radius where the jump occurs.

Strong spatial variations in temperature and density in the ICM due to merger shocks were suggested by early observations with ROSAT and ASCA in several dynamically active clusters (e.g. Henry & Briel 1995; Henriksen & Markevitch 1996; Donnelly et al. 1998, 1999; Markevitch et al. 1996a,b, 1998, 1999). However, only thanks to the superb sub-arcsec resolution of *Chandra* it has been possible to characterize shocks, as well as discover *cold fronts* (i.e. unexpected sharp features of a different nature), in the ICM. Shocks and cold fronts have been observed in several galaxy clusters that are clearly undergoing significant merging activity (e.g. Markevitch & Vikhlinin 2007; Owers et al. 2009; Ghizzardi et al. 2010; Markevitch 2010; Botteon et al. 2018a, for some collections). In Fig. 1.9, we show the most remarkable example: the Bullet Cluster (Markevitch et al. 2002), where an infalling sub-cluster (i.e. the “bullet”) creates a contact discontinuity between its dense and low-entropy core and the surrounding hot gas. Here, the pressure is almost constant

across the edge and the temperature of the gas downstream is lower than upstream. Ahead of this cold front (marked in green) another drop in SB but with reversed temperature jump, i.e. a shock front (marked in red), is also detected. These jumps are maximized when the fronts are seen edge-on, hence their observation requires that the collision occurs almost in the plane of the sky as projection effects can hide the SB and temperature discontinuities. Geometrical constraints and low count statistics in cluster outskirts make the search for shocks a difficult task. This is reflected in the modest number of merger shocks that have been confirmed using both X-ray imaging and spectral analysis (Chapter 6).

Recently, the high angular resolution achieved in millimetric band observations has enabled the search for shocks also in SZ (e.g. Kitayama et al. 2004; Korngut et al. 2011; Planck Collaboration X 2013; Erler et al. 2015; Basu et al. 2016; Adam et al. 2018b). Indeed, the SZ effect provides a direct probe of the integrated electron pressure along the line of sight in clusters (Eq. 1.10), allowing to characterize shocks directly via pressure jump (Eq. 1.19). Moreover, the SB of the SZ effect is independent of the redshift (for resolved sources), in contrast with that of X-rays, that scales as $\propto (1+z)^{-4}$, making SZ observations a potential tool to detect shocks in distant clusters.

1.3.3 Turbulence

Mergers between clusters and accretion of sub-structures are also expected to inject a non-negligible amount of turbulence in the ICM. A fluid becomes turbulent when its Reynolds number is $Re \gg 1$. In the case of pure Coulomb interactions (Eq. 1.5), the Reynolds number of the ICM is (e.g. Brunetti & Lazarian 2007)

$$Re \simeq 52 \left(\frac{V_L}{10^3 \text{ km s}^{-1}} \right) \left(\frac{L}{300 \text{ kpc}} \right) \left(\frac{n_e}{10^{-3} \text{ cm}^{-3}} \right) \left(\frac{kT}{8 \text{ keV}} \right)^{-5/2} \left(\frac{\ln \Lambda}{40} \right) \quad (1.22)$$

where L is a typical eddy size (ideally the injection scale of turbulence) and V_L is the root-mean-square velocity within this scale. Thus, based on typical values of the ICM, the Reynolds number would hardly reach $Re \sim 10^2$ in most conditions. However, in the presence of (even a small) stationary magnetic field the Reynolds number for motions in the direction perpendicular to the magnetic field gets extremely high essentially because the perpendicular mean free path of particles is limited to the Larmor gyroradius-scale (Eq. 1.6). Furthermore, in the weakly collisional regime (Section 1.2.1), plasma instabilities in the ICM imply that collisionless effects govern microphysics, reducing the effective mean free path. This increases the effective Reynolds number of the ICM to $Re \gg 10^3$, suggesting a highly turbulent medium (Schekochihin & Cowley 2006; Lazarian & Beresnyak 2006).

Numerical simulations of cluster mergers (Fig. 1.10) are customarily used to describe in details the turbulent motions generated by such energetic events (e.g. Norman & Bryan 1999; Dolag et al. 2005; Iapichino & Niemeyer 2008; Ryu et al. 2008; Vazza et al. 2009b, 2011, 2017b; Iapichino et al. 2011; Paul et al. 2011; Miniati 2014, 2015; Schmidt et al. 2014, 2016). These simulations also predict that turbulence in the ICM can account for up to $\sim 20\%$ of the thermal energy (e.g. Sunyaev et al. 2003; Vazza et al. 2006, 2012b, 2018a).

Hints of turbulent motions in the ICM have been firstly reported by Schuecker et al. (2004) from the study of spatially-resolved gas pressure maps obtained with *XMM-Newton* for the Coma cluster. Indeed, recent theoretical progress has shown that the analysis of X-ray SB fluctuations (that corresponds to density fluctuations) in the ICM can be connected to velocity fluctuations, allowing to constrain the turbulent Mach number of the medium (e.g. Churazov et al. 2012; Gaspari & Churazov 2013; Gaspari et al. 2014; Zhuravleva et al. 2014). X-ray spectral analysis has also the potential to measure the level of turbulence in the medium either via broadening of the emission lines due to

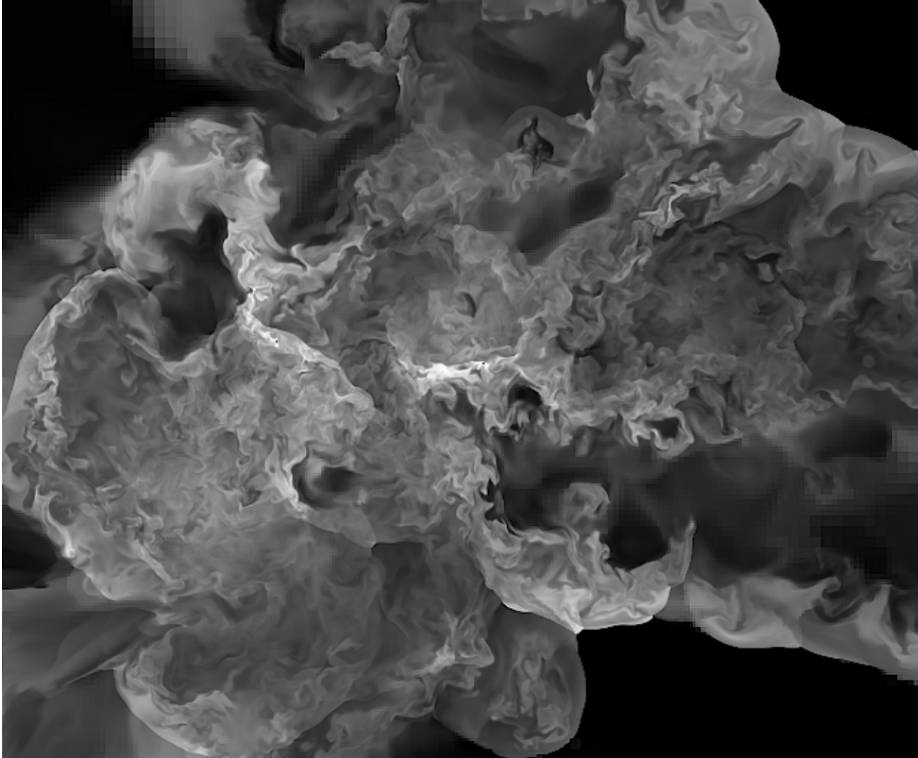


Figure 1.10: Two dimensional slice showing the gas temperature (*black* is for $T < 10^7$ K, *white* is for $T > 10^8$ K) and turbulent motions generated in a galaxy cluster during a major merger event. The side of the slice is 8.8 Mpc and the depth along the line of sight is 25 kpc. From Vazza et al. (2011).

gas motions or by the study of resonant scattering (e.g. Inogamov & Sunyaev 2003).

The Perseus cluster has been targeted for a long time with *XMM-Newton* and *Chandra* in the quest of turbulent motions (e.g. Churazov et al. 2003, 2004; Gastaldello & Molendi 2004; Sanders et al. 2004); however, the low energy resolution of Charge-Coupled Device (CCD) spectrometers makes these measurements a difficult task (Zhuravleva et al. 2013). In this respect, the first measurement of turbulence in a galaxy cluster was possible only thanks to the high spectral resolution of the calorimeter mounted on *Hitomi*, that constrained the line of sight velocity dispersion in the Perseus core to be $164 \pm 10 \text{ km s}^{-1}$ in the region 30 – 60 kpc from the central nucleus (Hitomi Collaboration 2016). Recent numerical simulations showed that the velocity dispersion measured by *Hitomi* can be reproduced by frequent and “gentle” AGN feedback in the core, and by accretion of infalling groups on larger ($\gtrsim 50$ kpc) scales (e.g. Bourne & Sijacki 2017; Hillel & Soker 2017; Lau et al. 2017). Unfortunately, *Hitomi* was lost after few weeks of operation and it was not possible to extend this kind of measurement to other galaxy clusters. In particular, clusters undergoing major mergers are expected to display larger velocity dispersion due to substantial bulk motions in the ICM. The future X-ray mission *Athena* will be able to perform measurements of turbulence with unprecedented details in a large number of galaxy clusters (Roncarelli et al. 2018).

1.4 Diffuse radio sources in merging galaxy clusters

In the past decades, observations at low frequencies revealed the presence of diffuse radio sources in some merging galaxy clusters (e.g. van Weeren et al. 2019, for a review). These sources show steep ($\alpha > 1$) synchrotron spectra, indicative of the presence of relativistic particles and magnetic fields. The diffuse, extended (up to Mpc-scales), low SB ($\sim \mu\text{Jy arcsec}^{-2}$ at 1.4 GHz) radio

emission in clusters is typically classified in two species². According to their location in the cluster, their radio properties, and their morphology, it is possible to distinguish *radio relics* and *radio halos*.

The evidence for CRs and magnetic fields in the ICM generating giant diffuse radio sources via synchrotron radiation opens fundamental questions on their origin as well as their impact on both the physics of the ICM and the evolution of galaxy clusters more broadly (e.g. Brunetti & Jones 2014, for a review). The connection between diffuse radio emission in the ICM and dynamically disturbed systems (e.g. Buote 2001; Cassano et al. 2010b, 2013; Cuciti et al. 2015) suggests that cluster mergers play a crucial role in the formation of non-thermal components in galaxy clusters.

In the following, we will describe the main properties of radio relics and radio halos according to the current nomenclature. We anticipate that the taxonomy of extended radio emission in galaxy clusters is evolving thanks to the advent of new instruments, for example LOFAR (Chapter 7), that are unveiling the wealth of complex diffuse steep spectrum sources in the ICM (e.g. Shimwell et al. 2016; de Gasperin et al. 2017; Duchesne et al. 2017; Botteon et al. 2018b; Bonafede et al. 2018; Brüggén et al. 2018; Kale et al. 2018; Mandal et al. 2018; Savini et al. 2018a,b; Wilber et al. 2018).

1.4.1 Radio relics

Radio relics are generally observed in the outskirts of galaxy clusters, have significant linear polarization (typically up to 30%), and usually show an elongated, arc-like, morphology characterized by sharp emission edges. The prototype of this class of sources is 1253+275, detected in the Coma cluster (Giovannini et al. 1991). Nowadays, the most spectacular example of relic is probably provided by the northern relic in CIZA J2242.8+5301 (van Weeren et al. 2010), that has been nicknamed the “Sausage” because of its remarkable regular arc-shaped structure that extends for ~ 2 Mpc with a width of only ~ 55 kpc at 610 MHz (Fig. 1.11). In the most impressive cases, symmetric *double relics* are observed on opposite sides of clusters (see de Gasperin et al. 2014; Bonafede et al. 2017, and references therein), as shown in Fig. 1.12 for the case of A3667 (Röttgering et al. 1997; Johnston-Hollitt 2003). Relics represent important probes of the magnetic field properties in the clusters outskirts, as they can be found at distances up to a large fraction of the cluster virial radius.

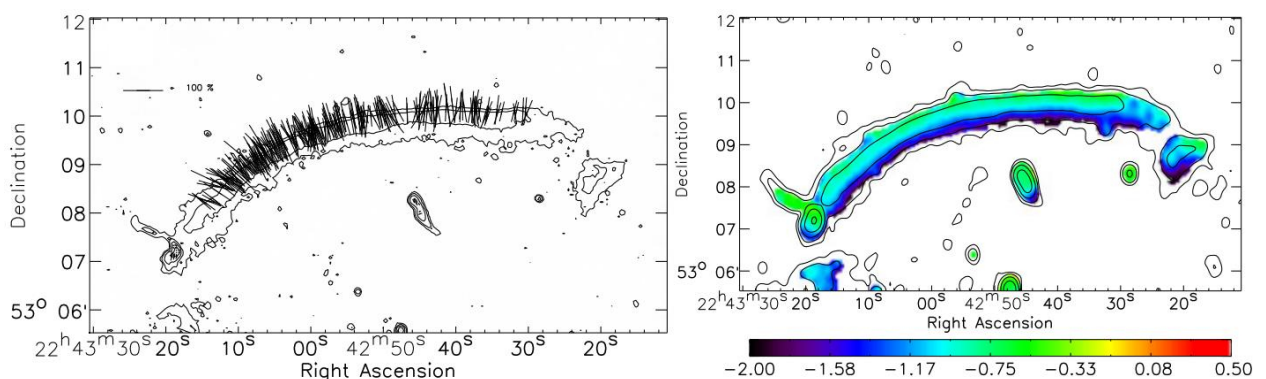


Figure 1.11: Radio polarization and spectral index maps of the Sausage relic. *Left:* lines represent the polarization electric field vectors. The length of the vectors are proportional in length to the polarization fraction. A reference vector for 100% polarization is shown in the upper left corner. *Right:* spectral index map obtained with a power-law fit to measurements at five frequencies between 2.3 GHz and 610 MHz. From van Weeren et al. (2010).

²Here we do not discuss radio mini halos, another kind of diffuse emission with smaller scales ($\lesssim 500$ kpc) found at the center of some CC clusters.

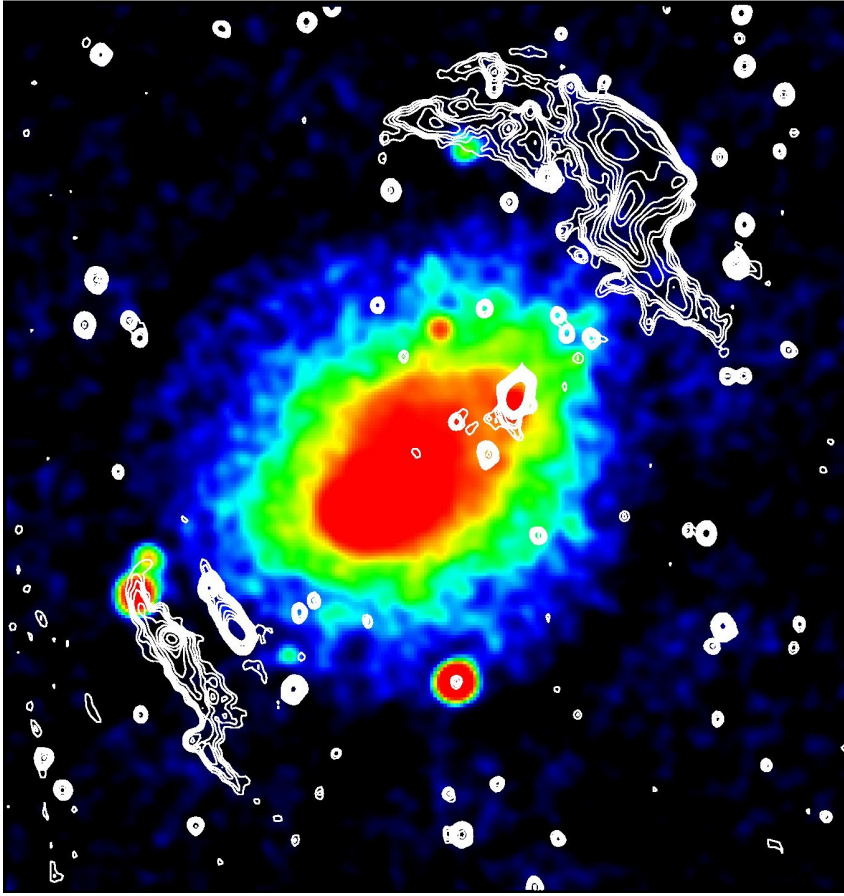


Figure 1.12: The double radio relic in A3667. Radio and X-ray emission are reported in contours and colors, respectively. From Hunstead & SUMSS Team (1999).

Relics show quite steep integrated spectra, while spectral index maps highlight spectral steepening, indicative of particle aging, toward the cluster center (e.g. Bonafede et al. 2009, 2012; van Weeren et al. 2010; de Gasperin et al. 2015a; Hoang et al. 2018a), as shown in Fig. 1.11 (right panel). A single power-law is usually adopted to fit the spectra of relics, and it is still under discussion whether a spectral curvature is present at frequencies $\gtrsim 2$ GHz (see Stroe et al. 2013, 2014, 2016; Loi et al. 2017, for the Sausage case).

The presence of correlations between relics and host cluster properties is fundamental to unveil the origin of these objects. In particular, given the luminosity distance D_L , the relic radio power at 1.4 GHz

$$P_{1.4} = 4\pi S_{1.4} D_L^2 (1+z)^{\alpha-1} \quad (1.23)$$

has been observed to be correlated with the X-ray luminosity of the host cluster (Feretti et al. 2012). The existence of this correlation could reflect a dependence of $P_{1.4}$ on the cluster mass, as the X-ray luminosity can be used as a proxy of the cluster mass (e.g. Pratt et al. 2009). However, possible biases may be introduced by the presence of CC clusters (Eckert et al. 2011) and by the boost of X-ray luminosity expected during mergers (e.g. Donnert et al. 2013), precluding the possibility to draw statistical constraints. In this respect, the SZ signal provides a more robust indicator of the cluster mass with respect to the X-ray luminosity (Motl et al. 2005; Nagai 2006), allowing to build cluster samples that are as close as possible to be mass-selected, such as those carried out with the *Planck* satellite (Planck Collaboration VIII 2011; Planck Collaboration XXIX 2014; Planck Collaboration XXVII 2016). For example, de Gasperin et al. (2014) found that the radio power of relics is a steep

function of M_{500} , namely the mass within the radius r_{500} that encloses a mean overdensity of 500 with respect to the critical density at the cluster redshift, as determined from *Planck* observations. The steep correlation found, i.e. $P_{1.4} \propto M_{500}^{2.83 \pm 0.39}$, indicates that it is more likely to find radio relics (as well as radio halos, as we will see in the Section below) in massive clusters and suggests that the magnetic field at the location of radio relics is rather uniform.

There is a broad consensus on the hypothesis that radio relics are connected with shocks (e.g. Brügggen et al. 2012a; Brunetti & Jones 2014, for reviews). The evidence includes (i) the arc-like morphology and peripheral location of some relics, which is consistent with numerical simulations of cluster shocks, (ii) the radial spectral gradients and/or spectral curvature, suggesting that relativistic electrons gain energy at the shock front and lose energy after the shock passage, (iii) the high degree of linear polarization, indicating a magnetic field aligned within the shock plane (Fig. 1.11, left panel) and (iv) the existence of double radio relics (Fig. 1.12), interpreted as traces of shocks moving outward after an head-on cluster merger in the plane of the sky. The consolidation of the relic–shock connection is supported by the detection in the X-rays of shock fronts underlying some radio relics (e.g. Akamatsu & Kawahara 2013; Bourdin et al. 2013; Shimwell et al. 2015; Botteon et al. 2016a,c; Eckert et al. 2016a; Urdampilleta et al. 2018). Although it is clear that shocks play a fundamental role in the formation of radio relics, the details of the mechanisms generating the relativistic electrons are still under debate (Section 1.5).

1.4.2 Radio halos

Radio halos are observed at the center of galaxy clusters. Their emission is fairly regular in morphology, unpolarized down to a few percent level (unlike relics), and permeates the volume of the ICM somewhat recalling the distribution of the thermal gas.

The prototype of this class of objects, i.e. the radio halo in the Coma cluster (Fig. 1.13), was detected a long time ago (Large et al. 1959) and has been the target of many observational campaigns (e.g. Willson 1970; Giovannini et al. 1993; Deiss et al. 1997; Brown & Rudnick 2011). It represents an unique case where the synchrotron spectrum is sampled over a broad range of frequencies (Thierbach et al. 2003; Brunetti et al. 2013). This allowed measurement of a spectral steepening at high frequencies, important to understand the mechanisms responsible of its origin (Schlickeiser et al. 1987). However, radio halo spectra are usually constrained by only a few data-points, covering a small range of frequencies, and are commonly fitted with simple single power-laws (e.g. Venturi et al. 2013). A reference spectral index values for halos is $\alpha = 1.3$ (e.g. Feretti et al. 2012, and references therein). An extreme class of radio halos with $\alpha > 1.5$, the so called *ultra-steep spectrum radio halos* (USSRH), is also observed (e.g. Brunetti et al. 2008; Dallacasa et al. 2009; Macario et al. 2010, 2013; Wilber et al. 2018). Due to their elusive nature at \gtrsim GHz, these sources can be best observed at low frequencies (e.g. Cassano et al. 2010a, 2012). USSRHs pose an energy runaway problem requiring that an excessive amount of energy is associated to the relativistic plasma if the steep power-law energy distribution is extrapolated to lower energies. A solution to this problem is that the observed synchrotron radiation comes from electrons whose energy distribution has a high-energy break at energies of a few GeV.

A remarkable link between the radio and X-ray properties of galaxy clusters exists. In fact, a close similarity in the morphology of radio halos and the X-ray emission (Fig. 1.13) of their host clusters has been noticed since the first studies (e.g. Deiss et al. 1997), and this led to study the connection between the point-to-point SB of the cluster radio and X-ray emission (Govoni et al. 2001a). Furthermore, several scaling relations between the radio and thermal gas properties of the ICM have been widely studied in the literature (e.g. Liang et al. 2000; Enßlin & Röttgering 2002; Bacchi et al. 2003; Cassano et al. 2006; Rudnick & Lemmerman 2009). In particular, thanks to the *Planck* satellite, it was possible to determine a steep correlation between the radio power at 1.4 GHz

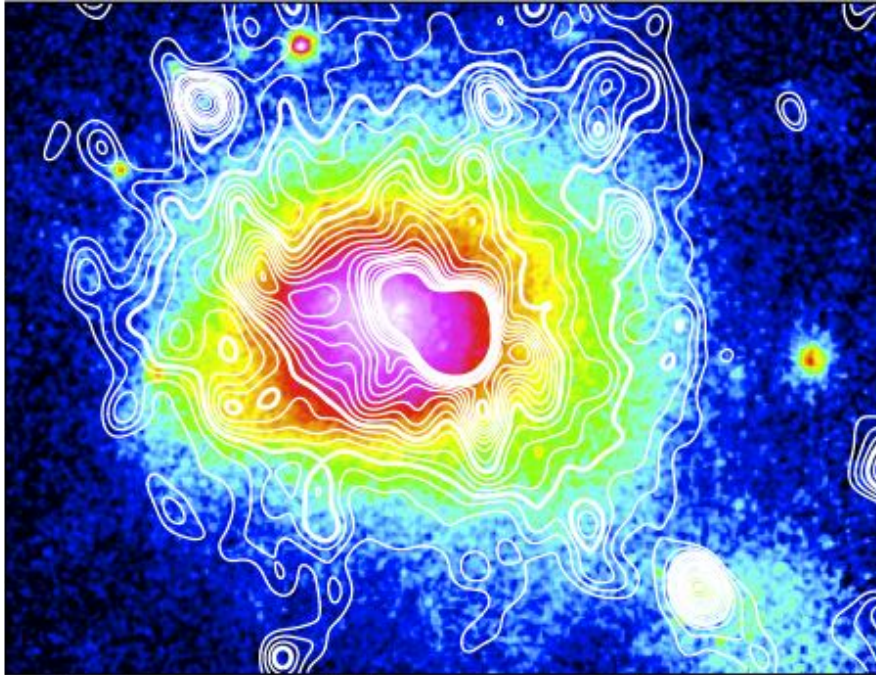


Figure 1.13: The radio halo in the Coma cluster. Radio and X-ray emission are reported in contours and colors, respectively. From Brown & Rudnick (2011).

of radio halos (Eq. 1.23) and the cluster mass, i.e. $P_{1.4} \propto M_{500}^{3.77 \pm 0.57}$ (Cassano et al. 2013), which is even steeper than the one found for radio relics. This indicates that the cluster mass is an important parameter that must be taken into account by the models of halo formation.

The most striking argument supporting the connection between cluster mergers and radio halos is the so called “radio bi-modality” (Brunetti et al. 2007, 2009; Kale et al. 2015). Essentially, it is observed that clusters can be divided into two populations: merging systems hosting radio halos and relaxed systems that do not host large-scale diffuse radio sources at the levels of merging systems. This, together with the fact that a limited number of clusters host radio halos, represents the starting point to understand the processes that generate synchrotron emission on cluster-wide scales (Section 1.6).

1.5 Origin of radio relics

Nowadays, the relic–shock connection is fairly well established. In this respect, we contributed to support this picture with the results obtained during this Thesis (Chapter 2 and 3). During the past years, three main models for the radio relic formation have been proposed. They are outlined below.

1.5.1 Adiabatic compression

For a class of models, radio relics might trace region where fossil radio plasma is confined and then it is re-energized by adiabatic compression due to a recent shock passage (Enßlin & Gopal-Krishna 2001; Enßlin & Brüggen 2002).

In a radio bubble, the momentum of relativistic particles changes due to radiative losses (Eq. 1.11) and adiabatic losses/gains associated to variations of volume V of the bubble as

$$-\frac{dp}{dt} = \frac{4}{3} \frac{\sigma_T}{m_e c} (\epsilon_B + \epsilon_{ph}) p^2 + \frac{1}{3} \frac{1}{V} \frac{dV}{dt} p \quad (1.24)$$

where $\varepsilon_B = B^2/8\pi$ and $\varepsilon_{ph} = B_{cmb}^2/8\pi$ are the energy density in the magnetic field and photon field, respectively. Coulomb and bremsstrahlung losses are neglected due to the very low particle density within the region filled by relativistic plasma. Given the volume compression ratio

$$C_V(t) = \frac{V_0}{V(t)}, \quad (1.25)$$

it is possible to integrate Eq. 1.24 with the temporary variable change $\tilde{p} = C_V(t)^{-1/3} p(t)$, yielding to the momentum of a particle with initial momentum p_0 at a time t

$$p(p_0, t) = \frac{p_0}{C_V(t)^{-1/3} + p_0/p_*(t)}, \quad (1.26)$$

where the characteristic momentum is given by

$$\frac{1}{p_*(t)} = \frac{4}{3} \frac{\sigma_T}{m_e c} \int_{t_0}^t dt' [\varepsilon_B(t') + \varepsilon_{ph}(t')] \left[\frac{C_V(t')}{C_V(t)} \right]^{1/3}. \quad (1.27)$$

For an initial power-law population of electrons in the form

$$N(p) = N_0 p^{-\delta}, \quad (1.28)$$

between p_{min} and p_{max} , the spectrum at time t is given by

$$N(p, t) = N_0 C_V(t)^{-\frac{\delta+2}{3}} p^{-\delta} \left[1 - \frac{p}{p_*(t)} \right]^{\delta-2} \quad (1.29)$$

between $p(p_{min}, t)$ and $p(p_{max}, t)$. The compression also changes the energy density in the magnetic field as

$$\varepsilon_B(t) = \varepsilon_{B,0} \left(\frac{V}{V_0} \right)^{-4/3} \quad (1.30)$$

and, as $\varepsilon_B \propto B^2$, the average magnetic field strength increases as

$$B(t) \propto C_V(t)^{\frac{2}{3}}. \quad (1.31)$$

The adiabatic compression model requires the presence of a cloud of fossil electrons, for example injected by a former AGN outflow, that already suffered major synchrotron and IC losses whose emission would be detectable at very low frequencies (tens of MHz and below), hence the name *radio ghosts* (Enßlin 1999). When this ghost is crossed by a shock, it is adiabatically compressed and not shocked because the high sound speed within the relativistic cloud. The compression results in the re-energization of the electrons (Eq. 1.26) and amplification of the magnetic field (Eq. 1.31). Note that for a relativistic gas (i.e. $\gamma_{ad} = 4/3$), the Rankine-Hugoniot jump conditions Eq. 1.17, 1.18 and 1.19 become

$$\mathcal{R} = \frac{8\mathcal{M}^4 + 47\mathcal{M}^2 - 6}{49\mathcal{M}^2} \quad (1.32)$$

$$\mathcal{C} = \frac{7\mathcal{M}^2}{\mathcal{M}^2 + 6} \quad (1.33)$$

$$\mathcal{P} = \frac{8\mathcal{M}^2 - 1}{7} \quad (1.34)$$

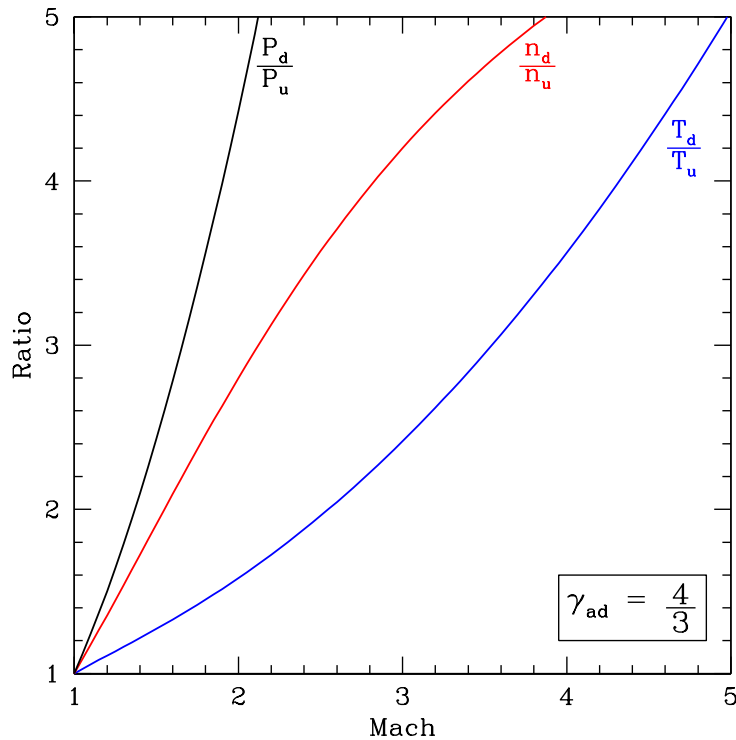


Figure 1.14: Temperature, density, and pressure ratios versus the shock Mach number (assuming $\gamma_{ad} = 4/3$). Note that, in this case, the compression factor is $\mathcal{C} \rightarrow 7$ for $\mathcal{M} \rightarrow \infty$ (cf. Fig. 1.8).

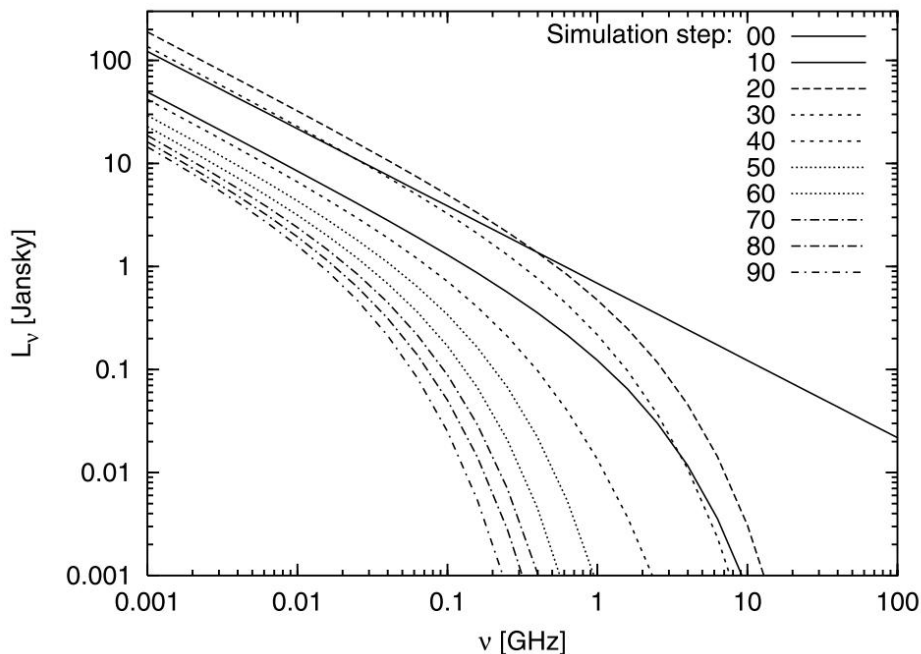


Figure 1.15: Simulation of the spectral evolution of a radio plasma cocoon filled with turbulent magnetic fields crossed by a shock. The numbers (00, 10, ..., 90) label different time-steps of the simulation (each step is approximately 7 Myr long). The cutoff frequency clearly decreases with time except in the interval 10 – 20 (70 – 140 Myr) where the shock compression reverses this. During this phase also the overall emissivity at lower radio frequencies increases, mainly owing to field strength amplification. At all other time-steps the low-frequency flux decreases artificially, owing to magnetic field annihilation by numerical field diffusion. From Enßlin & Brüggen (2002).

and the compression can increase up to 7 times the downstream density (Fig. 1.14). Thus, the cloud gets compressed along the direction of the shock motion, and expands perpendicularly to this direction, assuming the typical elongated shape of radio relics. As shown in Fig. 1.15, the spectrum of the compressed cloud is expected to be steep and curved due to the presence of the already existent population of fossil electrons; importantly, adiabatic compression just boosts the emission of the aged electrons without changing the original spectral slope. Diffuse radio emission in front of the shock is expected due to the presence of the pre-existing population of relativistic electrons.

This framework is mainly challenged by two facts. First of all, in order to experience adiabatic compression, the relativistic plasma should be well confined in the ICM to keep its internal sound speed close to the speed of light: however, the sound speed drops as soon as mixing with the thermal ICM occurs, leading shock (re)acceleration (Sections below) to be the main mechanism to produce relativistic electrons. Secondly, the observation of an increasing number of double relics disfavors this scenario because of the low probability to find two symmetric clouds of fossil electrons.

Adiabatic compression seems to play a more important role in the formation of the so-called *radio phoenixes* (Slee et al. 2001; van Weeren et al. 2009; Kale & Dwarakanath 2012; de Gasperin et al. 2015b, 2017; Kale et al. 2018), namely sources with very steep spectrum ($\alpha \gtrsim 1.8$) with amorphous morphology, sometimes recalling radio relics, connected to individual galaxies. The properties of this class of sources can be reproduced by numerical simulations of radio galaxies crossed by shocks (e.g. Enßlin & Brüggen 2002). Adiabatic compression may also play a role for radio halos. Indeed, it has been suspected that the sharp edges of some radio halos coincident with shocks could be caused by this mechanism (e.g. Markevitch et al. 2005; Markevitch 2010). However, recent observations seem to rule out this scenario for the most studied case of halo–shock connection (Wang et al. 2018; Hoang et al. 2018b).

1.5.2 Diffusive shock acceleration

Particle acceleration at shocks is customarily described by the diffusive shock acceleration (DSA) theory (e.g. Krymskii 1977; Bell 1978a,b; Drury 1983; Blandford & Eichler 1987; Jones & Ellison 1991; Malkov & Drury 2001). This process is based on the original idea of Fermi (1949), according to which particles are scattered upstream and downstream the shock by plasma irregularities, gaining energy at each reflection. In this respect, radio emitting electrons in relics could be generated by DSA from the ICM thermal pool (Enßlin et al. 1998; Roettiger et al. 1999a).

The momentum spectrum of electrons accelerated through DSA mechanism follows a power-law distribution (Eq. 1.28) where the slope δ_{inj} (i.e. the injection spectrum) is

$$\delta_{inj} = 2 \frac{\mathcal{M}^2 + 1}{\mathcal{M}^2 - 1} \quad (1.35)$$

and it depends only on the shock Mach number (e.g. Blandford & Eichler 1987).

The DSA theory was originally developed in the framework of supernova remnants (SNR) in our Galaxy, where strong shocks with $\mathcal{M} \sim 10^3$ are able to transfer $\sim 10\%$ or more of the energy flux through them into CRp, and a smaller fraction into CRe (e.g. Helder et al. 2012; Bell 2013, 2014, for reviews). By contrast, as shown in Fig. 1.7, most of the kinetic energy flux penetrating cluster merger shocks is associated with weak shocks (e.g. Ryu et al. 2003; Vazza et al. 2009a), where the acceleration efficiency of CRp is likely $< 1\%$ (e.g. Kang & Ryu 2013), although still poorly understood (e.g. Kang & Jones 2005; Hoeft & Brüggen 2007).

Once CRe in radio relics have been advected downstream, radiative cooling due to IC and synchrotron (Eq. 1.11) reduces the maximum electron energy causing the “volume integrated” electron spectrum to steepen by one in the power-law index

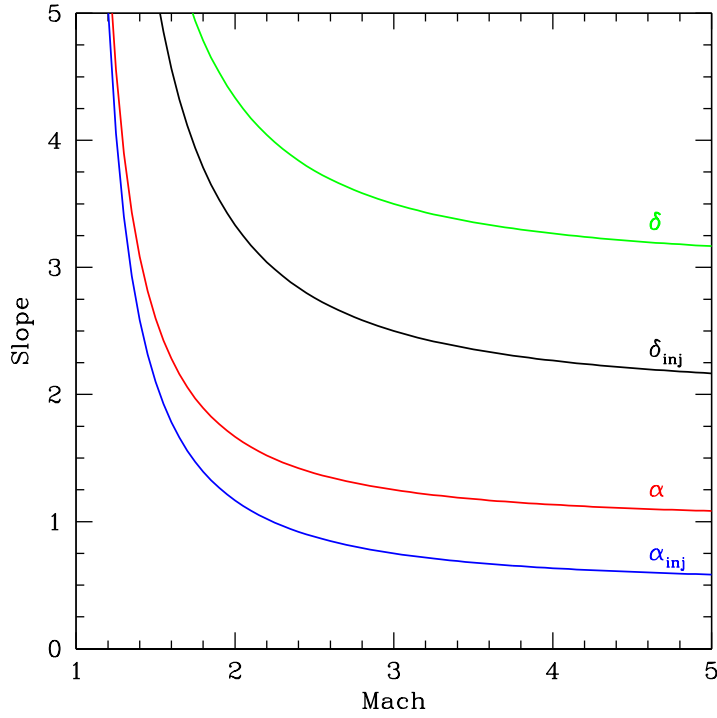


Figure 1.16: Injection and integrated slopes of the synchrotron radiation and electron spectrum versus the shock Mach number.

$$\delta = \delta_{inj} + 1 \quad (1.36)$$

provided that other mechanisms do not play a role behind the shock (Enßlin et al. 1998). Since the radio spectral index is connected with the electron spectrum via

$$\alpha = \frac{\delta - 1}{2}, \quad (1.37)$$

the observed relic spectral index is connected with the shock Mach number via

$$\alpha = \frac{\mathcal{M}^2 + 1}{\mathcal{M}^2 - 1} \equiv \alpha_{inj} + \frac{1}{2}. \quad (1.38)$$

As a consequence of the above relations, DSA predicts that for strong shocks ($\mathcal{M} \rightarrow \infty$) it is $\delta_{inj} \rightarrow 2$ (and $\alpha_{inj} \rightarrow 0.5$), while for weak shocks ($\mathcal{M} \lesssim 3 - 5$) it is $\delta_{inj} \gg 2$ (and $\alpha_{inj} \gg 0.5$), as shown in Fig. 1.16.

The electron acceleration efficiency η_e is evaluated assuming that a fraction of the kinetic energy flux through the shock surface A is converted into CRE acceleration to produce the bolometric ($\geq \nu_0$) synchrotron luminosity of the relic

$$\int_{\nu_0} L(\nu) d\nu \simeq \frac{1}{2} A \rho_u V_{sh}^3 \eta_e \Psi \left(1 - \frac{1}{\mathcal{C}^2} \right) \frac{B^2}{B_{cmb}^2 + B^2} \quad (1.39)$$

where

$$\Psi = \frac{\int_{p_0} N_{inj}(p) E dp}{\int_{p_{min}} N_{inj} E dp} \quad (1.40)$$

accounts for the ratio of the energy flux injected in “all” electrons and those visible in the radio band ($v \geq v_0$), p_{min} is the minimum momentum for which particles are efficiently accelerated while p_0 is the momentum of the relativistic electrons emitting the synchrotron frequency ν_0 . In DSA regime, the particle injection spectrum is $N_{inj}(p) \propto p^{-\delta_{inj}}$, with slope related to the shock Mach number via Eq. 1.35. In this respect, DSA is severely challenged by the large acceleration efficiencies required to reproduce the total radio luminosity of several relics, if particles are accelerated from the ICM thermal pool (Chapter 5).

A connected problem to the large acceleration efficiencies concerns the lack of γ -ray emission from galaxy clusters (Vazza & Brüggen 2014; Vazza et al. 2015a, 2016; Wittor et al. 2017). Indeed, even considering a conservative electron-to-proton ratio of $K_{e/p} = 0.01$ (as commonly assumed in our Galaxy, e.g. Schlickeiser 2002 for discussion), the resulting π^0 generated via inelastic collisions between the accelerated CRp and thermal protons should produce γ -ray emission in excess of the current limits derived from the *Fermi* satellite (Ackermann et al. 2010, 2014, 2016). The adoption of lower (and perhaps more realistic) values of $K_{e/p} \sim 10^{-3} - 10^{-5}$ similar to those generated in SNRs (e.g. Völk et al. 2005; Berezhko et al. 2009; Morlino et al. 2009; Ellison et al. 2010; Morlino & Caprioli 2012; Fukui et al. 2012; Park et al. 2015) would only exacerbate the problem.

Finally, the Mach number derived from X-ray (or SZ) observations (Section 1.3.2) can be compared with that expected by DSA (Eq. 1.38) to test this formation scenario for radio relics. The increasing number of shocks detected in coincidence with relics indicate that a discrepancy exists between the Mach numbers derived with these two different approaches, with the radio-derived Mach numbers generally biased high (Akamatsu & Kawahara 2013; Akamatsu et al. 2015, 2017a; Urdampilleta et al. 2018). Numerical simulations have been performed in order to clarify such an inconsistency. The emerging scenario is that Mach number variations over shocks (Skillman et al. 2013), projection effects along the line of sight (Hong et al. 2015), and additional mechanisms such as the Alfvénic drift (Kang & Ryu 2018) and superdiffusive shock acceleration (SSA; Zimbardo & Perri 2018) might mitigate the observed differences.

1.5.3 Shock re-acceleration

All the challenges faced by the DSA from the thermal ICM can be naturally circumvented by adopting a scenario where radio relics are generated by the re-acceleration of pre-existing CRe at merger shocks (e.g. Markevitch et al. 2005; Kang & Ryu 2011, 2016; Kang et al. 2012, 2014; Pinzke et al. 2013; Caprioli & Zhang 2018). Complementary models invoke the development of turbulence in the region downstream the shock that is able to re-accelerate stochastically the electrons (e.g. Fujita et al. 2015, 2016)

In DSA theory, a minimum momentum that leads to diffusive particle transport across the shock exists (Eq. 1.40). For this reason, non-relativistic electrons are difficult to inject from the thermal pool and this is the reason why a small electron-to-proton ratio $K_{e/p} < 0.01$ is predicted (e.g. Brunetti & Jones 2014). Although a mechanism such as the shock drift acceleration (SDA; Guo et al. 2014a,b) may lead to this result, it has not been possible yet to constrain this scenario due to computational limitations.

Assuming that a population of relativistic electrons already exists in the ICM, e.g. injected by cluster radio galaxies, the initial (upstream) and accelerated spectra of electrons are connected via

$$N_{inj}(p) = (\delta_{inj} + 2)p^{-\delta_{inj}} \int_{p_{min}}^p x^{\delta_{inj}-1} N_u(x) dx \quad (1.41)$$

here N_u is the spectrum of seed particles upstream. When a weak shock crosses a pre-existing population of CRe, DSA becomes a relatively more efficient process, although efficiencies above a few per cent are still problematic (e.g. Kang & Ryu 2011). The resulting spectrum of re-accelerated

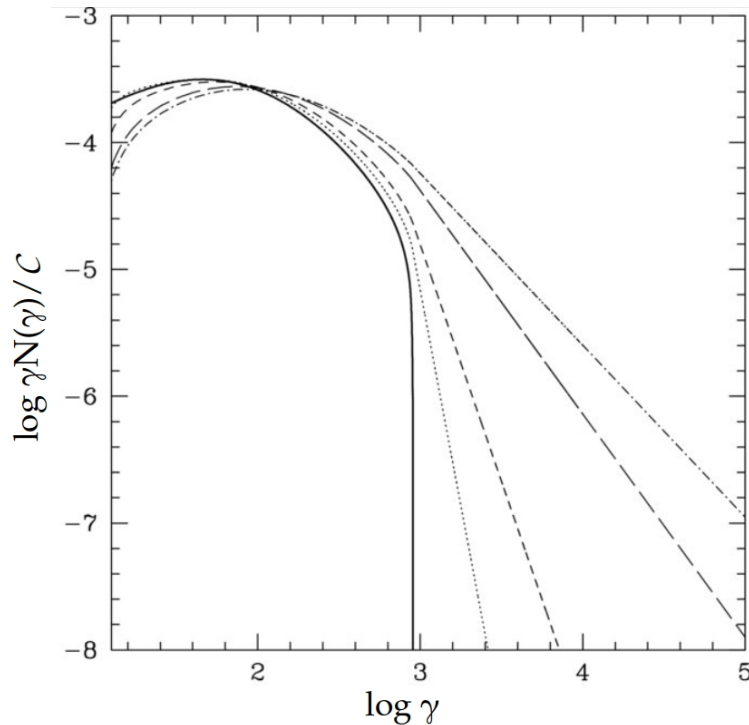


Figure 1.17: Spectrum of re-accelerated electrons according to Eq. 1.41. The *solid line* is the initial spectrum of fossil electrons (assuming an age of the population of a few Gyr and typical cluster physical parameters). Different models show the spectrum for Mach numbers 1.3 (*dotted line*), 1.57 (*dashed line*), 2.5 (*long dashed line*), and 3.5 (*dot-dashed line*). From Macario et al. (2011).

particles is not that predicted by DSA (Eq. 1.35): it is similar to the spectrum of the seed electrons if the latter is flat whereas it is that of DSA if the spectrum of seed electrons is steeper than the DSA one (e.g. Kang & Jones 2005; Kang & Ryu 2011), as shown in Fig. 1.17. The physical acceleration is still DSA, however; the change reflects only the assumed source of particles being accelerated.

Recently, the re-acceleration scenario has been corroborated by a number of observations of AGN located nearby or within some radio relics (e.g. Bonafede et al. 2014a; Shimwell et al. 2015; Botteon et al. 2016a; van Weeren et al. 2017a). Indeed, AGN can naturally provide seed electrons that are more easily accelerated by weak shocks, alleviating the high acceleration estimated in the case of DSA from the thermal pool for some relics (e.g. Botteon et al. 2016a; Eckert et al. 2016a; van Weeren et al. 2016a; Hoang et al. 2018a).

Although this formation mechanism solves most of the energetic problems of the DSA theory applied at cluster shocks, some challenges remain. Indeed, the collisions between accelerated CRp and thermal protons would still produce γ -ray emission in excess of current limits; this problem can be solved only if $K_{e/p}$ is very high. In addition, the connection between radio galaxies and relics is not obvious in most cases, indicating that a population of pre-existing CRe is not ubiquitous. The extremely regular structure extending on Mpc-scales of some relics, such as the Sausage (Fig. 1.11), further stresses this scenario as it would require that seed CRe are uniformly distributed in the ICM. Finally, as for the case of adiabatic compression, it is unlikely to have enough sources of CRe in diametrically opposite sides of the cluster to reproduce the number of double radio relics observed.

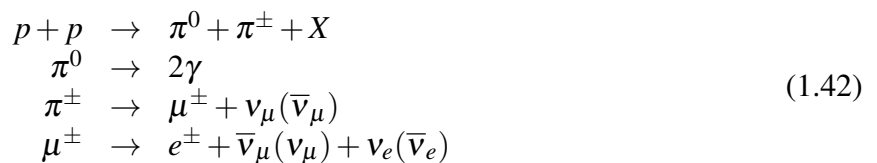
1.6 Origin of radio halos

The main difficulty in explaining the origin of radio halos is their Mpc-sizes. Indeed, CRe undergo radiative losses due to synchrotron and IC emission (Eq. 1.11) that prevent their diffusion

over such distances. To overcome this *slow diffusion problem*, CRe are required to be continuously generated “in situ” in the volume of the radio halo (Jaffe 1977). In the following, we summarize the two main classes of models proposed for the origin of radio halos.

1.6.1 Hadronic models

The CRp are long living in clusters and accumulate in the ICM because their energy losses are negligible (e.g. Völk et al. 1996; Berezhinsky et al. 1997). Inelastic hadronic collisions between CRp and the nuclei of the thermal ICM continuously produce electrons and positrons (Dennison 1980; Blasi & Colafrancesco 1999), which emission can be considered as a stationary signal (e.g. Blasi et al. 2007). The reactions involved are



where X represents some combination of protons, neutrons, and/or other particles. The electrons (and positrons) produced by this mechanism are the so called secondary electrons. For this reason, hadronic models are sometimes referred to as secondary models. The formation of radio halos via secondary electrons has been studied by several numerical simulations (e.g. Dolag & Enßlin 2000; Miniati et al. 2001; Pfrommer et al. 2008; Donnert et al. 2010a,b; Pinzke et al. 2017), where this formalism can be easily implemented in the code.

In this framework, all galaxy clusters should show diffuse radio emission on Mpc-scale that follows the X-rays thermal emission (which provides the targets for the proton collisions), as CRp are naturally injected in the ICM by AGN and starburst galaxies. This is in disagreement with the connection observed between halos and cluster mergers (e.g. Buote 2001; Govoni et al. 2004; Cassano et al. 2010b, 2013) as radio emission should be generated by secondary particles irrespectively of the dynamical state of the hosting system (see however Enßlin et al. 2011 for a possible solution to this problem). In addition, the discovery of halos with spectral steepening at high frequencies (e.g. Schlickeiser et al. 1987) and the existence of USSRHs (e.g. Brunetti et al. 2008) disfavors this scenario because the unrealistic energy budget in terms of CRp that would be implied to explain the radio emission in these cases (e.g. Brunetti 2004).

In this respect, a significant advance has been reached in the last decade thanks to γ -ray observations that provide the most important constraints on the role of proton-proton collisions. Indeed, the chain of reactions in Eq. 1.42 shows that γ -ray emission from π^0 decay is a natural by-product of this process (Dermer 1986). However, current upper limits from the *Fermi* satellite to the γ -ray emission from galaxy clusters severely challenge the hadronic origin for radio halos (Ackermann et al. 2010, 2014, 2016; Jeltema & Profumo 2011; Brunetti et al. 2012, 2017).

1.6.2 Turbulent re-acceleration models

The idea that the radio emitting electrons in radio halos could be generated by merger-driven turbulence in the ICM was firstly proposed by Brunetti et al. (2001) and Petrosian (2001). Whilst the complex details that channel turbulent energy into relativistic particles have been the focus of numerous papers, the microphysics of the processes involved is still poorly constrained (e.g. Fujita et al. 2003, 2015; Brunetti et al. 2004; Cassano & Brunetti 2005; Brunetti & Lazarian 2007, 2011a,b, 2016; Beresnyak et al. 2013; Miniati 2015; Brunetti 2016; Pinzke et al. 2017).

Major merger events are the main source of turbulent motions in the ICM (Section 1.3.3). Such

motions have scales of the order of $\sim 100 - 400$ kpc and velocities $\sim 300 - 700$ km s $^{-1}$ (e.g. Subramanian et al. 2006; Eckert et al. 2017b), meaning that they are subsonic (typically $\mathcal{M} \sim 0.2 - 0.5$). This large scale turbulence cascades to smaller scales leading to the stochastic re-acceleration of particles via several mechanisms (e.g. Brunetti & Jones 2014), and solving in this way the slow diffusion problem.

As the direct acceleration of CRe from the thermal ICM pool is a very inefficient mechanism (e.g. Petrosian & Bykov 2008; Brunetti & Jones 2014, for reviews), a population of seeds primary or secondary electrons distributed on cluster-scales is required. These particles may be injected in the ICM by radio galaxies, supernovae, galactic winds, etc., and, for this reason, this class of models are referred to as re-acceleration models.

The predictions of the turbulent models seem in agreement with the properties observed in radio halos (e.g. Cassano & Brunetti 2005; Cassano et al. 2006). In this picture, the connection between radio halos and dynamically disturbed systems is straightforward: halos are transient phenomena (with a typical life-time $\sim 1 - 2$ Gyr) connected with merger-driven turbulence and their properties depend on the evolutionary stage of the merger (e.g. Kuo et al. 2004; Donnert et al. 2013). This argument agrees with the observed radio bi-modality of galaxy clusters (Brunetti et al. 2009). The occurrence of radio halos at any redshift thus reflects the interplay between the rate of cluster mergers and the fraction of energy that is channeled into turbulence and particle re-acceleration. Remarkably, the existence of USSRHs, that is a challenge for the hadronic models, is a natural consequence of the turbulent scenario: in this case very steep spectra are interpreted as the consequence of the fact that radiative losses (Eq. 1.11) dominate over the re-acceleration rate at higher energies producing a steepening of the observed spectrum (e.g. Thierbach et al. 2003; Dallacasa et al. 2009). This class of sources should be the most common in the Universe as USSRHs can be triggered also by minor mergers, where the turbulent energy involved is smaller (e.g. Cassano et al. 2006). Observations at low frequencies have the potential to further test this scenario (Chapter 7).

In literature there is only one reported case of a giant radio halo discovered in a CC/non-merging system, i.e. CL1821+643 (Bonafede et al. 2014b; Boschini & Girardi 2018). If further studies will increase the statistical occurrence of these objects, it would imply that other mechanisms (or minor mergers) may generate Mpc-scale diffuse radio emission also in dynamically relaxed systems.

1.7 Non-thermal X-ray emission

The CRe with $\gamma \sim 10^4$ in $\sim \mu\text{G}$ magnetic fields that produce radio synchrotron emission in the form of relics and halos are also expected to emit in the hard X-rays by IC scattering with CMB photons (Harris & Grindlay 1979; Rephaeli 1979). Indeed, the typical energy of relativistic electrons emitting photons with energy E_{ph} observed in the hard X-ray band (> 20 keV) via IC is

$$E_e \simeq 3 \left(\frac{E_{ph}}{30 \text{ keV}} \right)^{1/2} \quad [\text{GeV}] \quad (1.43)$$

while the energy of relativistic electrons emitting synchrotron radiation, emitted at redshift z and observed at frequency ν_0 , is

$$E_e \simeq 7 \left(\frac{\mu\text{G}}{B} \frac{\nu_0}{\text{GHz}} \right)^{1/2} (1+z)^{1/2} \quad [\text{GeV}]. \quad (1.44)$$

As a consequence, the two processes sample pretty much the same population of CRe.

The detection of non-thermal IC emission in galaxy clusters in data of satellites like *Chandra* and *XMM-Newton* (sensitive up to ~ 10 keV) is challenged by the mixing with to the thermal

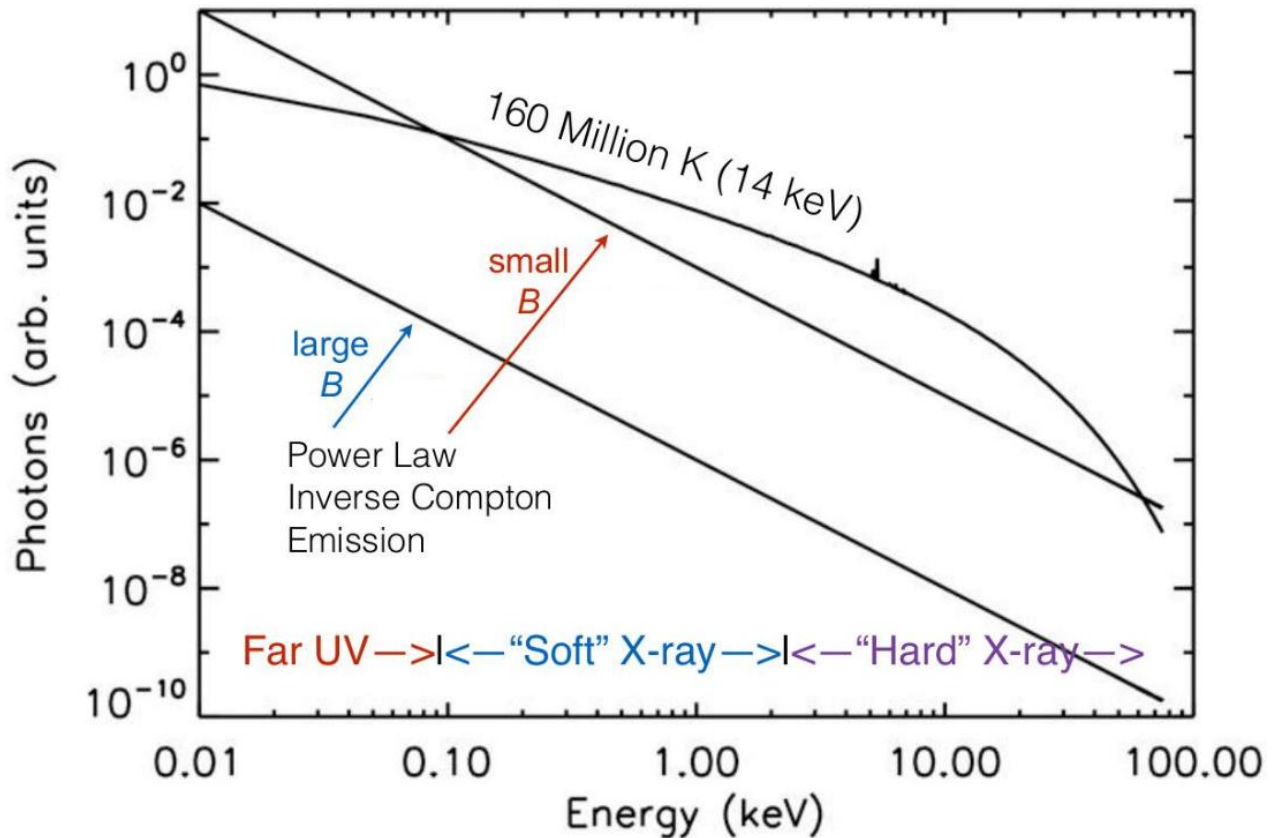


Figure 1.18: Schematic representation of the ICM spectrum. The thermal bremsstrahlung emission is characterized by a cutoff at high energy, while the IC component is reported with two power-laws (corresponding to two different values of magnetic field). Credit: D. Wik.

bremsstrahlung ICM emission. Nonetheless, for typical ICM temperatures, the exponential cutoff of bremsstrahlung (Eq. 1.7) prevents thermal emission above $\gtrsim 10$ keV (Fig. 1.18), enabling the search for IC in the hard X-rays. However, the IC component can be also hindered by the presence of multi-temperature structures that naturally originate in merging galaxy clusters, and that require to be modeled accurately to avoid false IC detections.

The search for IC emission from galaxy clusters has been undertaken for many years with many instruments. The first observational campaigns were carried out with non-imaging and high background instruments like the High Energy Astronomy Observatory-1 (HEAO-1) that yielded only upper limits on the IC flux. The next generation of hard X-ray satellites, such as *Beppo-SAX* and the Rossi X-Ray Timing Explorer (RXTE), allowed to produce the first claims of detection of non-thermal emission in the hard X-rays in several clusters, although mostly of marginal significance and controversial (e.g. Fusco-Femiano et al. 1999, 2000, 2001, 2003, 2005, 2007; Rephaeli et al. 1999; Rephaeli & Gruber 2002; Rossetti & Molendi 2004). More recently, new instruments such as the INTERNATIONAL Gamma-Ray Astrophysics Laboratory (INTEGRAL), *Suzaku* and *Swift*, largely failed to confirm IC at similar levels (see Ota et al. 2014, and references therein). The hope to detect the long-sought IC signal with the *NuSTAR*, i.e. the first satellite with imaging capabilities in the hard X-ray band (3 – 79 keV), appears disheartened by recent observations (Wik et al. 2014; Gastaldello et al. 2015).

In principle, the detection of IC from synchrotron sources in galaxy clusters would allow to measure the magnetic field in the ICM. Indeed, a proportionality between synchrotron and IC luminosities exists

$$\frac{L_{syn}}{L_{IC}} \propto \frac{\epsilon_B}{\epsilon_{ph}}, \quad (1.45)$$

where the only unknown quantity in the above equation is the energy density of the magnetic field. Assuming that both X-ray and radio emissions arise from the same power-law electrons population (Eq. 1.28), synchrotron and IC spectra result in power-laws sharing the same spectral index (Eq. 1.37). The IC flux received by the observer at frequency ν_X can be calculated from the synchrotron flux received at the frequency ν_R with

$$F_{IC}(\nu_X) = 1.38 \times 10^{-34} \left(\frac{F_{syn}(\nu_R)}{\text{Jy}} \right) \frac{(1+z)^{\alpha+3}}{\langle B_{\mu G}^{1+\alpha} \rangle} \left(\frac{\frac{\nu_X}{\text{keV}}}{\frac{\nu_R}{\text{GHz}}} \right)^{-\alpha} \zeta(\alpha) \quad [\text{erg s}^{-1}] \quad (1.46)$$

where $\langle \dots \rangle$ denotes the emission-weighted quantity in the emitting volume and $\zeta(\alpha)$ is a dimensionless function whose values for different spectral indexes can be found in Brunetti & Jones (2014). Eq. 1.46 reveals that the detection of IC emission from galaxy clusters in the X-ray band constrains the average value of the magnetic field in the emitting region. In the case of non-detection, the upper limit on the IC flux is still a useful quantity as it can be converted to a lower limit on B . For example, so far, the non-detection of IC emission in galaxy clusters made possible to derive only lower limits of the order of $B \gtrsim 0.1 \mu\text{G}$ on the magnetic field strength in the ICM (e.g. Rephaeli et al. 2008).

Radio relics are appealing targets in the search for the IC signal (Chapter 4). Indeed, relics have angular sizes smaller than halos and are located in peripheral locations, where thermal emission is fainter. This makes possible to check the presence of IC emission also in the soft X-rays with instruments such as *Chandra* and *XMM-Newton*. Nonetheless, the average magnetic field in relics is likely enhanced than that (averaged) in the region of radio halos by the shock compression, decreasing the expected IC flux (Fig. 1.18).

A shock at the radio relic position in Abell 115[†]

ABSTRACT

As explained in Section 1.5, radio relics are thought to be generated by shock acceleration or re-acceleration. Here we analyze a deep *Chandra* observation of the galaxy cluster Abell 115 and detect a shock co-spatial with the radio relic. The X-ray SB and temperature profiles across the western portion of the relic suggest the presence of a weak shock with Mach number $\mathcal{M} \sim 1.8$. So far, only few other shocks discovered in galaxy clusters have been consistently detected from both density and temperature jumps (Section 1.3.2). The spatial coincidence between this discontinuity and the radio relic edge strongly supports the view that shocks play a crucial role in powering these synchrotron sources. We suggest that the relic is originated by shock re-acceleration of fossil relativistic electrons rather than acceleration from the thermal pool. The position and curvature of the shock and the associated relic are consistent with an off-axis merger with unequal mass ratio where the shock is expected to bend around the core of the less massive cluster.

2.1 Introduction

Abell 115 (hereafter A115) is an X-ray luminous ($L_X = 1.5 \times 10^{45}$ erg s⁻¹ in the 0.1 – 2.4 keV band) and dynamically disturbed cluster at $z = 0.197$. Early X-rays observations (Forman et al. 1981; Shibata et al. 1999) revealed that A115 has a X-ray brightness distribution characterized by two peaks, the brightest one being in the North region and roughly coincident with the position of the powerful radio galaxy 3C28. More recently, *Chandra* observations (Gutierrez & Krawczynski 2005) suggested that A115 is undergoing an off-axis merger, while optical studies confirmed the presence of two sub-clusters in a merging state (Barrena et al. 2007). In the radio band, A115 exhibits a giant radio relic at the edge of the northern part of the cluster that extends for ~ 1.5 Mpc (Govoni et al. 2001b). In this Chapter, we report on the discovery of a shock associated with such a relic from the analysis of *Chandra* and VLA observations of A115.

[†]Based on Botteon et al. (2016a,b).

2.2 Observations and data reduction

2.2.1 X-ray data reduction

We analyzed the *Chandra* ACIS-I observations of A115 in VFaint mode (ObsID: 3233, 13458, 13459, 15578, 15581) with CIAO v4.7 and *Chandra* CALDB v4.6.9. All data were reprocessed from level=1 event file following the standard *Chandra* reduction threads. For the observations in which the S2 chip was active (ObsID: 3233, 13459, 15581), we extracted light curves from this chip in the 0.5 – 2.0 keV band and we cleaned from soft proton flares using the `deflare` task with the `clean=yes` option. For the other ObsIDs, light curves were instead extracted from a cluster free emission region in one ACIS-I chip. We combined the observations with the `merge_obs` script and produced the 0.5 – 2.0 keV image binned by a factor of 2 shown in Fig. 2.1. The total effective exposure time of this image is 334 ks.

For each observation we created a point spread function (PSF) map at 1.5 keV. These were combined with the corresponding exposure maps in order to obtain a single exposure-corrected PSF map with minimum size. We then ran the `wavdetect` task on the merged image in order to detect point sources. Sources were visually confirmed and then excluded in the further analysis. We used the task `reproject_event` to match background templates to the corresponding event files for every ObsID. Then they were normalized by counts in the 9.5 – 12.0 keV energy band and combined in a single background image subtracted in the SB analysis.

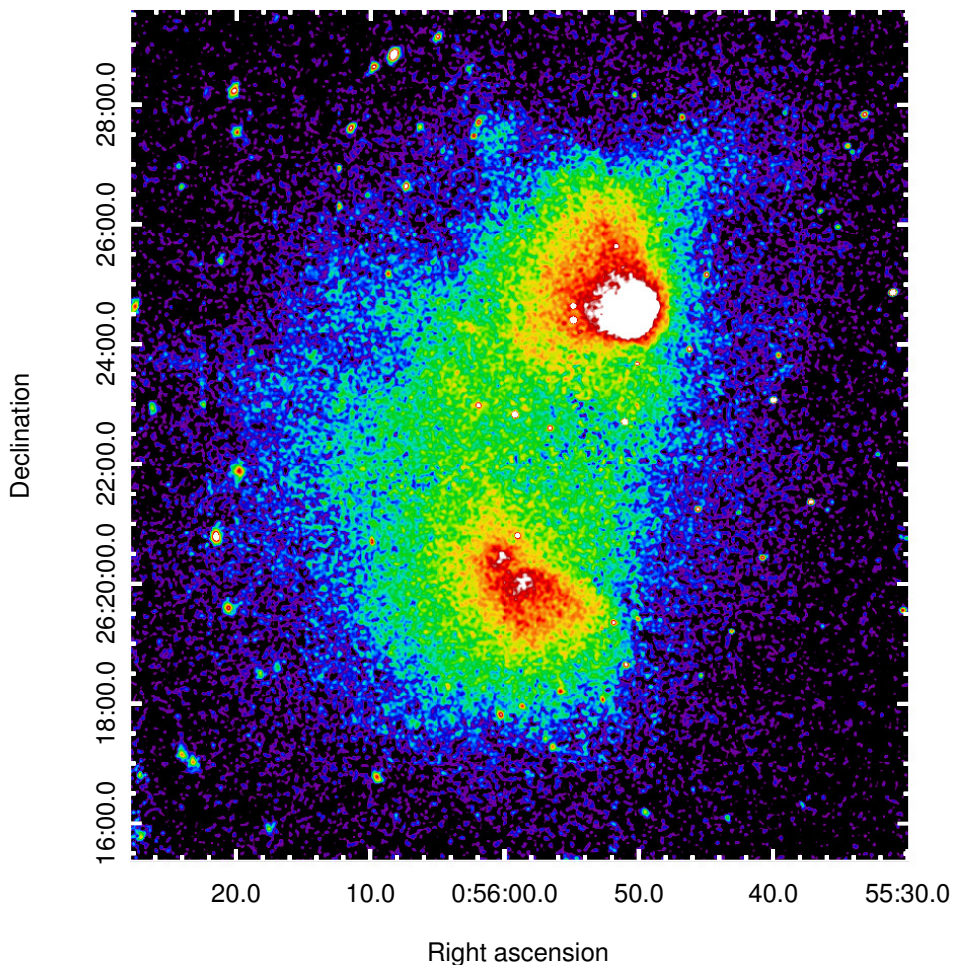


Figure 2.1: *Chandra* exposure-corrected image in the 0.5 – 2.0 keV band of A115. The image is smoothed on a 3'' scale.

Spectral extraction was performed for every ObsID using the same regions. We modeled the instrumental non-X-ray background (NXB) following Bartalucci et al. (2014) and the sky component with two thermal plasmas at temperatures of 0.14 and 0.25 keV to account for the Local Hot Bubble (LHB) and the Galactic Halo (GH) emission, respectively, and an absorbed power-law with photon index $\Gamma = 1.4$ to account for the cosmic X-ray background (CXB). The background parameters were determined by fitting spectra extracted from cluster-free emission regions at the edge of the field-of-view (FoV) in the 0.5 – 11.0 keV energy band. The cluster emission was fitted with a thermal model with metal abundance fixed at $0.3 Z_{\odot}$. All fits were performed using Cash statistics (Cash 1979). The robustness of the fits was verified by checking for systematic errors due to the background determination. For this reason, we re-performed the cluster spectral analysis with the background normalization levels fixed at $\pm 1\sigma$ within their best fit values. In addition, the impact of ACIS-I Quantum Efficiency contamination at low energy was verified by fitting in the 0.5 – 11.0 and 1.0 – 11.0 keV bands. In both cases, the thermal parameters of the fits are consistent within 1σ .

2.2.2 Radio data reduction

We re-analyzed VLA archival data at 1.4 GHz in the C and D configurations. Details of observations can be found in Govoni et al. (2001b). The two datasets were edited, calibrated and imaged separately. Particular care was devoted to the identification and removal of bad data corrupted by intermittent radio frequency interference (RFI). After a number of phase-only self-calibration iterations and an accurate comparison of the flux densities of the sources, the data of the first Intermediate Frequency channel, at 1364 MHz for both datasets, were combined (the second Intermediate Frequency channel could not be used given the significantly different frequency). The final dataset (4.5 hr and $\Delta\nu = 50$ MHz) was once again self-calibrated a number of times and final images were obtained using different weighting schemes. The image shown in Fig. 2.2a was made with a two-scale clean where the extended emission was deconvolved using a larger beam ($\sim 30''$). The restoring beam is $15'' \times 14''$ in position angle -35° and the off-source noise level is $70 \mu\text{Jy beam}^{-1}$. Errors on flux densities were estimated via

$$\Delta S = \sqrt{\left(\sigma_{rms} \times \sqrt{\frac{A_s}{A_b}}\right)^2 + (\xi \times S)^2} \quad (2.1)$$

where ξ is the calibration uncertainty, σ_{rms} is the root-mean-square noise while A_s and A_b are the source and beam areas, respectively. We adopted an uncertainty of 5% on the absolute flux scale calibration.

2.3 Results

A visual inspection of the X-ray image of A115 led us to identify a SB jump in the northern part of the system, co-spatially located with the relic position (Fig. 2.2). The SB profile was extracted in the red sector shown in Fig. 2.2b and fitted with PROFFIT v1.3 (Eckert et al. 2011). As outlined in Section 1.3.2, SB discontinuities are generally characterized assuming an underlying broken power-law density profile (Eq. 1.21). We performed this kind of analysis in the northern sector of A115 leaving all the parameters of the fit free to vary. The curvature radius of the putative shock relative to the line-of-sight was assumed to be the same as that in the plane of the sky. The best fit broken power-law is shown in Fig. 2.3. The compression factor taken from the red sector in Fig. 2.2b is $\mathcal{C} = 2.0 \pm 0.1$. By using the Rankine-Hugoniot jump conditions this leads to a Mach number $\mathcal{M}_{\text{SB}} = 1.7 \pm 0.1$ (Eq. 1.18). Obviously, this value does not include systematics deriving from 3D

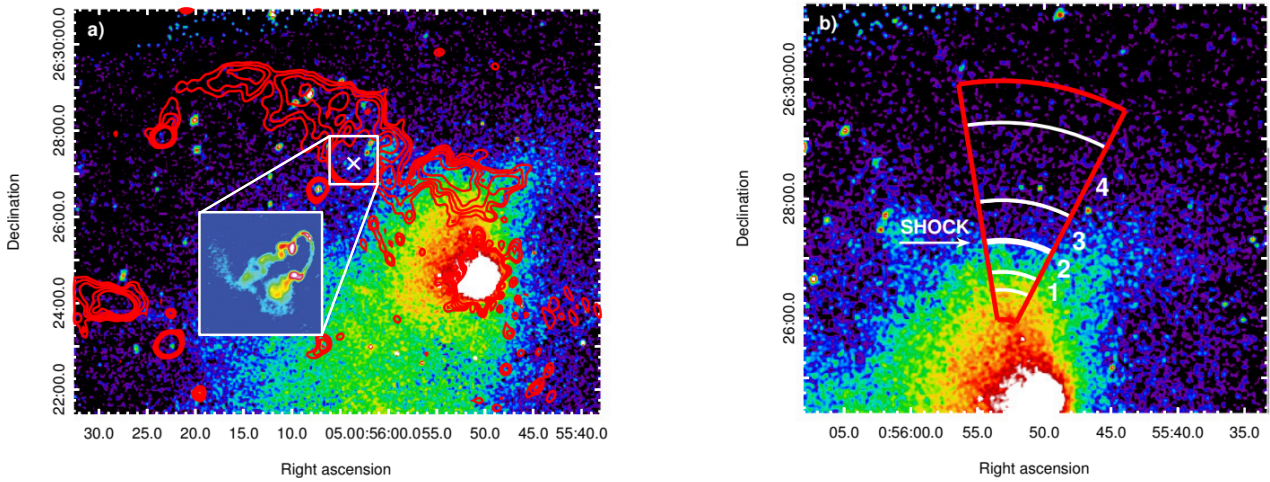


Figure 2.2: Zoom on the northern region of A115. *a)* Radio contours at 1.4 GHz of the relic source in A115. The resolution is $15'' \times 14''$. Contour levels are $3\sigma \times \pm(\sqrt{2})^n$, with $n = 1, 2, 3, 4$. The 1σ noise level is $70 \mu\text{Jy beam}^{-1}$. White cross denotes the 0056 + 26 B radio galaxy. The zoom-in panel shows the combined VLA B and C configuration radio map between 4 and 8 GHz of 0056 + 26 B by Harwood et al. (2015). *b)* Red sector delineates the region where the X-ray SB profile was extracted; white sectors represent the four bins where spectral analysis was performed. In both panels colors represent the *Chandra* image (same of Fig. 2.1).

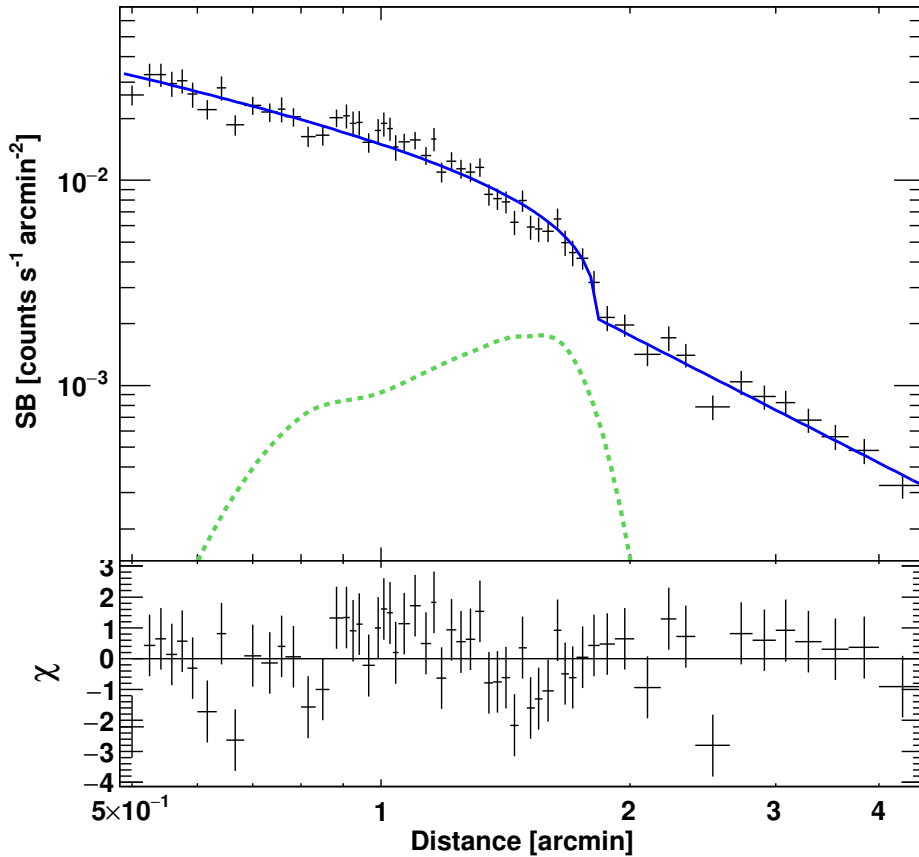


Figure 2.3: X-ray SB profile in the 0.5 – 2.0 keV band extracted in the red region shown in Fig. 2.2b. Data were rebinned to reach a minimum signal-to-noise ratio (S/N) of 7. The fit had $\chi^2/\text{d.o.f.} = 1.2$. The best fit model and the radio relic brightness profile (in arbitrary units) are shown in *solid blue* and *green dashed*, respectively. The bottom panel shows the fit residuals.

model geometry and the shape of the extraction region. We explored uncertainties due to the sector choice by varying its curvature radius, aperture and position angle. Tests were made keeping the discontinuity distance frozen. Changing the shock curvature radius from its best value 360 kpc by a factor 0.5 and 1.5 gives the highest variation in terms of the compression factor, 1.6 – 2.1, corresponding to $\mathcal{M}_{\text{SB}} = 1.4 - 1.8$. Varying the other parameters of the region results in values of \mathcal{M}_{SB} within this range. We did not introduce any ellipticity in the problem as the SB edge looks quite straight. The red sector in Fig. 2.2b represents the best compromise to highlight the discontinuity in terms of $\chi^2/\text{d.o.f.}$.

In a shock wave, the downstream region is characterized by an increase of the temperature; in a cold front instead the denser region has a lower temperature (see e.g. Markevitch & Vikhlinin 2007). For this reason, we extracted spectra in the four white regions shown in Fig. 2.2b and performed spectral fitting. We found a temperature jump from $kT_u = 4.3_{-0.6}^{+1.0}$ keV to $kT_d = 7.9_{-1.1}^{+1.4}$ keV in the two bins closer to the SB discontinuity, confirming the shock nature of this feature. By using Eq. 1.17, this temperature jump corresponds to $\mathcal{M}_{\text{kT}} = 1.8_{-0.4}^{+0.5}$, in agreement with the Mach number derived from the density jump. Projection effects, if they play a role, are expected to make the intrinsic jump slightly smaller. The temperature profile taken across the shock region is shown in Fig. 2.4. The first bin exhibits a low temperature, this could either be the result of the gas expansion behind the shock or the presence of a sub-structure along the line-of-sight (e.g. Markevitch et al. 2002). For a sanity check we re-performed the SB fit avoiding this temperature bin by excluding data points at $r < 1.5'$; in this case we achieve $\mathcal{C} = 2.0 \pm 0.3$, leading to $\mathcal{M}_{\text{SB}} = 1.7_{-0.2}^{+0.3}$.

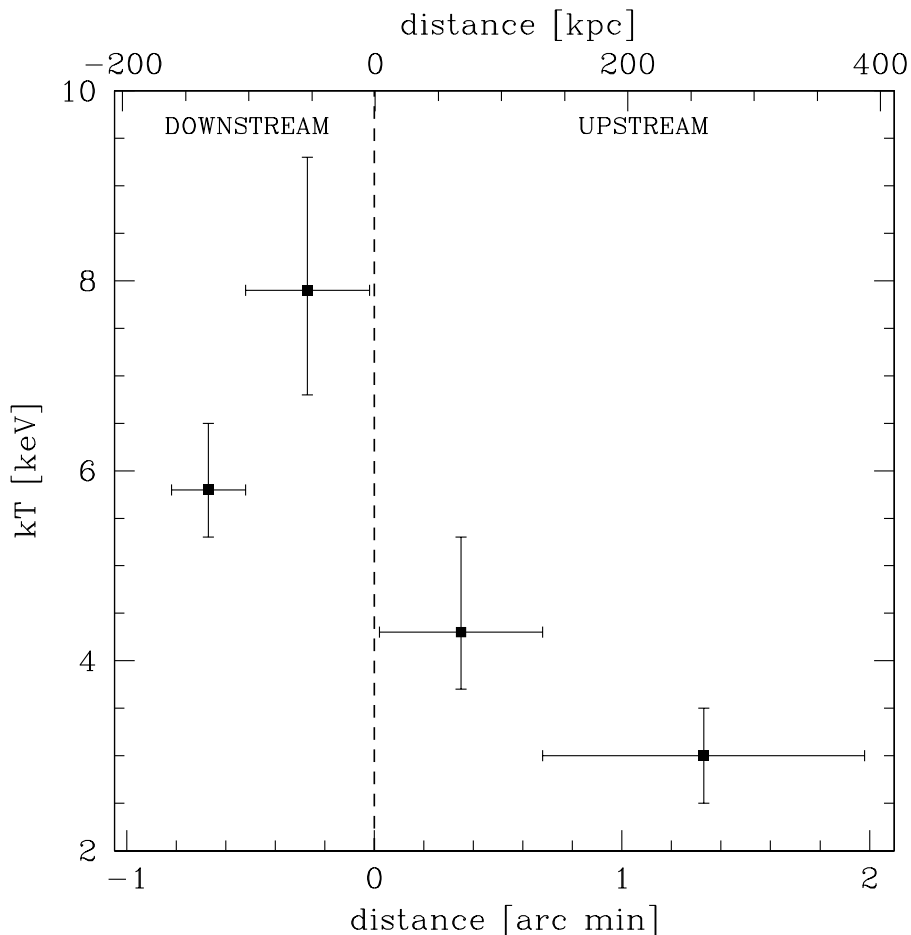


Figure 2.4: Temperature profile across the shock. The vertical dashed line sets the location of the X-ray SB discontinuity.

2.4 Discussion

2.4.1 Radio relic–shock connection

At the resolution of $15'' \times 14''$, the radio relic in A115 presents a discontinuity in the center of its northern edge structure, roughly splitting it in two parts (Fig. 2.2a). One is quite short, straight in the E-W direction and coincides with the shock location, while the remainder extends in the eastern direction beyond the cluster X-ray emission and appears slightly bent. Given the spatial coincidence with the shock we suggest that the former is a “classical” radio relic where particles are accelerated or re-accelerated by the passage of the shock. In this restricted region, the radio flux density at 1.4 GHz is $S = 34 \pm 2$ mJy. The eastern radio emission is more difficult to interpret and it could be produced by the uplifting of the plasma coming from the cluster radio bright source 0056 + 26 B (a narrow angle tailed radio galaxy whose emission fades away in the East direction, see inset panel in Fig. 2.2a), located in the middle of the relic, after the shock passage.

In the case of a head-on merging in the plane of the sky between two clusters with similar mass, radio relics are expected to come into pairs in opposite directions along the axis merger (e.g. Röttgering et al. 1997). This is clearly not the case of A115 where the relic has an unusual location as it is oriented almost parallel to the northern sub-cluster motion. This led to doubts about the nature of relic extended emission and to the interpretation as tails of radio plasma trailing the radio galaxies (Gutierrez & Krawczynski 2005). However, numerical simulations of an off-axis merger between clusters with different mass predicts that the shock bends around the core of the minor cluster (see Fig. 7 in Ricker & Sarazin 2001), in agreement with A115N sub-cluster being less massive (Barrena et al. 2007).

2.4.2 Acceleration efficiency

There is consensus on the hypothesis that shocks play an important role for the origin of radio relics (Section 1.5). However, the case of shock acceleration of CRe from the thermal ICM is challenged by the large efficiencies that are required to reproduce the total radio luminosity of several relics (e.g. Brunetti & Jones 2014, for a review). To alleviate the large requirements for acceleration efficiencies of CRe, recent models for cluster relics assume shock re-acceleration of a pre-existing population of CRe (Markevitch et al. 2005; Kang et al. 2012; Pinzke et al. 2013; Kang et al. 2014).

A115 is a test case to constrain the origin of the shock–relic connection, because the underlying shock is well constrained. Assuming a shock surface $A = \pi \times 180 \times 180$ kpc² and upstream density $n_u = 9.5 \times 10^{-4}$ cm³, we can calculate the efficiency of the shock acceleration process via Eq. 1.39.

A model of shock acceleration from the thermal pool for the relic is readily ruled out by our measurements. According to DSA theory the particles injection spectrum is a power-law with slope given by Eq. 1.35 (e.g. Blandford & Eichler 1987), that for $\mathcal{M} = 1.7 - 1.8$ would imply $\delta_{inj} = 4 - 3.8$ (and integrated spectral index $\alpha = 2 - 1.9$). Not only this is inconsistent with the measured spectrum of the relic ($\alpha \sim 1.1$, Govoni et al. 2001b), but from Eq. 1.39 it also requires an unrealistically large acceleration efficiency.

Alternatively, we can assume re-acceleration. In this case the initial (upstream) and accelerated spectra of electrons are connected via Eq. 1.41; re-acceleration efficiencies can be larger compared to the case of acceleration from thermal ICM, because seed ultra-relativistic electrons diffuse efficiently across the shock discontinuity (e.g. Brunetti & Jones 2014). In Fig. 2.5 we show the case of a spectrum of re-accelerated electrons with power-law $\delta_{inj} = 3.8$ and $p_{min}/m_e c = 20$ and 200. Re-acceleration of electrons with $p_{min} \geq 100m_e c$ appears energetically viable. In this case, however, the spectrum of the relic would be very steep ($\alpha \sim 2$). Alternatively, the shock may re-accelerate a cloud of electrons that are not very old and have a flatter spectrum. In this case the shock essentially

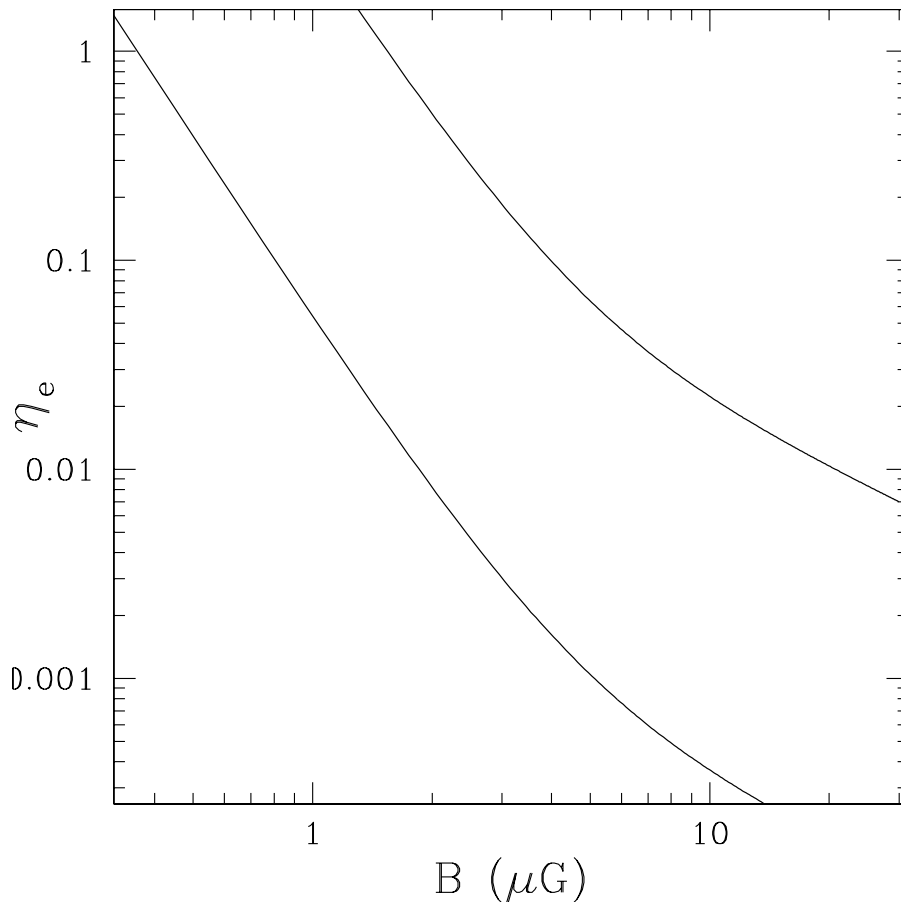


Figure 2.5: Electron acceleration efficiency versus magnetic field in the downstream region in the shock in A115. Lines represent efficiencies evaluated for re-accelerated electrons with two initial energies, namely $p_{min}/m_e c = 20$ (*top*) and 200 (*bottom*) and $\delta_{inj} = 3.8$.

boosts their emission at higher frequencies preserving the seed spectrum (Eq. 1.41, see e.g. Kang & Ryu 2016, for details). As already discussed in Section 2.4.1, re-acceleration is also suggested by the morphology of the radio relic and by the fact that the relic embeds a few radio galaxies that would be natural sources of seed particles. Finally, we note that the eastern part of the radio relic deploys into a region of low X-ray SB where the thermal energy density is small and where a scenario of shock acceleration of thermal electrons would require an efficiency that is even larger than that shown in Fig. 2.5.

2.5 Conclusions

In this Chapter, we presented results concerning the merging galaxy cluster A115 at $z = 0.197$ focusing on its northern sub-cluster, where a giant radio relic stands out. Our analysis was based on a *Chandra* dataset for a total exposure time of 334 ks and archival VLA radio observations at 1.4 GHz.

The deep *Chandra* observations led us to detect a shock spatially coincident with the radio relic in A115. Assuming a broken power-law density profile, the SB discontinuity is consistent with a density compression factor $\mathcal{C} = 2.0 \pm 0.1$, which in turn results in $\mathcal{M}_{SB} = 1.7 \pm 0.1$; the Mach number is in the range 1.4 – 2 including systematic uncertainties. The shock nature of the discontinuity was confirmed by spectral analysis of the downstream and the upstream regions, where

a temperature jump from $kT_d = 7.9^{+1.4}_{-1.1}$ keV to $kT_u = 4.3^{+1.0}_{-0.6}$ keV was found, implying $\mathcal{M}_{\text{KT}} = 1.8^{+0.5}_{-0.4}$. This is one of the few cases where the SB and temperature drops in a merger shock are clearly detected and are in excellent agreement.

In the radio band, the relic can be roughly divided into a W and an E part. The former is a “classical” relic spatially coincident with the shock found in the X-rays. The relic location is in agreement with an off-axis merger between two clusters with unequal mass, where the shock bends around the core of the less massive system. The eastern relic radio emission is harder to interpret as, in this region, a proper X-ray analysis cannot be performed given its low SB. An attractive scenario is the uplifting of the cluster radio galaxy 0056+26 B plasma after the shock sweeping in the cluster outskirts.

Since the shock in A115 is well constrained, we were able to test the models for the origin of radio relics that have been described in Section 1.5. Given the low Mach number, spectrum and morphology of the relic, models in which relativistic seed electrons are re-accelerated by the shock passage are favored. In this respect, the few cluster radio galaxies embedded in the relic in A115 could naturally provide the required seed particles.

A $\mathcal{M} \gtrsim 3$ shock for El Gordo and the origin of the NW radio relic[†]

ABSTRACT

We present an X-ray and radio study of the famous El Gordo, a massive and distant ($z = 0.87$) galaxy cluster. In the deep *Chandra* observation, the cluster appears with an elongated and cometary morphology, a distinctive sign of its current merging state. The GMRT radio observations at 610 MHz confirm the presence of a radio halo which remarkably overlaps the X-ray cluster emission and connects a couple of radio relics. We detect a strong shock ($\mathcal{M} \gtrsim 3$) in the NW periphery of the cluster, co-spatially located with the radio relic. This is the most distant ($z = 0.87$) and one of the strongest shock detected in a galaxy cluster. This discovery allows us to investigate the origin of the radio relic and to test the models discussed in Section 1.5. Our results support the relic–shock connection and allow us to investigate the origin of these radio sources in a uncommon regime of $\mathcal{M} \gtrsim 3$. For this particular case, we found that shock acceleration from the thermal pool is still a viable possibility.

3.1 Introduction

ACT-CL J0102–4915 is the most massive cluster detected in the far Universe, at a redshift of $z = 0.87$ (Menanteau et al. 2012). For its extraordinary mass of $M_{500} \sim 8.8 \times 10^{14} M_{\odot}$ (Planck Collaboration XXIX 2014), it is also known with the nickname of “El Gordo” (which means “The Fat/Big One” in Spanish). The cluster was firstly discovered by its strong SZ signal (Marriage et al. 2011) and later confirmed through optical and X-ray observations. The system is in a complex merger state, as revealed by the double peaked galaxy distribution and the elongated morphology of its hot ($kT \sim 15$ keV) ICM (Menanteau et al. 2010, 2012). In the radio band, a tenuous halo and a double relic system at the cluster NW and SE X-ray boundaries were discovered (Lindner et al. 2014). In this Chapter, we report on the discovery of a strong shock associated with a radio relic in El Gordo cluster. In particular, our joint *Chandra* and GMRT analysis provides interesting insights about the origin of the relic.

[†]Based on Botteon et al. (2016c).

3.2 Observations and data reduction

3.2.1 X-ray data reduction

El Gordo was observed three times (ObsID: 12258, 14022, 14023) with *Chandra* in ACIS-I configuration and VFaint mode for a total exposure time of 360 ks. We carried out the standard data reduction by using CIAO v4.7 and *Chandra* CALDB v4.6.9. In particular, soft proton flares were inspected analyzing the light curves extracted from the S2 chip in the 0.5 – 2.0 keV band for each ObsID and removed using the `lc_clean` routine. We then used the `merge_obs` task to make the final 0.5 – 2.0 keV cleaned image (340 ks) shown in Fig. 3.1a.

We created a single exposure-corrected PSF map with minimum size for the merged image by combining the PSF and exposure maps of each ObsID. Once the PSF of the instrument is known, the `wavdetect` task allows to identify discrete sources in the SB image of the cluster. These were detected using wavelet radii of 1, 2, 4, and 8 pixels, confirmed by eye and excluded in the subsequent analysis. In order to create a single background image, the `reproject_event` task was used to match the background templates to the corresponding event files for every ObsID. This single background image was normalized by counts in the band 9.5 – 12.0 keV and subtracted during the SB analysis.

Dealing with spectral analysis of low SB sources as in the case of cluster outskirts requires a detailed treatment of the astrophysical and instrumental background emission. In this respect, we modeled the sky component due to the Galactic emission with two thermal plasmas with $kT_1 = 0.14$ keV and $kT_2 = 0.25$ keV, the CXB with an absorbed power-law with photon index $\Gamma = 1.4$ and the ACIS-I particle background by using the analytical approach proposed by Bartalucci et al. (2014). Spectra were extracted in the same region for every ObsID and simultaneously fitted in the 0.5 – 11.0 keV energy band with the package XSPEC v12.9.0o. Since the low X-ray count rate, we kept the metal abundance of the APEC model, which accounts for the ICM thermal emission, fixed at the value of $0.3 Z_{\odot}$ (solar abundance table by Anders & Grevesse 1989) and used Cash statistics (Cash 1979) for the fits.

3.2.2 Radio data reduction

Archival GMRT 610 MHz observations of El Gordo (project code 22_001, PI: R. R. Lindner) taken on 26 August 2012 were analyzed using AIPS. The GMRT Software Backend was used to record the parallel polarization products RR and LL with a bandwidth of 33.3 MHz divided into 256 channels. The source 3C48 was used for flux and bandpass calibration and the calibrator 0024 – 420 was used for phase calibration toward the target. The total on-target observing time was 170 min. Standard steps of flagging (excision of bad data) and calibration were carried out. The resulting calibrated visibilities of the target were then split from the multi-source file and used for imaging. A few rounds of phase-only self-calibration and a round of amplitude and phase self-calibration were carried out to improve the quality of the image. The final image with visibilities weighted according to ROBUST 0 in the task IMAGR and resolution $11'' \times 4.8''$ (position angle 4.8°) is presented in Fig. 3.1b. The image was corrected for the GMRT primary beam using the task PBCOR. The off-source noise level is $50 \mu\text{Jy beam}^{-1}$ and a 10% error on the absolute flux calibration scale was assumed. Quoted errors on flux densities were estimated via Eq. 2.1. As a preliminary result of new GMRT data, we also used observations taken at 327 MHz (project code 25_023, PI: R. Kale) to perform spectral analysis.

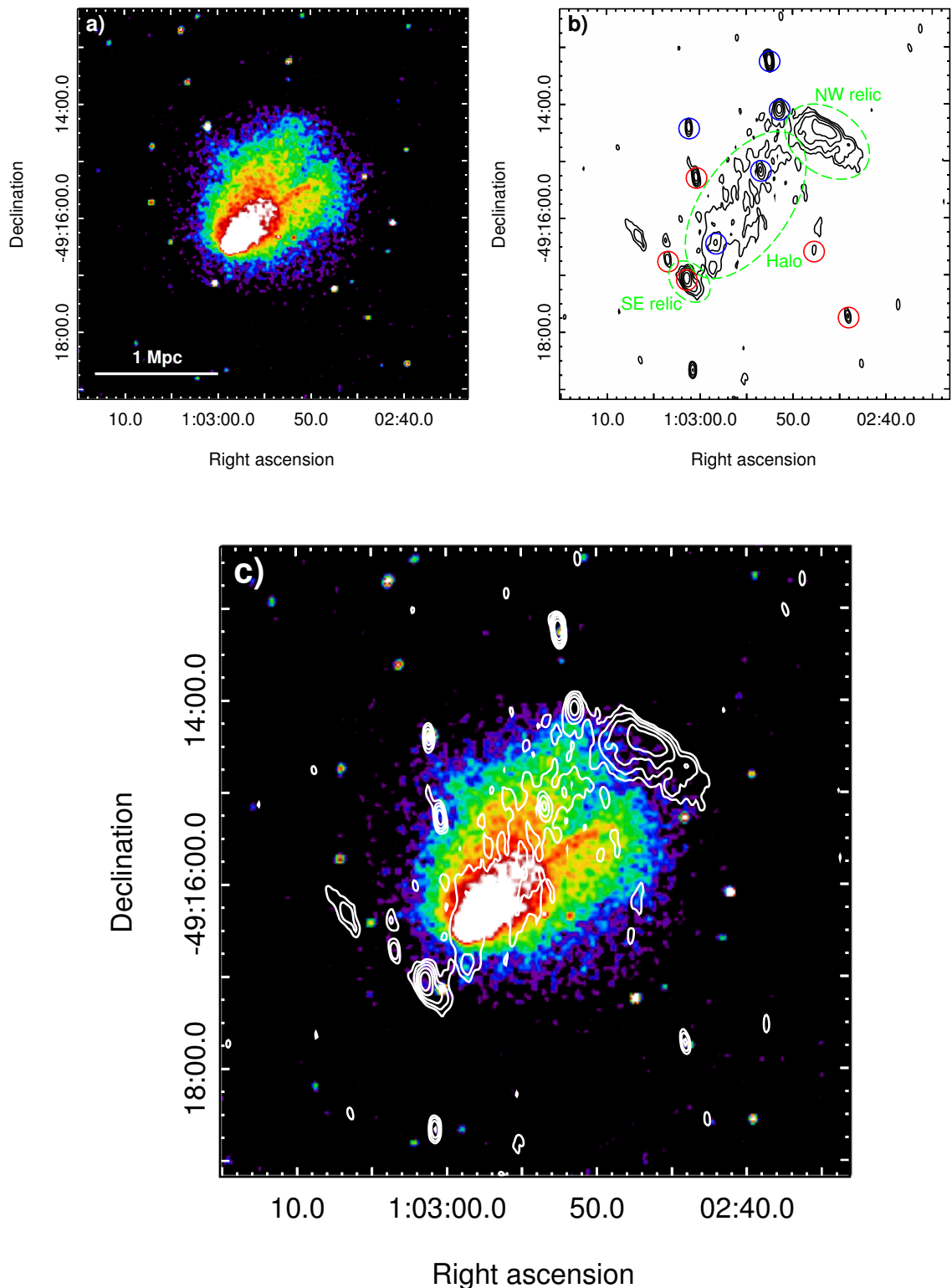


Figure 3.1: El Gordo galaxy cluster. *a*) *Chandra* 0.5 – 2.0 keV band exposure-corrected image smoothed on a 3'' scale. *b*) GMRT 610 MHz radio emission at a resolution of 11'' × 4.8''. The 1σ noise level is 50 μJy beam⁻¹, contours are drawn at levels of 3σ × (-1, 1, 2, 4, 8, 16). Circles denote the compact radio sources identified in Lindner et al. (2014) as cluster members (red) or not (blue). *c*) In the *Chandra*/GMRT comparison the location of the radio relics at the cluster X-ray boundaries and the spatial connection between the halo and the northern X-ray tail are evident.

3.3 Results

3.3.1 X-ray/radio analysis

El Gordo X-ray emission is remarkably reminiscent of the famous Bullet Cluster (Markevitch et al. 2002): a dense CC ($kT \sim 6$ keV) is moving in the SE-NW direction producing a prominent cold front (Menanteau et al. 2012) which is expected to follow a shock wave (e.g. Vikhlinin et al. 2001b; Markevitch et al. 2002). The cluster is elongated along the merger direction and presents two X-ray tails giving a comet-like morphology to the system (Fig. 3.1a).

Our 610 MHz radio image of El Gordo recovers extended emission better than previously done by Lindner et al. (2014, Fig. 2 and 15) as we considered baselines down to $0.2 \text{ k}\lambda$ (instead of $0.48 \text{ k}\lambda$). This allows us to study the morphology of the diffuse sources in more detail. In our image shown in Fig. 3.1b, the prominent and elongated radio halo connects a pair of radio relics, located in opposite directions at the NW and SE edges of the cluster X-ray emission (Fig. 3.1c). The strongest part of the halo coincides with the disrupted cluster core, whereas a radio tail appears to remarkably follow the northern tail visible in the X-rays (Fig. 3.1c).

Our work is focused on the NW radio relic, whose flux densities at 610 and 327 MHz are $S_{610} = 27.5 \pm 2.8$ mJy and $S_{327} = 64.6 \pm 6.6$ mJy, respectively, providing a radio spectral index $\alpha = 1.37 \pm 0.20$. The flux density of the relic at 2.1 GHz measured by Lindner et al. (2014) with the ATCA implies $\alpha \sim 1.5$ from 2100 to 327 MHz, which is consistent with what we estimated in the narrower frequency range. Nevertheless, we will use the spectral index from 610 to 327 MHz since it is taken from two high sensitivity images obtained from GMRT observations with matched inner- uv coverage ($uv_{min} = 0.2 \text{ k}\lambda$).

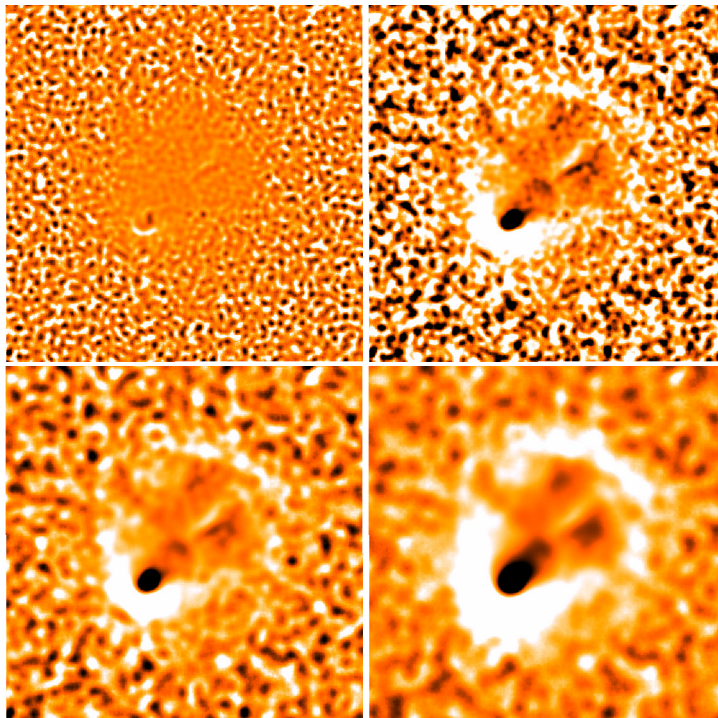


Figure 3.2: Unsharp-masked *Chandra* images for El Gordo cluster created by subtracting images convolved with Gaussians with σ_1 and σ_2 and dividing by the sum of the two. From top left panel in clockwise order $(\sigma_1, \sigma_2) = (3'', 5''), (3'', 20''), (7'', 30''), (5'', 20'')$.

3.3.2 Relics and shocks

In Section 1.4.1 we mentioned that double relics have been observed in different systems (e.g. de Gasperin et al. 2014, and references therein) and that are believed to form in mergers between two clusters with similar mass where diametrically opposite shocks move outwards along the merger axis (re)accelerating particles (van Weeren et al. 2011a). Menanteau et al. (2012) pointed out the possible presence of two shocks by analyzing a 60 ks *Chandra* unsharp-masked image of El Gordo. For these reasons, we created the unsharp-masked images shown in Fig. 3.2 and searched for sharp edges in the X-ray SB image, identifying at least one discontinuity in the cluster. We used PROFFIT v1.3.1 (Eckert et al. 2011) to extract the SB profiles in the red sectors shown in Fig. 3.3, where the NW relic stands out. Following Section 1.3.2, we adopted an underlying broken power-law density to describe the SB in presence of a discontinuity (Eq. 1.21). We used this density shape to fit the X-ray SB keeping all parameters of the model free to vary. The center of the sector in Fig. 3.3 in J2000 coordinates is RA: $+15^{\circ}.7275$, DEC: $-49^{\circ}.2724$.

We firstly report results concerning sector 1+2 (opening angle: $30^{\circ} - 98^{\circ}$) because it covers the whole extension of the feature shown in Fig. 3.2 and it gives the maximum SB drop with the best statistics (a discussion on the sector choice is presented in Section 3.3.2). In Fig. 3.4 we report the best broken power-law model fit, which is in excellent agreement with data. We detect a large SB drop, corresponding to a density compression factor $\mathcal{C} = 3.4_{-0.3}^{+0.4}$, co-spatially located with the relic. For a shock, the Rankine-Hugoniot jump conditions for a monatomic gas (Eq. 1.18) would lead to a Mach number $\mathcal{M}_{\text{SB}} = 4.1_{-0.9}^{+3.4}$. A $\mathcal{M} > 3$ shock is quite a rarity in galaxy clusters and so far only two of them have been detected ($\mathcal{M} = 3.0 \pm 0.4$ in the Bullet Cluster, Markevitch 2006; $\mathcal{M} = 3.0 \pm 0.6$ in A665, Dasadia et al. 2016).

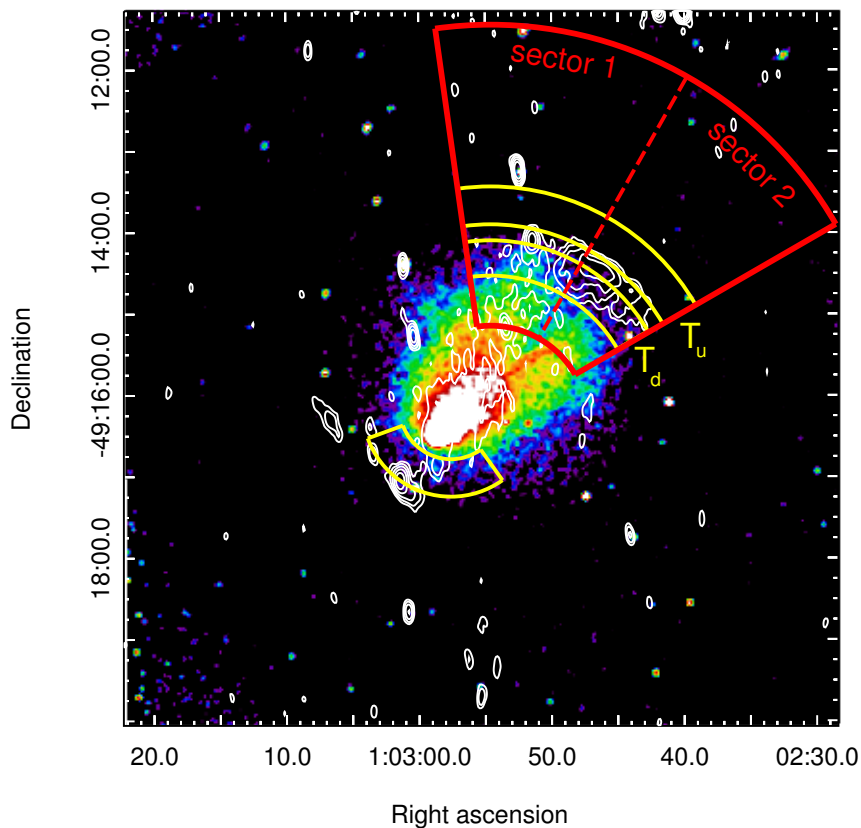


Figure 3.3: Radio/X-ray overlay of El Gordo. *Red* sectors outline the SB extracting regions. Spectral analysis was performed in the *yellow* sectors. Colors and contours are the same reported in Fig. 3.1.

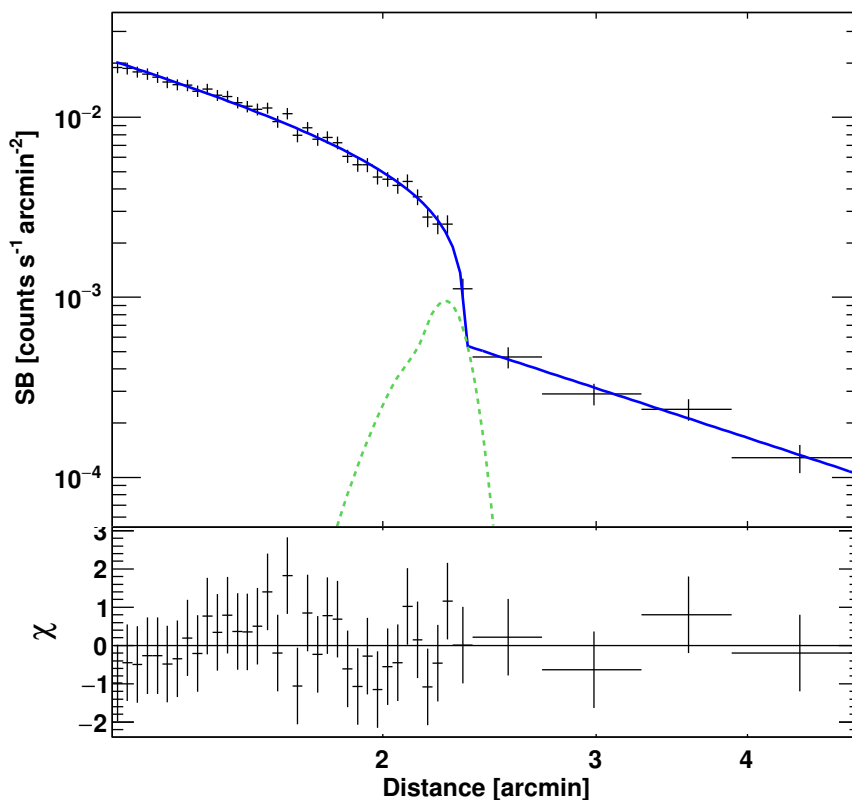


Figure 3.4: X-ray SB profile in the 0.5 – 2.0 keV band extracted in sector 1+2 (Fig. 3.3). Data were rebinned to reach a minimum S/N of 7. The best fit model is reported with the *solid blue line*. The *green dashed line* shows the NW radio relic brightness profile (in arbitrary units). Bottom panel shows the residuals of the fit.

As explained in Section 1.3.2, shocks heat the downstream gas allowing to distinguish them from cold fronts, other kinds of SB discontinuities found in galaxy clusters with inverted temperature jumps (e.g. Markevitch & Vikhlinin 2007). For this reason, we performed spectral analysis in the yellow sectors shown in Fig. 3.3. Spectra for sector 1+2 are reported in Fig. 3.5. We found evidence for a very high downstream temperature, $kT_d = 17.9^{+3.3}_{-2.8}$ keV, while only a lower limit on the upstream one was obtained, $kT_u > 6.1$ keV. In principle, this is not enough to confirm the shock nature of the discontinuity but, similarly to the E shock in the Bullet Cluster (Shimwell et al. 2015), the presence of a cold front is very unlikely because it would imply a too high temperature ($kT_u > 20$ keV) at such a large cluster distance.

Although current data do not allow to measure a temperature jump at the position of the shock, we can use the lower limit on such a jump to provide an independent constraint on the shock Mach number. According to the Rankine-Hugoniot conditions, the upstream and downstream temperatures are related by Eq. 1.17, which implies $\mathcal{M}_{kT} < 2.9$ if we use the upper 1σ limit of kT_d and the lower limit on kT_u . We anticipate that this value is consistent with the Mach number inferred from SB jump once systematic errors are taken into account (see the following Section)

A visual inspection of Fig. 3.1a suggests the presence of a drop in SB also at the position of the SE relic. A shock in this region is expected due to the presence of the radio relic and in analogy with the Bullet Cluster (Markevitch et al. 2002). However, current data do not allow us to characterize statistically the SB drop because of the low X-ray counts in this region. Nevertheless, we found evidence for a high temperature in the putative downstream gas, $kT_d = 30.1^{+10.5}_{-6.2}$ keV in the yellow sector in the SE (Fig. 3.3), somewhat supporting this possibility. As typical temperatures in cluster outskirts are of a few keV, such an high kT_d would likely imply another strong shock in the ICM.

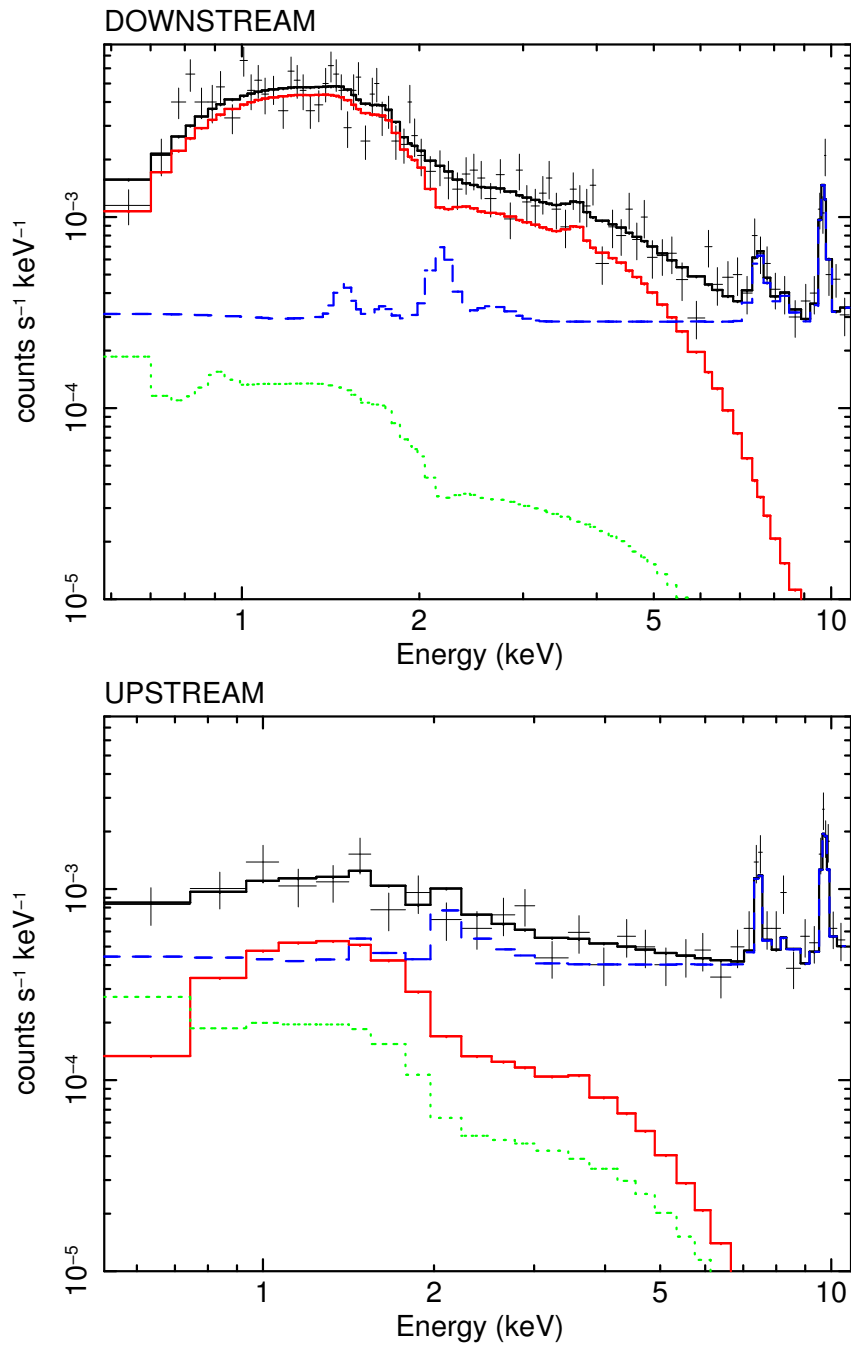


Figure 3.5: Downstream (*top*) and upstream (*bottom*) spectra of sector 1+2. Data points are shown in *black* together with the best fitting model. Different colors highlight the model components: the cluster emission (in *solid red*), the particle background (in *dashed blue*) and the sky background (in *dotted green*). The c -stat/d.o.f. of the fits are 203/168 and 128/115 for the downstream and upstream spectrum, respectively. Although spectra were simultaneously fitted, only one ObsID was reported in order to avoid confusion in the plot.

Systematic errors on X-ray analysis

Results discussed above are based on measurements obtained for a particular sector (1+2). This entirely covers the feature found in the unsharp-mask images (Fig. 3.2) and provides the best characterization of the SB jump due to the statistics of the fit.

We checked the impact due to the choice of the SB extracting region in the determination of the NW X-ray discontinuity and the resulting Mach number. Firstly, we re-performed SB and spectral

Table 3.1: Results of the SB and spectral fits of the regions shown in Fig. 3.3. Fits in the $2.0' - 4.9'$ radial range were made keeping r_{sh} frozen at the best fit value achieved in the wider range.

Sector	Radial range	r_{sh} ($'$)	\mathcal{C}	\mathcal{M}_{SB}	$\chi^2/\text{d.o.f.}$	kT_d (keV)	kT_u (keV)	\mathcal{M}_{kT}
1	$1.2' - 4.9'$	$2.359^{+0.006}_{-0.004}$	$3.5^{+0.7}_{-0.5}$	> 3.0	20.4/32	$18.3^{+4.1}_{-3.2}$	$6.8^{+10.8}_{-2.8}$	$1.9 - 3.4$
	$2.0' - 4.9'$		$3.1^{+0.7}_{-0.5}$	$3.2^{+4.3}_{-0.8}$	0.9/6			
2	$1.2' - 4.9'$	$2.321^{+0.065}_{-0.041}$	$3.7^{+1.2}_{-0.7}$	> 3.0	35.4/24	$15.8^{+7.9}_{-3.9}$	> 6.1	< 3.1
	$2.0' - 4.9'$		$4.2^{+1.6}_{-0.9}$	> 3.8	7.3/2			
1+2	$1.2' - 4.9'$	$2.338^{+0.007}_{-0.005}$	$3.4^{+0.4}_{-0.3}$	$4.1^{+3.4}_{-0.9}$	18.9/34	$17.9^{+3.3}_{-2.8}$	> 6.1	< 2.9
	$2.0' - 4.9'$		$3.4^{+0.5}_{-0.4}$	$4.1^{+6.7}_{-1.1}$	5.0/8			

Table 3.2: Impact on the SB profile fits in sector 1+2 due to different shock curvature radii. Note that $r_{curv} \sim 1$ Mpc in Fig. 3.4.

r_{curv} (Mpc)	\mathcal{C}	\mathcal{M}_{SB}	$\chi^2/\text{d.o.f.}$
0.6	2.5 ± 0.2	$2.2^{+0.3}_{-0.2}$	96.1/48
0.8	3.1 ± 0.3	$3.2^{+0.9}_{-0.6}$	91.5/52
1.2	$3.4^{+0.4}_{-0.3}$	$4.1^{+3.4}_{-0.9}$	41.0/45
1.4	$3.2^{+0.4}_{-0.3}$	$3.5^{+1.7}_{-0.6}$	24.7/28
1.6	3.1 ± 0.3	$3.2^{+0.9}_{-0.6}$	37.5/27
1.8	$2.9^{+0.3}_{-0.2}$	$2.8^{+0.6}_{-0.3}$	43.1/25

analysis by splitting the red and yellow sectors of Fig. 3.3 in two sub-regions; the dashed line distinguishes between sector 1 (opening angle: $60^\circ.5 - 98^\circ$), which is oriented in the N direction, to sector 2 (opening angle: $30^\circ - 60^\circ.5$), which is in the NW direction and better overlaps the relic. In both regions, the SB profile is well described by a compression factor $\mathcal{C} \gtrsim 3$, implying $\mathcal{M}_{SB} \gtrsim 3$. We then repeated the SB analysis by excluding data at $r < 2'$ and keeping the discontinuity distance frozen at the values found in the $1.2' - 4.9'$ radial range. Although with a large error, spectral analysis allowed to constrain the upstream temperature in sector 1, implying a 68% confidence interval estimate for the Mach number $\mathcal{M}_{kT} = 1.9 - 3.4$ (taking into account the asymmetric errors on the two temperatures), whereas only lower limits on kT_u can be obtained in sectors 1+2 and 2. The results of the fits obtained for the three regions are summarized in Tab. 3.1. Finally, we checked the variation on \mathcal{M}_{SB} in sector 1+2 due to different shock curvature radii from the best fit value found in Fig. 3.4 (i.e. $r_{curv} \sim 1$ Mpc). Results are reported in Tab. 3.2 and the impact of r_{curv} on the shock compression factor is presented in Fig. 3.6.

Spectral analysis requires a careful determination of the background sources and its systematic uncertainties. In this respect, we varied the background normalization levels within $\pm 1\sigma$ and re-performed the spectral fits. We achieved results consistent with the reported cluster parameters within 1σ . Nonetheless, we highlight that the measurement of high temperatures is critical with *Chandra* given its low effective area at energies higher than 5 keV; in particular, the estimated confidence range may not reflect entirely the true statistical and systematic error range.

As a final test, a more complex model of a two-temperature thermal plasma was adopted to fit the downstream spectra. In this case, the high- kT component is not constrained while the low- kT component gives unreasonably low temperatures (e.g. $kT_{high} > 21.2$ keV and $kT_{low} = 2.2^{+4.0}_{-1.2}$ keV, for sector 1+2). As pointed out in the case of the Coma cluster (Gastaldello et al. 2015), the low- kT component mitigates the fit residuals at low energy rather than describing a physical condition. The high- kT spectral component instead supports the presence of a high temperature plasma in the downstream region.

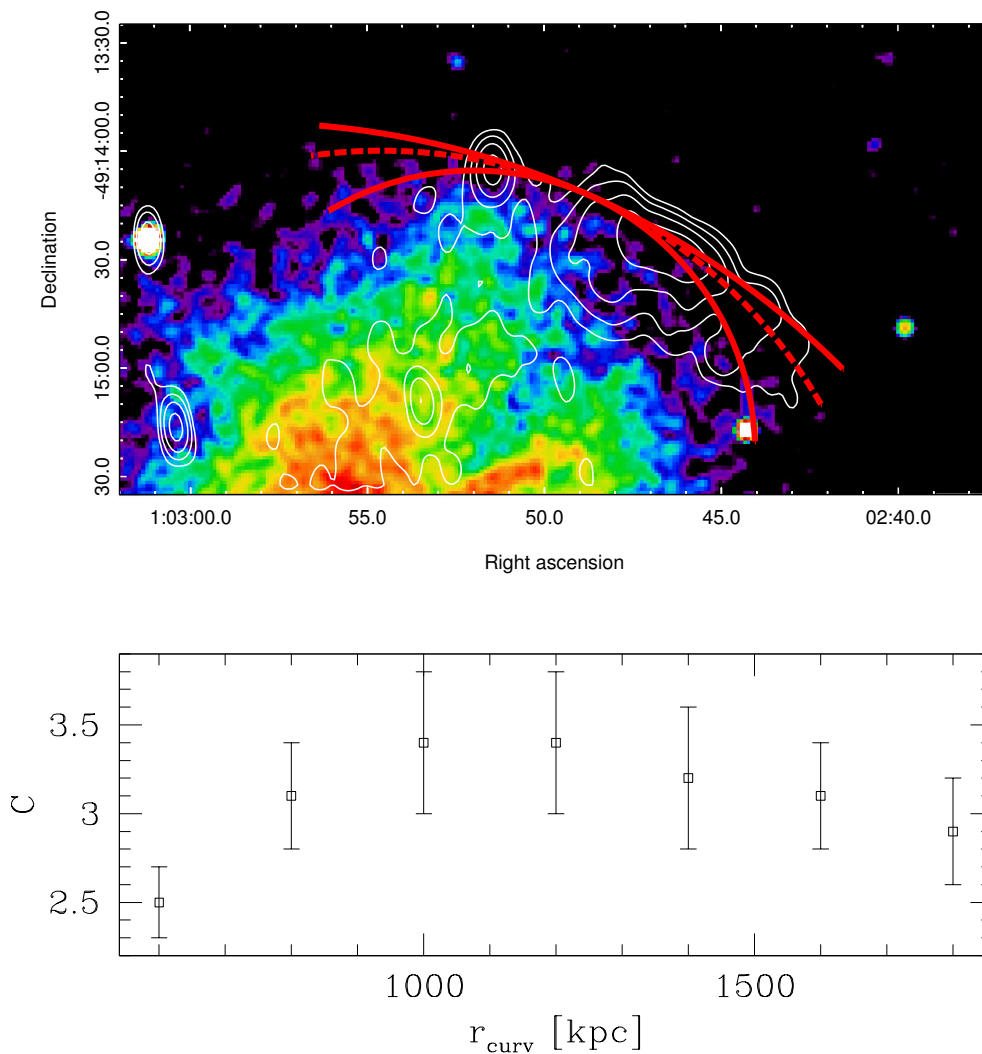


Figure 3.6: In the *top* panel we show the difference between the best fit curvature radius of ~ 1 Mpc (*dashed line*) and the two extreme cases with $r_{\text{curv}} = 600$ and 1800 kpc (lower and upper *solid lines*, respectively). In the *bottom* panel we compare compression factors achieved for different values of r_{curv} (see Tab. 3.2).

3.3.3 Constraints on the downstream magnetic field

Relativistic electrons scattering with the CMB photons are expected to produce IC emission (Section 1.7). From the ratio between radio and X-ray emission it is possible to constrain the magnetic field in the source region (e.g. Blumenthal & Gould 1970). For this reason, we performed spectral analysis in a sector enclosing the NW relic and introduced, in addition to the canonical thermal model for the ICM, a power-law in the spectral fit.

We assume that the IC spectrum is a power-law with photon index related to the synchrotron spectral index via $\Gamma = \alpha + 1$. Initially we set $\Gamma = 2.37$ (see Section 3.3.1) and kept it frozen in the fit while thermal parameters were free to vary. In this case, we obtain upper limit on the non-thermal component in the $0.5 - 2.0$ keV band of $F_{[0.5-2\text{keV}]} < 6.76 \times 10^{-15} \text{ erg s}^{-1} \text{ cm}^{-2}$.

The IC measurement is a very complicated issue and can be influenced by several factors. We investigated the impact on IC flux estimation by: using the IC power-law slope in the range $2.17 - 2.57$ (consistently with the values reported in Section 3.3.1), keeping the temperature frozen at 13.5 and 17 keV (which covers a range of kT obtained for different sector choices in the relic

region), varying the background normalization levels within $\pm 1\sigma$ and re-performing the fits in the 0.7 – 11.0 and 0.9 – 11.0 keV energy bands. In summary, we found upper limits in the range $(2.95 - 8.51) \times 10^{-15} \text{ erg s}^{-1} \text{ cm}^{-2}$ for the IC flux, representing $\lesssim 50\%$ of the thermal model flux in the same energy band (0.5 – 2.0 keV). Interestingly, in the case of temperature frozen at 17 keV, the fits formally result in a IC detection both for $\Gamma = 2.17$ and 2.57; however, we do not consider these detections solid enough due to the systematics related to the presence of multi-temperature components and background characterization. The possibility of IC detection in El Gordo will be discussed also in Chapter 4.

By using our upper limits on the IC flux, from Eq. 1.46 we obtained the following lower limits on the downstream magnetic field strength: $B \geq 3.1 \mu\text{G}$ for $\Gamma = 2.17$, $B \geq 4.9 \mu\text{G}$ for $\Gamma = 2.37$ and $B \geq 7.6 \mu\text{G}$ for $\Gamma = 2.57$. These values are in line with other estimates for radio relics (e.g. Bonafede et al. 2009; Finoguenov et al. 2010; van Weeren et al. 2010, 2011b; Botteon et al. 2015).

3.3.4 Acceleration efficiency

As explained in Section 1.4.1, the relic–shock connection is nowadays supported by many observational studies. Nevertheless, theoretical models of relic formation are challenged by the low Mach numbers associated with cluster shocks. In fact, the commonly adopted DSA model is severely challenged for weak shocks if CRe are accelerated by the thermal pool (e.g. Brunetti & Jones 2014, for a review).

For the NW shock in El Gordo, we measured an upstream number density and temperature $2.4 \times 10^{-4} \text{ cm}^{-3}$ and 6.1 keV, respectively, and a surface of the relic $A = \pi \times 350^2 \text{ kpc}^2$. Thus, having in hands the parameters of the shock and the radio measurements, we are in the position to constrain the electron acceleration efficiency following the procedure outlined in Section 1.5.2. In the case of CRe acceleration from the thermal pool, the spectrum of seed particles upstream is a power-law with slope given by Eq. 1.35, which is related to the synchrotron spectral index (Eq. 1.37) in the case of steady state conditions (e.g. Blandford & Eichler 1987).

In Fig. 3.7 we report the acceleration efficiency that is necessary to explain the radio luminosity observed in the NW relic assuming DSA of thermal electrons upstream. We assumed shock Mach numbers $\mathcal{M} = 3.5$ and 2.5, in line with the values derived from the X-ray analysis. These Mach numbers would imply a synchrotron spectrum of the relic $\alpha = 1.18$ and 1.38, respectively, that are consistent with the radio measurements (Section 3.3.1).

In Fig. 3.7 we also show the lower limits on the magnetic field in the relic that are derived from the upper limits on the IC flux assuming the two values of the spectral index (Section 3.3.3). Despite we are dealing with a high-velocity shock, $V_{sh} \sim 4000 \text{ km s}^{-1}$, we note that the efficiency of CRe acceleration that is requested to explain the radio relic is large. This is due to the fact that the NW relic in the El Gordo is one of the most luminous radio relics known so far and because, for few μG magnetic fields, most of the CRe energy is radiated via IC emission (due to the high redshift of the cluster). Still, contrary to the case of weaker shocks (see e.g. 1RXS J0603.3+4214, van Weeren et al. 2016a and A115, Botteon et al. 2016a), we conclude that in this case DSA of thermal electrons is still a viable option. Indeed, for $\mathcal{M} \geq 3.5$ the electron acceleration efficiency appears energetically viable $\eta_e \leq 0.01$, whereas for $\mathcal{M} \sim 3 - 3.5$ additional mechanisms of pre-acceleration of thermal electrons downstream (see Guo et al. 2014a,b) may be required.

The other possibility is that the NW relic is due to shock re-acceleration of seeds (relativistic or supra-thermal) electrons. In this case the efficiency necessary to explain the radio emission is much smaller simply because the bulk of the energy is channelled directly into highly relativistic particles (Eq. 1.41, e.g. Markevitch et al. 2005; Kang et al. 2012). Seeds can be widely distributed in the cluster outskirts where the life time of 100 MeV electrons is very long (e.g. Pinzke et al. 2013; Donnert et al. 2016) or they can be in radio ghost/clouds generated by past AGN activity (e.g.

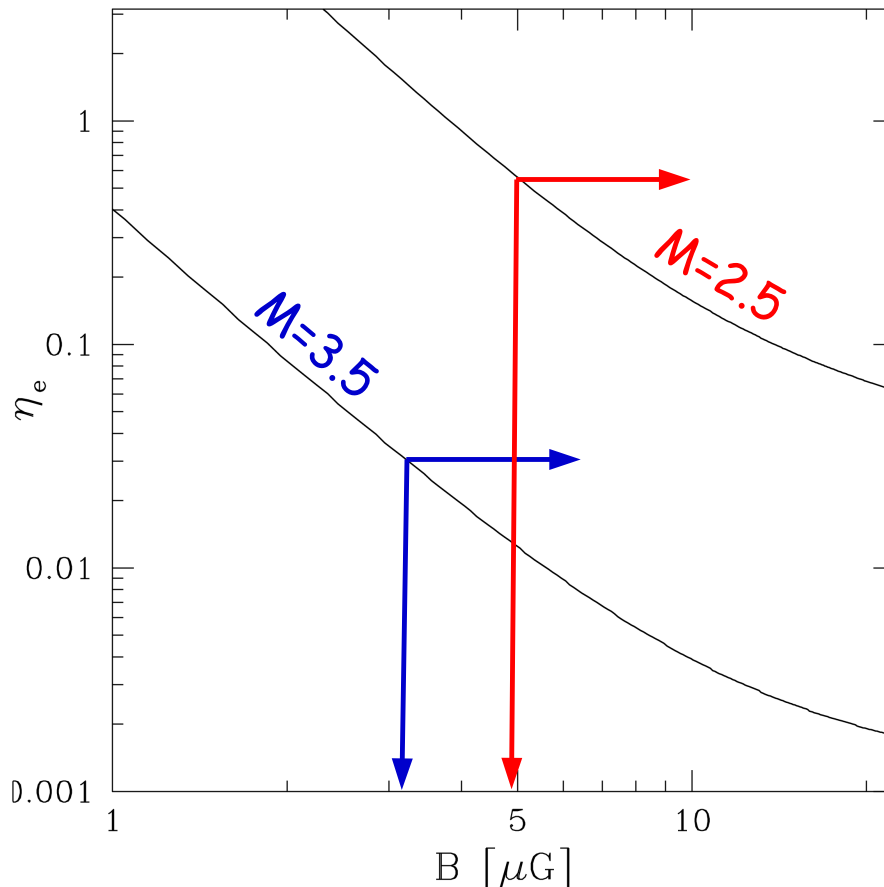


Figure 3.7: Electron acceleration efficiency versus magnetic field in the downstream region in the NW shock in El Gordo. Black lines represent efficiencies evaluated for a Mach number with $\mathcal{M} = 2.5$ (*top*) and 3.5 (*bottom*). Calculations were obtained with $p_{min} = 0.1m_e c$ in Eq. 1.41. Vertical lines denote the lower limits on the downstream magnetic field strength achieved from the lack of IC emission from the relic.

Kang & Ryu 2016). The two possibilities have different predictions on the upstream synchrotron emission that, in principle, can be tested with very deep radio observations.

3.3.5 Overall considerations on El Gordo

El Gordo is a high redshift ($z = 0.87$, Menanteau et al. 2012) and high mass ($M_{500} \sim 8.8 \times 10^{14} M_{\odot}$, Planck Collaboration XXIX 2014) galaxy cluster. It is the most distant massive cluster with the brightest X-ray and SZ emission and the farthest hosting diffuse radio sources (halo and relics). Our study makes it is also the most distant cluster where a shock (with one of the highest Mach number) has been detected.

Optical and X-ray observations revealed that El Gordo is in a merging state (Menanteau et al. 2010, 2012). Recent numerical simulations were able to reproduce the overall system properties assuming a nearly head on major merger (Donnert 2014; Molnar & Broadhurst 2015; Zhang et al. 2015; Ng et al. 2015).

Double relic systems are expected to trace shocks moving outwards in cluster outskirts. So far, studies on El Gordo were mainly focused on the SE relic located in front of the dense CC, which is expected to follow a shock in analogy with the well known Bullet Cluster case (Markevitch et al. 2002). However, current X-ray data do not allow to characterize the jump in this region because of

the low count statistics. We instead discovered a $\mathcal{M} \gtrsim 3$ shock spatially coincident with the NW relic. Our detection is based on the *Chandra* SB jump. Although with large uncertainties, spectral analysis is also consistent with the presence of a strong shock in the ICM. Further indications of the shock are given by the unsharp-masked images of Fig. 3.2. We also mention the striking similarity between El Gordo shock/reverse-shock and X-ray morphology with A2146 (Russell et al. 2010, 2012) even though the latter is a less massive system ($M_{500} \sim 3.8 \times 10^{14} M_{\odot}$, Planck Collaboration XXIX 2014).

3.4 Conclusions

In this Chapter, we presented an X-ray/radio study of the famous El Gordo cluster located at $z = 0.87$ focusing on the non-thermal activity in the cluster.

Our GMRT radio observations at 610 and 327 MHz confirmed the presence of a halo and a double relic system. These represent the most distant diffuse radio sources detected in a galaxy cluster so far. The halo is quite elongated in the NW-SE, i.e. in the merger direction, and remarkably follows the ICM emission of the northern X-ray tail. The two relics are found at the boundaries of the X-ray emission. We focused on the NW relic, which has a synchrotron spectral index $\alpha = 1.37 \pm 0.20$ between 610 and 327 MHz.

The deep *Chandra* observations (340 ks) allowed us to discover a shock at the position of the NW relic. The SB profile taken in this region abruptly drops at the relic location. The density compression factor $\mathcal{C} \gtrsim 3$ and the high downstream temperature provide the indication of a strong shock ($\mathcal{M} \gtrsim 3$) in the ICM. This is among the three strongest shocks detected in galaxy clusters and the most distant ($z = 0.87$) observed so far.

The detection of a shock co-spatially located with a relic strongly supports the relic–shock connection. The NW shock in El Gordo allowed us to study particle acceleration in a rare regime of strong shock. We found that DSA of thermal electrons is consistent with the measured synchrotron spectrum. Nonetheless, only shocks with $\mathcal{M} > 3.5$ appear energetically viable while for weaker shocks re-acceleration models would be preferred.

The presence of relativistic particles emitting a bright synchrotron relic at $z = 0.87$ makes El Gordo a suitable cluster candidate to search for IC emission from the relic. From the X-ray spectral analysis we obtained possible hints of IC emission from the relic; however, we could not firmly conclude the presence of IC excess and conservatively we derived only lower limits on the downstream magnetic field that have been used to improve constraints on particle acceleration. Nonetheless, we also found hints of an excess in the 0.5 – 2.0 keV SB profile across the relic region that will be discussed in the next Chapter.

Inverse Compton emission and magnetic fields in radio relics: the case of El Gordo

ABSTRACT

The knowledge of structure and intensity of magnetic fields in galaxy clusters is still limited (Section 1.2.4). A method to constrain the magnetic field strength in the ICM is the comparison between the synchrotron and IC emission from diffuse radio sources. However, the contamination of thermal emission and/or the presence of multi-temperature components make these studies very difficult. In this respect, radio relics are promising tools in the IC search as they are bright sources laying in the cluster outskirts, where the contribution of the thermal bremsstrahlung emission decreases. Here, we show how it is possible to search for IC emission from the X-ray SB analysis of radio relics. Constraining the magnetic field strength in these regions gives important information on the particle acceleration efficiency and magnetic field amplification at cluster merger shocks. We use El Gordo cluster as a test case to show what would be the impact of such a discovery and its observational cost.

4.1 Introduction

IC emission from the scattering of the CMB photons with relativistic electrons in the ICM has never been observed to date. No confirmed detection has been obtained mainly due to the difficulty to disentangle a “hard tail” of emission in the X-ray spectra from thermal emission with a combination of temperatures (e.g. Wik et al. 2011, 2014; Ota et al. 2014; Gastaldello et al. 2015). This precluded the fundamental task of measuring the magnetic field strength and its energy density ratio with the relativistic electrons in synchrotron radio sources.

In the outskirts of merging galaxy clusters, shocks may power Mpc-scale synchrotron emission in the form of radio relics through a complex combination of mechanisms that (re)accelerate relativistic particles and amplify magnetic fields in the ICM (e.g. Feretti et al. 2012; Brunetti & Jones 2014; van Weeren et al. 2019). Relativistic electrons in relics generate also IC emission that is expected to be detected in the SB profiles extracted in the soft X-ray band across the relics themselves as a downstream SB enhancement. Detecting IC from a radio relic has the potential to constrain important aspects of the physics of cluster shocks. In this Chapter, we compare the expected SB

due to IC emission of the 9 most powerful radio relics known to date and determine the feasibility of the detection for the best candidate.

4.2 The definitive approach to detect IC

The detection of IC from the SB profile analysis relies on the capability of the instrument to resolve the non-thermal excess due to the radio relic and to measure the contrast in SB between its peak and the underlying thermal emission downstream (Fig. 4.1). The excess (or “bump”) is larger for larger IC contribution, i.e. when the flux ratio between the two components F_{IC}/F_d increases. Thus, as the ratio of IC to synchrotron fluxes scales like $F_X/F_{\text{radio}} \propto (1+z)^{3+\alpha}/B^{1+\alpha}$, this analysis can provide a direct measure of B in the post-shock region.

The SB approach described above has a decisive advantage over the spectral analysis. Indeed, the low effective area above 10 keV of *Chandra* and *XMM-Newton* makes the measurement of high temperatures in post-shock regions already critical. Even approved future major X-ray missions like *Athena* will suffer this problem. Additionally, higher energy satellites like *Suzaku* and *NuSTAR* showed that the spectral confirmation of IC in the Bullet Cluster and in A2163 is severely challenged by the presence of clumps of very hot gas (20 – 30 keV) that can be easily confused with a non-thermal IC component (Wik et al. 2014; Ota et al. 2014). Similarly, the evidence of gas with temperatures up to 25 keV in El Gordo cluster (Hughes et al. 2014) will strongly hinder the detection of IC in the spectra of this exceptional target (see Section below). The SB profile analysis of radio relics appears to be the only promising method in the long quest for IC emission.

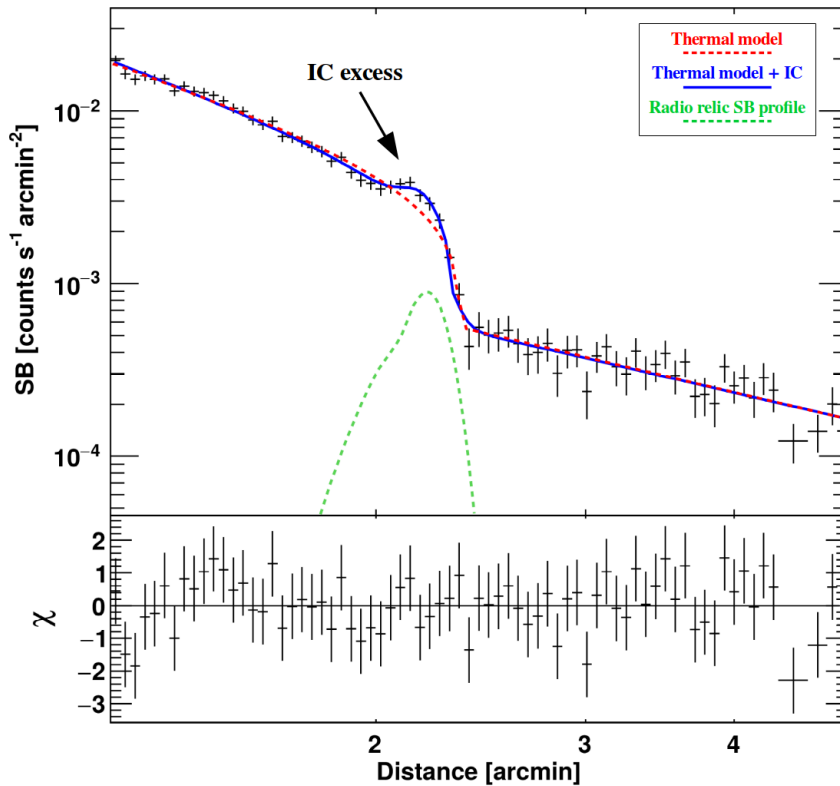


Figure 4.1: Simulated SB profile extracted in the 0.5 – 2.0 keV band across the NW relic in El Gordo for a 1 Ms exposure and assuming a flux ratio between the IC excess and the underlying downstream thermal emission of 22%. The IC excess is visible as a “bump” in the downstream region. The radio relic SB profile is in arbitrary units.

4.3 El Gordo: the best target

For the purpose of maximizing the chance of IC detection, one may exploit the fact that the SB scales as $\propto (1+z)^{-4}$ while the IC emission scales as $\propto (1+z)^4$, thus statistically the most luminous sources will also be brighter in IC. For this reason, we selected from the recent collections of cluster diffuse radio sources of Yuan et al. (2015) and Nuza et al. (2017) the most powerful relics with $P_{1.4} > 10^{25} \text{ W Hz}^{-1}$. The 9 radio relics satisfying this power threshold are listed in Tab. 4.1 and shown in Fig. 4.2. All these relics belong to double radio relic systems and, in two cases, two relics with $P_{1.4} > 10^{25} \text{ W Hz}^{-1}$ are found in the same cluster (i.e. PSZ1 G108.18-11.53 and MACS J1752.0+4440). The cluster redshifts range from $z = 0.056$ to $z = 0.870$, important due to the dependency of IC losses on the redshift. Despite that the E radio relic in the Bullet Cluster has $P_{1.4} = 2.3 \times 10^{25} \text{ W Hz}^{-1}$ (Shimwell et al. 2015), it was not included in our sample because 94% of its observed flux density comes from a bright “bulb” of emission likely related to the remnant of a radio galaxy.

We adopted the parameters in Tab. 4.1 to compute the expected values of IC flux, luminosity, and SB, as a function of the magnetic field strength for each relic in the sample. Calculations were performed using Eq. 1.46 integrated in the energy range 0.5 – 2.0 keV band, which represents a compromise between the maximum effective area of current X-ray satellites and a favorable thermal/non-thermal flux ratio in the ICM (cf. Fig. 1.18). Results are shown in Fig. 4.3.

El Gordo (Fig. 4.4) turns out to be the best target for the first discovery of IC emission from the ICM. It is the highest redshift ($z = 0.87$) cluster with a detected radio relic and an underlying shock (Lindner et al. 2014; Botteon et al. 2016c). Due to its high- z , the NW radio relic in El Gordo has a small angular extension, meaning that the IC signal is concentrated in a compact region. This results in a SB due to IC that is at least an order of magnitude higher than other bright and extended relics (Fig. 4.3), such as the Sausage (van Weeren et al. 2010) and the Toothbrush (van Weeren et al. 2012b).

Table 4.1: Properties of the 9 most powerful radio relics discovered so far. The second reference, if present, provides the work where the reported spectral index has been retrieved. Redshifts are taken from the NASA/IPAC Extragalactic Database (NED).

Name	Position	z	S_ν (mJy)	ν (GHz)	Area ^a (arcmin ²)	α	$P_{1.4}^b$ (W Hz ⁻¹)	Reference
A3667	NW	0.056	2470	1.372	60.61	0.80	1.8×10^{25}	1,2
CIZA J2242.8+5301 [†]	N	0.192	337	0.608	9.63	1.11	1.4×10^{25}	3,4
1RXS J0603.3+4214 ^{††,c}	N	0.225	751	0.610	12.21	1.15	4.5×10^{25}	5,6
PSZ1 G108.18-11.53	NE	0.335	422	0.323	4.84	1.25	2.7×10^{25}	7
PSZ1 G108.18-11.53	SW	0.335	323	0.323	5.95	1.28	2.0×10^{25}	7
MACS J1752.0+4440	NE	0.366	55.1	1.714	4.04	1.21	3.4×10^{25}	8,9
MACS J1752.0+4440	SW	0.366	25.7	1.714	2.91	1.13	1.5×10^{25}	8,9
PSZ1 G287.0+32.9	NW	0.385	216	0.323	3.33	1.16	2.1×10^{25}	10
ACT-CL J0102-4915 ^{†††}	NW	0.870	27.5	0.610	0.73	1.37	4.1×10^{25}	11

Notes. [†]Sausage Cluster; ^{††}Toothbrush Cluster; ^{†††}El Gordo; ^aEvaluated within the 3σ contour level at the reported frequency; ^bRadio power at 1.4 GHz, k -corrected and spectral index rescaled (Eq. 1.23); ^cThe other relic in this cluster is not in the diametrically opposite side as in the other double radio relic systems but it is located toward the E direction. References: ¹Röttgering et al. (1997), we verified that by using the updated values of Johnston-Hollitt (2003, 2004) our results in Fig. 4.3 do not change significantly; ²Riseley et al. (2015); ³van Weeren et al. (2010); ⁴Hoang et al. (2017); ⁵van Weeren et al. (2012b); ⁶Rajpurohit et al. (2018); ⁷de Gasperin et al. (2015a); ⁸van Weeren et al. (2012a); ⁹Bonafede et al. (2012); ¹⁰Bonafede et al. (2014a); ¹¹Botteon et al. (2016c).

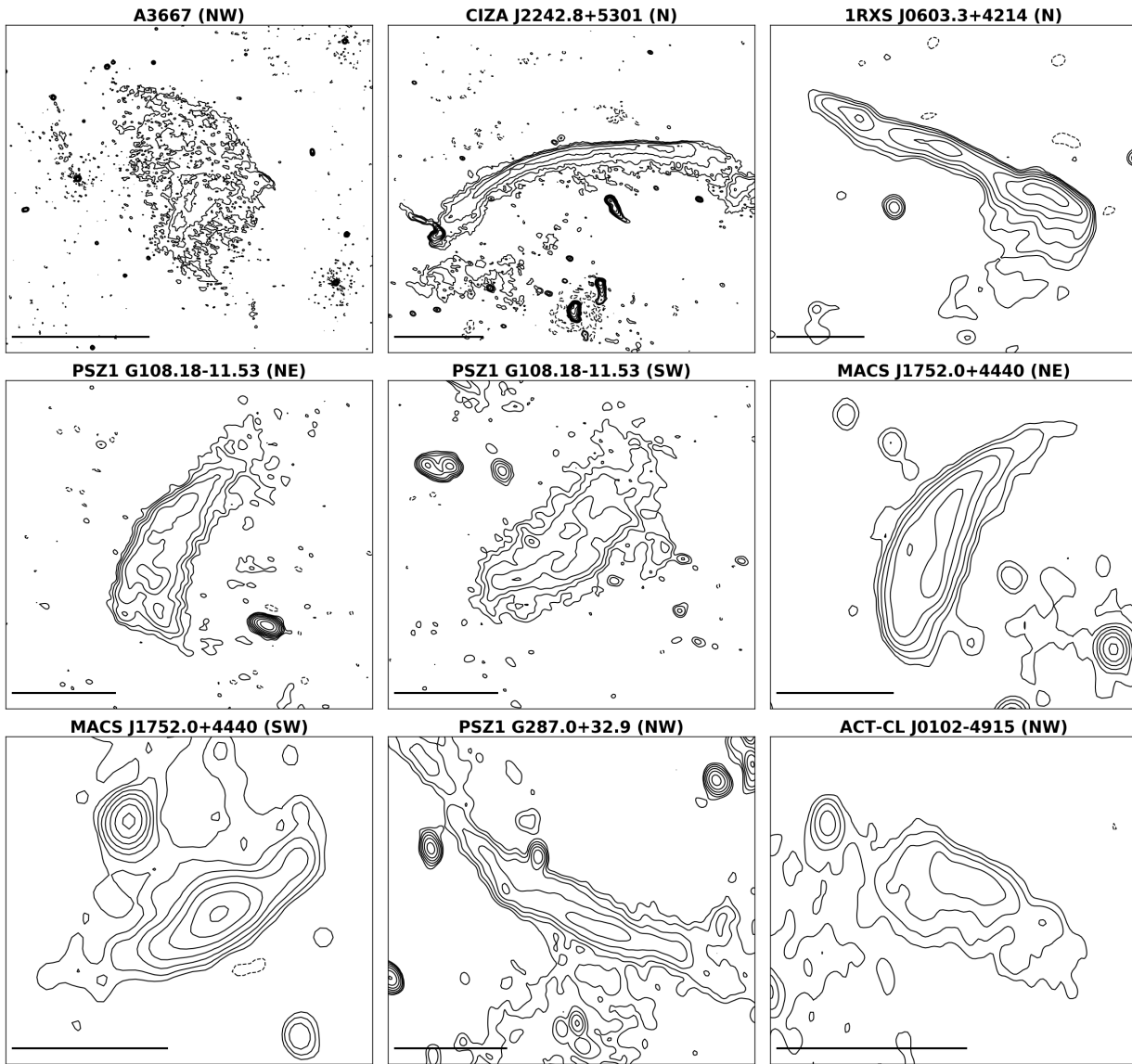


Figure 4.2: The 9 most powerful radio relics known to date. Radio contours are spaced by a factor of 2 starting from 3σ . The negative -3σ contours are shown in dashed. Bars in the bottom left corners denote a linear size of 500 kpc at the cluster redshift. The properties reported in Tab. 4.1 have been derived from these images. We thank A. Bonafede (PSZ1 G287.0+32.9), F. de Gasperin (PSZ1 G108.18-11.53), H. Röttgering (A3667) and R. van Weeren (CIZA J2242.8+5301, 1RXS J0603.3+4214, MACS J1752.0+4440) for kindly providing us the displayed images.

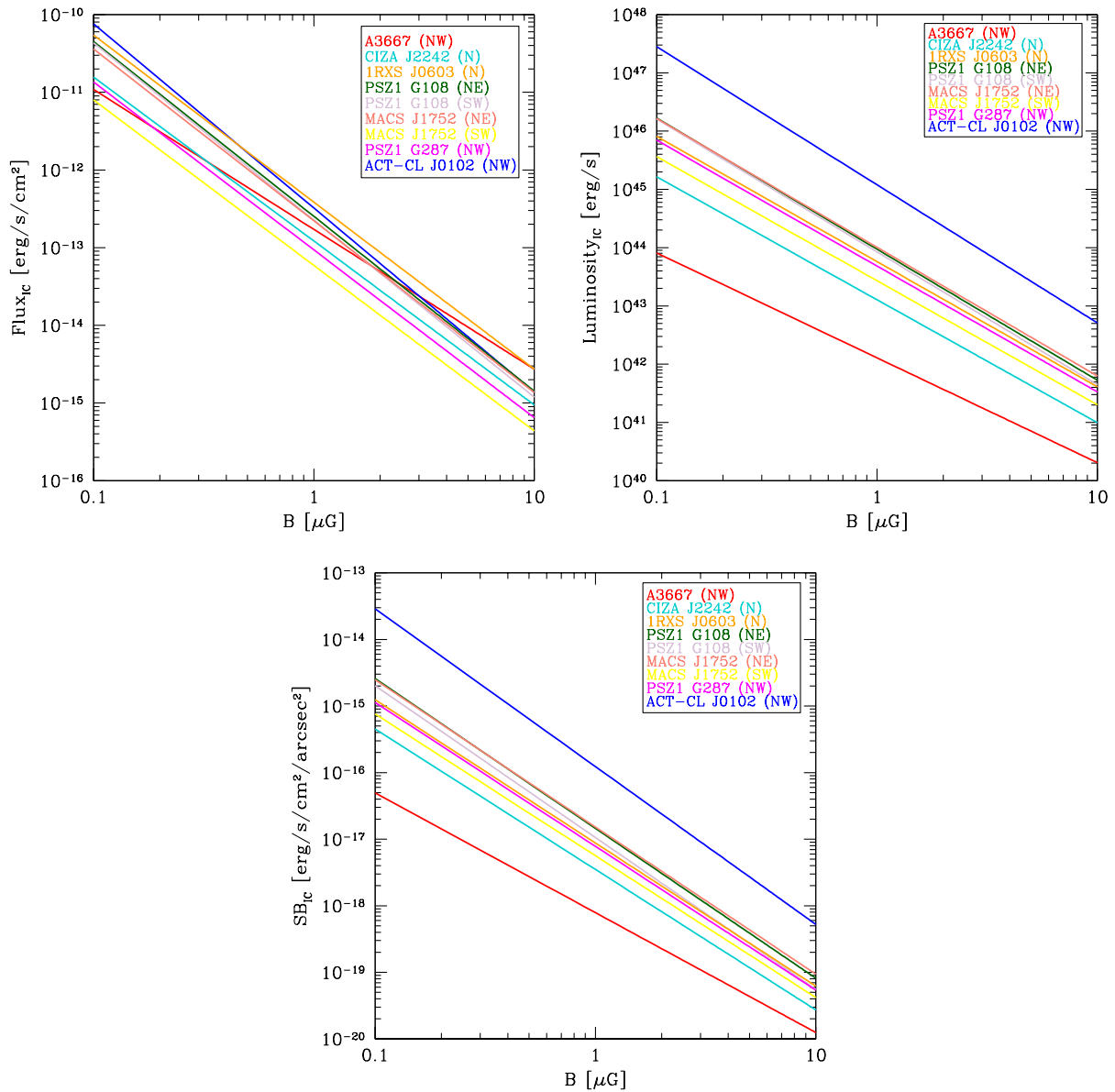


Figure 4.3: IC flux (*top left*), luminosity (*top right*), and SB (*bottom*) in the 0.5 – 2.0 keV band expected as a function of the magnetic field for the 9 radio relics considered in the analysis.

Hints of the presence of IC signal in El Gordo have been already reported in Botteon et al. (2016c). In Section 3.3.3, we showed that the spectral analysis provides a formal detection in the case where the temperature is frozen at 17 keV, but we did not consider this result solid enough for a proper claim. Nonetheless, if real, a significant fraction (up to 40 – 50%) of the X-ray brightness across the relic would be contributed by IC emission from the relic itself. This should be visible in the X-ray images and profiles across the relic (cf. Fig. 4.1). For this reason, we extracted a SB profile in the 0.5 – 2.0 keV across a narrow sector (opening angle: $37^{\circ}.2 - 67^{\circ}.5$) containing the NW radio relic (Fig. 4.4). The fit of a broken power-law model (Eq. 1.21) in this restricted region provides a good description of the SB jump, leading to $\chi^2/\text{d.o.f.} = 48.5/41$. However, a SB excess is present in the region of the diffuse radio source. In this respect, we also attempted to fit the SB by adding a Gaussian component to the downstream power-law. The addition of this Gaussian improves the fit, leading to $\chi^2/\text{d.o.f.} = 40.3/38$. Small changes in the choice of the sector center and aperture do not influence this excess. The Gaussian component coincident with the relic could

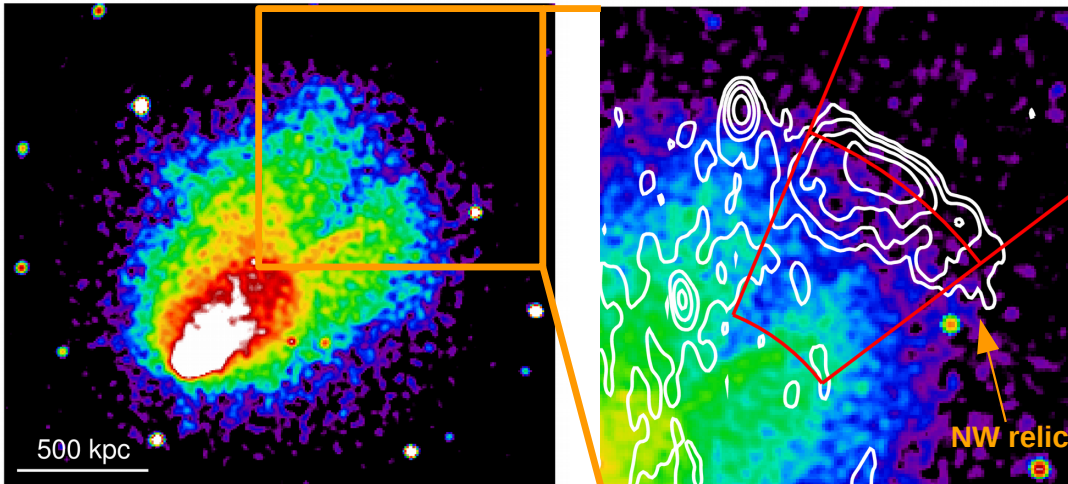


Figure 4.4: *Chandra* image of El Gordo in the 0.5 – 2.0 keV band. The zoom-in panel shows the GMRT 610 MHz radio contours of the NW relic at a resolution of $11'' \times 4.8''$. The red sector denotes the region where the SB profile of Fig. 4.1 was extracted. Adapted from Botteon et al. (2016c).

represent an excess due to IC emission from electrons in the relic. The excess flux associated with the Gaussian component is in line with that expected from the spectral analysis. The combination of this excess with the formal detection of IC emission obtained from the spectral analysis (with kT frozen) is tantalizing, however deeper observations are required to firmly conclude about this possible detection.

4.4 Future steps toward the detection of IC emission

4.4.1 Feasibility study

The detection of IC signal is a demanding goal even for El Gordo cluster. Indeed, the IC contribution is still sub-dominant compared to thermal bremsstrahlung in the 0.5 – 2.0 keV band. In addition, characterizing the excess in the SB profile taken across the relic requires an instrument with good angular resolution. The *Chandra* satellite appears to be the only instrument able to perform this task but, as we show below, only with major time investments.

The existing 360 ks *Chandra* data on El Gordo leading to the tantalizing detection reported in Botteon et al. (2016c) allow us to quantify the exposure needed to firmly claim the presence of IC emission from the NW relic. We simulated SB profiles across the relic assuming four different values of $F_{\text{IC}}/F_{\text{d}}$ in the 0.5 – 2.0 keV and exposure times of 500 ks, 1 Ms and 1.5 Ms. The IC component was assumed to have a Gaussian profile centered at the peak and approximately with the same full width at half maximum of the relic emission. Each profile was simulated 200 times with the `fakeit` task in `PROFFIT` (Eckert et al. 2011) and was fitted with two models consisting in a broken power-law and in a broken power-law + Gaussian (added to take into account the IC excess). The $\chi^2/\text{d.o.f.}$ of the fits were compared and the significance of the “bump” was evaluated with the F-test. The results of our simulations are shown in Fig. 4.5. An example of a simulated SB profile with $F_{\text{IC}}/F_{\text{d}} = 22\%$ and exposure 1 Ms is shown in Fig. 4.1. According to Fig. 4.5, a flux ratio $> 20\%$ between the IC and the thermal downstream emission will be constrained at $> 3.5\sigma$ with exposures > 1 Ms, providing a direct measure of B in the post-shock region (see Fig. 4.6). Conversely, a non-detection of the excess would require $B > 6 \mu\text{G}$, resulting in a limit of the magnetic field that is 30 times larger than that derived in the Bullet Cluster (Wik et al. 2014).

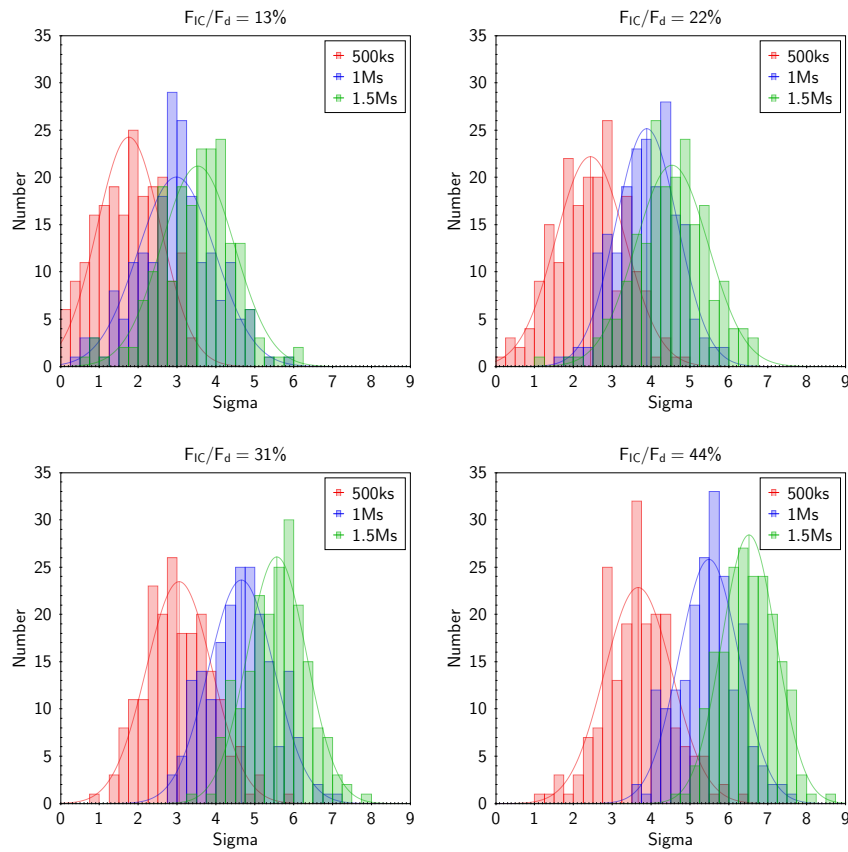


Figure 4.5: Distribution of the significance of the excess detection for a given F_{IC}/F_d and exposure time.

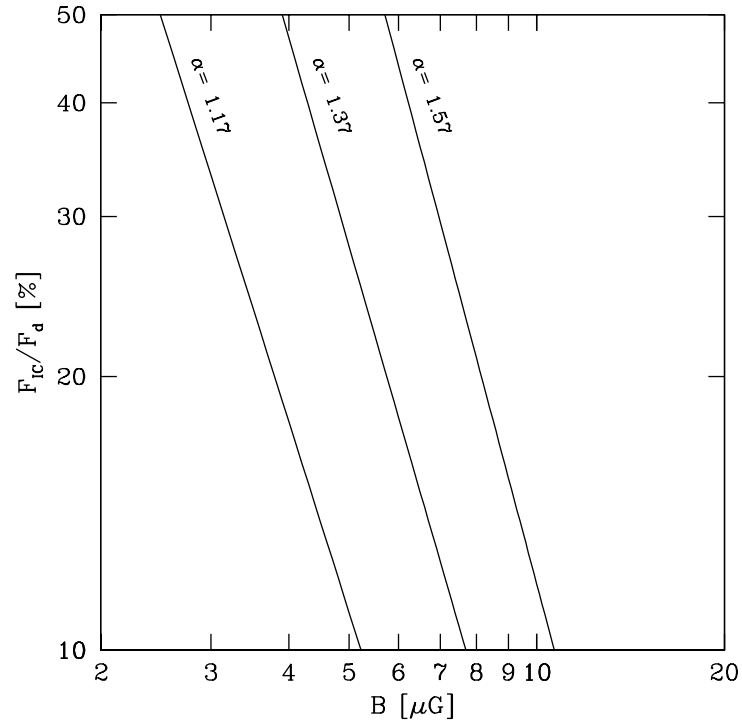


Figure 4.6: Flux ratio between the IC excess and the underlying downstream thermal emission in the 0.5 – 2.0 keV versus B . The relic spectral index reported in the literature is $\alpha = 1.37 \pm 0.20$ (Botteon et al. 2016c).

4.4.2 Impact of the discovery

The discovery of IC emission from the NW relic in El Gordo would provide the first direct measurement of the magnetic field strength in the outskirts of a galaxy cluster. This is fundamental to (i) discriminate between the models of particle (re)acceleration and (ii) understand the role of shocks in the magnetic field amplification, as described below.

1. Contrary to the above-mentioned Sausage and Toothbrush relics, the shock underlying the NW relic in El Gordo has been clearly detected using X-rays and SZ effect (Botteon et al. 2016c; Basu et al. 2016). In combination with the shock parameters derived from X-ray and SZ observations, the measurement of the magnetic field strength via IC allows to constrain the particle acceleration efficiency at the shock. In radio relics, the commonly adopted DSA model is severely challenged by the typical weak cluster shocks if the relativistic electrons are accelerated from the thermal pool (Brunetti & Jones 2014). However, the shock in El Gordo is one of the strongest shocks ever observed in the ICM and DSA appears to be energetically possible, provided that $B > 10 \mu\text{G}$ (Botteon et al. 2016c). This is an extraordinary case as a number of recent observations (Bonafede et al. 2014a; Shimwell et al. 2015; Botteon et al. 2016a; van Weeren et al. 2017a) seemed to have found in the re-acceleration of seed particles the holy grail to explain the origin of radio relics. According to Fig. 4.6, a clear detection of IC signal from the relic in El Gordo would imply the presence of a low magnetic field strength. This would support the re-acceleration of relativistic seed electrons at the shock confirming the trend of recent observations even in the case of one of the strongest shocks ever detected in the ICM and definitively ruling out the DSA origin for radio relics.
2. The detection of IC emission from El Gordo would also place important limits on magnetic field amplification in collisionless shocks, not accessible in any other way, constraining the effects of magnetic field compression and non-linear amplification in the downstream region (e.g. Iapichino & Brüggen 2012; Ji et al. 2016; Donnert et al. 2016). This is a unique way to determine the role of shocks in the amplification of B in the ICM. In particular, the measurement of strong fields in El Gordo would put in tension the primordial origin of seed fields due to the restricted time available even for a well-developed dynamo amplification at high- z .

In conclusion, such a discovery will enable a targeted search for the IC signal in other radio relics and establish an entirely new way to observe magnetic fields in galaxy clusters and to constrain the physics of cluster shocks. These results will serve as landmark measurements for particle-in-cell simulations, which target magnetic field amplification and particle acceleration in collisionless shocks from first principles, but are currently largely unconstrained in cluster shocks (e.g. Caprioli & Zhang 2018).

4.5 Conclusions

The relativistic electrons producing synchrotron emission in radio relics lose energy also via IC emission. The ratio between the fluxes due to the two processes constrains the strength of B in the emitting region. Measuring the magnetic field strength in a post-shock region is fundamental to understand the efficiency of particle acceleration and magnetic field amplification in the ICM.

A fraction of the X-ray SB profile across a relic is expected to be contributed by IC emission. Spatially resolving the SB excess due to the non-thermal signal in the soft X-rays overcome the uncertainties of spectral analysis and the connected problem of the low effective area of satellites above 10 keV.

In this Chapter, we computed the expected SB due to IC emission for the 9 most powerful radio relics observed so far. The NW relic in El Gordo cluster resulted to be the best target for this search because its high redshift leads to increase the IC losses and to reduce its angular size. Indeed, hints of IC signal were already reported for this relic (Botteon et al. 2016c). Thus, we investigated in more detail the possibility to clearly detect IC relaying upon the existing *Chandra* dataset and by simulating SB profiles with different levels of IC emission and exposure times. The emerging scenario is that the detection is feasible, but only with major time investments. Nonetheless, this detection would lead to an unprecedented discovery with the potential to rule out DSA in all the relics. A non-detection would also be useful, implying a large magnetic field strength downstream and thus providing important constraints on the mechanisms of magnetic field amplification in shocks.

Currently, *Chandra* is able to perform this measure in the face of a large observational cost. Future satellites with high resolution and large effective area, such as the mission concepts *Lynx*¹ (Gaskin et al. 2017) and the Advanced X-ray Imaging Satellite² (AXIS; Mushotzky 2018), will make possible the demanding goal of detecting IC emission for a number of clusters even with modest campaign programs. This represents the first step for a statistical study of magnetic field amplification and particle acceleration at cluster shocks.

¹<https://wwwastro.msfc.nasa.gov/lynx/>

²<http://axis.astro.umd.edu/>

Shock acceleration efficiency in a sample of radio relics[†]

ABSTRACT

Merger shocks are thought to play a fundamental role in the generation of radio relics (Section 1.5). Despite this, the details leading to the acceleration of CRs at low Mach number shocks are still poorly understood. In Chapters 2 and 3 we explored the cases of the relics in Abell 115 and El Gordo providing constraints on the acceleration efficiency and acceleration models. In this Chapter, we extend the study to a sample of well studied radio relics with detected underlying shocks. We developed a self-consistent method based on a small number of observable quantities that allowed us to determine the efficiency of particle acceleration. We found that DSA can not explain the origin of all the relics (but El Gordo), if particles are accelerated from the thermal pool. We conclude that other mechanisms, such as shock re-acceleration of supra-thermal seed electrons, are required to explain the formation of radio relics.

5.1 Introduction

Astrophysical shock waves are able to accelerate particles over a broad range of scales, from astronomical units in the Sun heliosphere to Mpc-sizes in clusters of galaxies (e.g. Blandford & Eichler 1987). Among the numerous physical processes proposed, DSA provides a general explanation of particle acceleration in most of the astrophysical environments.

To date, the acceleration efficiency of CRs at astrophysical shocks is mainly constrained by studies of SNRs in our Galaxy (e.g. Helder et al. 2012, for a review), where strong shocks ($\mathcal{M} \sim 10^3$) propagate in a low-beta plasma ($\beta_{pl} = P_{th}/P_B$, i.e. the ratio between the thermal and magnetic pressures) medium. In contrast, radio relics in the outskirts of merging galaxy clusters probe particle acceleration in action at much weaker shocks ($\mathcal{M} \lesssim 3 - 5$) and in a high- β_{pl} environment such as the ICM, where the thermal pressure dominates over the magnetic pressure. It is not still clear whether merger shocks in clusters can accelerate CRs in the diluted ICM at meaningful levels, and this poses fundamental questions on the mechanisms leading to the formation of relativistic particles in radio relics (e.g. Brunetti & Jones 2014). In this Chapter, for the first time we evaluate the efficiency of particle acceleration at cluster shocks using a homogeneous approach for a sample of radio relics.

[†]Based on Botteon et al. (in preparation).

5.2 Relic sample

We selected a sample of 11 galaxy clusters with radio relics and underlying shocks observed. The clusters are listed in Tab. 5.1 and include also a few double radio relics systems. The sample is composed of well studied radio relics with good radio and X-ray data available that are essential to determine the spectral index of the relics and the properties of the underlying shocks. In particular, the detection of a shock across the relic (or, at least, a part of it) is necessary to evaluate the particle acceleration efficiency.

Table 5.1: The sample of galaxy clusters with radio relics and detected underlying shocks. Reported values of M_{500} and N_{H} are taken from Planck Collaboration XXIX (2014) and Willingale et al. (2013), respectively. For the Sausage Cluster, M_{500} is from de Gasperin et al. (2014). Redshifts are taken from the NASA/IPAC Extragalactic Database (NED).

Cluster name	RA _{J2000} (h,m,s)	DEC _{J2000} (°,′,″)	M_{500} ($10^{14} M_{\odot}$)	z	N_{H} (10^{20} cm^{-2})	Instrument	Ref.	
							R	X
A2744	00 14 19	−30 23 22	9.56	0.308	1.46	<i>XMM-Newton</i>	1	2
A115	00 55 60	+26 22 41	7.20	0.197	6.38	<i>Chandra</i>	3	3
El Gordo	01 02 53	−49 15 19	8.80	0.870	1.78	<i>Chandra</i>	4	4
A521	04 54 09	−10 14 19	6.90	0.253	6.06	<i>Chandra</i>	5	6
A3376	06 01 45	−39 59 34	2.27	0.046	5.81	<i>XMM-Newton</i>	7	8
Toothbrush Cluster	06 03 13	+42 12 31	11.1	0.225	33.4	<i>Chandra</i>	9	10
Bullet Cluster	06 58 31	−55 56 49	12.4	0.296	6.43	<i>Chandra</i>	11	12
RXC J1314.4-2515	13 14 28	−25 15 41	6.15	0.247	8.91	<i>XMM-Newton</i>	13	14
A2146	15 56 09	+66 21 21	3.85	0.234	3.35	<i>Chandra</i>	15	16
A3667	20 12 30	−56 49 55	5.77	0.056	5.25	<i>XMM-Newton</i>	17	18,19
Sausage Cluster	22 42 53	+53 01 05	7.97	0.192	46.4	<i>Chandra</i>	20	21

Notes. References (R=radio, X=X-ray): ¹Giacintucci et al. (in preparation); ²Eckert et al. (2016a); ³Botteon et al. (2016a); ⁴Botteon et al. (2016c); ⁵Giacintucci et al. (2008); ⁶Bourdin et al. (2013); ⁷Kale et al. (2012); ⁸Urdampilleta et al. (2018); ⁹van Weeren et al. (2012b); ¹⁰van Weeren et al. (2016a); ¹¹Shimwell et al. (2014); ¹²Shimwell et al. (2015); ¹³Venturi et al. (2013); ¹⁴Mazzotta et al. (2011); ¹⁵Russell et al. (2012); ¹⁶Hoang et al. (2018c); ¹⁷Mauch et al. (2003); ¹⁸Sarazin et al. (2016); ¹⁹Storm et al. (2018); ²⁰van Weeren et al. (2010); ²¹Akamatsu et al. (2015).

5.3 Methods and data reduction

We retrieved all the ObsIDs available on the clusters of the sample (Tab. 5.1) from the *Chandra*¹ and *XMM-Newton*² archives. In the cases where the clusters have been observed with both instruments, we used the *Chandra* data because its higher angular resolution allows us to better characterize the sharp edges of the shocks and to excise more accurately the point sources. However, for A2744, we used the *XMM-Newton* dataset because the shock is located on the edge of a CCD chip in the available *Chandra* ObsIDs.

5.3.1 *Chandra*

In our analysis, we used *Chandra* data for 7 out of 11 clusters of our sample (cf. Tab. 5.1). We carried out a standard data reduction by using CIAO v4.10 and *Chandra* CALDB v4.7.8. Datasets

¹<http://cda.harvard.edu/chaser/>

²<http://nxsas.esac.esa.int/>

consist both of ACIS-I and ACIS-S observations taken either in FAINT or VFAINT mode. Contamination by soft proton flares was removed by inspecting the light curves extracted³ in the 0.5 – 7.0 keV band using the `lc_filter` routine. Multiple ObsIDs were merged together with the task `merge_obs` to create images in the 0.5 – 2.0 keV band.

5.3.2 *XMM-Newton*

For 4 out of 11 clusters of our sample we used *XMM-Newton* observations (cf. Tab. 5.1). We used the ESAS tools developed within the *XMM-Newton* SAS v16.1.0 to analyze EPIC observations. The analysis steps have been collected in the pipeline exhaustively described in Ghirardini et al. (2019), developed in the context of the *XMM-Newton* Cluster Outskirts Project (X-COP; Eckert et al. 2017a) and adopted in this work. Soft proton flare contamination is higher in *XMM-Newton* than in *Chandra*, and observation periods affected by high background levels were filtered out with the tasks `mos-filter` and `pn-filter`. EPIC cluster images in the 0.5 – 2.0 keV band were created by adding together single detector images and multiple ObsIDs.

5.3.3 Surface brightness and density profiles

After the excision of contaminating point sources, SB profiles across the shocks were extracted from the 0.5 – 2.0 keV exposure-corrected images of the clusters and fitted with PROFFIT v1.5 (Eckert et al. 2011). An underlying broken power-law with a density jump (Eq. 1.21) was assumed to fit the data, that were rebinned to reach a minimum S/N of 7. PROFFIT performs a modeling of the 3D density profile that is numerically projected along the line of sight under spherical assumption (following the Appendix in Owers et al. 2009). Deprojected density profiles were recovered from the emission measure of the plasma evaluated in the case of an absorbed APEC model (Smith et al. 2001) with metallicity assumed to be $0.3 Z_{\odot}$ and total (i.e. atomic + molecular) hydrogen column density N_{H} measured in the direction of the clusters fixed to the values of Willingale et al. (2013) listed in Tab. 5.1. The choice of the soft band 0.5 – 2.0 keV ensures that the bremsstrahlung emissivity is almost independent of the gas temperature for $kT \gtrsim 3$ keV (e.g. Etori et al. 2013).

For *Chandra*, we made use of the blank sky fields normalized by counts in the 9.5 – 12.0 keV band to subtract the background from the SB profiles (see Botteon et al. 2018a, for more details). For *XMM-Newton*, the particle background was subtracted from the data while the Galactic foreground was taken into account by leaving a constant free to vary during the fitting procedure.

5.4 Computation of the acceleration efficiency

Following Section 1.5.2, we calculated the acceleration efficiency of electrons η_e and the relevant parameters that are necessary to reproduce the bolometric synchrotron luminosity of the relics in the clusters⁴ of Tab. 5.1 as a function of the magnetic field B . Rearranging Eq. 1.39 for the electron acceleration efficiency, we obtain

$$\eta_e \simeq \frac{2 \int_{v_0} L(v) dv}{A \rho_u V_{sh}^3} \left(1 - \frac{1}{c^2}\right)^{-1} \frac{1}{\Psi} \frac{B_{cmb}^2 + B^2}{B^2} \quad (5.1)$$

³For ACIS-I, in the S2 chip kept on during the observation or in a source region in the ACIS-I FoV, if S2 was turned off. For ACIS-S, light curves were extracted in the S1 chip. See Botteon et al. (2018a) for more details.

⁴We anticipate that we did not consider the double radio relic system in A3667 in our analysis, see end of Section 5.4.1 for more details.

Table 5.2: Parameters used to compute the acceleration efficiency. Values of the downstream temperature kT_d and radio flux density S are derived from the works listed at the bottom of Tab. 5.1.

Cluster name	Position	\mathcal{C}	n_d (cm^{-3})	kT_d (keV)	A ($\pi \text{ kpc}^2$)	S_ν (mJy)	ν (MHz)
A2744 [†]	NE	$1.90^{+0.60}_{-0.40}$	1.8×10^{-4}	12.3	740^2	20	1400
A115	N	$2.15^{+0.16}_{-0.14}$	1.5×10^{-3}	7.9	180^2	34	1400
El Gordo	NW	$2.88^{+0.30}_{-0.25}$	8.5×10^{-4}	17.9	350^2	28	610
A521	SE	$2.41^{+0.71}_{-1.41}$	3.0×10^{-4}	7.0	490^2	42	610
A3376	E	$1.98^{+0.27}_{-0.30}$	9.0×10^{-4}	4.7	260^2	40	1400
Toothbrush Cluster	N	$1.37^{+0.18}_{-0.17}$	5.5×10^{-4}	8.2	300^2	480	610
Bullet Cluster	E	$2.15^{+0.16}_{-0.14}$	5.0×10^{-4}	13.5	250^2	5	2100
RXC J1314.4-2515	W	$1.96^{+0.42}_{-0.36}$	1.0×10^{-3}	13.5	330^2	85	325
A2146	NW	$1.69^{+0.06}_{-0.06}$	3.5×10^{-3}	14.5	160^2	0.8	1500
Sausage Cluster	N	n.a.	3.0×10^{-4}	8.5	900^2	337	610

Notes. [†]Compression factor and downstream density taken from Eckert et al. (2016a).

where Ψ is given in Eq. 1.40 and it depends on p_{min} . Given the kinetic energy flux available at the shock ΔF_{KE} and the energy flux of the accelerated relativistic electrons at relic E_{relic} , invoking flux conservation we can write

$$\overbrace{\frac{1}{2} V_{sh}^3 \rho_u \left(1 - \frac{1}{\mathcal{C}^2}\right)}^{\Delta F_{KE}} \eta_e = \overbrace{V_d \epsilon_{e,d}}^{E_{relic}} \quad (5.2)$$

where

$$\epsilon_{e,d} = \int_{p_{min}} K_e p^{-\delta_{inj}} E dp \quad (5.3)$$

is the downstream electron energy density (K_e is the normalization of the spectrum) and

$$V_d = c_s \frac{\mathcal{M}^2 + 3}{4\mathcal{M}} \quad (5.4)$$

is the downstream velocity. We deployed a self-consistent method to calculate η_e that relies on the small number of observable quantities listed in Tab. 5.2. In particular, we started from downstream quantities (i.e. temperature and density), usually better constrained by X-ray observations, and from the Mach number of the shock derived from the density jump (Eq. 1.18) to derive upstream quantities using the Rankine-Hugoniot jump conditions (Landau & Lifshitz 1959). Downstream temperatures were taken from the literature while downstream densities were obtained from the re-analysis of the SB profiles extracted across the shocks. The spectrum of the accelerated particles δ_{inj} is related to the shock Mach number in the case of DSA via Eq. 1.35.

In the commonly adopted *thermal leakage injection* scenario (Gieseler et al. 2000), only particles with $p \gtrsim p_{min}$ are allowed to cross the shock front and take part into the acceleration process. However, the physical details which determine p_{min} are still poorly known, making the choice of p_{min} a guess (e.g. Ryu et al. 2003; Blasi 2004; Caprioli & Spitkovsky 2014). In our framework, electrons are accelerated from the thermal pool starting from a minimum momentum as shown in Fig 5.1. This implies a relationship between the minimum momentum and the normalization of the spectrum that can be derived matching the number density of non-thermal electrons with that of thermal electrons with momentum p_{min}

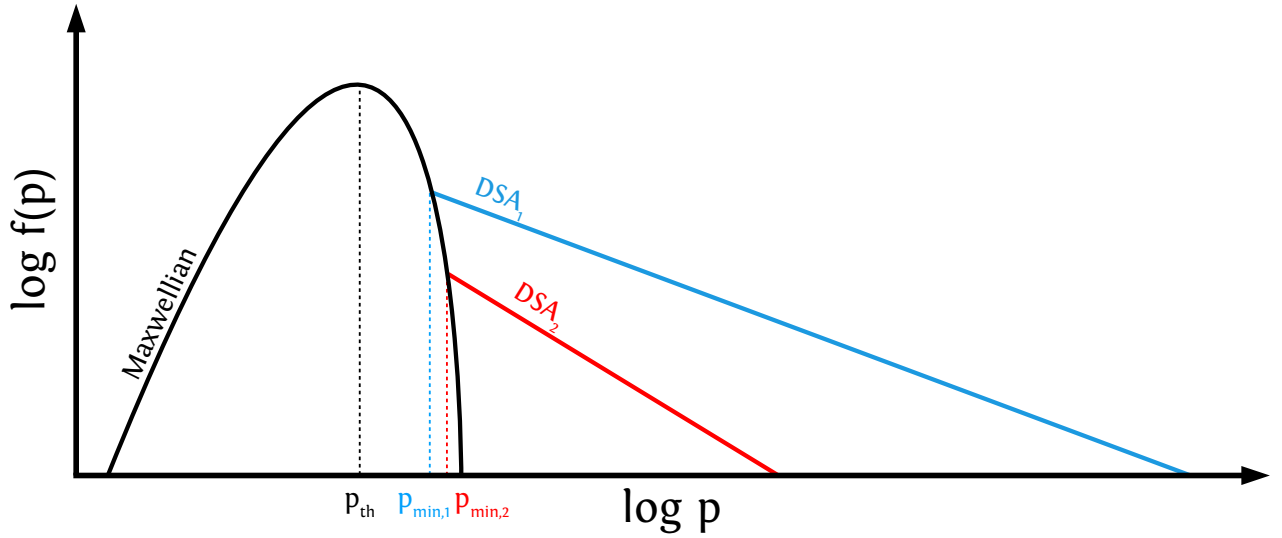


Figure 5.1: Schematic representation of the electron momentum distribution in a post-shock region. The two power-laws show the DSA spectra (Eq. 1.35) in the case of two Mach numbers \mathcal{M}_1 (blue) $>$ \mathcal{M}_2 (red).

$$K_e p_{min}^{-\delta_{inj}} = \frac{4}{\sqrt{\pi}} n_d \frac{p_{min}^2}{p_{th}^3} \exp \left[- \left(\frac{p_{min}}{p_{th}} \right)^2 \right] \quad (5.5)$$

which leads to

$$K_e = \frac{4}{\sqrt{\pi}} n_d \frac{p_{min}^{2+\delta_{inj}}}{p_{th}^3} \exp \left[- \left(\frac{p_{min}}{p_{th}} \right)^2 \right] \quad (5.6)$$

where $p_{th} = \sqrt{2m_e k T_d}$ is the electron thermal peak momentum in the post-shock gas (Fig. 5.1). At this point the question is what kind of acceleration efficiency (or parameters p_{th} , K_e) is necessary to generate the observed radio properties of radio relics. To address this point we combine Eq. 5.1, 5.2 and 5.6, we obtain

$$p_{min}^{2+\delta_{inj}} \exp \left[- \left(\frac{p_{min}}{p_{th}} \right)^2 \right] = \frac{\sqrt{\pi} \int_{v_0} L(v) dv}{4 n_d V_d A} \frac{p_{th}^3}{\int_{p_0} p^{-\delta_{inj}} E dp} \frac{B_{cmb}^2 + B^2}{B^2} \quad (5.7)$$

which can be used to determine the minimum momentum of the electrons which are efficiently accelerated as a function of the magnetic field. The surface of the shock is assumed to be $A = \pi R^2$, where R is the semi-axis of the relic emission crossed by the shock. At this point, the only unknown in our problem is the magnetic field downstream (i.e. in the radio relic).

Our knowledge of B in clusters is poor (Section 1.2.4) and only a few constraints on the field strength in relics, based on questionable assumptions (e.g. equipartition), are available in the literature (e.g. Johnston-Hollitt 2004; Bonafede et al. 2009; Finoguenov et al. 2010; van Weeren et al. 2010, 2011b). In particular, the magnetic fields can be boosted by shock compression/amplification in these dynamically active regions (Bonafede et al. 2013), perhaps reaching values up to $5 \mu\text{G}$ (e.g. van Weeren et al. 2010; Botteon et al. 2016c; Rajpurohit et al. 2018). This is important to keep in mind because the required acceleration efficiency is smaller for higher magnetic fields (see below). Note that Eq. 5.7 requires that $p_{min} > p_{th}$ or all the thermal distribution will be accelerated (Fig. 5.1). Thus, Eq. 5.7 might provide physical solutions only above a certain value of B (for a fixed set of observable quantities). After that p_{min} is determined, the electron acceleration efficiency can be computed via Eq. 5.1.

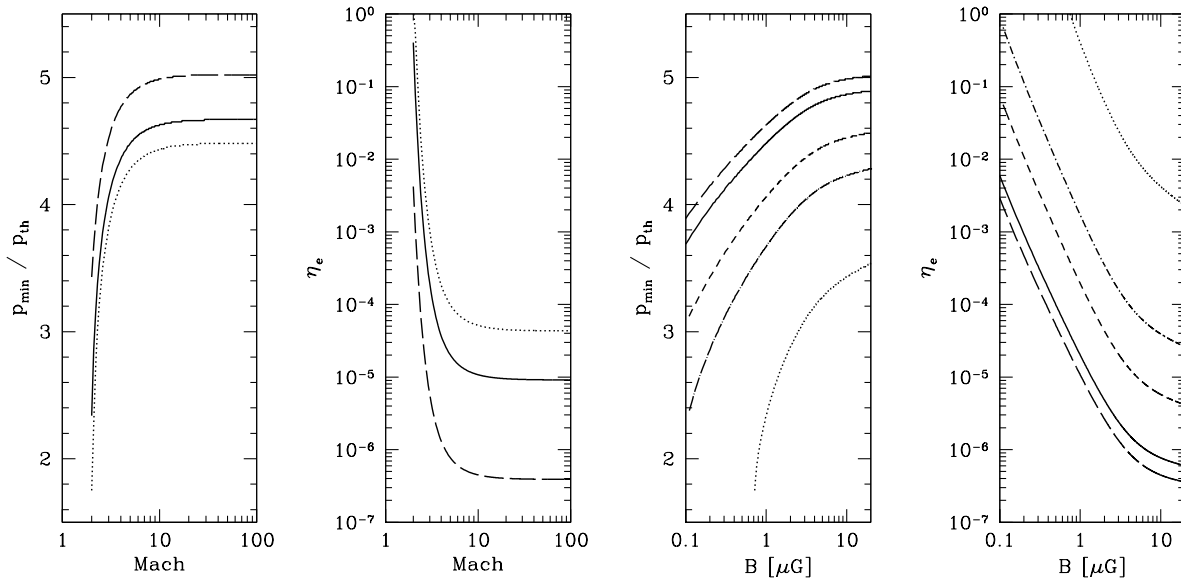


Figure 5.2: Values of p_{\min}/p_{th} and η_e for a mock radio relic (see text) at fixed magnetic field (*left*) and Mach number (*right*). In the left panels, curves denote different values of B : 0.5 μG (*dotted*), 1 μG (*solid*) and 10 μG (*dashed*). In the right panels, curves denote different values of \mathcal{M} : 2 (*dotted*), 2.5 (*dot-dashed*), 3 (*short dashed*), 5 (*solid*) and 10 (*long dashed*).

In Fig. 5.2, we plot the p_{\min}/p_{th} and η_e for a mock radio relic at $z = 0.1$ with an optimistic combination of $kT_d = 10$ keV, $n_d = 1.0 \times 10^{-3} \text{ cm}^{-3}$, $S_{1.4\text{GHz}} = 5$ mJy, and $A = 750^2 \pi \text{ kpc}^2$, for different values of Mach number and magnetic field strength. Despite the optimistic parameters, these plots already demonstrate that DSA from the thermal pool requires too large efficiencies (or, equivalently, too large magnetic fields) to reproduce the bolometric luminosity of the mock relic in the case of a $\mathcal{M} = 2$ shock (which is a typical value observed in clusters). As discussed in Section 1.5.2, the acceleration efficiency of CRp for weak shocks is likely $< 1\%$ (e.g. Kang & Ryu 2013) and that of CRe is reasonably a fraction of this value. In the following, we will consider a conservative value of $\eta_e = 0.1$, which is generally associated to protons in strong SNR shocks ($\mathcal{M} \sim 10^3$), and a more realistic value of $\eta_e = 0.01$, considering that in SNRs the acceleration efficiency of CRp is higher than that of CRe.

5.4.1 X-ray and DSA Mach numbers

In Tab. 5.3 and Fig. 5.3 we compare the measured values for X-ray Mach number and integrated spectral index with the expectations from DSA theory for the relics in our sample. In a number of cases, a discrepancy between the observed spectral index of the relic and that implied by DSA exists. In particular, the Mach numbers derived from radio observations are generally biased high than those coming from X-ray data (e.g. Akamatsu et al. 2017a; Urdampilleta et al. 2018). However, numerical simulations showed that the inconsistency between radio and X-ray derived Mach numbers might emerge from projection effects of multiple shock surfaces (Skillman et al. 2013; Hong et al. 2015). As a consequence, the discrepancy between the Mach numbers inferred from X-ray and radio observations can not be used to readily rule out the scenario of DSA of thermal particles. Furthermore, as mentioned in Section 1.5.2, natural modifications to the basic DSA theory (e.g. considering Alfvénic drift or including superdiffusion regimes at the shocks, Kang & Ryu 2018; Zimbaro & Perri 2018) change the spectral index expected from DSA.

In our framework, calculations are based adopting the Mach number estimated from the X-ray

Table 5.3: Observed X-ray Mach number derived from the SB analysis (\mathcal{M}_X) and integrated spectral index from literature (α_{radio}). These were used to compute the expected integrated spectral index (α_{DSA}) and Mach number (\mathcal{M}_{DSA}) from DSA (Eq. 1.38).

Cluster name	Position	\mathcal{M}_X	\mathcal{M}_{DSA}	α_{radio}	α_{DSA}	Reference
A2744	NE	$1.65^{+0.59}_{-0.31}$	$2.69^{+0.42}_{-0.27}$	$1.32^{+0.09}_{-0.09}$	$2.61^{+1.35}_{-0.66}$	1
A115	N	$1.87^{+0.16}_{-0.13}$	$4.58^{+\infty}_{-2.50}$	$1.10^{+0.50}_{-0.50}$	$1.80^{+0.19}_{-0.16}$	2
El Gordo	NW	$2.78^{+0.63}_{-0.38}$	$2.53^{+1.04}_{-0.41}$	$1.37^{+0.20}_{-0.20}$	$1.30^{+0.12}_{-0.11}$	3
A521	SE	$2.13^{+1.13}_{-1.13}$	$2.33^{+0.05}_{-0.04}$	$1.45^{+0.02}_{-0.02}$	$1.57^{+\infty}_{-0.36}$	4
A3376	E	$1.71^{+0.25}_{-0.24}$	$2.53^{+0.28}_{-0.20}$	$1.37^{+0.08}_{-0.08}$	$2.04^{+0.68}_{-0.34}$	5
Toothbrush Cluster	N	$1.25^{+0.13}_{-0.12}$	$3.79^{+0.26}_{-0.22}$	$1.15^{+0.02}_{-0.02}$	$4.56^{+3.67}_{-1.34}$	6
Bullet Cluster	E	$1.87^{+0.16}_{-0.13}$	$2.01^{+0.19}_{-0.14}$	$1.66^{+0.14}_{-0.14}$	$1.80^{+0.19}_{-0.16}$	7
RXC J1314.4-2515	W	$1.70^{+0.40}_{-0.28}$	$3.18^{+0.87}_{-0.45}$	$1.22^{+0.09}_{-0.09}$	$2.06^{+0.91}_{-0.47}$	8
A2146	NW	$1.48^{+0.05}_{-0.05}$	$3.91^{+1.95}_{-0.73}$	$1.14^{+0.08}_{-0.08}$	$2.68^{+0.23}_{-0.19}$	9
Sausage Cluster	N	n.a.	$4.38^{+1.06}_{-0.59}$	$1.11^{+0.04}_{-0.04}$	n.a.	10

Notes. References for integrated spectral indexes: ¹Pearce et al. (2017); ²Govoni et al. (2001b); ³Botteon et al. (2016c); ⁴Macario et al. (2013); ⁵George et al. (2015); ⁶Rajpurohit et al. (2018); ⁷Shimwell et al. (2015); ⁸George et al. (2017); ⁹Hoang et al. (2018c); ¹⁰Hoang et al. (2017).

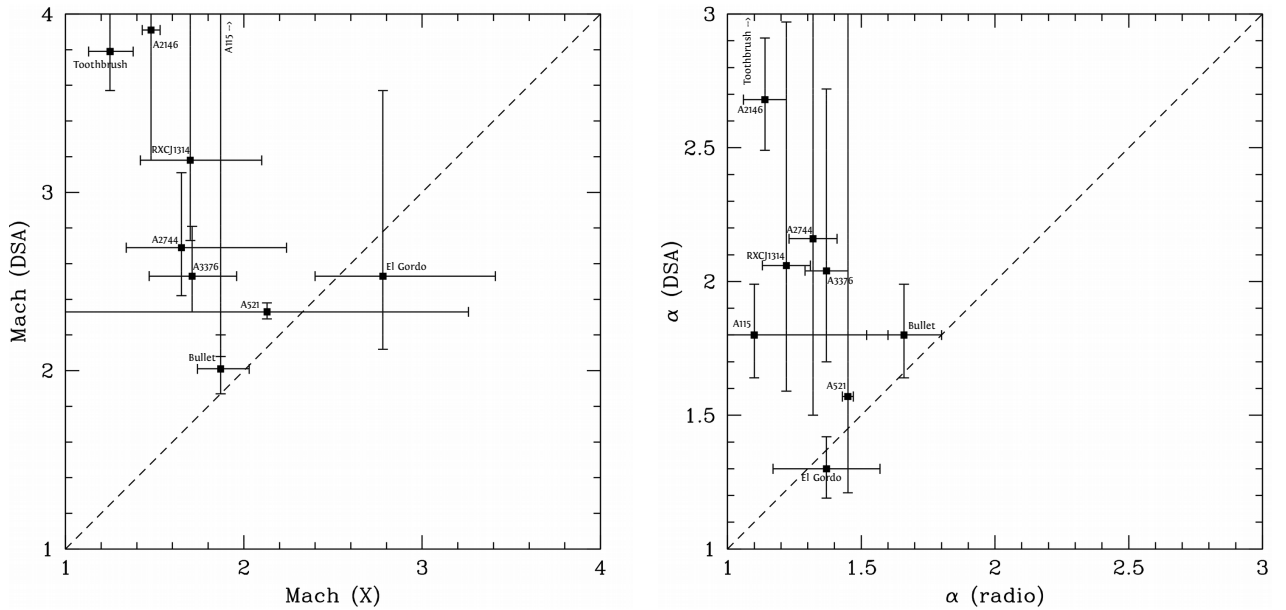


Figure 5.3: Observed Mach numbers and spectral indexes versus the expected values from DSA theory. The values used to produce the plots are those listed in Tab. 5.3. The dashed lines indicate the linear correlation as a reference.

SB analysis (usually better constrained than that obtained with the spectral analysis). Since the Mach number has important implications for the shock energetics and particle acceleration process (e.g. Donnert et al. 2017), we also performed the calculations of the acceleration efficiency adopting the Mach number implied from the observed integrated spectrum of the relic by DSA (Eq. 1.38).

From the clusters listed in Tab. 5.1, A3667 represents a peculiar case. Indeed, the measured spectral indexes of the two radio relics hosted in this system have integrated values ≤ 1 (Hindson et al. 2014; Riseley et al. 2015). Spectral indexes < 1 are not allowed by DSA, where $\alpha_{DSA} \rightarrow 1$ for $\mathcal{M} \rightarrow \infty$ (Eq. 1.38). However, also the case $\alpha = 1$ is in tension with DSA due to the low Mach number of the shocks observed in the X-rays underlying the two relics (Sarazin et al. 2016; Storm et al. 2018). For this reason, we did not consider A3667 in the subsequent analysis.

5.5 Results

We extracted and fitted the X-ray SB profiles across 10 radio relics in the sample. The broken power-law (Eq. 1.21) fit confirmed the presence of a discontinuity coincident with the outer edge of radio emission for 9 out of 10 relics. The only case where we used a single power-law model to fit the SB profile is for the Sausage relic, which is known to not exhibit a SB jump across its surface (see discussion below). Therefore, we computed the electron density profiles across the shocks (whose nature was already determined by the spectral analysis performed in literature works) and derived the compression factors and downstream densities (Tab. 5.2). In Fig. 5.4–5.13 we show the *Chandra* and *XMM-Newton* images in the 0.5 – 2.0 keV band of the clusters in the sample, and the SB and density profiles for the 10 radio relics considered in the analysis. Radio contours of the relics have been superimposed onto the X-ray images. In the following we discuss the individual cases. In Section 5.6 we summarize and discuss our results.

A2744. This system is known to be a massive cluster experiencing multiple merger events (Kempner & David 2004; Boschin et al. 2006; Owers et al. 2011) at the crossroads of several filaments (Eckert et al. 2015). In the radio band, it hosts a powerful radio halo and a prominent radio relic toward the NE direction (Govoni et al. 2001b; Orrù et al. 2007; Pearce et al. 2017), as shown in Fig. 5.4. Two shocks have been detected in A2744: one ahead the bullet like feature toward the SE direction (Owers et al. 2011) and the other underlying the relic in the NE cluster outskirts (Eckert et al. 2016a).

We were not able to reproduce the SB profile reported in Eckert et al. (2016a). Three are the main reasons that might have caused this: the not optimized choice of the extracting sector, the different energy band used (0.5 – 2.0 keV versus 0.5 – 1.2 keV), and the presence of the X-ray filament in the E direction observed by Eckert et al. (2015) which can alter the upstream slope of the SB profile. For this case, we used the values reported in Eckert et al. (2016a) for the electron downstream density at the relic location (extrapolated from the β -model solution for A2744 at the relic position), compression factor and Mach number to compute the electron acceleration efficiency in Fig. 5.14. Due to the low Mach number of the shock (which implies a small energy flux at the shock and a steep spectrum of the accelerated electron), it is challenging to explain the radio relic luminosity via DSA of thermal electrons. Indeed, a solution is found (i.e. $p_{min} > p_{th}$) only for the upper bound of the shock Mach number derived from X-ray observations; in this case, acceleration efficiencies $\eta_e \lesssim 0.1$ are achieved for $B \gtrsim 6.8 \mu\text{G}$ and $\eta_e \lesssim 0.01$ for $B \gg 20 \mu\text{G}$ (Fig. 5.14). The relic in A2744 is located approximately at the virial radius, and explaining such strong magnetic field strengths at such a large distance from the cluster center is problematic. On the other hand, the requirement of strong B can be released if we assume the higher Mach number implied by DSA from the integrated radio spectrum of the relic (Tab. 5.3).

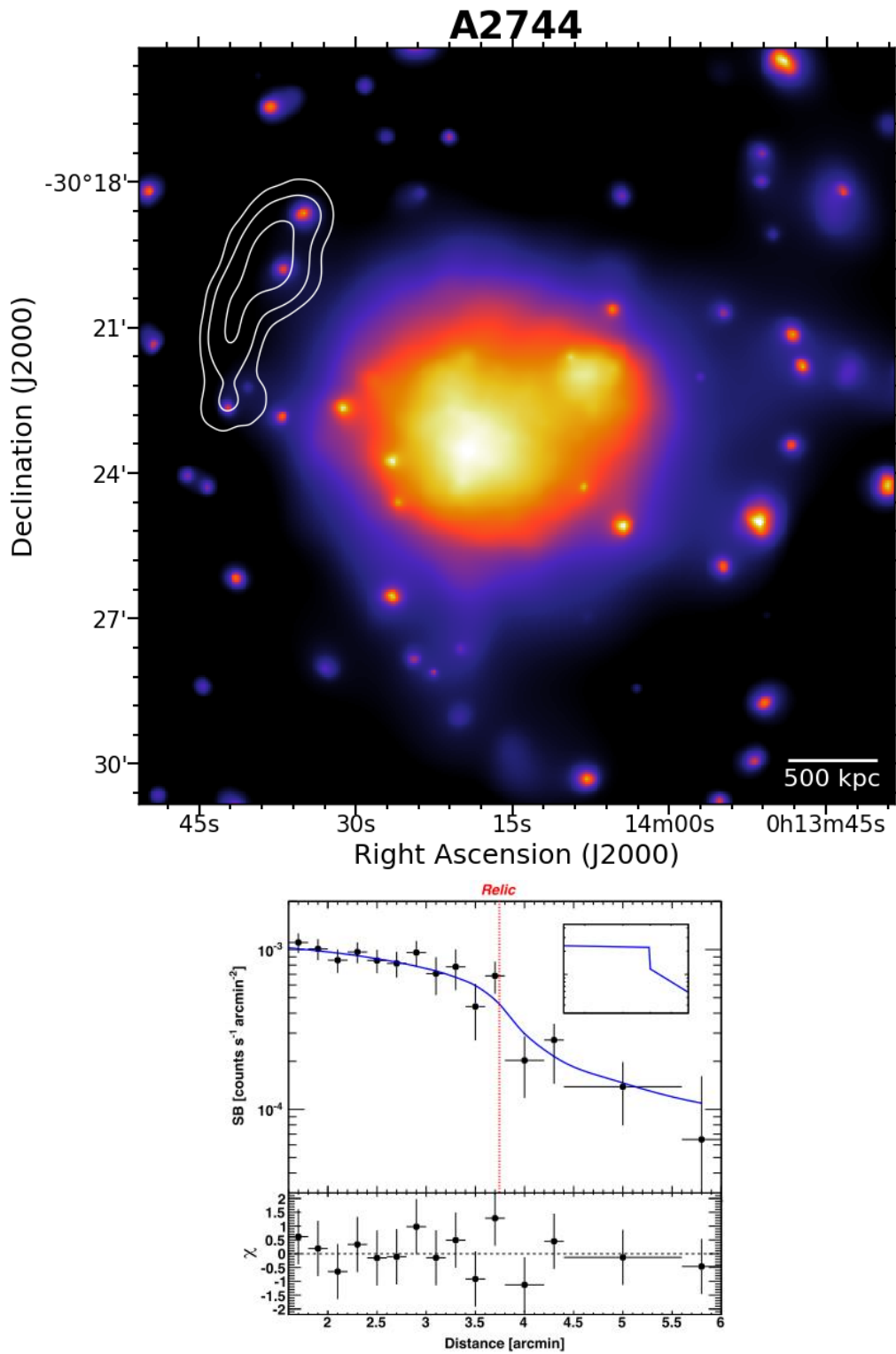


Figure 5.4: A2744. *Top:* XMM-Newton image with overlaid the VLA 1.4 GHz radio contours from Giacintucci et al. (in preparation). *Bottom:* X-ray SB profile across the radio relic from Eckert et al. (2016a). We thank S. Giacintucci for kindly providing us the displayed radio contours.

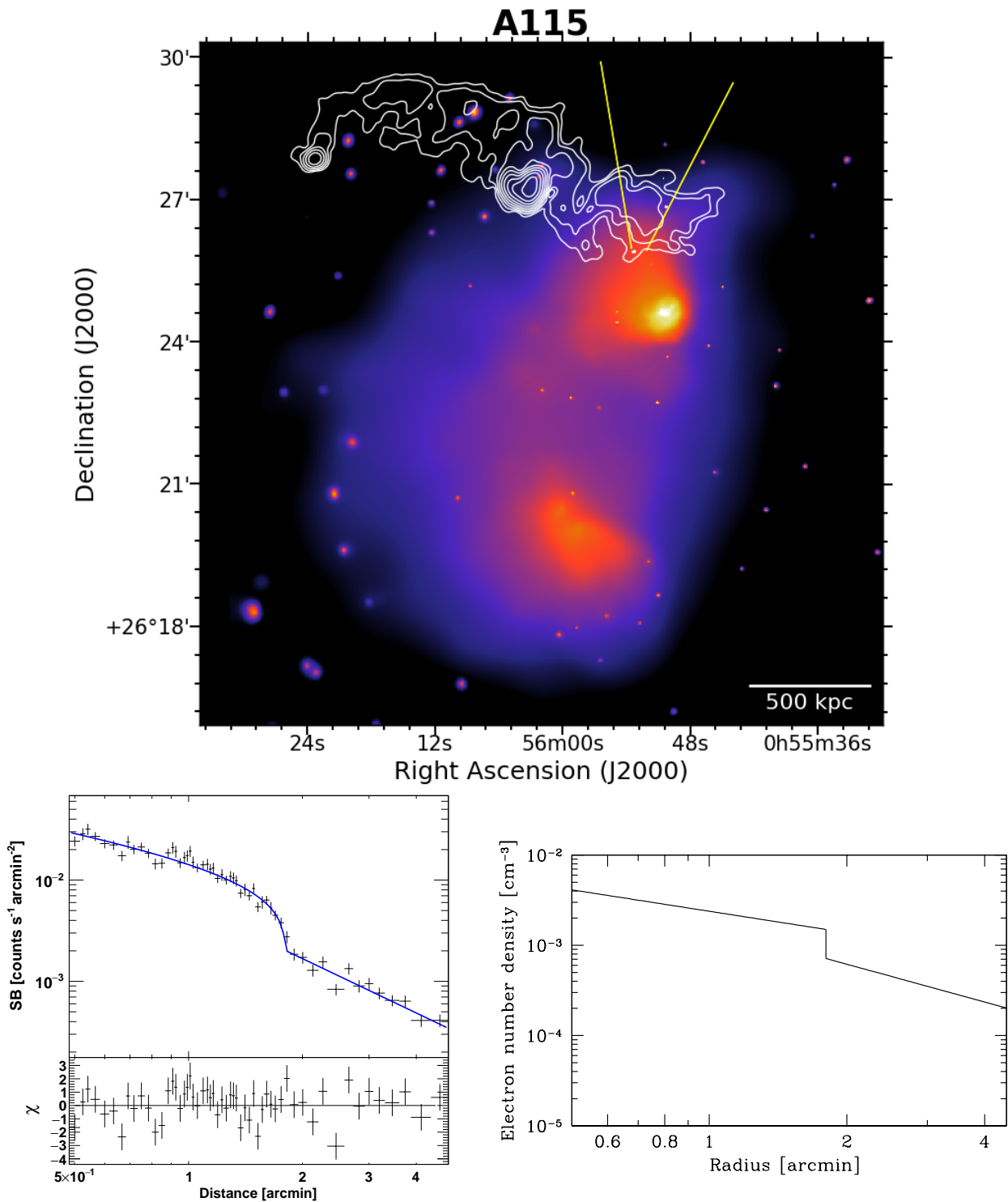


Figure 5.5: A115. *Top:* *Chandra* image with overlaid the VLA 1.4 GHz radio contours from Botteon et al. (2016a) and the yellow sector used for the analysis of the shock front. *Bottom:* X-ray SB profile (*left*) and density profile (*right*) across the radio relic.

A115. It is a galaxy cluster characterized by two components in the initial stage of an off-axis merger (Forman et al. 1981; Gutierrez & Krawczynski 2005; Barrena et al. 2007). A giant radio relic with a largest linear size of ~ 1.5 Mpc is observed in the outskirts of the northern sub-cluster (Govoni et al. 2001b), as shown in Fig. 5.5. A shock covering the E portion of the relic has been detected by Botteon et al. (2016a), who suggested that it may actually trace the entire extension of the relic as a result of the off-axis collision. Recently, this scenario has been further corroborated by Hallman et al. (2018) from the comparison between high fidelity temperature map of the whole system and hydrodynamical simulations.

In Chapter 2 we presented the discovery of the shock in A115 and discussed its acceleration efficiency. Here, we re-performed the analysis following the same procedures used for the other relics in the sample and obtained consistent results. In particular, if we adopt the Mach number from X-rays, the efficiency is too large (i.e. $p_{min} < p_{th}$) and DSA of thermal particles is readily ruled out. The second approach is to rely on the Mach number inferred from radio. Unfortunately, the spectral index reported in Govoni et al. (2001b) has large uncertainties since it was computed over a narrow frequency range. With the quoted errors, the integrated spectral index can be < 1 , which is not possible in the case of DSA (see the discussion on A3667 in Section 5.4.1). For this reason, in Fig. 5.14 we computed only the curves corresponding to the best and lower values of \mathcal{M}_{DSA} calculated from the radio spectral index measured by Govoni et al. (2001b). The lower bound of \mathcal{M}_{DSA} is similar to the upper bound of \mathcal{M}_X but provides extremely high acceleration efficiency (Fig. 5.14). We mention that the relic in A115 is one of the cases where DSA was already ruled out in favor of a re-acceleration scenario (Botteon et al. 2016a).

El Gordo. It is famous to be a massive cluster at high redshift (Menanteau et al. 2010, 2012) and to host the most distant radio halo and radio relics known so far (Lindner et al. 2014). Botteon et al. (2016c) reported the discovery of a strong shock co-located with the NW relic (Fig. 5.6), which has been confirmed by the combined X-ray/SZ analysis (Basu et al. 2016).

As for the case of A115, we discovered and studied the acceleration efficiency for NW relic in El Gordo during the PhD Thesis (Chapter 3); here we re-performed the analysis in a homogeneous manner with the other relics in the sample. The NW relic in El Gordo is one out of the three relics where the measurements of \mathcal{M}_X and α_{radio} from X-ray and radio observations are in agreement with the predictions of DSA (Fig. 5.3). This makes possible to define a region in the (η_e, B) plane which is consistent with both \mathcal{M}_X and \mathcal{M}_{DSA} (Fig. 5.14). In such a region, efficiencies $\eta_e \lesssim 0.1$ are achieved for $B \gtrsim 1.8 \mu\text{G}$, which is a reasonable value for a cluster post-shock region. A more realistic acceleration efficiency $\eta_e \sim 0.01$ would require $B \sim 5.2 \mu\text{G}$, a likely high value of magnetic field for a cluster periphery which, however, in this case can not be firmly excluded due to the presence of a quite strong ($\mathcal{M} \sim 3$) shock and the lack of IC emission from the relic (Chapter 4). As concluded by Botteon et al. (2016c), DSA is still consistent with the observed properties of the relic/shock and it appears to be also energetically viable in El Gordo.

A521. The cluster complex internal dynamics was unveiled by X-ray and optical observations (Arnaud et al. 2000; Maurogordato et al. 2000; Ferrari et al. 2003, 2006). In the radio band, this system is known to be the first galaxy cluster where an USSRH has been detected (Brunetti et al. 2008). As shown in Fig. 5.7, a radio relic is observed in the SE cluster periphery (Giacintucci et al. 2008), where a shock has been claimed by Bourdin et al. (2013).

We performed the X-ray analysis on A521 using public, but unpublished, *Chandra* observations. The Mach number and downstream density obtained are consistent with those reported by Bourdin et al. (2013) with *XMM-Newton*. Thanks to the combination of steep integrated spectral index and small error on its measurement (Giacintucci et al. 2008), \mathcal{M}_{DSA} is well determined and even better

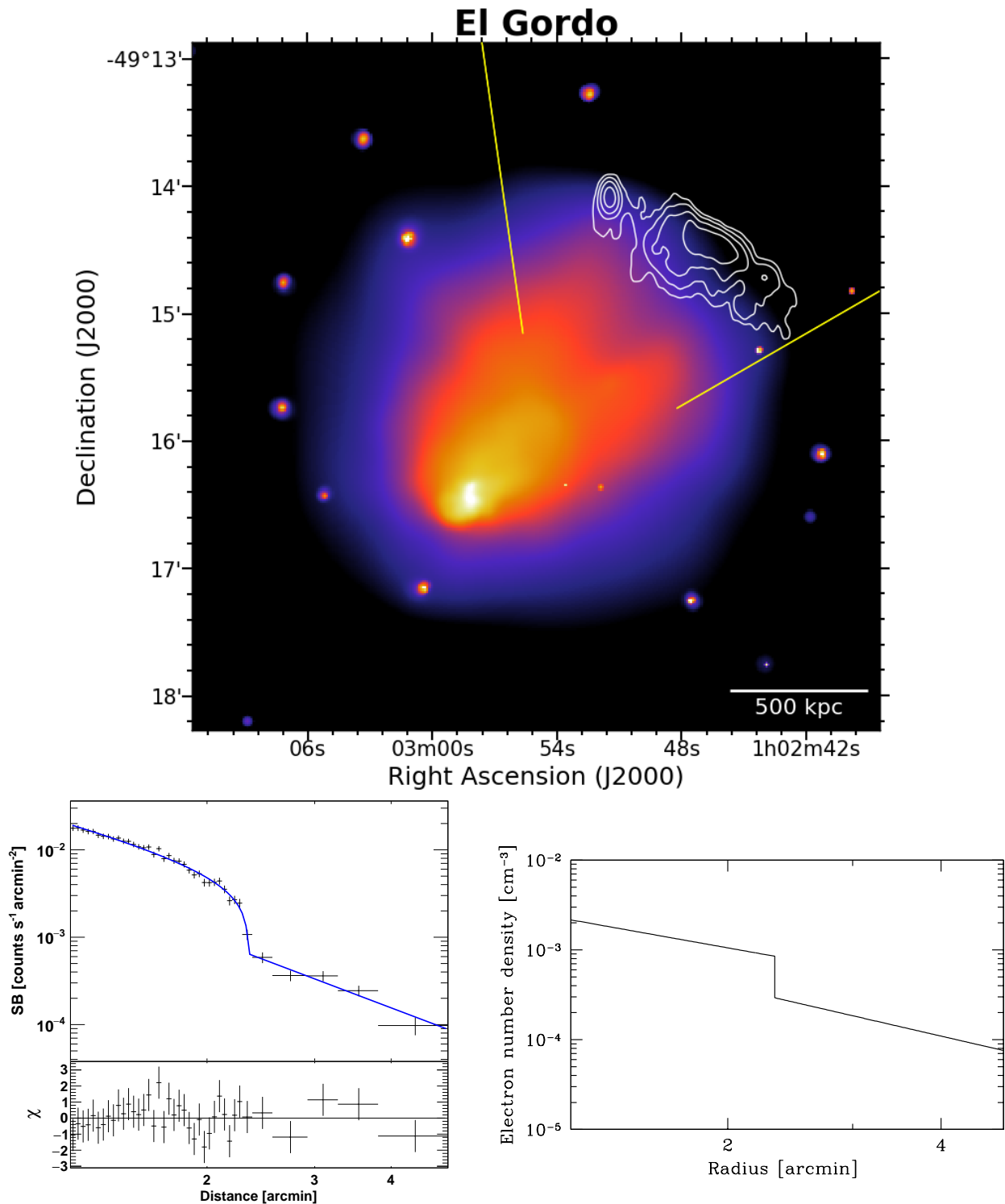


Figure 5.6: El Gordo. *Top:* *Chandra* image with overlaid the GMRT 610 MHz radio contours from Botteon et al. (2016c) and the yellow sector used for the analysis of the shock front. *Bottom:* X-ray SB profile (*left*) and density profile (*right*) across the radio relic.

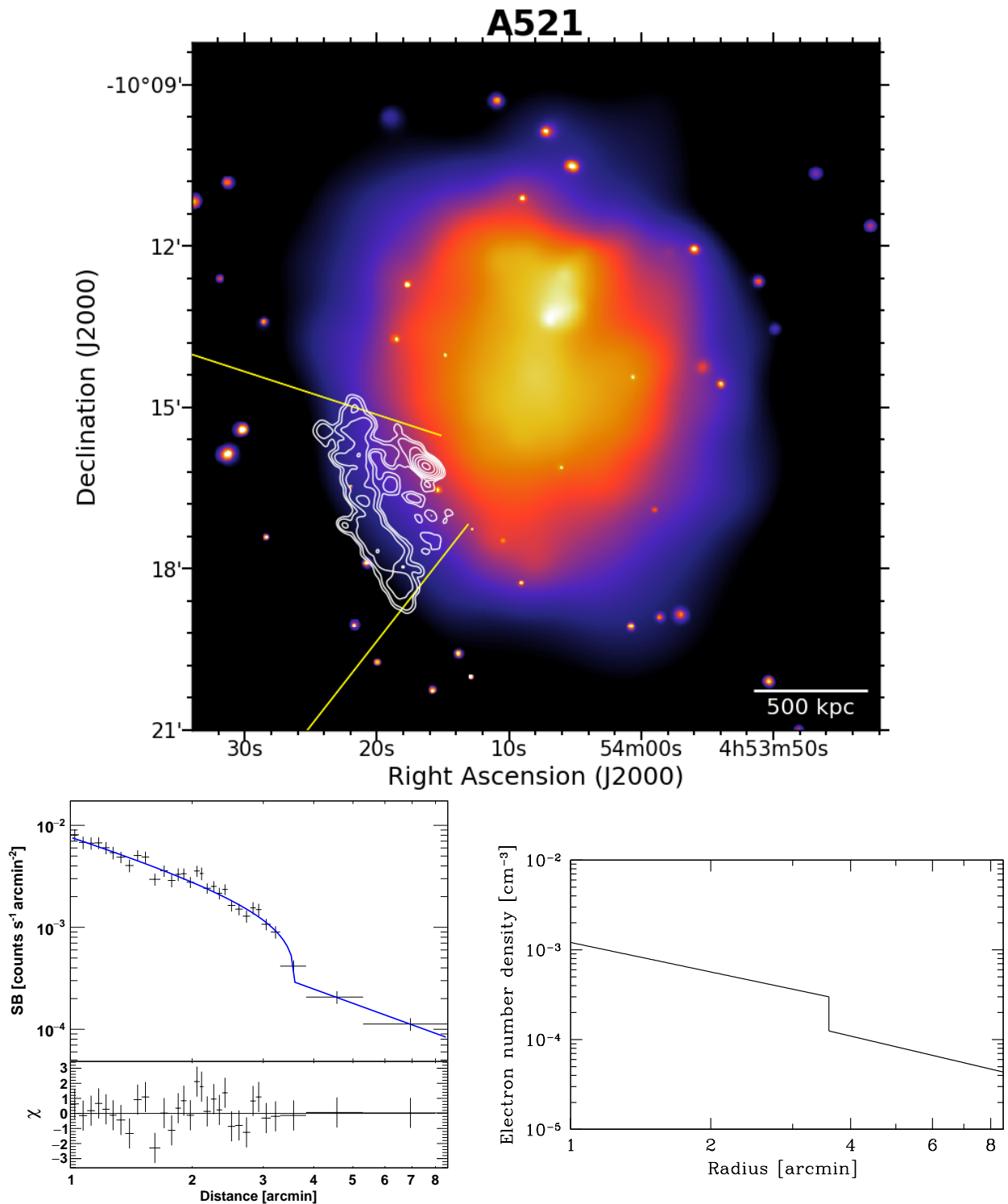


Figure 5.7: A521. *Top:* *Chandra* image with overlaid the GMRT 610 MHz radio contours from Giacintucci et al. (2008) and the yellow sector used for the analysis of the shock front. *Bottom:* X-ray SB profile (*left*) and density profile (*right*) across the radio relic. We thank S. Giacintucci for kindly providing us the displayed radio contours.

constrained than the one derived from X-rays (in contrast with all the other relics). This is the second relic where DSA predictions are consistent with the observed Mach number and integrated spectral index (Fig. 5.3). Similarly to El Gordo case, this allows us to study the region of the efficiency plot in Fig. 5.14 that satisfies both the measured and the DSA-predicted Mach numbers. For A521, this region is essentially constrained by the DSA expectations, implying $\eta_e \lesssim 0.1$ for $B \gtrsim 3.9 \mu\text{G}$. This value might not be critical for a post-shock region. However, we recall that $\eta_e = 0.1$ represents a conservative value; if we consider a lower and more realistic value of $\eta_e \lesssim 0.01$, the magnetic field would become $B \gg 20 \mu\text{G}$, which is difficult to justify (Fig. 5.14). A combination of low acceleration efficiencies and low magnetic field strengths is possible only if we use the upper bound value on \mathcal{M}_X , which is, however, not consistent with the observed integrated spectral index assuming DSA (Fig. 5.7).

A3376. It is a nearby and low mass cluster (cf. Tab. 5.1) with a comet-like appearance in the X-rays which hosts two spectacular radio relics (Bagchi et al. 2006). The relics are separated by a distance of ~ 2 Mpc and are found in diametrically opposite directions, toward the E and W cluster outskirts (Fig. 5.8). Kale et al. (2012) provided a detailed spectral and polarization study of the relics, whose properties are in agreement with two shocks moving out in the cluster peripheries after a nearly head-on merger (Machado & Lima Neto 2013). Indeed, both the putative shocks underlying the radio relics have been confirmed by X-ray observations (Akamatsu et al. 2012; Akamatsu & Kawahara 2013; Urdampilleta et al. 2018).

We confirmed the SB jump only for the E relic in A3376, obtaining a Mach number which is consistent with that reported by Urdampilleta et al. (2018). The W relic lays in a very low SB region at the edge of CCD FoV, making the study of the potential SB discontinuity critical. Nonetheless, Urdampilleta et al. (2018) characterized an edge in this position of the cluster with *XMM-Newton* data. We note that they found that this discontinuity is located in the middle of the relic, and not on the leading edge of the source as expected and usually observed. We were not able to reproduce their SB profile; different procedures adopted to subtract the background (I. Urdampilleta, private communication) may possibly explain this discrepancy. For the purposes of the PhD Thesis, we limited the analysis only to the E relic. The acceleration efficiency was computed only for the upper bound of \mathcal{M}_X , which is not energetically viable for any value of B (Fig. 5.14). On the other hand, the problem is alleviated if we assume the higher Mach number derived from the integrated spectral of the relic under the assumption of DSA.

Toothbrush Cluster. The nickname of this cluster derives from the peculiar shape of the giant radio relic discovered by van Weeren et al. (2012b). This relic is the most powerful and among the largest known so far, covering a linear size of ~ 2 Mpc (Fig. 5.9). Numerical simulations were able to reproduce the relic morphology from the collision between three systems (Brüggen et al. 2012b). Surprisingly, only a weak discontinuity covering a portion (i.e. the “brush”) of the relic was found in the X-rays (van Weeren et al. 2016a), in contrast with the strong shock expected from the analysis of the radio data. Although no temperature jump has been observed with *Chandra* at this SB edge (van Weeren et al. 2016a), *Suzaku* measurements provided evidence for a temperature discontinuity (Itahana et al. 2015) which implies a shock with Mach number somewhat in agreement with that derived from *Chandra* data.

We used the same sector reported in van Weeren et al. (2016a) to compute the SB and density profile across the NW part of the Toothbrush relic. We confirmed the presence of a small density jump which implies the presence of weak shock. For the Mach number measured in the X-rays, it was not possible to compute the acceleration efficiency (Fig. 5.14). In turns, under DSA assumptions, the integrated spectral index implies a strong shock. This would require acceptable values of

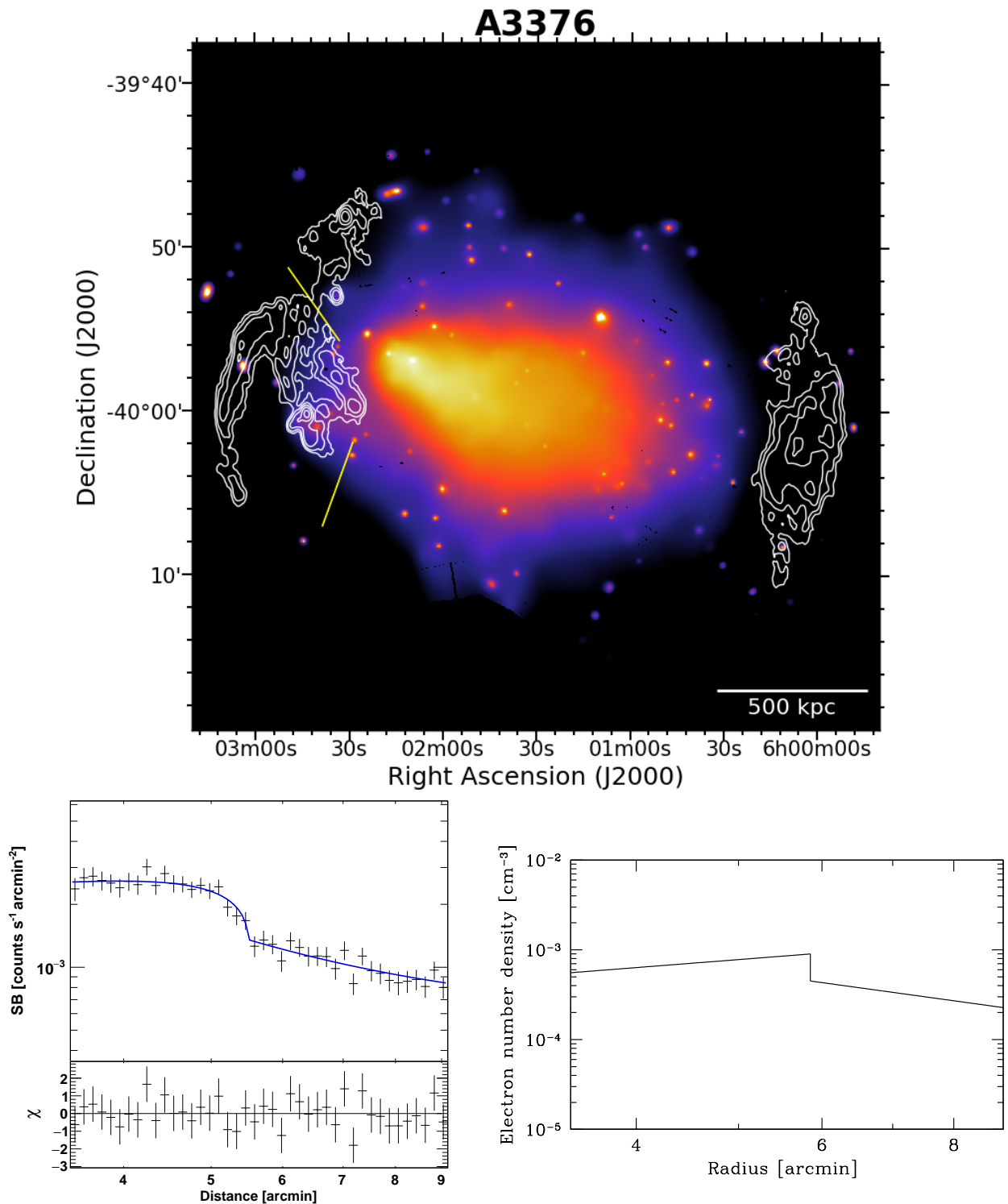


Figure 5.8: A3376. *Top:* *XMM-Newton* image with overlaid the VLA 1.4 GHz radio contours from Kale et al. (2012) and the yellow sector used for the analysis of the shock front. *Bottom:* X-ray SB profile (*left*) and density profile (*right*) across the E radio relic. We thank R. Kale for kindly providing us the displayed radio contours.

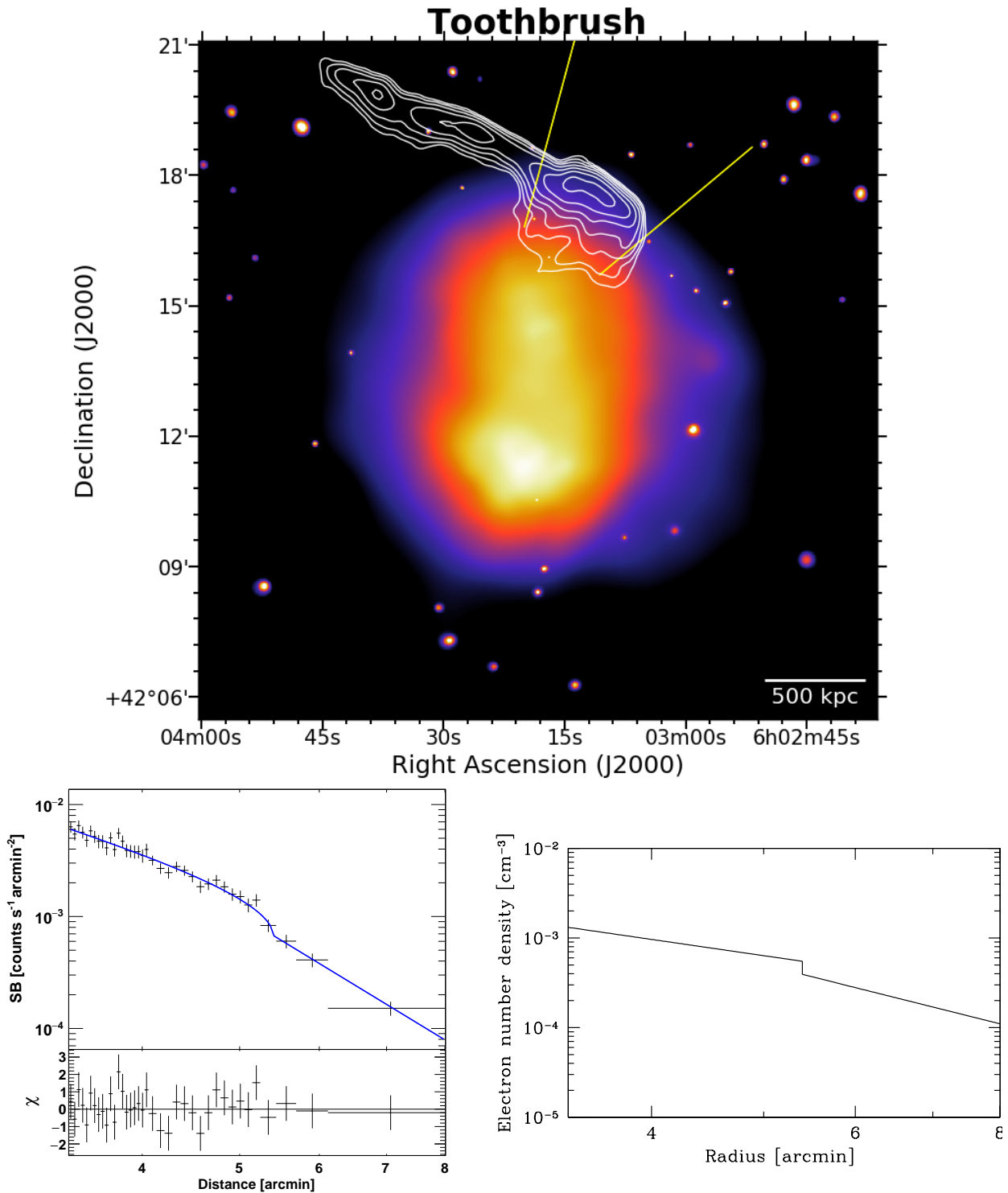


Figure 5.9: Toothbrush Cluster. *Top:* *Chandra* image with overlaid the GMRT 610 MHz radio contours from van Weeren et al. (2012b) and the yellow sector used for the analysis of the shock front. *Bottom:* X-ray SB profile (*left*) and density profile (*right*) across the radio relic. We thank R. van Weeren for kindly providing us the displayed radio contours.

$B \gtrsim 1.5 \mu\text{G}$ to achieve $\eta_e \lesssim 0.1$ and somewhat high values of $B \gtrsim 5.6 \mu\text{G}$ to achieve $\eta_e \lesssim 0.01$. Nevertheless, the discrepancy between $\mathcal{M}_{\text{DSA}} \sim 3.9$ and $\mathcal{M}_X \sim 1.3$ is surprisingly large.

Bullet Cluster. It is the first object where a shock front was discovered by *Chandra* (Markevitch et al. 2002). This prominent bow shock to the W is generated by an infalling sub-system that acts as a “bullet” in the ICM, giving the nickname to the cluster. A powerful radio halo is bounded by the W shock (Liang et al. 2000; Shimwell et al. 2014). More recently, also a counter-shock co-spatially located with a radio relic in the E (Fig. 5.10) has been detected (Shimwell et al. 2015).

We obtained consistent values with Shimwell et al. (2015) for the Mach number of the E shock in the Bullet Cluster. This is the third case where the measured shock strength and integrated spectral index are consistent with the DSA expectations (Fig. 5.3). Although DSA is not tension with the observed properties of the relic/shock, our calculations in Fig. 5.14 show that the acceleration efficiency requested to match the bolometric radio luminosity of the relic is too large. Indeed, Shimwell et al. (2015) suggested that shock re-acceleration is in act in the Bullet Cluster due to the connection of the relic with a bright “bulb” region that may be a remnant of a radio galaxy supplying seed electrons.

RXC J1314.4-2515. It is an X-ray luminous cluster which hosts a small radio halo at its center and two Mpc-size relics in the outskirts, one to the E and one to the W (Feretti et al. 2005; Venturi et al. 2007, 2013). Mazzotta et al. (2011) detected a shock front with an M-like shape at the edge of the W relic (Fig. 5.11).

We analyzed the “nose” of the M-shock and obtained SB and density profiles consistent with those reported by Mazzotta et al. (2011). Also in this case, only the upper bound of the Mach number measured from X-rays allows a viable solution in terms of acceleration efficiency (Fig. 5.14). Similarly to A2744, $\eta_e \lesssim 0.1$ for magnetic field strengths $B \gtrsim 5.9 \mu\text{G}$, which are likely too high for cluster outskirts, and $\eta_e \lesssim 0.01$ is achieved for $B \gg 20 \mu\text{G}$. These energy problems are significantly alleviated if we assume the higher Mach number implied by DSA from the integrated spectral index.

A2146. This is a low-mass system (cf. Tab. 5.1) where two shocks in diametrically opposite directions have been detected (Russell et al. 2010, 2012). In the past, this cluster was dubbed a “merger mystery” as no diffuse radio emission was found in the ICM (Russell et al. 2011). However, recent sensitive observation performed with the JVLA (Hlavacek-Larrondo et al. 2018) and LOFAR (Hoang et al. 2018c) made possible the detection of a radio relic at the position of the NW shock (Fig. 5.12) and of a diffuse emission bounded by the SE bow shock that has been classified as a radio halo.

Our SB profile across the NW relic well recovers the discontinuity of the underlying weak shock. The density jump and profile are consistent with those reported by Russell et al. (2010, 2012). For such a low Mach number, a model for the radio relic based on DSA of thermal electrons is ruled out as it would require $p_{\text{min}} < p_{\text{th}}$ (Fig. 5.14). Conversely, if we assume the Mach number implied by DSA theory from the integrated spectrum, it is possible to match the observed radio luminosity of the relic with reliable efficiencies (Fig. 5.14). As for the Toothbrush case, we underline the substantial discrepancy between $\mathcal{M}_X \sim 1.5$ and $\mathcal{M}_{\text{DSA}} \sim 3.9$.

Sausage Cluster. The N radio relic with an extremely regular morphology discovered in this cluster (and from which derives its nickname) is nowadays iconic for this class of sources (van Weeren et al. 2010). It has a linear extension of ~ 2 Mpc over its largest projected size, and a transversal width at 610 MHz of ~ 55 kpc only (Fig. 5.13). Another smaller and more irregular relic is located in the diametrically opposite direction of the Sausage, likely generated during a

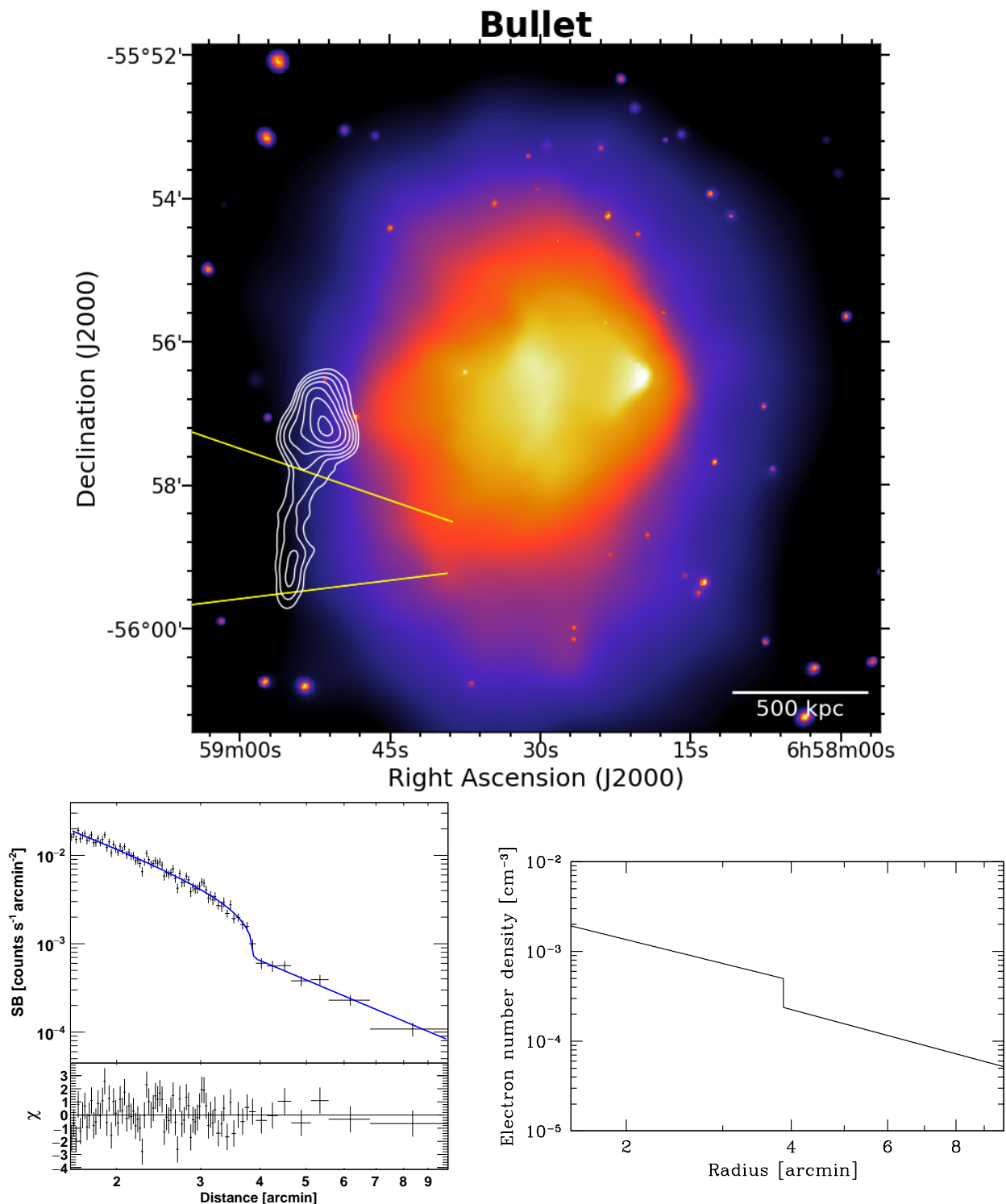


Figure 5.10: Bullet Cluster. *Top:* *Chandra* image with overlaid the ATCA 2.1 GHz radio contours from Shimwell et al. (2015) and the yellow sector used for the analysis of the shock front. *Bottom:* X-ray SB profile (*left*) and density profile (*right*) across the radio relic. We thank T. Shimwell for kindly providing us the displayed radio contours.

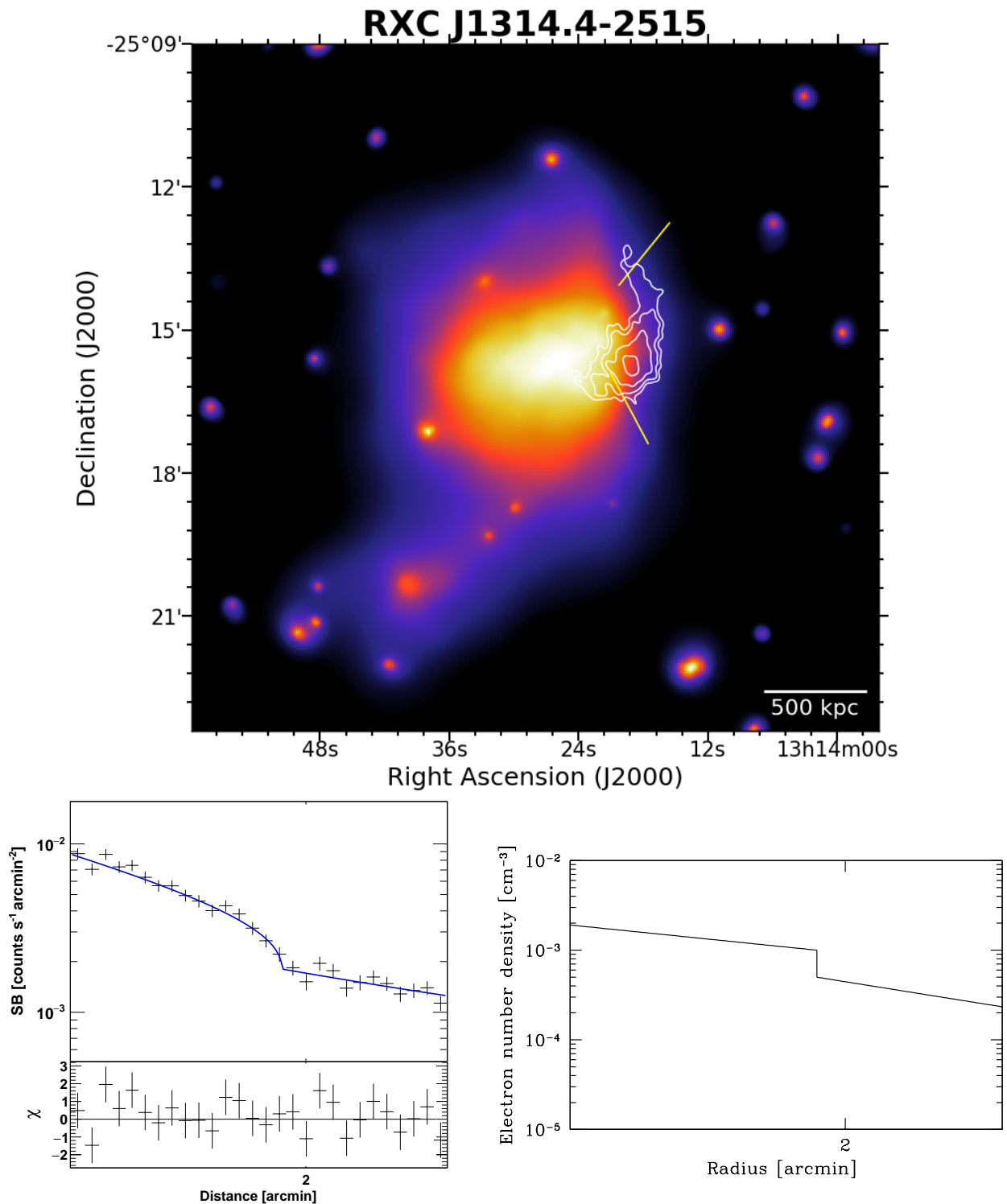


Figure 5.11: RXCJ 1314.4-2515. *Top:* XMM-Newton image with overlaid the GMRT 325 MHz radio contours from Venturi et al. (2013) and the yellow sector used for the analysis of the shock front. *Bottom:* X-ray SB profile (*left*) and density profile (*right*) across the radio relic. We thank T. Venturi for kindly providing us the displayed radio contours.

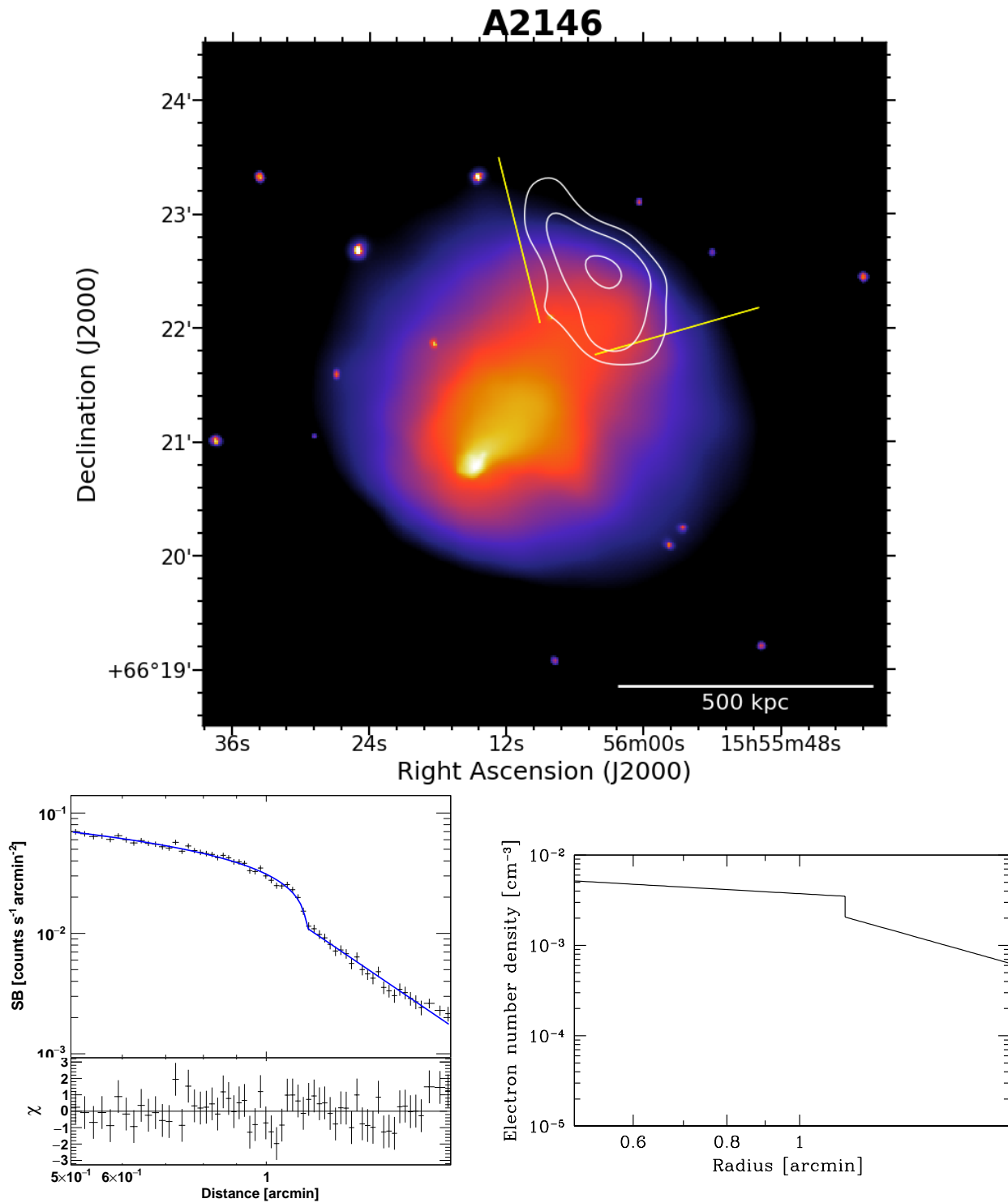


Figure 5.12: A2146. *Top:* *Chandra* image with overlaid the JVLA 1.5 GHz radio contours from Hoang et al. (2018c) and the yellow sector used for the analysis of the shock front. *Bottom:* X-ray SB profile (*left*) and density profile (*right*) across the radio relic. We thank D. Hoang for kindly providing us the displayed radio contours.

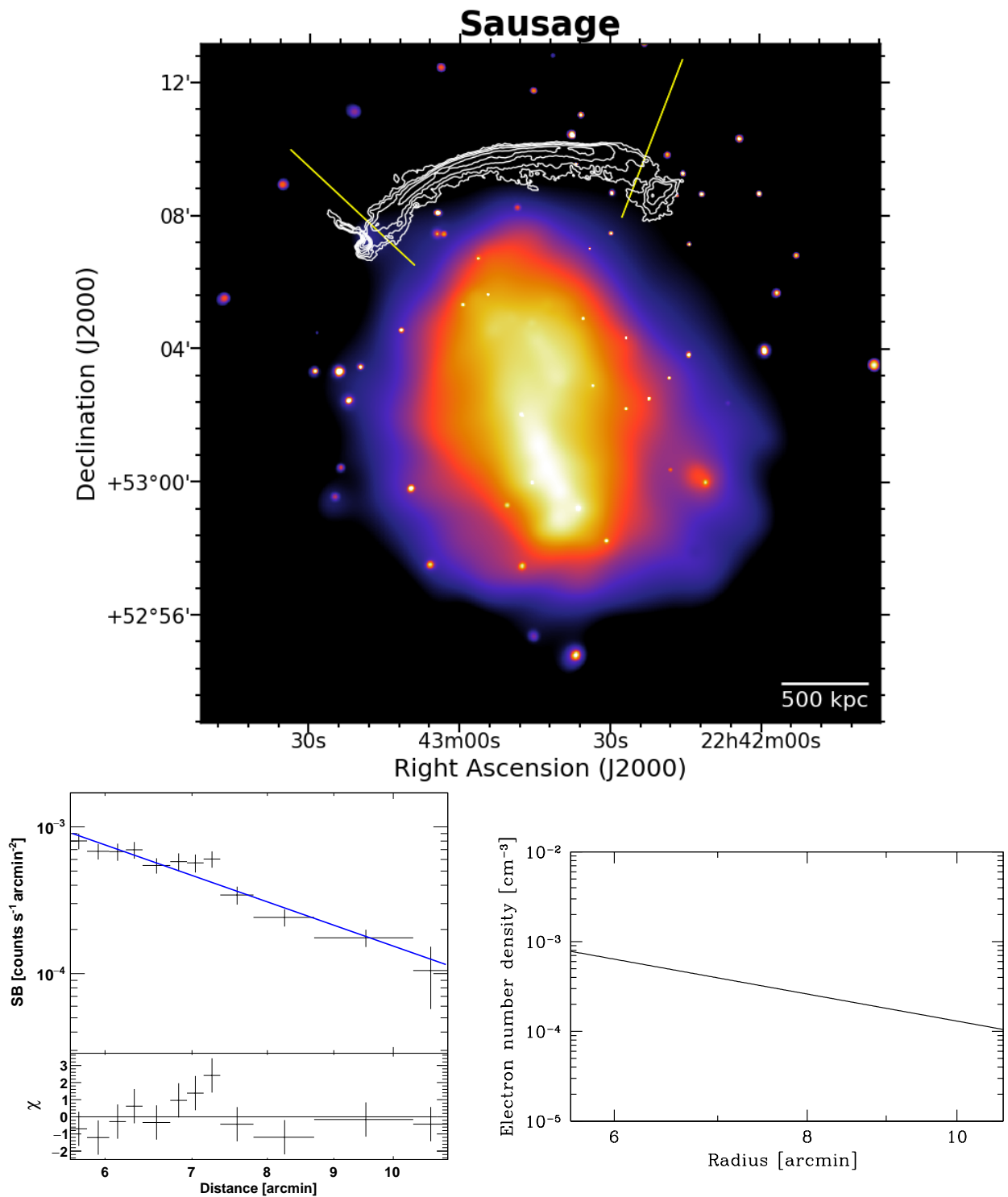


Figure 5.13: Sausage Cluster. *Top:* *Chandra* image with overlaid the GMRT 610 MHz radio contours from van Weeren et al. (2010) and the yellow sector used for the analysis of the shock front (not found). *Bottom:* X-ray SB profile (*left*) and density profile (*right*) across the radio relic. We thank R. van Weeren for kindly providing us the displayed radio contours.

head-on merger (van Weeren et al. 2011a; Donnert et al. 2017). Both radio analysis and numerical simulations suggest that a strong shock should be located at the position of the Sausage. Although *Suzaku* observations provided evidence for a large temperature jump across this relic (Akamatsu & Kawahara 2013; Akamatsu et al. 2015), observations at higher resolution with *Chandra* and *XMM-Newton* failed to detect the SB jump implied by *Suzaku* spectral analysis (Ogreaan et al. 2013a, 2014). In addition, a shock across the S relic in the Sausage cluster has been claimed by Akamatsu et al. (2015) with *Suzaku* data. However, we did not include this relic in our analysis because the shock lays at the border of the FoV of both the *Chandra* and *XMM-Newton* observations available, preventing us to perform a proper SB analysis.

In the literature, no SB discontinuity has been detected across the Sausage relic in the X-rays (Ogreaan et al. 2013a, 2014). Indeed, this is the only case where we used a single power-law model to fit the SB profile extracted with *Chandra*. The possibility of an edge is discussed in Appendix A. For the acceleration efficiency analysis (Fig. 5.14), we used the density measured at the location of the relic from the single power-law model and assumed different Mach numbers. We found that acceleration efficiencies $\eta_e \lesssim 0.1$ with reasonable magnetic field strengths are required for $\mathcal{M} \gtrsim 2.5$. In particular, if we consider the case of $\mathcal{M} = 3$, which is in agreement with the temperature jump measured with *Suzaku* (Akamatsu et al. 2015), a realistic value of $\eta_e \sim 0.01$ would match the observed radio luminosity of the relic under the assumption of a magnetic field $B \sim 2.7 \mu\text{G}$ (Fig. 5.14). The case is thus interesting but enigmatic: on the one hand there is the claim based on *Suzaku* data of a shock with Mach number sufficiently high to explain the Sausage via DSA (even though the integrated spectral index of the relic would require a higher Mach number assuming DSA), on the other hand a density drop of a factor of 3 has not observed yet in the *Chandra* and *XMM-Newton* SB profiles. Future deep *Chandra* observations (PI: M. Markevitch) are planned and may resolve this puzzle.

5.6 Discussion

In order to summarize the results reported in Fig 5.14, in Fig. 5.15 we computed the acceleration efficiency that is requested to match the observed radio luminosity of the 10 radio relics in the sample as a function of the shock Mach number (measured in the X-rays or derived under DSA assumption) at fixed downstream magnetic field of $B = 5 \mu\text{G}$; smaller magnetic fields will increase the requested value of η_e . For the Sausage relic, where no SB is observed in the X-rays, we assumed $\mathcal{M}_X = 2.5$ and $\mathcal{M}_X = 3$. Points are calculated using the upper bounds on \mathcal{M} and, for this reason, results are presented as lower limits in Fig. 5.15.

Assuming the Mach number measured in the X-rays, the only relics whose bolometric radio luminosity can be reproduced with efficiencies $\eta_e < 0.1$ are those in El Gordo and A521 (which are among the few cases where \mathcal{M}_X and \mathcal{M}_{DSA} are consistent). For these two relics the (lower limit to the) acceleration efficiency is actually $\eta_e < 0.01$. We mention that for A521 the upper bound on \mathcal{M}_X is not consistent with the lower, and well constrained, Mach number predicted by DSA. Nonetheless, if we take into account the highest Mach number allowed by both X-ray observation and DSA theory, the luminosity of the relic in A521 for $B = 5 \mu\text{G}$ can still be reproduced with $\eta_e < 0.1$ (Fig. 5.15). Therefore, we conclude that DSA of thermal electrons can not be readily ruled out in these two relics if $\eta_e < 0.1$. With a more realistic value of $\eta_e < 0.01$, DSA from the thermal pool appears to be energetically viable only for El Gordo. In all the other cases the luminosity of the relics can not be explained using DSA of thermal electrons adopting the Mach number measured from the X-rays.

On the other hand, if we assume the higher Mach number implied by DSA from the relic integrated spectral index, models of DSA from the thermal pool would require efficiencies that in many

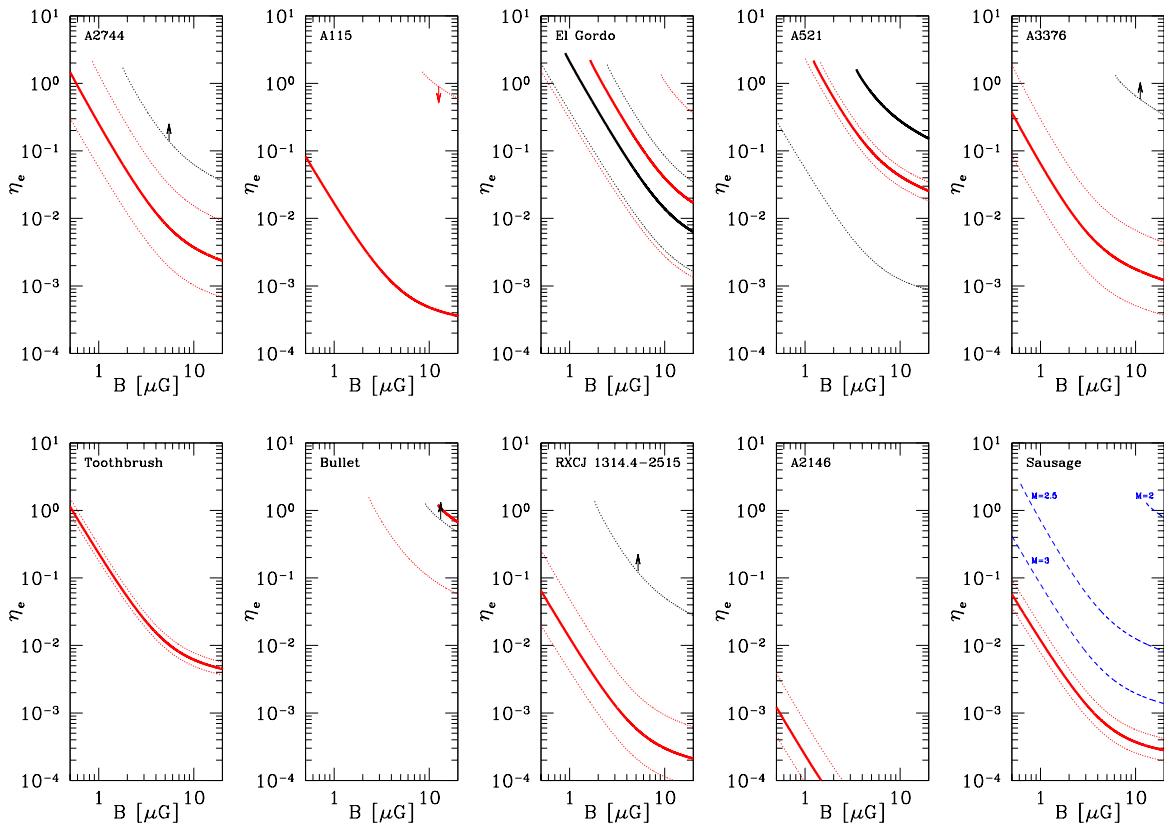


Figure 5.14: Electron acceleration efficiency for the radio relics of the sample versus magnetic field in the downstream region. Calculations were performed using the Mach numbers listed in Tab. 5.3 measured in the X-rays (*black*) and derived from the integrated spectral index in the case of DSA (*red*). Lines denote the best fit Mach number (*solid*) and its upper and lower bounds (*dotted*). For the Sausage relic, lines in *blue dashed* represent assumed Mach numbers of $\mathcal{M} = 2, 2.5, 3$ (from *top to bottom*).

cases are $\eta_e \ll 0.1$. By adopting these models we would match both the observed luminosity and spectrum of the relics. However, we should admit that the Mach number measured in the X-rays is not representative of the real Mach number of the shock. Numerical simulations suggest that a combination of multiple shock surfaces and projection effects could smear the observed X-ray Mach numbers (Skillman et al. 2013; Hong et al. 2015), leading to the observed discrepancy between the Mach numbers measured in the X-rays and those derived under DSA assumptions (Fig. 5.3). In this case, however, we note that the radio-inferred Mach number would trace only a small fraction of the shock surface whereas the X-ray Mach number would be representative of the majority of the surface. As a consequence, in this case we should use a surface of the shock A in Eq. 5.1 which is much smaller than that estimated from the observed surface of the radio relics. This would result in acceleration efficiencies much larger than those calculated in Fig. 5.14 and 5.15. Therefore, also this model does not appear to explain the properties of the radio relics in our sample.

Another *ad hoc* possibility is given by a scenario of DSA from the thermal pool where the spectrum differs from the classical expectations based on the DSA theory (Eq. 1.37). In fact, the efficiencies calculated assuming the Mach number from the X-rays and the measured radio spectrum are similar to those calculated assuming the radio Mach number and spectrum (Fig. 5.16). We find that such a modified DSA model can explain the properties of the radio relics in our sample and their connection with the underlying shocks observed in the X-rays. The point here is to understand why clusters shocks, contrary to shocks in SNRs, produce a spectrum that is different from that implied by DSA. A possibility is to admit that the transport of electrons across the shock is not diffusive but,

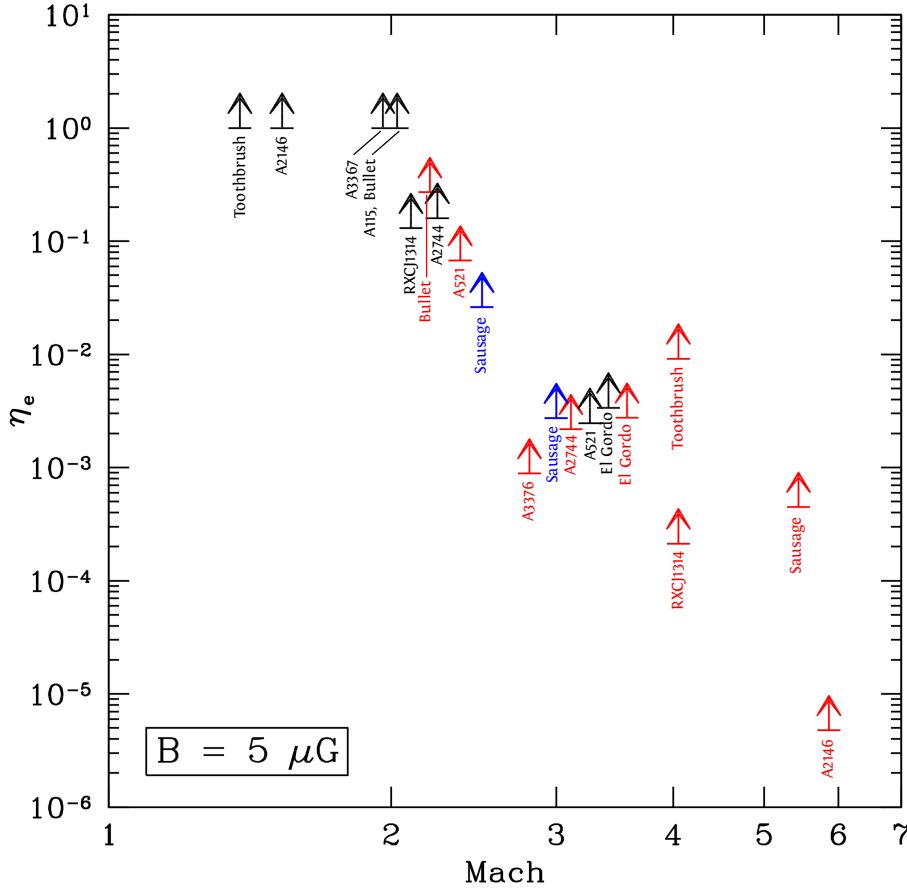


Figure 5.15: Electron acceleration efficiency versus the upper bound of \mathcal{M}_X (black) and \mathcal{M}_{DSA} (red) obtained for $B = 5 \mu\text{G}$. For the Sausage relic, we assumed $\mathcal{M}_X = 2.5$ and 3 (blue) as no shock is observed in SB (Fig. 5.13).

e.g., superdiffusive, as recently proposed by Zimbaro & Perri (2018). At this stage, however, this hypothesis is rather speculative.

In general, our results suggest that DSA of thermal electrons is not the mechanism responsible of radio relics. Re-acceleration of seeds supra-thermal or relativistic electrons is favored simply because, in this scenario, the requested efficiency is orders of magnitude smaller than the classical DSA of thermal electrons (e.g. Kang & Ryu 2011; Pinzke et al. 2013, and Brunetti & Jones 2014, for a review).

5.7 Conclusions

We selected a sample of radio relics with detected underlying shock and computed the electron acceleration efficiency versus magnetic field strength for 10 of them. We adopted a self-consistent framework which is based on the smallest number possible of observable quantities, namely the shock Mach number and surface, the downstream temperature and density, and the relic flux density.

In this Chapter, we demonstrated that the bolometric luminosity of radio relics can not be reproduced by DSA (even under optimistic assumptions of efficiency and magnetic field) due to the low Mach number of the underlying shocks observed in the X-rays. Instead, the high Mach number shocks derived from the relic integrated spectral indexes using DSA appear energetically viable. Nonetheless, one has to face the fact that the observed properties of the relic/shock are usually in

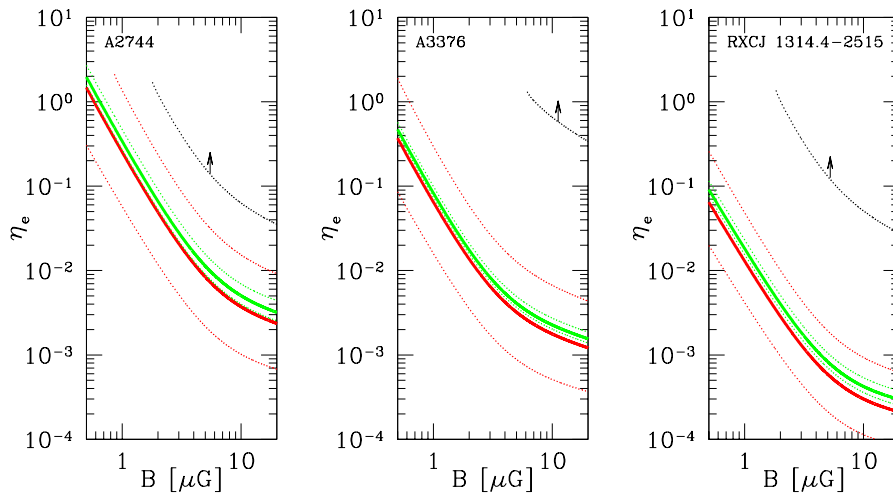


Figure 5.16: Same as Fig. 5.14 except the *green* lines that denote the case where the electron acceleration efficiency was computed adopting the Mach number measured in the X-rays (with its error bounds) and the central value of integrated spectral index measured in radio (cf. Tab. 5.3). For visualization purposes, we just reported the case of 3 radio relics.

contrast with those predicted by DSA theory. The commonly invoked way to reconcile X-rays and radio Mach numbers is to admit that the relic emission is mainly contributed by the fraction of the shock surface where the Mach number is higher and the acceleration more efficient. However, in the case of substantial differences between the two Mach numbers, this would mean that the shock kinetic energy is efficiently dissipated into particle acceleration only in a small fraction of the surface that is traced by the diameter of the radio relic, implying that the effective acceleration efficiency is much larger than that measured assuming a homogeneous relic/shock surface. We thus conclude that also this possibility is challenged by our study.

As anticipated in Chapter 3, the shock observed in the X-rays associated with the NW relic in El Gordo is consistent with the DSA predictions and the acceleration process appears also energetically viable. This is the only case where we found that DSA of thermal particles can not be firmly ruled out. The quite high lower limits on B inferred from the lack of IC emission from the relic further support the possibility of DSA. However, this is a very peculiar case as El Gordo hosts the radio relic with the strongest underlying shock detected so far. Our results indicate that for all the other radio relics in the sample, generally associated with $\mathcal{M} \lesssim 2$ shocks, other mechanisms, such as shock re-acceleration, are in act lowering the requirement of high acceleration efficiencies.

Shocks and cold fronts in merging and massive galaxy clusters: new detections with *Chandra*[†]

ABSTRACT

A number of merging galaxy clusters shows the presence of shocks and cold fronts, i.e. sharp discontinuities in SB and temperature (Section 1.3.2). The observation of these features requires an X-ray telescope with high spatial resolution like *Chandra*, and allows to study important aspects concerning the physics of the ICM, such as its thermal conduction and viscosity, as well as to provide information on the physical conditions leading to the acceleration of CRs and magnetic field amplification in the cluster environment. We searched for new discontinuities in 15 merging and massive clusters observed with *Chandra* by using different imaging and spectral techniques of X-ray observations. Our analysis led to the discovery of 22 edges: six shocks, eight cold fronts and eight with uncertain origin. All the six shocks detected have $\mathcal{M} < 2$ derived from density and temperature jumps. This work contributed to increase the number of discontinuities detected in clusters and shows the potential of combining diverse approaches aimed to identify edges in the ICM. A radio follow-up of the shocks discovered in this work will be useful to study the connection between weak shocks and radio relics.

6.1 Introduction

Currently, the number of detected edges in galaxy clusters is modest for observational limitations. This is reflected in the handful of merger shocks that have been confirmed using both X-ray imaging and spectral analysis. In this Chapter, we aim to search in an objective way for new merger induced shocks and cold fronts in massive and NCC galaxy clusters. The reason is to look for elusive features that can be followed-up in the radio band. To do that in practice we analyzed 15 clusters that were essentially selected because of the existence of adequate X-ray data available in the *Chandra* archive. The *Chandra* satellite is the the best instrument capable to resolve these sharp edges thanks to its excellent spatial resolution. We applied different techniques for spatial

[†]Based on Botteon et al. (2018a).

and spectral analysis including the application of an edge detection algorithm on the cluster images, the extraction and fitting of SB profiles, the spectral modeling of the X-ray (astrophysical and instrumental) background and the production of maps of the ICM thermodynamical quantities. This analysis is designed to properly characterize sharp edges distinguishing shocks from cold fronts.

6.2 Cluster sample

We selected a number of galaxy clusters where it is likely to detect merger-induced discontinuities searching for (i) massive systems in a dynamical disturbed state and (ii) with an adequate X-ray count statistics, based on current observations available in the *Chandra* archive. In particular the following.

1. Using the first *Planck* catalog of SZ sources (PSZ1; Planck Collaboration XXIX 2014) we selected clusters with mass $M_{500} > 5 \times 10^{14} M_{\odot}$, as inferred from the SZ signal. Searching for diffuse radio emission connected with shocks (radio relics and edges of radio halos) is a natural follow-up of our study, hence this high mass threshold has been set mainly because non-thermal emission is more easily detectable in massive merging systems (e.g. Cassano et al. 2013; de Gasperin et al. 2014; Cuciti et al. 2015). As a second step, we selected only dynamically active systems excluding all the CC clusters. In this respect, we used the Archive of *Chandra* Cluster Entropy Profile Tables (ACCEPT; Cavagnolo et al. 2009) and the recent compilation by Giacintucci et al. (2017) to look for the so-called core entropy value K_0 (see Eq. 4 in Cavagnolo et al. 2009), which is a good proxy to identify NCC systems (e.g. McCarthy et al. 2007): clusters with $K_0 < 30 - 50 \text{ keV cm}^2$ exhibit all the properties of a CC hence they were excluded in our analysis.
2. Detecting shocks and cold fronts requires adequate X-ray count statistics as in particular the latter discontinuities are found in cluster outskirts, where the X-ray brightness is faint. For this reason, among the systems found in the *Chandra* data archive¹ satisfying (i), we excluded clusters with $\lesssim 4 - 5 \times 10^4$ counts in the *Chandra* broad-band 0.5 – 7.0 keV with the exposure available at the time of writing. We did that by converting the ROSAT flux in the 0.1 – 2.4 keV band reported in the main X-ray galaxy cluster catalogs (BCS, Ebeling et al. 1998; eBCS, Ebeling et al. 2000; NORAS, Böhringer et al. 2000; REFLEX, Böhringer et al. 2004; MACS, Ebeling et al. 2007, 2010) into a *Chandra* count rate using the PIMMS software² and assuming a thermal emission model. Clusters without a reported ROSAT flux in the catalogs were individually checked by measuring the counts in a circle enclosing the cluster SB profile when it is below the level of the background and thus rejected adopting the same count threshold.

We ended up with 37 massive and NCC cluster candidates for our study (Tab. 6.1). In 22 of these systems (bottom of Tab. 6.1) shocks/cold fronts (or both) have been already discovered and consequently we focused on the analysis of the remaining 15 clusters (top of Tab. 6.1). We anticipate that the results on the detection of shocks and cold fronts in these clusters are summarized in Section 6.5.2.

¹<http://cda.harvard.edu/chaser/>

²<http://heasarc.gsfc.nasa.gov/Tools/w3pimms.html>

Table 6.1: The galaxy clusters analyzed in this work (*top*) and the ones that have been excluded as the presence of a shock/cold front (or both) has been already claimed (*bottom*). Reported values of M_{500} and K_0 are taken from Planck Collaboration XXIX (2014) and Cavagnolo et al. (2009), respectively. Redshifts are taken from the NASA/IPAC Extragalactic Database (NED).

Cluster name	RA _{J2000} (h,m,s)	DEC _{J2000} (°,′,″)	M_{500} ($10^{14} M_{\odot}$)	z	K_0 (keV cm ²)	Shock (ref.)	Cold front (ref.)
A2813	00 43 24	−20 37 17	9.16	0.292	268 ± 44
A370	02 39 50	−01 35 08	7.63	0.375	322 ± 91	...	$\bar{1}$
A399	02 57 56	+13 00 59	5.29	0.072	153 ± 19	...	1
A401	02 58 57	+13 34 46	6.84	0.074	167 ± 8	...	1
MACS J0417.5-1154	04 17 35	−11 54 34	11.7	0.440	27 ± 7	...	1
RXC J0528.9-3927	05 28 53	−39 28 18	7.31	0.284	73 ± 14	...	1
MACS J0553.4-3342	05 53 27	−33 42 53	9.39	0.407	...	1	1
AS592	06 38 46	−53 58 45	6.71	0.222	59 ± 14	1	...
A1413	11 55 19	+23 24 31	5.98	0.143	164 ± 8
A1689	13 11 29	−01 20 17	8.86	0.183	78 ± 8
A1914	14 26 02	+37 49 38	6.97	0.171	107 ± 18	1	1
A2104	15 40 07	−03 18 29	5.91	0.153	161 ± 42	1	...
A2218	16 35 52	+66 12 52	6.41	0.176	289 ± 20	1	...
Triangulum Australis	16 38 20	−64 30 59	7.91	0.051	$\bar{1}$
A3827	22 01 56	−59 56 58	5.93	0.098	165 ± 12
A2744	00 14 19	−30 23 22	9.56	0.308	438 ± 59	2	3
A115	00 55 60	+26 22 41	7.20	0.197	...	4	...
El Gordo	01 02 53	−49 15 19	8.80	0.870	...	5	...
3C438	01 55 52	+38 00 30	7.35	0.290	...	6	6
A520	04 54 19	+02 56 49	7.06	0.199	325 ± 29	7	...
A521	04 54 09	−10 14 19	6.90	0.253	260 ± 36	8	8
Toothbrush Cluster	06 03 13	+42 12 31	11.1	0.225	...	9,10	10
Bullet Cluster	06 58 31	−55 56 49	12.4	0.296	307 ± 19	11,12	11
MACS J0717.5+3745	07 17 31	+37 45 30	11.2	0.546	220 ± 96	...	13
A665	08 30 45	+65 52 55	8.23	0.182	135 ± 23	14	14
A3411	08 41 55	−17 29 05	6.48	0.169	270 ± 5	15	...
A754	09 09 08	−09 39 58	6.68	0.054	270 ± 24	16	17
MACS J1149.5+2223	11 49 35	+22 24 11	8.55	0.544	281 ± 39	...	18
Coma Cluster	12 59 49	+27 58 50	5.29	0.023	...	19,20	...
A1758	13 32 32	+50 30 37	7.99	0.279	231 ± 37	...	21
A2142	15 58 21	+27 13 37	8.81	0.091	68 ± 3	...	22
A2219	16 40 21	+46 42 21	11.0	0.226	412 ± 43	23	...
A2256	17 03 43	+78 43 03	6.34	0.058	350 ± 12	24	25
A2255	17 12 31	+64 05 33	5.18	0.081	529 ± 28	26	...
A2319	19 21 09	+43 57 30	8.59	0.056	270 ± 5	...	27
A3667	20 12 30	−56 49 55	5.77	0.056	160 ± 15	28,29	30
AC114	22 58 52	−34 46 55	7.78	0.312	200 ± 28	...	31

Notes. References: ¹this work (if a tilde is superimposed the edge nature is uncertain); ²Eckert et al. (2016a); ³Owers et al. (2011); ⁴Botteon et al. (2016a); ⁵Botteon et al. (2016c); ⁶Emery et al. (2017); ⁷Markevitch et al. (2005); ⁸Bourdin et al. (2013); ⁹Ogreaan et al. (2013b); ¹⁰van Weeren et al. (2016a); ¹¹Markevitch et al. (2002); ¹²Shimwell et al. (2015); ¹³van Weeren et al. (2017b); ¹⁴Dasadia et al. (2016); ¹⁵van Weeren et al. (2017a); ¹⁶Macario et al. (2011); ¹⁷Ghizzardi et al. (2010); ¹⁸Ogreaan et al. (2016); ¹⁹Akamatsu et al. (2013); ²⁰Ogreaan & Brüggén (2013); ²¹David & Kempner (2004); ²²Markevitch et al. (2000); ²³Canning et al. (2017); ²⁴Trasatti et al. (2015); ²⁵Sun et al. (2002); ²⁶Akamatsu et al. (2017a); ²⁷O’Hara et al. (2004); ²⁸Finoguenov et al. (2010); ²⁹Storm et al. (2018); ³⁰Vikhlinin et al. (2001b); ³¹De Filippis et al. (2004).

6.3 Methods and data analysis

To firmly claim the presence either of a shock or a cold front in the ICM, both imaging and spectral analysis are required. Our aim is to search for SB and temperature discontinuities in the most objective way as possible, without being too much biased by prior constraints due to guesses of the merger geometry or presence of features at other wavelengths (e.g. a radio relic). To do so, we did the following.

1. Applied an edge detection filter to pinpoint possible edges in the clusters that were also visually searched in the X-ray images for a comparison.
2. Selected the most clear features above three times the root mean square noise level of the filtered images following a coherent arc-shaped structure extending for > 100 kpc in length.
3. Investigated deeper the pre-selected edges with the extraction and fitting of SB profiles.
4. Performed the spectral analysis in dedicated regions to confirm the nature of the jumps.

In addition, we produced maps of the ICM thermodynamical quantities to help in the interpretation of the features found with the above-mentioned procedure.

In the following sections we describe into details the X-ray data analysis performed in this work.

6.3.1 X-ray data preparation

In Tab. 6.2 we report all the *Chandra* ACIS-I and ACIS-S observations of our cluster sample. Data were reprocessed with CIAO v4.9 and *Chandra* CALDB v4.7.3 starting from level=1 event file. Observation periods affected by soft proton flares were excluded using the `deflare` task after the inspection of the light curves extracted in the 0.5 – 7.0 keV band. For ACIS-I, these were extracted from the front-illuminated S2 chip that was kept on during the observation or in one front-illuminated ACIS-I chip, avoiding the cluster diffuse emission, if S2 was turned off. In ACIS-S observations the target is imaged in the back-illuminated S3 chip hence light curves were extracted in S1, also back-illuminated³.

Cluster images were created in the 0.5 – 2.0 keV band and combined with the corresponding monochromatic exposure maps (given the restricted energy range) in order to produce exposure-corrected images binned to have a pixel size of 0.984 arcsec. The datasets of clusters observed multiple times (11 out of 15) were merged with `merge_obs` before this step. The `mkpsfmap` script was used to create and match PSF map at 1.5 keV with the corresponding exposure map for every ObsID. For clusters with multiple ObsIDs we created a single exposure-corrected PSF map with minimum size. Thus, point sources were detected with the `wavdetect` task, confirmed by eye and excised in the further analysis.

6.3.2 Edge detection filter

In practice, the visual inspection of X-ray images allows to identify the candidate discontinuities (Markevitch & Vikhlinin 2007). We complement this approach with the visual inspection of filtered images. Sanders et al. (2016a) presented a Gaussian gradient magnitude (GGM) filter that aims to highlight the SB gradients in an image, similarly to the Sobel filter (but assuming Gaussian derivatives); in fact, it has been shown that these GGM images are particularly useful to identify candidate sharp edges, such as shocks and cold fronts (e.g. Walker et al. 2016). The choice of the

³In the ACIS-S ObsID 515 the light curve was extracted in S2 as S1 was turned off.

Table 6.2: Summary of the *Chandra* observations analyzed in this work. The net exposure time is after the flare filtering. The averaged values of N_{H_i} (Kalberla et al. 2005) and $N_{\text{H,tot}}$ (Willingale et al. 2013) measured in the direction of the clusters are also reported; these are compared in Fig. 6.1.

Cluster name	Observation ID	Detector (ACIS)	Exposure (ks)	Total exposure (net ks)	N_{H_i} 10^{20} cm^{-2}	$N_{\text{H,tot}}$ 10^{20} cm^{-2}
A2813	9409, 16278, 16366	I, I, S	20, 8, 37	114	1.83	1.93
	16491, 16513	S, S	37, 30			
A370	515 [†] , 7715	S*, I	90, 7	64	3.01	3.32
A399	3230	I	50	42	10.6	17.1
A401	518 [†] , 2309, 10416, 10417	I*, I*, I, I	18, 12, 5, 5	176	9.88	15.2
	10418, 10419, 14024	I, I, I	5, 5, 140			
MACS J0417.5-1154	3270, 11759, 12010	I, I, I	12, 54, 26	87	3.31	3.87
RXC J0528.9-3927	4994, 15177, 15658	I, I, I	25, 17, 73	96	2.12	2.26
MACS J0553.4-3342	5813, 12244	I, I	10, 75	77	3.32	3.79
AS592	9420, 15176	I, I	20, 20	98	6.07	8.30
	16572, 16598	I, I	46, 24			
A1413	537, 1661, 5002	I, I, I	10, 10, 40	128	1.84	1.97
	5003, 7696	I, I	75, 5			
A1689	540, 1663, 5004	I*, I*, I	10, 10, 20	185	1.83	1.98
	6930, 7289, 7701	I, I, I	80, 80, 5			
A1914	542 [†] , 3593	I, I	10, 20	23	1.06	1.10
A2104	895	S*	50	48	8.37	14.5
A2218	553 [†] , 1454 [†]	I*, I*	7, 13	47	2.60	2.83
	1666, 7698	I, I	50, 5			
Triangulum Australis	17481	I	50	49	11.5	17.0
A3827	3290	S	50	45	2.65	2.96

Notes. ObsIDs marked with [†] were excluded in the spectral analysis as the focal plane temperature was warmer than the standard -119.7°C observations and there is not Charge Transfer Inefficiency correction available to apply to this data with subsequent uncertainties in the spectral analysis of these datasets. All the observations were taken in VFaint mode except the ones marked by * that were instead taken in FAINT mode.

Gaussian width σ in which the gradient is computed depends on the physical scale of interest, magnitude of the jump and data quality: edges become more easily visible with increasing jump size and count rate; this requires images filtered on multiple scales to best identify candidate discontinuities (e.g. Sanders et al. 2016a,b). In this respect, we applied the GGM filter adopting $\sigma = 1, 2, 4$, and 8 pixels (a pixel corresponds to 0.984 arcsec) to the exposure-corrected images of the clusters in our sample. We noticed that the use of small length filters (1 and 2 pixels) is generally ineffective in detecting discontinuities in cluster outskirts due to the low counts in these peripheral regions (see also Sanders et al. 2016a). Instead Gaussian widths of $\sigma = 4$ and 8 pixels better highlight the SB gradients without saturating too much the ICM emission (as it would result with the application of filters with scales $\sigma = 16$ and 32 pixels). For this reason, here we will report GGM filtered images with these two scales.

6.3.3 Surface brightness profiles

After looking at X-ray and GGM images, we extracted and fitted SB profiles of the candidate discontinuities on the 0.5 – 2.0 keV exposure-corrected images of the clusters using PROFFIT v1.4 (Eckert et al. 2011). A background image was produced by matching (with `reproject_event`) the background templates to the corresponding event files for every ObsID. This was normalized by counts in the 9.5 – 12.0 keV band and subtracted in the SB analysis. Corrections were typically within 10% except for the S3 chip in FAINT mode (ObsIDs 515 and 895) where the correction was $\sim 45\%$. For clusters observed multiple times, all the ObsIDs were used in the fits. In the profiles, data were grouped to reach a minimum S/N threshold per bin of 7.

6.3.4 Spectra

The scientific aim of our work requires a careful treatment of the background of X-ray spectra, as in particular shock fronts are typically observed in the cluster outskirts, where the source counts are low. We modeled the background by extracting spectra in source free regions at the edge of the FoV. This was not possible for ACIS-I observations of nearby objects and for clusters observed with ACIS-S as the ICM emission covers all the chip area. In this respect, we used observations within 3° to the target pointing (i.e. ObsID 15068 for A399 and A401, ObsID 3142 for A2104, ObsID 2365 for Triangulum Australis and ObsID 17881 for A3827) to model the components due to the CXB and to the Galactic local foreground. The former is due to the superposition of the unresolved emission from distant point sources and can be modeled as a power-law with photon index $\Gamma_{\text{cxb}} = 1.42$ (e.g. Lumb et al. 2002). The latter can be decomposed into two-temperature thermal emission components (Kuntz & Snowden 2000) due to the GH and the LHB emission, with temperature $kT_{\text{gh}} = 0.25$ keV and $kT_{\text{lhb}} = 0.14$ keV and solar metallicity. Galactic absorption for GH and CXB was taken into account using the averaged values measured in the direction of the clusters from the Leiden/Argentine/Bonn survey of Galactic H_I (Kalberla et al. 2005). However, it has to be noticed that the total hydrogen column density is formally $N_{\text{H,tot}} = N_{\text{H}_\text{I}} + 2N_{\text{H}_2}$, where N_{H_2} accounts for molecular hydrogen whose contribution seems to be negligible for low-density columns. In Tab. 6.2 we reported the values of N_{H_I} (Kalberla et al. 2005) and $N_{\text{H,tot}}$ (Willingale et al. 2013) in the direction of the clusters in our sample, while in Fig. 6.1 we compared them. In Appendix B we discuss the five clusters (A399, A401, AS592, A2104 and Triangulum Australis) that do not lay on the linear correlation of Fig. 6.1.

Additionally to the astrophysical CXB, GH and LHB emission, an instrumental NXB component due to the interaction of high-energy particles with the satellite and its electronics was considered. Overall, the background model we used can be summarized as

$$apec_{\text{lhb}} + phabs * (apec_{\text{gh}} + powerlaw_{\text{cxb}}) + bkg_{\text{nxb}} \quad (6.1)$$

where the bkg_{nxb} was modeled with

$$\begin{aligned} expdec + power + \sum gaussian, & \quad \text{for ACIS-I} \\ expdec + bknpower + \sum gaussian, & \quad \text{for ACIS-S} \end{aligned} \quad (6.2)$$

where a number of Gaussian fluorescence emission lines were superimposed onto the continua. For more details on the NXB modeling the reader is referred to Appendix C.

The ICM emission was described with a thermal model taking into account the Galactic absorption in the direction of the clusters (cf. Tab. 6.2 and Appendix B)

$$phabs * apec_{\text{icm}}, \quad (6.3)$$

the metallicity of the ICM was set to $0.3 Z_\odot$ (e.g. Werner et al. 2013).

Spectra were simultaneously fitted (using all the ObsIDs available for each cluster, unless stated otherwise) in the 0.5 – 11.0 keV energy band for ACIS-I and in the 0.7 – 10.0 keV band for ACIS-S, using the package XSPEC v12.9.0o with Anders & Grevesse (1989) abundances table. Since the counts in cluster outskirts are poor, Cash statistics (Cash 1979) was adopted.

Contour binning maps

We used CONTBIN v1.4 (Sanders 2006) to produce projected maps of temperature, pressure and entropy for all the clusters of our sample. The clusters were divided into regions varying the

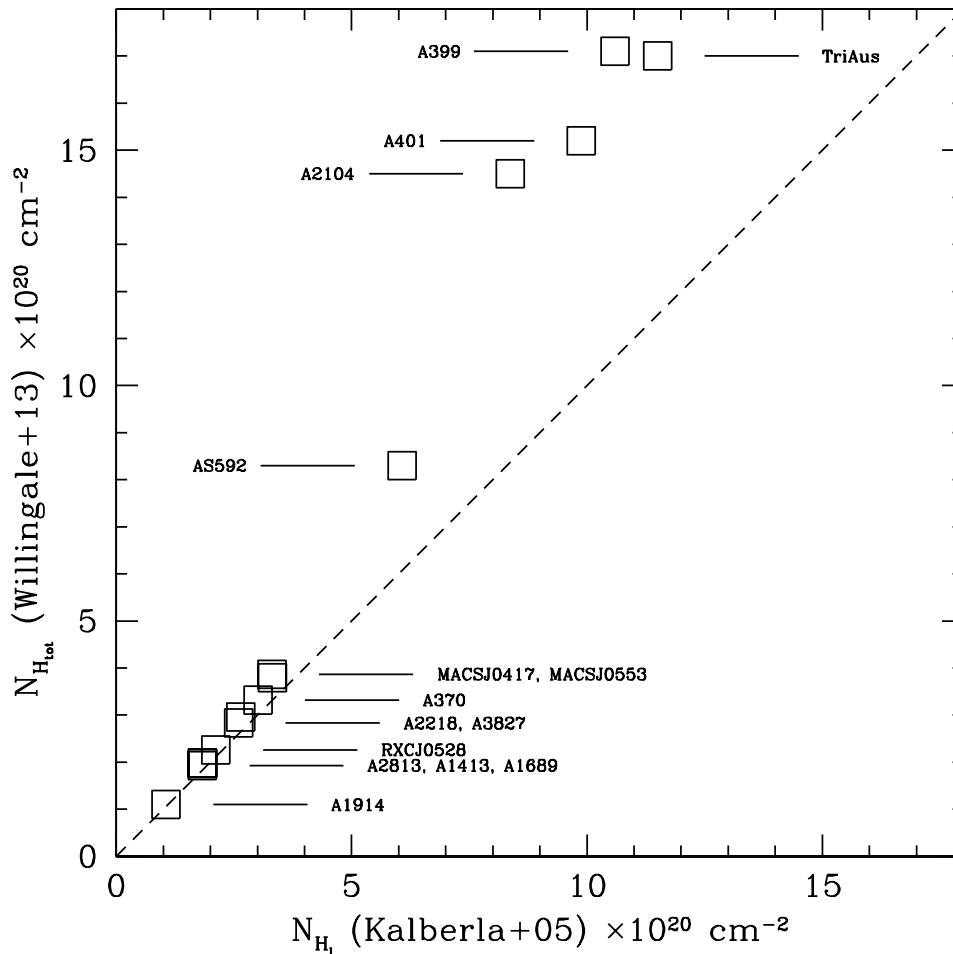


Figure 6.1: Comparison between the H_I density column from Kalberla et al. (2005) and the total (H_I+H_2) density column from Willingale et al. (2013). The *dashed line* indicates the linear correlation as a reference.

geometric constraint value (see Sanders 2006, for details) according to the morphology of each individual object to better follow the SB contour of the ICM. We required ~ 2500 background-subtracted counts per bin in the 0.5 – 2.0 keV band. Spectra were extracted and fitted as described in the previous section.

While the temperature is a direct result of the spectral fitting, pressure and entropy require the passage through the normalization value of the thermal model, i.e.

$$\mathcal{N} = \frac{10^{-14}}{4\pi[D_A(1+z)]^2} \int n_e n_H dV \quad [\text{cm}^{-5}] \quad (6.4)$$

where D_A is the angular diameter distance to the source (cm) whereas n_e and n_H are the electron and hydrogen density (cm^{-3}), respectively. The projected emission measure is

$$\text{EM} = \mathcal{N}/A \quad [\text{cm}^{-5} \text{arcsec}^{-2}] \quad (6.5)$$

with A the area of each bin, and it is proportional to the square of the electron density integrated along the line of sight. Using Eq. 6.5 we can compute the pseudo-pressure

$$P = kT(\text{EM})^{1/2} \quad [\text{keV cm}^{-5/2} \text{arcsec}^{-1}] \quad (6.6)$$

and pseudo-entropy

$$K = kT(\text{EM})^{-1/3} \quad [\text{keV cm}^{5/3} \text{ arcsec}^{-2/3}] \quad (6.7)$$

values for each spectral bin. The prefix pseudo- underlines that these quantities are projected along the line of sight (e.g. Mazzotta et al. 2004).

6.4 Characterization of the edges

The inspection of the cluster X-ray and GGM filtered images provides the first indication of putative discontinuities in the ICM. These need to be characterized with standard imaging and spectral analysis techniques to be firmly claimed as edges.

The SB profiles of the candidate shocks and cold fronts were modeled assuming that the underlying density profile follows a broken power-law (e.g. Markevitch & Vikhlinin 2007, and references therein). In the case of spherical symmetry, this density profile is described by Eq. 1.21. In the fitting procedure, all the parameters were free to vary. We stress that the values of \mathcal{C} reported throughout the Chapter have been deprojected along the line of sight under the spherical assumption by PROFIT (Eckert et al. 2011).

A careful choice of the sector where the SB profile is extracted is needed to properly describe a sharp edge due to a shock or a cold front. In this respect, the GGM filtered images help in determining that region. During the analysis, we adopted different apertures, radial ranges and positions for the extracting sectors, then we used the ones that maximize the jump with the best-fitting statistics. Errors reported for \mathcal{C} however do not account for the systematics due to the sector choice.

Spectral fitting is necessary to discriminate the nature of a discontinuity as the temperature ratio $\mathcal{R} \equiv T_d/T_u$ is > 1 in the case of a shock and < 1 in the case of a cold front (e.g. Markevitch et al. 2002). The temperature map can already provide indication about the sign of the jump. However, once that the edge position is well identified by the SB profile analysis, we can use a sector with the same aperture and center of that maximizing the SB jump to extract spectra in dedicated sectors covering the downstream and upstream regions. In this way we can carry out a self-consistent analysis and avoid possible contamination due to large spectral bins that might contain plasma at different temperatures and unrelated to the shock/cold front.

In the case of a shock, the Mach number \mathcal{M} can be determined by using the Rankine-Hugoniot jump conditions (e.g. Landau & Lifshitz 1959) for the density (Eq. 1.18) and temperature (Eq. 1.17).

6.5 Results

We find 29 arc-shaped features three times above the root mean square noise level in the GGM filtered images, 22 of them were found to trace edges in the SB profiles. In Fig. 6.2–6.12 and 6.15–6.18 we show a *Chandra* image in the 0.5 – 2.0 keV energy band, the products of the GGM filters, the maps of the ICM thermodynamical quantities and the SB profiles for each cluster of the sample. The c-stat/d.o.f. and the temperature fractional error for each spectral region are reported in Appendix D. The edges are highlighted in the *Chandra* images in white for shocks and in green for cold fronts. Discontinuities reported in yellow are those where the spectral analysis was not conclusive. The temperature values obtained by fitting spectra in dedicated upstream and downstream regions are reported in shaded boxes (whose lengths cover the radial extent of the spectral region) in the panels showing the SB profiles. If the jump was detected also in temperature, the box is colored in red for the hot gas and in blue for the cold gas; conversely, if the upstream and downstream temperatures are consistent (within 1σ), the box is displayed in yellow. As a general approach, in the case of weak discontinuities we also compare results with the best fit obtained with a single

power-law model.

In the following we discuss the individual cases. In particular, in Sections 6.5.1 and 6.5.3 we report the clusters with and without detected edges, respectively. The results of our detections are summarized in Section 6.5.2 and in Tab. 6.3. In Appendix E we show the seven arc-like features selected by the GGM filtered images that do not present a discontinuity in the SB profile fitting.

6.5.1 Detections

A370. This represents the most distant object in Abell catalog (Abell et al. 1989), at a redshift of $z = 0.375$. It is famous to be one of the first galaxy clusters where a gravitational lens was observed (Soucail et al. 1987; Kneib et al. 1993). The X-ray emission is elongated in the N-S direction (Fig. 6.2a); the bright source to the north is a nearby ($z = 0.044$) elliptical galaxy not associated with the cluster.

A370 was observed twice with *Chandra*. The longer observation (ObsID 515) was performed in an early epoch after *Chandra* launch in which an accurate modeling of the ACIS background is not possible, making the spectral analysis of this dataset unfeasible (see notes in Tab. 6.2 for more details). The other observation of A370 (ObsID 7715) is instead very short. For this reason, we did only a spatial analysis for this target.

The GGM images in Fig. 6.2b,c suggest the presence of a sharp SB variation both in the W and E direction. The SB profiles taken across these directions were precisely modeled in our fits in Fig. 6.2d,e, revealing jumps with similar entity ($\mathcal{C} \sim 1.5$). Their origin is unknown given that it was not possible to perform a spectral analysis in this cluster. An additional SB gradient suggested by the GGM images toward the S direction did not reveal the presence of an edge with the SB profile fitting (Fig. E.1).

A399 and A401. These two objects constitute a close system ($z = 0.072$ and $z = 0.074$, respectively) of two interacting galaxy clusters (e.g. Fujita et al. 1996). Their X-ray morphology is disturbed (Fig. 6.3a and 6.4a) and the ICM temperature distribution irregular (Bourdin & Mazzotta 2008), revealing the unrelaxed state of the clusters. Recently, Akamatsu et al. (2017b) claimed the presence of an accretion shock between the two using *Suzaku* data. This cluster pair hosts two radio halos (Murgia et al. 2010). The boundary of the halo in A399 is coincident with an X-ray edge, as already suggested by *XMM-Newton* observations (Sakelliou & Ponman 2004).

Only one *Chandra* observation is available for A399, whereas several observations were performed on A401. Despite this, we only used ObsID 14024 (which constitutes the 74% of the total observing time) to produce the maps shown in Fig. 6.4d,e,f as the remainder ObsIDs are snapshots that cover the cluster emission only partially. This is also the only case where we required ~ 5000 counts in each spectral bin given the combination of high brightness and long exposure on A401. The temperature maps in Fig. 6.3d and 6.4d indicate an overall hot ICM and the presence of some hot sub-structures, in agreement with earlier studies (Sakelliou & Ponman 2004; Bourdin & Mazzotta 2008).

The GGM images of A399 reveal a SB gradient toward the SE direction. The SB profile across this region and its temperature jump reported in Fig. 6.3g show that this “inner” edge is a cold front with $\mathcal{R} = 0.74_{-0.12}^{+0.14}$ and $\mathcal{C} = 1.72_{-0.12}^{+0.13}$. Ahead of that, the X-ray SB rapidly fades away, as well as the radio emission of the halo (Murgia et al. 2010). The “outer” SB profile in this direction indeed shows another discontinuity with $\mathcal{C} = 1.45_{-0.10}^{+0.10}$ (Fig. 6.3h). The broken power-law model provides a better description of the data ($\chi^2/\text{d.o.f.} = 68.6/72$) compared to a single power-law fit ($\chi^2/\text{d.o.f.} = 122.6/74$), corresponding to a null-hypothesis probability of 8×10^{-10} (6.1σ level) with the F-test. In this case, however, the temperatures across the edge are consistent, not allowing

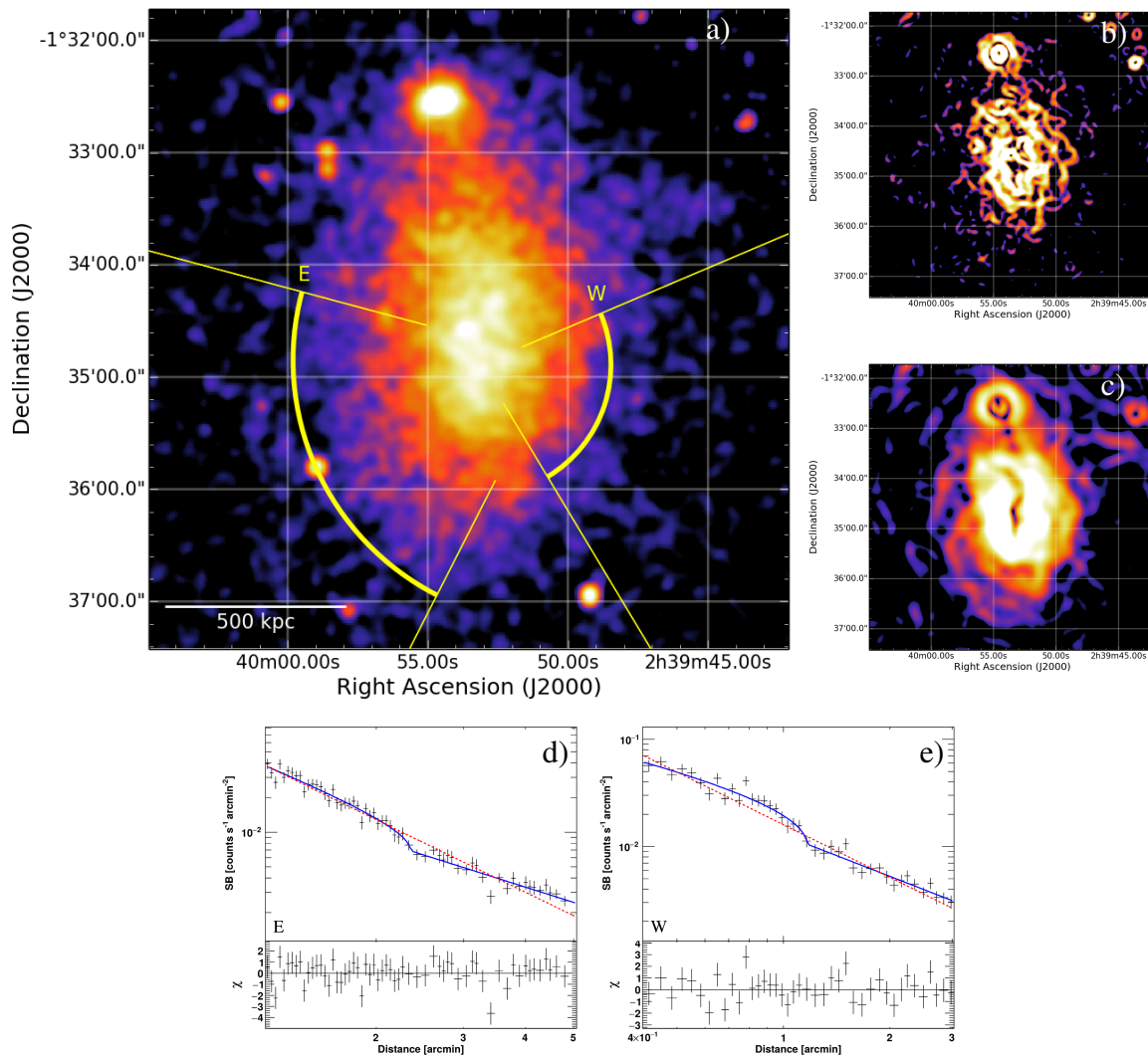


Figure 6.2: A370. *Chandra* 0.5 – 2.0 keV image (a), GGM filtered images on scales of 4 (b) and 8 (c) pixels and best-fitting broken power-law (solid blue) and single power-law (dashed red) models (residuals on the bottom are referred to the former) of the extracted SB profiles (d,e). The sectors where the SB profiles were fitted and the positions of the relative edges are marked in the *Chandra* image in yellow.

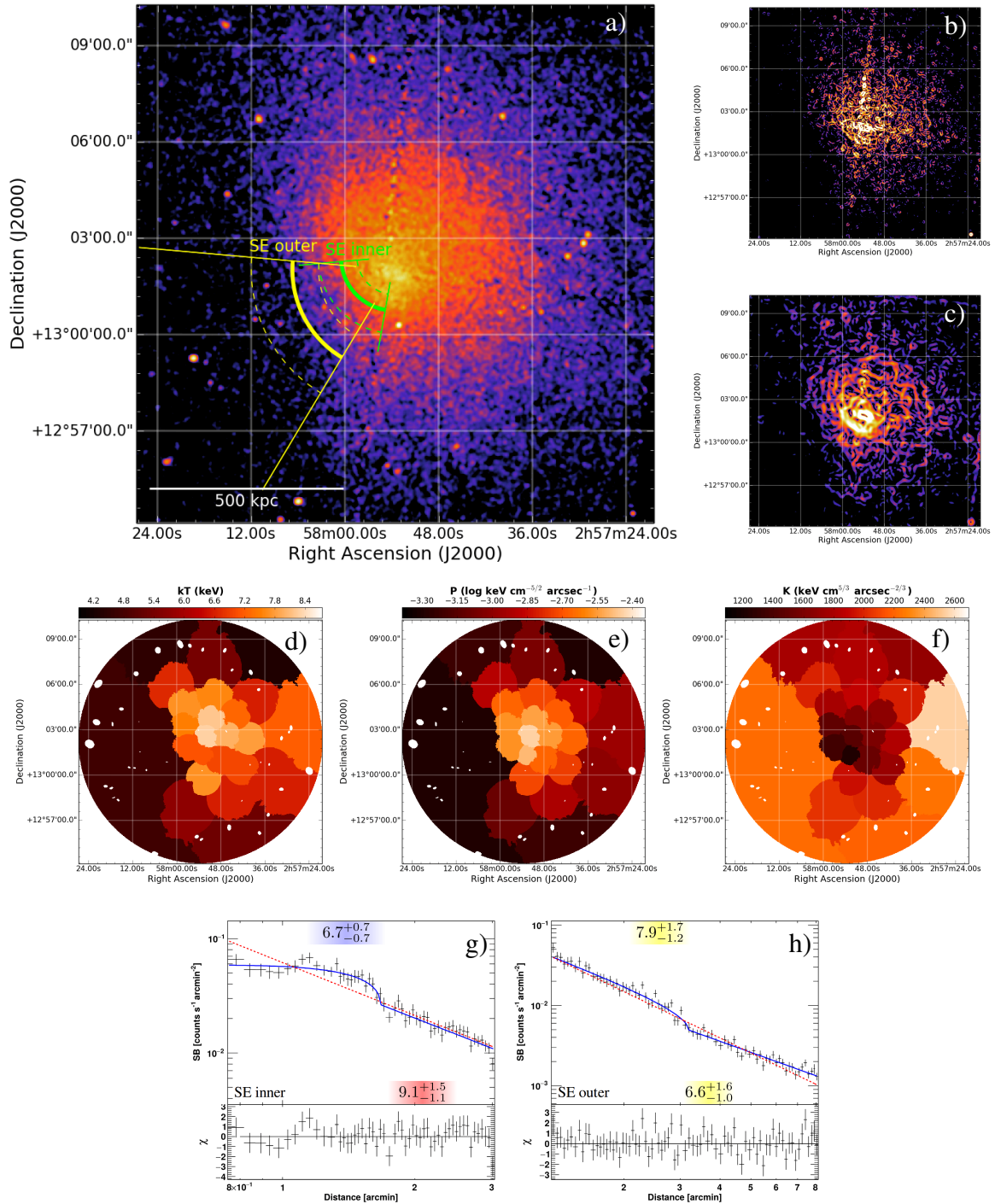


Figure 6.3: A399. *Chandra* 0.5 – 2.0 keV image (a), GGM filtered images on scales of 4 (b) and 8 (c) pixels, projected maps of temperature (d), pressure (e), entropy (f) and best-fitting broken power-law (solid blue) and single power-law (dashed red) models (residuals on the bottom are referred to the former) of the extracted SB profiles (g,h). The statistical precision of the fits is reported in Fig. D.1. The sectors where the SB profiles were fitted and the positions of the relative edges are marked in the *Chandra* image in green (cold front) and yellow. The dashed arcs show the radial limits used for measuring the temperature downstream and upstream the front, which values (in keV) are reported in the shaded boxes in the SB profiles. Note that in the GGM filtered images the straight and perpendicular features are artifacts due to chip gaps.

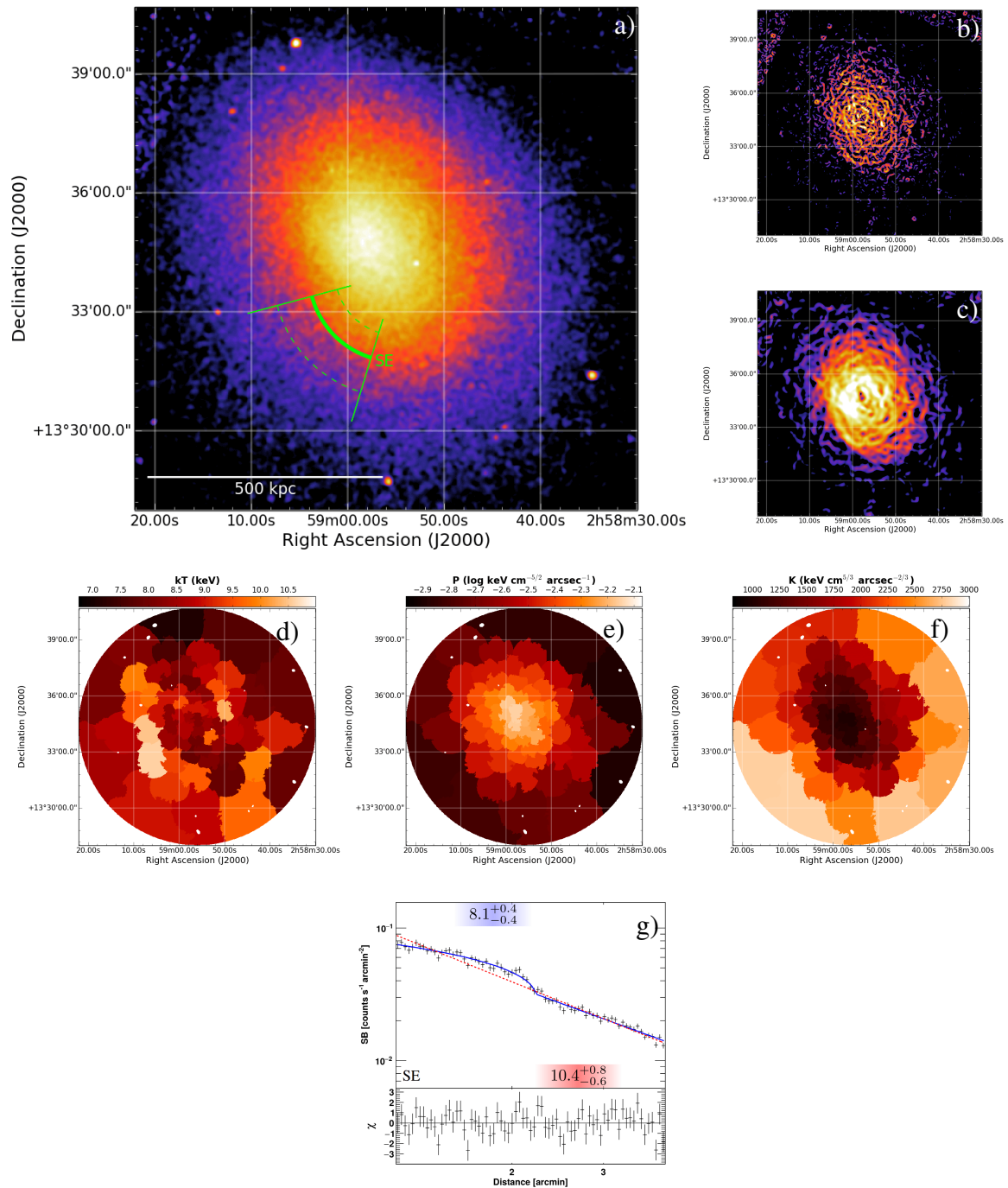


Figure 6.4: A401. The same as for Fig 6.3. The statistical precision of the fits is reported in Fig. D.2. The position of the edge is marked in the *Chandra* image in green (cold front).

us to firmly claim the nature of the SB jump. We mention that the presence of a shock would be in agreement with the fact that cold fronts sometimes follow shocks (e.g. Markevitch et al. 2002) and that shocks might (re)accelerate cosmic rays producing the synchrotron emission at the boundary of some radio halos (e.g. Shimwell et al. 2014).

A401 has a more elliptical X-ray morphology and an average temperature higher than A399. The hottest part of the ICM is found on the E direction. Indeed, the GGM image with $\sigma = 8$ pixels in Fig. 6.4c highlights a kind of spiral structure in SB on this side of the cluster, with maximum contrast toward the SE. The SB profile in this sector is well described by a broken power-law with compression factor $\mathcal{C} = 1.39_{-0.04}^{+0.04}$ (Fig. 6.4g). The higher temperature in the upstream region ($kT_u = 10.4_{-0.6}^{+0.8}$ keV against $kT_d = 8.1_{-0.4}^{+0.4}$ keV) confirms that this is a cold front. This could be part of a bigger spiral-shaped structure generated by a sloshing motion.

MACS J0417.5-1154. It is the most massive ($M_{500} = 1.2 \times 10^{15} M_{\odot}$) and most distant ($z = 0.440$) cluster of our sample. Its extremely elongated X-ray morphology (Fig. 6.5a) suggests that this cluster is undergoing a high speed merger (Ebeling et al. 2010; Mann & Ebeling 2012). Despite this, the value of $K_0 = 27 \pm 7$ keV cm² indicates that its compact core has not been disrupted yet, acting as a “bullet” in the ICM (e.g. Markevitch et al. 2002, for a similar case). Radio observations show the presence of a giant radio halo that remarkably follows the ICM thermal emission (Dwarakanath et al. 2011; Parekh et al. 2017).

The most striking feature of MACS J0417.5-1154 is certainly its prominent cold front in the SE generated by an infalling cold and low-entropy structure, as highlighted by our maps in Fig. 6.5d,e,f. The SB across this region abruptly drops ($\mathcal{C} = 2.44_{-0.25}^{+0.31}$) in the upstream region (Fig. 6.5g), for which spectral analysis provided a clear jump in temperature of $\mathcal{R} = 0.44_{-0.10}^{+0.17}$, leading us to confirm the cold front nature of the discontinuity. The high-temperature value of $kT_u = 16.9_{-3.3}^{+6.1}$ keV found upstream is an indication of a shock-heated region; a shock is indeed expected in front of the CC similarly to other clusters observed in an analogous state (e.g. Markevitch et al. 2002; Russell et al. 2012; Botteon et al. 2016c) and is also suggested by our temperature and pseudo-pressure maps. Nonetheless, we were not able to characterize the SB jump of this potential feature. On the opposite side, the GGM images pinpoint another edge toward the NW direction, representing again a huge jump ($\mathcal{C} = 2.50_{-0.25}^{+0.29}$) in the SB profile (Fig. 6.5h). The spectral analysis in a dedicated region upstream of this feature allowed us only to set a lower limit of $kT_u > 12.7$ keV, suggesting the presence of a hot plasma, in agreement with our temperature map and the one reported in Parekh et al. (2017), where the pressure is almost continuous (Fig. 6.5e), as expected for a cold front.

RXC J0528.9-3927. No dedicated studies exist on this cluster located at $z = 0.284$. The ICM emission is peaked on the cluster core, the coldest region in the cluster (Finoguenov et al. 2005), and fades away in the outskirts where the emission is faint and diffuse (Fig. 6.6a).

Our maps of the ICM thermodynamical quantities in Fig. 6.6d,e,f are affected by large spectral bins due to the low counts of the cluster. The X-ray emission is peaked on the central low entropy region, which is surrounded by hot gas. An edge on the W is suggested both from the GGM images and from the above-mentioned maps. The SB profile in Fig. 6.6g is well fitted with a broken power-law with $\mathcal{C} = 1.51_{-0.09}^{+0.10}$ and the dedicated spectral analysis confirms the value reported in the temperature map ($kT_u = 10.5_{-1.8}^{+3.6}$ keV and $kT_d = 7.2_{-0.7}^{+0.9}$ keV), indicating the presence of a cold front. Two more SB gradients pinpointed in the GGM images to the E and W directions did not provide evidence for any edge with the SB profile fitting (Fig. E.2).

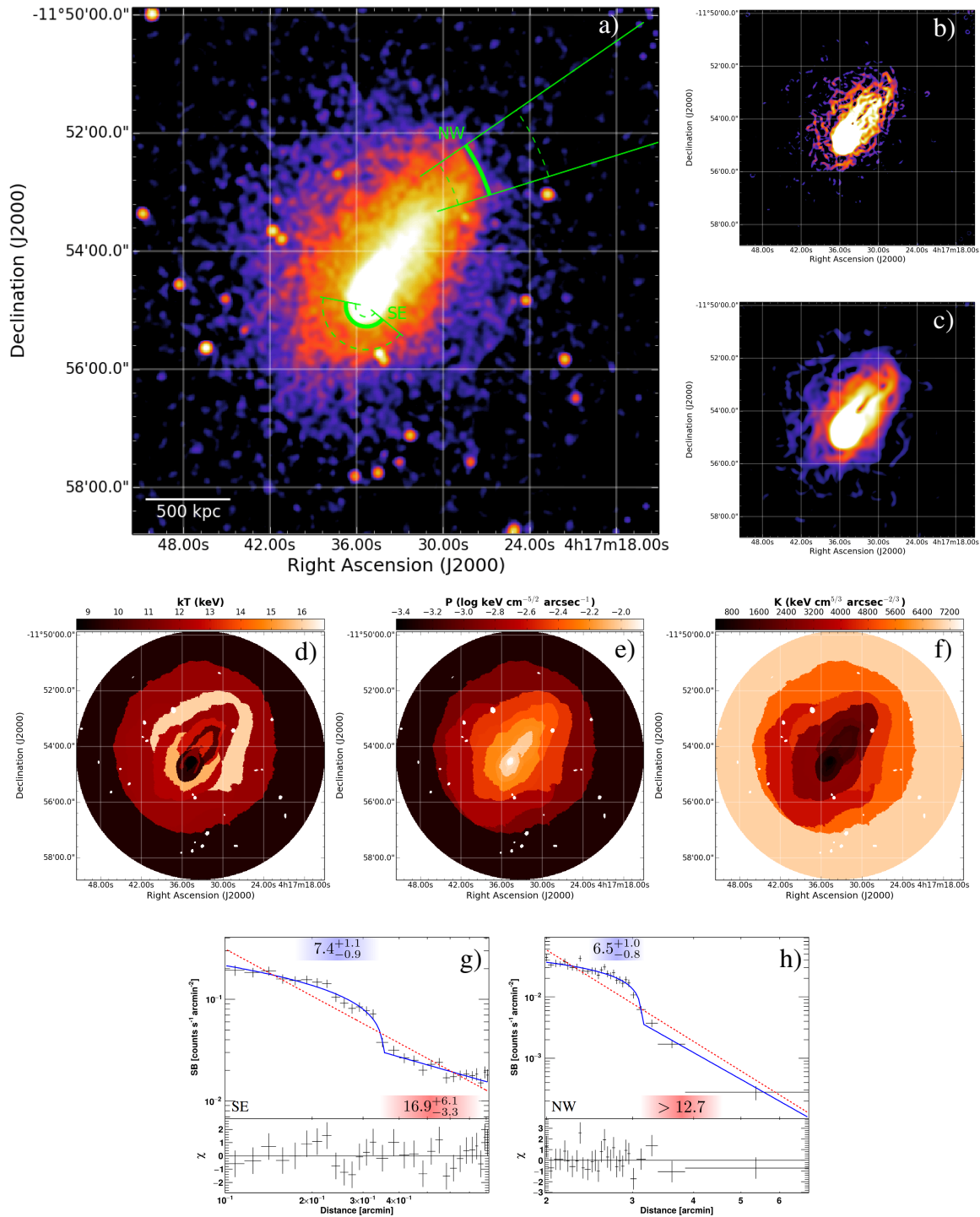


Figure 6.5: MACSJ0417. The same as for Fig 6.3. The statistical precision of the fits is reported in Fig. D.3. The positions of the edges are marked in the *Chandra* image in green (cold fronts).

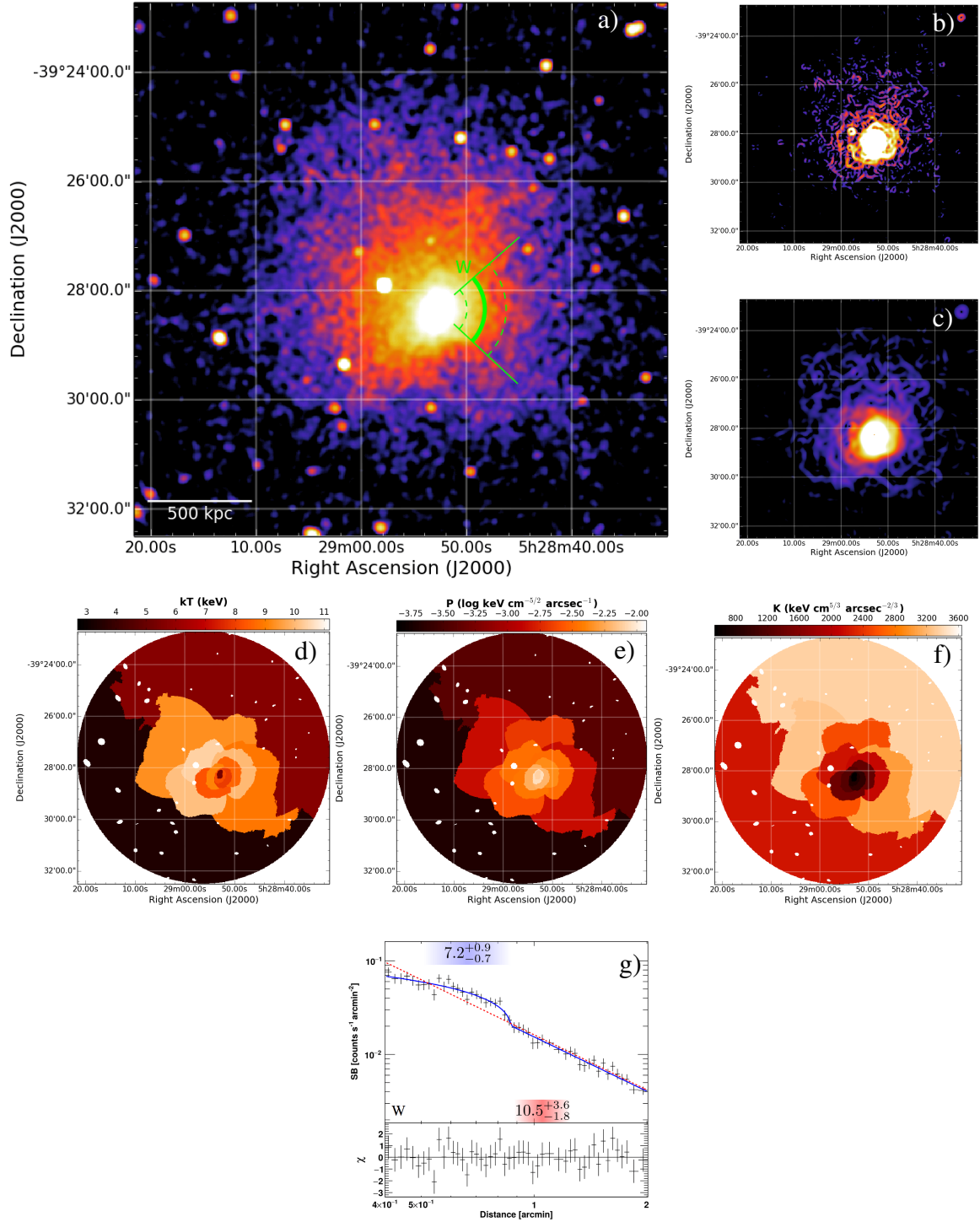


Figure 6.6: RXCJ0528. The same as for Fig 6.3. The statistical precision of the fits is reported in Fig. D.4. The position of the edge is marked in the *Chandra* image in green (cold front).

MACS J0553.4-3342. It is a distant cluster ($z = 0.407$) in a disturbed dynamical state, as shown from both optical and X-ray observations (Ebeling et al. 2010; Mann & Ebeling 2012). The X-ray morphology (Fig. 6.7a) suggests that a binary head-on merger is occurring approximately in the plane of the sky (Mann & Ebeling 2012). No value of the central entropy K_0 is reported either in Cavagnolo et al. (2009) or in Giacintucci et al. (2017). A radio halo that follows the ICM emission has been detected in this system (Bonafede et al. 2012). At the time of preparation of this work, two more papers on MACS J0553.4-3342, both containing a joint analysis of Hubble Space Telescope and *Chandra* observations, were published (Ebeling et al. 2017; Pandge et al. 2017).

The maps of the ICM thermodynamical quantities shown in Fig. 6.7d,e,f further support the scenario of an head-on merger in the E-W direction for MACS J0553.4-3342 in which a low-entropy structure is moving toward E, where GGM images highlight a steep SB gradient. This is confirmed by the SB profile fit (Fig. 6.7g) that leads to a compression factor of $\mathcal{C} = 2.49_{-0.26}^{+0.32}$, while the temperature jump found by spectral analysis of $\mathcal{R} = 0.62_{-0.18}^{+0.33}$ indicates that this discontinuity is a cold front (see also Ebeling et al. 2017; Pandge et al. 2017). The high value of $kT_u = 13.7_{-3.7}^{+6.9}$ keV suggests a shock-heated region to the E of the cold front; indeed the “outer” SB profile of Fig. 6.7h indicates the presence of an edge in the cluster outskirts. We used for the characterization of the SB profile a sector of aperture $133^\circ - 193^\circ$ (where the angles are measured in an anticlockwise direction from W) whereas we used a wider sector ($133^\circ - 245^\circ$) as depicted in Fig. 6.7a to extract the spectra in order to ensure a better determination of the downstream and upstream temperatures, whose ratio $\mathcal{R} = 2.00_{-0.63}^{+1.14}$ confirms the presence of a shock with Mach number $\mathcal{M}_{\text{SB}} = 1.58_{-0.22}^{+0.30}$ and $\mathcal{M}_{\text{kT}} = 1.94_{-0.56}^{+0.77}$, respectively derived from the SB and temperature jumps. This edge is spatially connected with the boundary of the radio halo found by Bonafede et al. (2012). On the opposite side of the cluster, another roundish SB gradient is suggested from the inspection of the GGM images (Fig. 6.7b,c). The W edge is well described by our fit (Fig. 6.7i) that leads to $\mathcal{C} = 1.70_{-0.11}^{+0.12}$, while spectral analysis provides $\mathcal{R} = 0.33_{-0.12}^{+0.22}$, consistent with the presence of another cold front. Even though the upstream temperature is poorly constrained, the spectral fit suggests high temperature values, also noticed in Ebeling et al. (2017), possibly indicating another shock-heated region ahead of this cold front; however, the presence of a possible discontinuity associated with this shock can not be claimed with the current data. The symmetry of the edges strongly supports the scenario of a head-on merger in the plane of the sky. However, the serious challenges to this simple interpretation described in Ebeling et al. (2017) in terms of the relative positions of the brightest central galaxies, X-ray peaks, and dark matter distributions need to be reconsidered in view of the presence and morphology of the extended X-ray tail discussed in Pandge et al. (2017) and clearly highlighted by the GGM image (see Fig. 6.7c).

AS592. Known also with the alternative name RXC J0638.7-5358, this cluster located at $z = 0.222$ is one of those listed in the supplementary table of southern objects of Abell et al. (1989). The ICM has an overall high temperature (Menanteau et al. 2010; Mantz et al. 2010) and is clearly unrelaxed (Fig. 6.8a), despite the fact that AS592 has one of the lowest K_0 value of our sample (cf. Tab. 6.1).

The maps in Fig. 6.8d,e,f highlight the presence of two low entropy and low temperature CCs surrounded by an overall hot ICM. In the SW, a feature in SB is suggested from the GGM image with $\sigma = 8$ pixels. The analysis of the X-ray profile and spectra across it result in a SB discontinuity with compression factor $\mathcal{C} = 1.99_{-0.15}^{+0.17}$ and temperature ratio $\mathcal{R} = 1.61_{-0.43}^{+0.66}$ (Fig. 6.8g), leading us to claim the presence of a shock front with Mach number derived from the SB jump of $\mathcal{M}_{\text{SB}} = 1.72_{-0.12}^{+0.15}$, in agreement with that derived by the temperature jump $\mathcal{M}_{\text{kT}} = 1.61_{-0.42}^{+0.54}$. The SB variation indicated by the GGM images toward the NE direction did not show the presence of a discontinuity with the SB profile fitting (Fig. E.3).

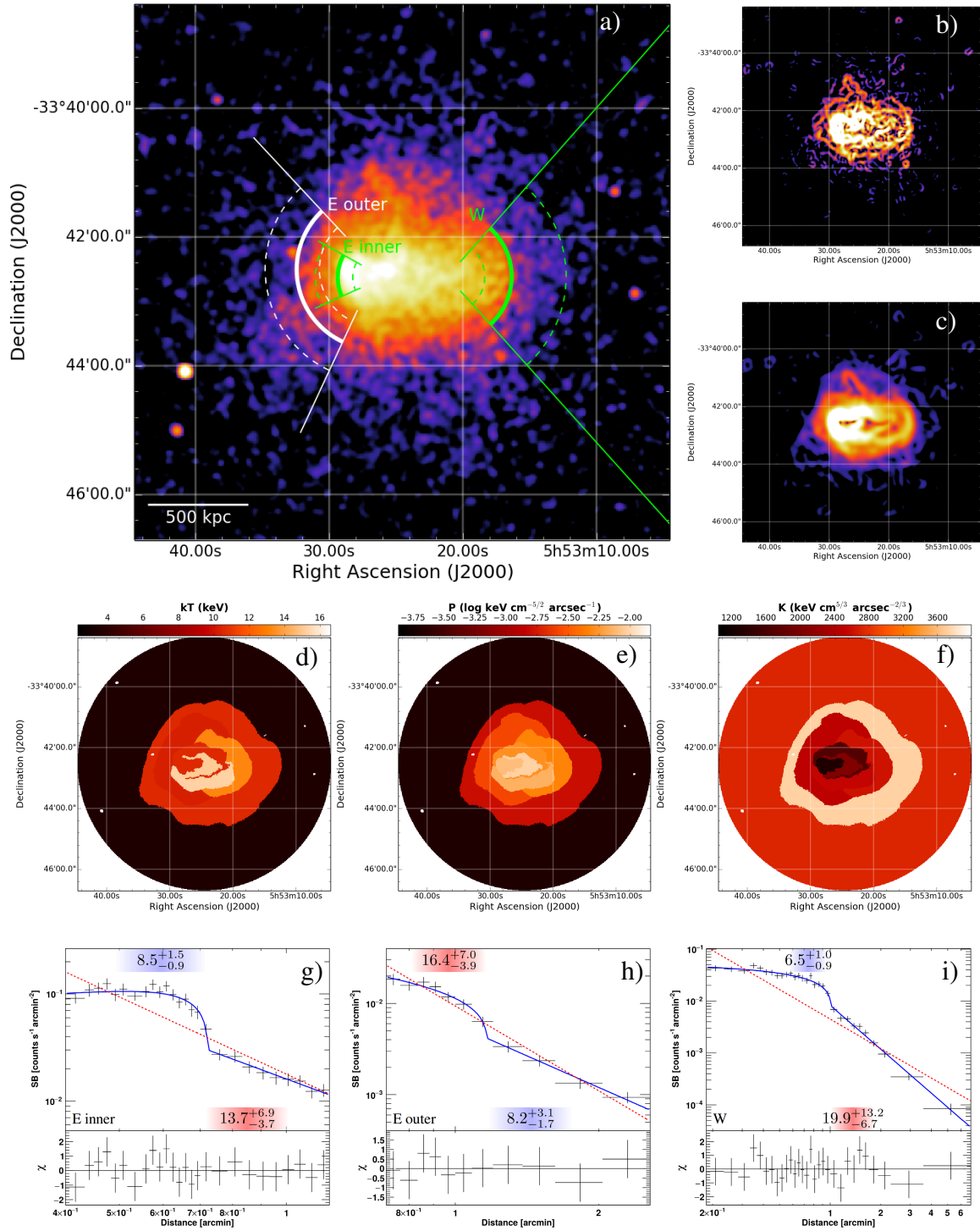


Figure 6.7: MACS J0553. The same as for Fig 6.3. The statistical precision of the fits is reported in Fig. D.5. The positions of the edges are marked in the *Chandra* image in green (cold fronts) and white (shock).

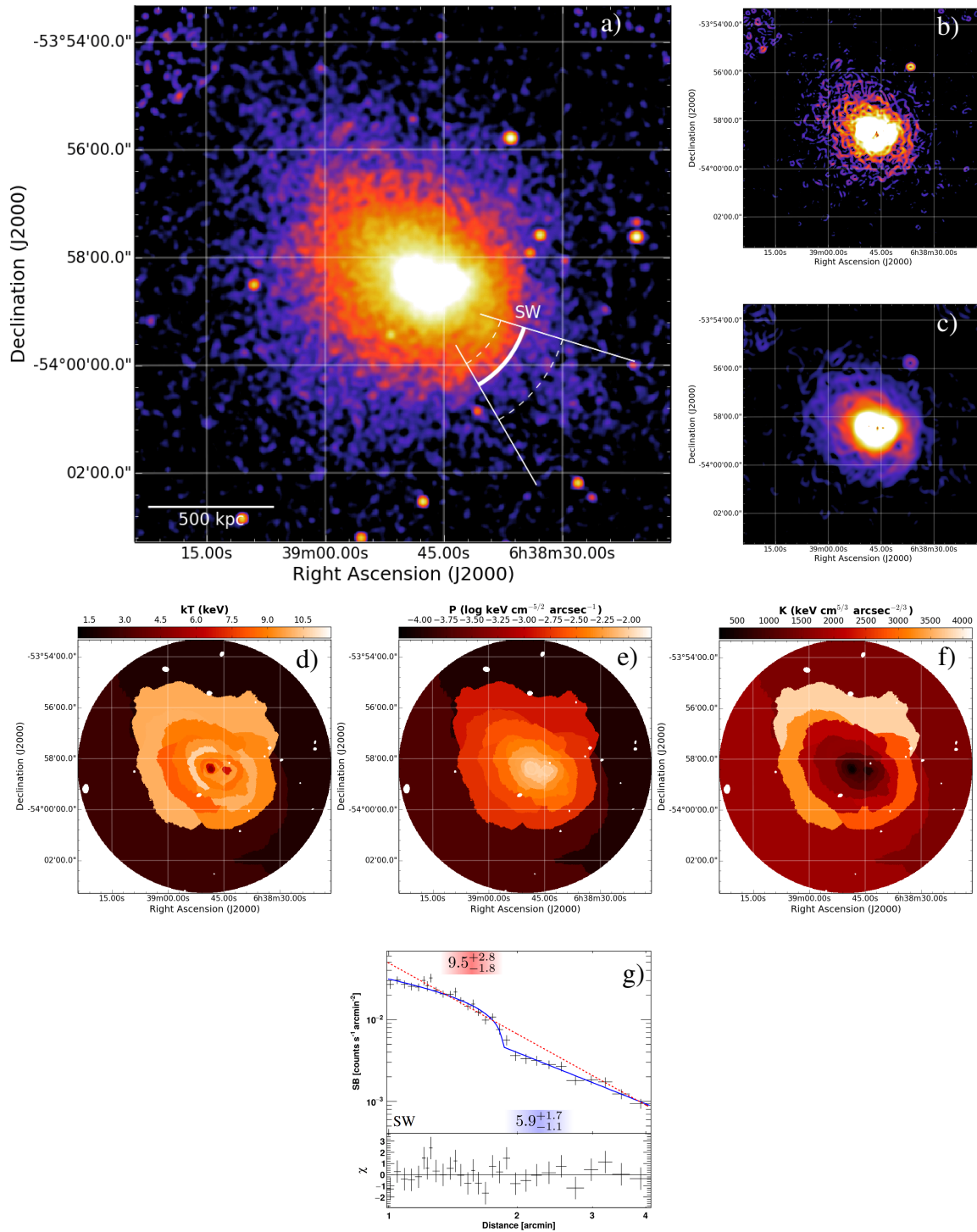


Figure 6.8: AS592. The same as for Fig 6.3. The statistical precision of the fits is reported in Fig. D.6. The position of the edge is marked in the *Chandra* image in white (shock).

A1914. It is a system at $z = 0.171$ in a complex merger state (e.g. Barrena et al. 2013), whose geometry has not been still understood well (Mann & Ebeling 2012). In particular, the irregular mass distribution inferred from weak lensing data (Okabe & Umetsu 2008) is puzzling if compared to near-spherical X-ray emission of the ICM on larger scales (Fig. 6.9a). Previous *Chandra* studies highlighted the presence of a heated ICM with temperature peak in the cluster center (Govoni et al. 2004; Baldi et al. 2007). At low frequencies, a bright steep spectrum source 4C 38.39 (Roland et al. 1985) and a radio halo (Kempner & Sarazin 2001) are detected.

Among the two *Chandra* observations on A1914 retrieved from the archive we had to discard ObsID 542 since it took place in an early epoch of the *Chandra* mission, as described above for the case of A370 (see also notes in Tab. 6.2). We mention that in the *Chandra* archive other four datasets (ObsIDs 12197, 12892, 12893, 12894) can be found for A1914. However, these are 5 ks snapshots pointed in four peripheral regions of the cluster that are not useful for our edge research; for this reason, they were not considered in our analysis.

Our maps of the ICM thermodynamical quantities in Fig. 6.9d,e,f indicate the presence of a bright low-entropy region close to the cluster center with a lower temperature with respect to an overall hot ICM. The adjacent spectral bin to the E suggests the presence of high-temperature gas while GGM images indicate a rapid SB variation. This feature is quite sharpened, recalling the shape of a tip, and can not be described under a spherical assumption. For this reason, two different, almost perpendicular, sectors were chosen to extract the SB profiles to the E, one in an “upper” (toward the NE) and one a “lower” (toward the SE) direction of the tip. Their fits in Fig. 6.9g,h both indicate a similar drop in SB ($\mathcal{C} \sim 1.5$). Spectra were instead fitted in joint regions downstream and upstream of the two SB sectors, leading to a single value for kT_u and kT_d . The temperature jump is consistent with a cold front ($\mathcal{R} = 0.40_{-0.12}^{+0.21}$). Although the large uncertainties, spectral analysis provides indication of a high upstream temperature, likely suggesting the presence of a shock-heated region. This scenario is similar to the Bullet Cluster (Markevitch et al. 2002) and to the above-mentioned MACS J0417.5-1154. A shock moving into the outskirts can not be claimed with the current data but it is already suggested in Fig. 6.9g,h by the hint of a slope change in the upstream power-law at the outer edge of the region that we used to extract the upstream spectrum. Another SB feature to the W direction is highlighted by the GGM images and confirmed by the profile shown in Fig. 6.9i. Its compression factor of $\mathcal{C} = 1.33_{-0.07}^{+0.08}$ and temperature ratio achieved from spectral analysis of $\mathcal{R} = 1.27_{-0.21}^{+0.26}$ allow us to claim the presence of a weak shock with Mach number consistently derived from the SB and temperature jumps, i.e. $\mathcal{M}_{\text{SB}} = 1.22_{-0.05}^{+0.06}$ and $\mathcal{M}_{\text{kT}} = 1.28_{-0.21}^{+0.26}$ respectively. This underlines the striking similarity of A1914 with other head-on mergers where a counter-shock (i.e. a shock in the opposite direction of the infalling sub-cluster) has been detected, such as the Bullet Cluster (Shimwell et al. 2015) and El Gordo (Botteon et al. 2016c), for which it also shares a similar double tail X-ray morphology.

A2104. This is a rich cluster at $z = 0.153$. Few studies exist in the literature on A2104. Pierre et al. (1994) first revealed with ROSAT that this system is very luminous in the X-rays and has a hot ICM. This result was confirmed more recently with *Chandra* (Gu et al. 2009), which also probed a slight elongation of the ICM in the NE-SW direction (Fig. 6.10a), and a temperature profile declining toward the cluster center (Baldi et al. 2007).

The maps of the ICM thermodynamical quantities (Fig. 6.10d,e,f) and GGM filtered images (Fig. 6.10b,c) of A2104 confirm an overall high temperature of the system as well as some SB contrasts in the ICM. We extract SB profiles across two sectors toward the SE and one toward the SW directions. The most evident density jump ($\mathcal{C} = 1.54_{-0.14}^{+0.16}$) is detected for the SE “outer” sector shown in Fig. 6.10h, while the others show only the hint of a discontinuity (Fig. 6.10g,i). However, the fit statistics of the broken power-law and single power-law models indicate that the

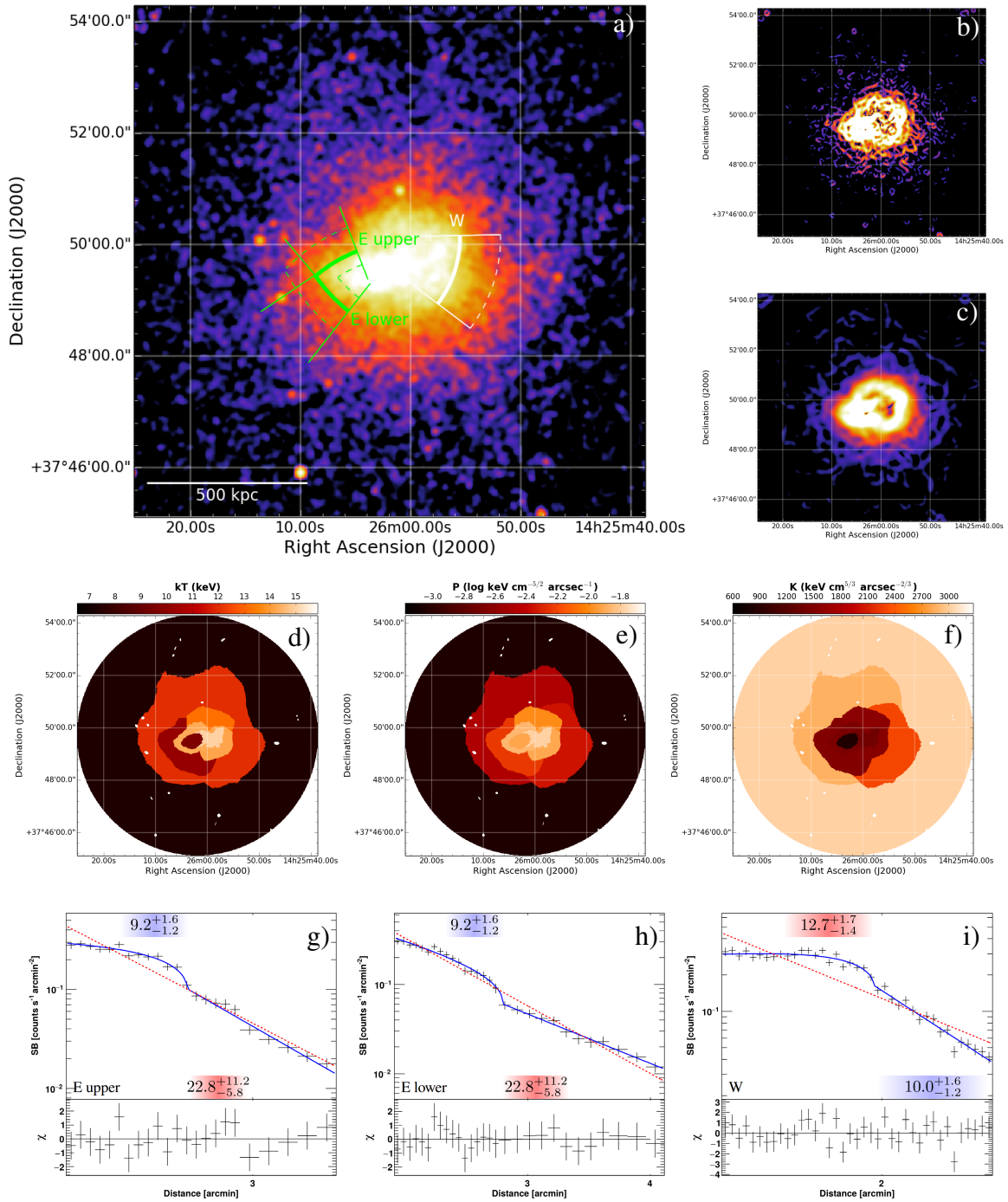


Figure 6.9: A1914. The same as for Fig 6.3. The statistical precision of the fits is reported in Fig. D.7. The positions of the edges are marked in the *Chandra* image in green (cold front) and white (shock).

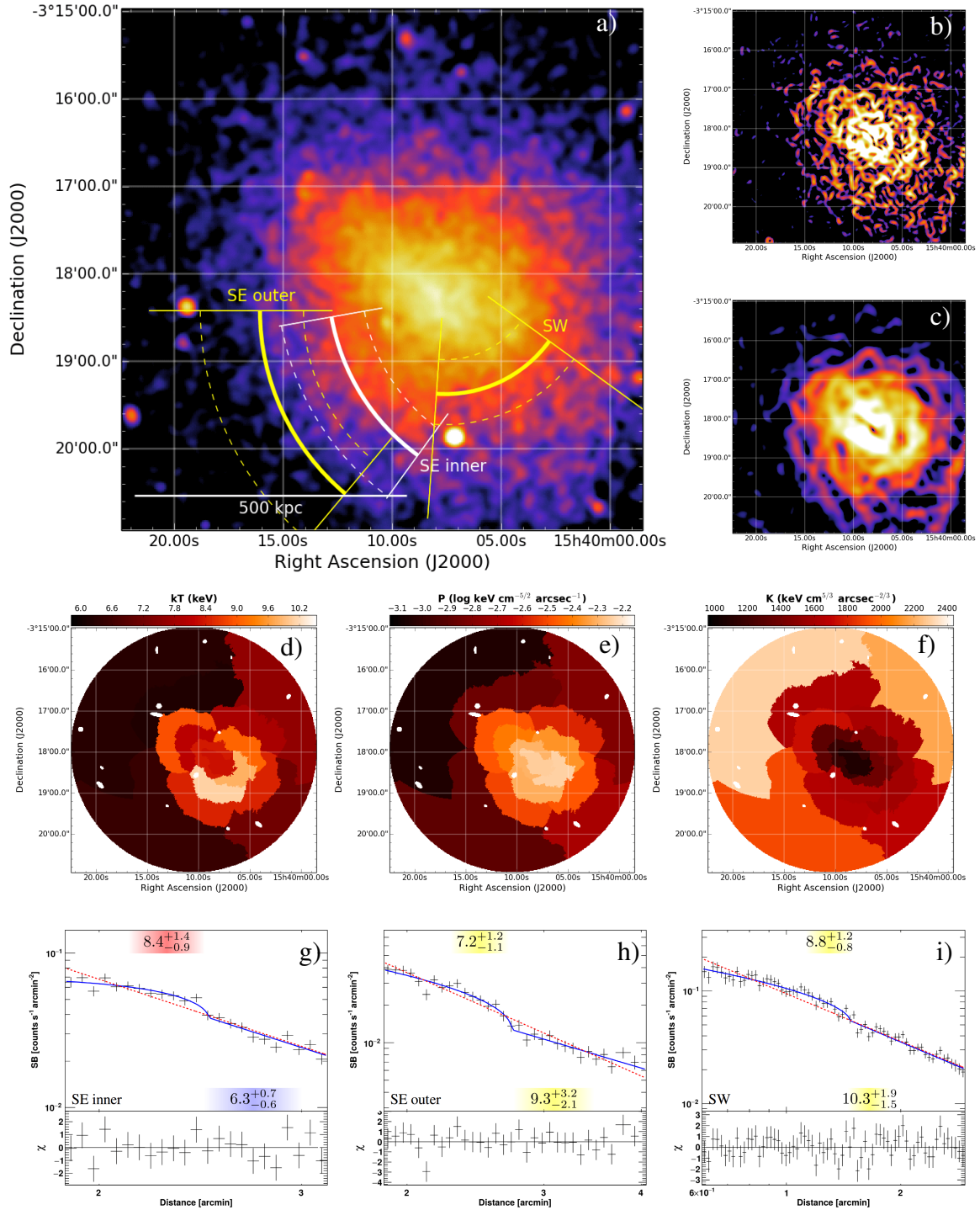


Figure 6.10: A2104. The same as for Fig 6.3. The statistical precision of the fits is reported in Fig. D.8. The positions of the edges are marked in the *Chandra* image in white (shock) and in yellow.

jump model is in better agreement with the data in both the cases, being respectively $\chi^2/\text{d.o.f.} = 17.2/16$ and $\chi^2/\text{d.o.f.} = 37.4/18$ for the SE “inner” sector (3.1σ significance, F-test analysis) whereas it is $\chi^2/\text{d.o.f.} = 64.5/63$ and $\chi^2/\text{d.o.f.} = 122.5/65$ for the SW sector (6.0σ significance, F-test analysis). Spectral analysis allowed us only to find a clear temperature jump for the SE “inner” edge, leaving the nature of the other two SB jumps more ambiguous. The temperature ratio across the SE “inner” sector is $\mathcal{R} = 1.33_{-0.19}^{+0.27}$, leading us to claim a shock with Mach number $\mathcal{M}_{\text{kT}} = 1.34_{-0.20}^{+0.26}$, comparable to the one computed from the upper limit on the compression factor ($\mathcal{C} < 1.47$) of the SB jump, i.e. $\mathcal{M}_{\text{SB}} < 1.32$.

A2218. Located at $z = 0.176$, this cluster is one of the most spectacular gravitational lens known (Kneib et al. 1996). The system is in a dynamically unrelaxed state, as revealed by its irregular X-ray emission (Fig. 6.11a; Machacek et al. 2002) and by the sub-structures observed in optical (Girardi et al. 1997). Detailed spectral analysis already provided indication of a hot ICM in the cluster center (Govoni et al. 2004; Pratt et al. 2005; Baldi et al. 2007). A small and faint radio halo has also been detected in this system (Giovannini & Feretti 2000).

Four *Chandra* observations exist on A2218. Unfortunately, two of these (ObsIDs 553 and 1454) can not be used for the spectral analysis because, as mentioned above for A370 and A1914, they are early *Chandra* observations for which the ACIS background modeling is not possible (see notes in Tab. 6.2 for more details), hence we only used the remainder two ObsIDs to produce the maps shown in Fig. 6.11.

The low counts on A2218 result in maps of the ICM thermodynamical quantities with large bins, as shown in Fig. 6.11d,e,f. The ICM temperature is peaked toward the cluster center, in agreement with previous studies (Pratt et al. 2005; Baldi et al. 2007). The analysis of GGM images highlights the presence of rapid SB variations in more than one direction. The SB profile toward the N shows the greatest of these jumps, corresponding to $\mathcal{C} = 1.47_{-0.18}^{+0.21}$ (Fig. 6.11g). From the spectral analysis we achieve a temperature ratio $\mathcal{R} = 1.38_{-0.28}^{+0.40}$ across the edge, indicating the presence of a shock with consistent Mach number derived from the SB jump, i.e. $\mathcal{M}_{\text{SB}} = 1.32_{-0.13}^{+0.15}$, and from the temperature jump, i.e. $\mathcal{M}_{\text{kT}} = 1.39_{-0.29}^{+0.37}$. The presence of a shock in this cluster region is consistent with the temperature map variations reported in Govoni et al. (2004). In the SE direction, there is indication of two discontinuities from the SB profile analysis (Fig. 6.11h,i): spectra suggest that the “inner” discontinuity is possibly a cold front (however, the temperature jump is not clearly detected, i.e. $\mathcal{R} = 0.84_{-0.17}^{+0.35}$) while the “outer” one is consistent with a shock ($\mathcal{R} = 1.44_{-0.33}^{+0.48}$) and might be connected with the SE edge of the radio halo. The shock Mach numbers derived from SB and temperature jump are $\mathcal{M}_{\text{SB}} = 1.17_{-0.09}^{+0.10}$ and $\mathcal{M}_{\text{kT}} = 1.45_{-0.33}^{+0.43}$, respectively. The SB profile taken in the SW region shows the hint of a kink (Fig. 6.11j); in this case, the broken power-law model ($\chi^2/\text{d.o.f.} = 7.0/15$) yields to an improvement compared to a single power-law fit ($\chi^2/\text{d.o.f.} = 15.0/17$), which according to the F-test corresponds to a null-hypothesis probability of 3×10^{-3} (3.0σ level). Spectral analysis leaves the nature of this feature uncertain.

Triangulum Australis. It is the closest ($z = 0.051$) cluster of our sample. Despite its proximity, it has been overlooked in the literature due to its low Galactic latitude. Markevitch et al. (1996b) performed the most detailed X-ray analysis to date on this object using ASCA and ROSAT and revealed an overall hot temperature (~ 10 keV) in its elongated ICM (Fig. 6.12a). Neither *XMM-Newton* nor *Chandra* dedicated studies have been published on this system. Its K_0 value is reported neither in Cavagnolo et al. (2009) nor in Giacintucci et al. (2017), nonetheless its core was excluded to have low entropy by Rossetti & Molendi (2010). Recently, a diffuse radio emission classified as a halo has been detected (Scaife et al. 2015; Bernardi et al. 2016).

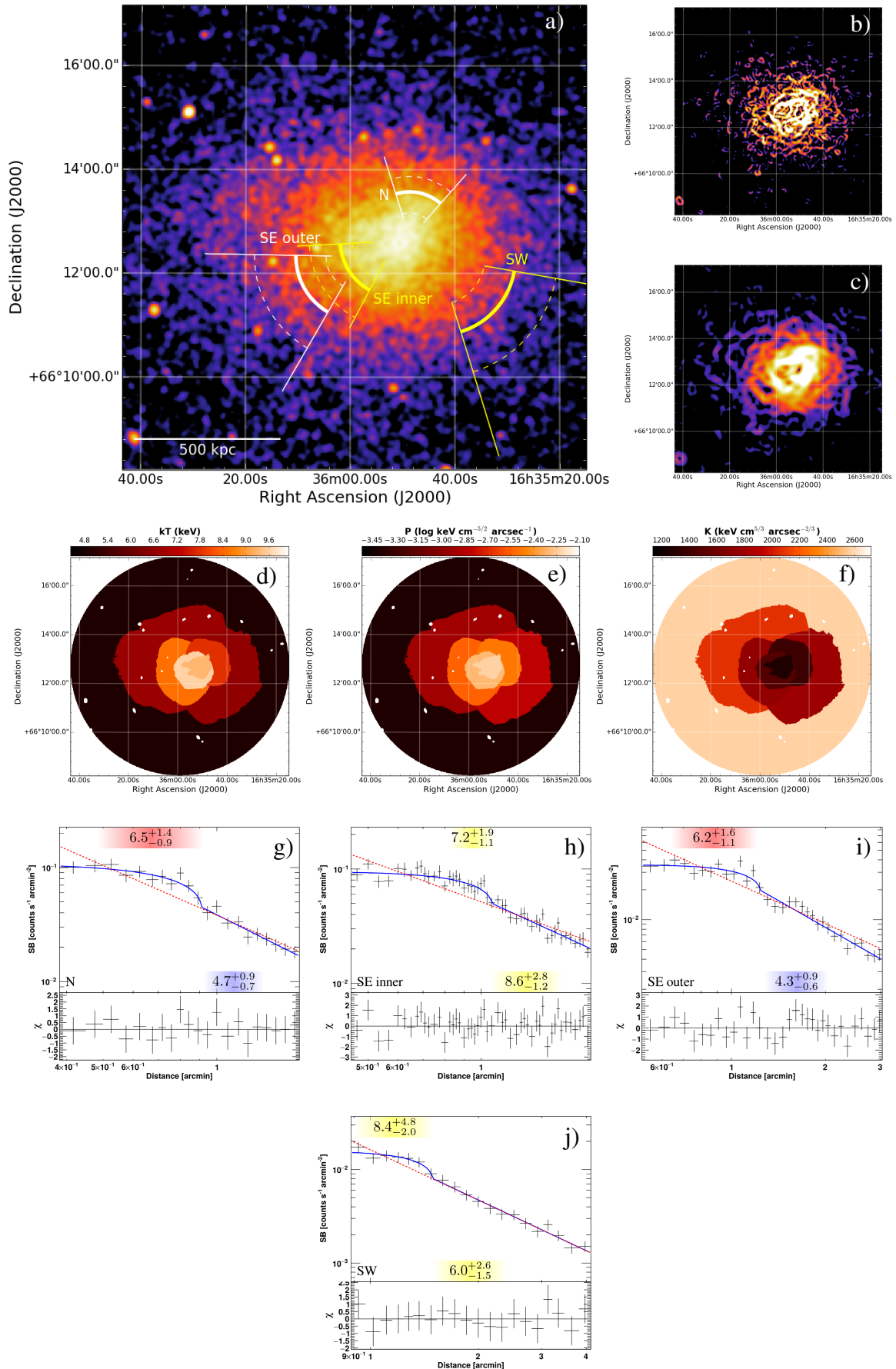


Figure 6.11: A2218. The same as for Fig 6.3. The statistical precision of the fits is reported in Fig. D.9. The positions of the edges are marked in the *Chandra* image in green (cold front), white (shocks) and yellow.

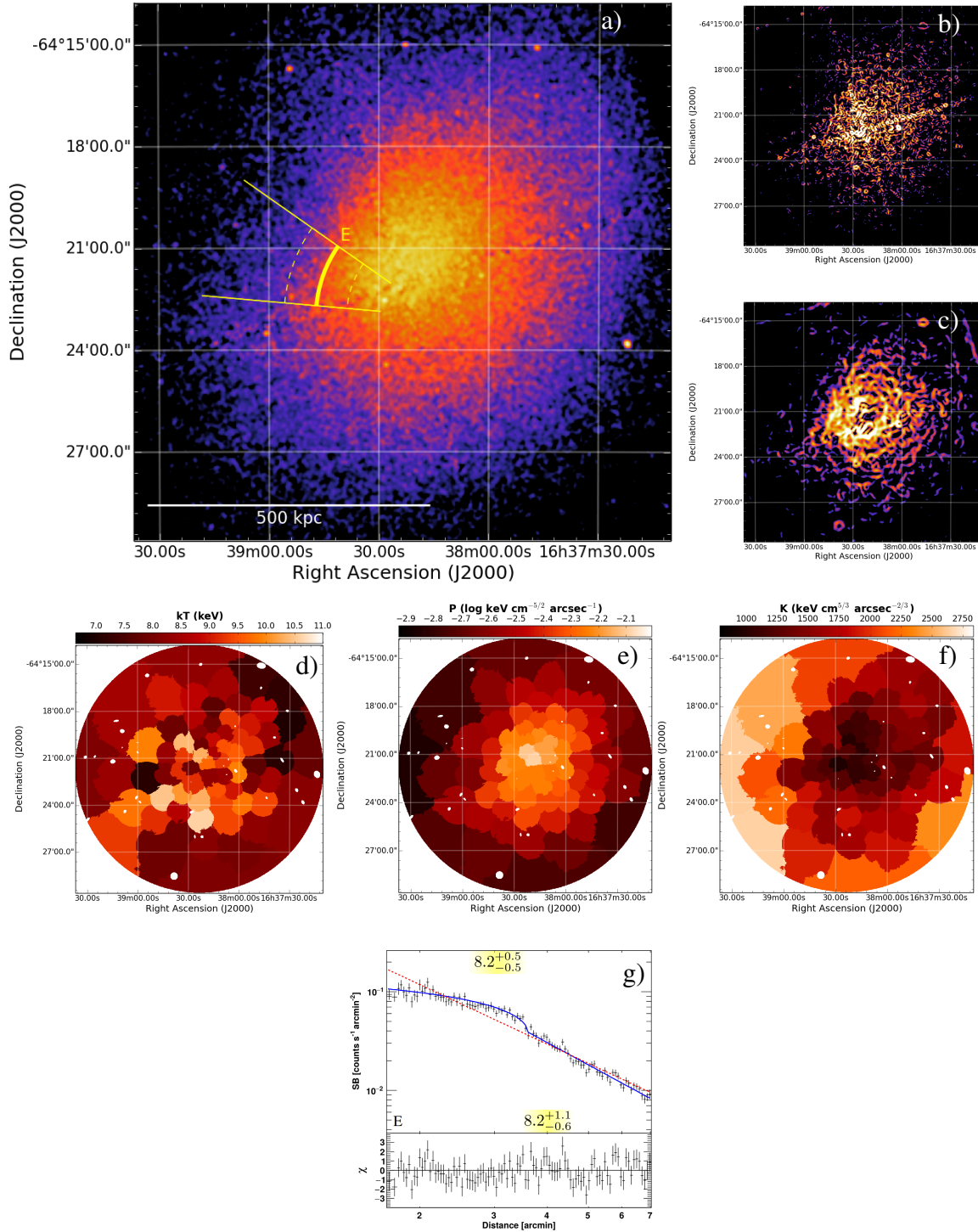


Figure 6.12: Triangulum Australis. The same as for Fig 6.3. The statistical precision of the fits is reported in Fig. D.10. The position of the edge is marked in the *Chandra* image in yellow. Note that in the GMF filtered images the straight and perpendicular features are artifacts due to chip gaps.

Table 6.3: Properties of the jumps detected. Upper and lower bound errors on \mathcal{R} and \mathcal{P} were computed adding separately the negative error bounds and the positive error bounds in quadrature. Mach numbers from SB and temperature jumps are reported for shocks (S), for discontinuities whose nature is still uncertain (U) only the Mach derived from the SB is displayed while for spectroscopically confirmed cold fronts (CF) the Mach number determination is not applicable (n.a.).

Cluster name	Position	\mathcal{C}	\mathcal{R}	\mathcal{P}	\mathcal{M}_{SB}	\mathcal{M}_{KT}	Nature
A370	E	$1.48^{+0.11}_{-0.10}$	$1.33^{+0.08}_{-0.07}$...	U
	W	$1.56^{+0.13}_{-0.12}$	$1.38^{+0.10}_{-0.09}$...	U
A399	SE inner	$1.72^{+0.13}_{-0.12}$	$0.74^{+0.14}_{-0.12}$	$1.27^{+0.26}_{-0.22}$	n.a.	n.a.	CF
	SE outer	$1.45^{+0.10}_{-0.10}$	$1.20^{+0.39}_{-0.26}$	$1.74^{+0.58}_{-0.40}$	$1.31^{+0.07}_{-0.07}$...	U
A401	SE	$1.39^{+0.04}_{-0.04}$	$0.78^{+0.07}_{-0.06}$	$1.08^{+0.10}_{-0.09}$	n.a.	n.a.	CF
MACS J0417.5-1154	NW	$2.50^{+0.29}_{-0.25}$	< 0.59	< 1.64	n.a.	n.a.	CF
	SE	$2.44^{+0.31}_{-0.25}$	$0.44^{+0.17}_{-0.10}$	$1.07^{+0.44}_{-0.27}$	n.a.	n.a.	CF
RXC J0528.9-3927	E	$1.51^{+0.10}_{-0.09}$	$0.73^{+0.25}_{-0.14}$	$1.10^{+0.38}_{-0.22}$	n.a.	n.a.	CF
MACS J0553.4-3342	E inner	$2.49^{+0.32}_{-0.26}$	$0.62^{+0.33}_{-0.18}$	$1.54^{+0.85}_{-0.48}$	n.a.	n.a.	CF
	E outer	$1.82^{+0.35}_{-0.29}$	$2.00^{+1.14}_{-0.63}$	$3.64^{+2.19}_{-1.28}$	$1.58^{+0.30}_{-0.22}$	$1.94^{+0.77}_{-0.56}$	S
	W	$1.70^{+0.12}_{-0.11}$	$0.33^{+0.22}_{-0.12}$	$0.56^{+0.38}_{-0.21}$	n.a.	n.a.	CF
AS592	SW	$1.99^{+0.17}_{-0.15}$	$1.61^{+0.66}_{-0.43}$	$3.20^{+1.34}_{-0.89}$	$1.72^{+0.15}_{-0.12}$	$1.61^{+0.54}_{-0.42}$	S
A1914	E upper	$1.48^{+0.11}_{-0.12}$	$0.40^{+0.21}_{-0.12}$	$0.59^{+0.31}_{-0.18}$	n.a.	n.a.	CF
	E lower	$1.64^{+0.13}_{-0.12}$		$0.66^{+0.35}_{-0.20}$			
	W	$1.33^{+0.08}_{-0.07}$	$1.27^{+0.26}_{-0.21}$	$1.69^{+0.36}_{-0.29}$	$1.22^{+0.06}_{-0.05}$	$1.28^{+0.26}_{-0.21}$	S
A2104	SE inner	< 1.47	$1.33^{+0.27}_{-0.19}$	< 2.36	< 1.32	$1.34^{+0.26}_{-0.20}$	S
	SE outer	$1.54^{+0.16}_{-0.14}$	$0.77^{+0.30}_{-0.21}$	$1.19^{+0.48}_{-0.34}$	$1.37^{+0.12}_{-0.10}$...	U
	SW	$1.27^{+0.07}_{-0.06}$	$0.85^{+0.20}_{-0.15}$	$1.08^{+0.26}_{-0.20}$	$1.18^{+0.05}_{-0.04}$...	U
A2218	N	$1.47^{+0.21}_{-0.18}$	$1.38^{+0.40}_{-0.28}$	$2.03^{+0.66}_{-0.48}$	$1.32^{+0.15}_{-0.13}$	$1.39^{+0.37}_{-0.29}$	S
	SE inner	$1.38^{+0.14}_{-0.11}$	$0.84^{+0.35}_{-0.17}$	$1.16^{+0.50}_{-0.25}$	$1.26^{+0.10}_{-0.08}$...	U
	SE outer	$1.26^{+0.14}_{-0.14}$	$1.44^{+0.48}_{-0.33}$	$1.81^{+0.64}_{-0.46}$	$1.17^{+0.10}_{-0.09}$	$1.45^{+0.43}_{-0.33}$	S
	SW	$1.41^{+0.23}_{-0.21}$	$1.41^{+0.83}_{-0.49}$	$1.99^{+1.21}_{-0.75}$	$1.28^{+0.17}_{-0.14}$...	U
Triangulum Australis	E	$1.34^{+0.04}_{-0.04}$	$1.00^{+0.15}_{-0.10}$	$1.34^{+0.20}_{-0.14}$	$1.23^{+0.03}_{-0.03}$...	U

Three observations of Triangulum Australis can be found in the *Chandra* data archive. However, the oldest two (ObsIDs 1227 and 1281) are calibration observations from the commissioning phase and took place less than two weeks after *Chandra* first light, when the calibration products had very large uncertainties. For this reason, we only used ObsID 17481 in our analysis.

From the maps of the ICM thermodynamical quantities in Fig. 6.12d,e,f, one can infer the complex dynamical state of Triangulum Australis. The GGM filtered on the larger scale gives a hint of a straight structure in SB in the E direction, and it is described by our broken power-law fit ($\mathcal{C} \sim 1.3$) in Fig. 6.12g. However, no temperature jump is detected across the edge, giving no clue about the origin of this SB feature. We mention that this region was also highlighted by Markevitch et al. (1996b) with ASCA and ROSAT as a direct proof of recent or ongoing heating of the ICM in this cluster.

6.5.2 Summary of the detected edges

Overall, we found six shocks, eight cold fronts and other eight discontinuities whose origin remains uncertain due to the poorly constrained temperature jump. The properties of the detected edges are summarized in Tab. 6.3, while the distributions of \mathcal{C} and \mathcal{R} are displayed in Fig. 6.13. Although we are not carrying out a statistical analysis of shocks and cold fronts in galaxy clusters, we

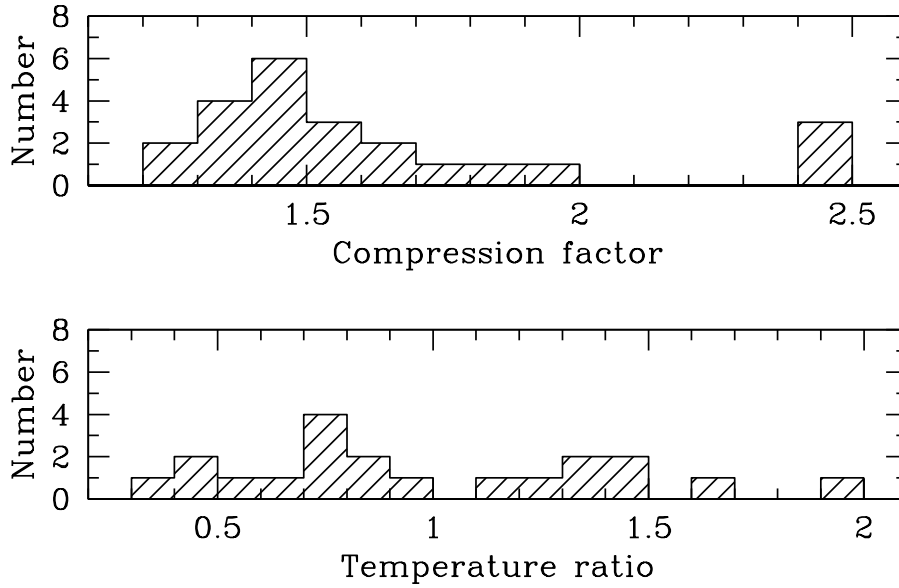


Figure 6.13: Distribution of the central values of \mathcal{C} (*top*) and \mathcal{R} (*bottom*) reported in Tab. 6.3.

notice that the majority of the reported jumps are associated with weak discontinuities with $\mathcal{C} < 1.7$ and $0.5 < \mathcal{R} < 1.5$. This may indicate that the GGM filters allow to pick up also small SB jumps that are usually lost in a visual inspection of unsmoothed cluster images.

We mention that in the case of a shock the SB and temperature jumps allow to give two independent constraints on the Mach number (Eq. 1.18 and 1.17). However, only few shocks reported in the literature have Mach number consistently derived from both the jumps so far (e.g. A520, Markevitch et al. 2005; A665, Dasadia et al. 2016; A115, Botteon et al. 2016a). Instead, in our analysis there is a general agreement between these two quantities, further supporting the robustness of the results.

One could argue that the nature of the weakest discontinuities claimed is constrained at slightly more than 1σ level from the temperature ratio. This is a consequence of the small temperature jump implied by these fronts and the large errors associated with the spectral analysis (despite the careful background treatment we have performed). However, we can check the presence of pressure discontinuities at these edges by combining the density and temperature jumps achieved from SB and spectral analysis. The values of $\mathcal{P} \equiv P_d/P_u = \mathcal{C} \times \mathcal{R}$ computed for all the discontinuities are reported in Tab. 6.3 and show at higher confidence levels the presence of a pressure discontinuity in the shocks and the absence of a pressure jump in the cold fronts, strengthening our claims. Although this procedure combines a deprojected density jump with a temperature evaluated along the line of sight, we verified that given the uncertainties on the temperature determination and the errors introduced by a deprojection analysis, the projected and deprojected values of temperature and pressure ratios are statistically consistent even in the cases of the innermost edges (i.e. those more affected by projection effects).

With the present work, we have increased the number of known shocks and cold fronts in galaxy clusters. The contribution of our detections compared to edges reported in Tab. 6.1 is highlighted in red in Fig. 6.14. These histograms do not have a statistical purpose but serve to probe the fairly relevant improvement of our analysis on the number of discontinuities observed in the ICM. The detected shocks have all $\mathcal{M} < 2$ likely due to the combination of the fact that shocks crossing the central Mpc regions of galaxy clusters are weak (e.g. Vazza et al. 2012a, and references therein) and that fast moving shocks would be present for a short time in the ICM.

The distinction between shock and cold fronts for the eight discontinuities with uncertain origin can tentatively be inferred from the current values of \mathcal{R} and \mathcal{P} reported in Tab. 6.3. In this respect, deeper observations of these edges will definitely shed light about their nature.

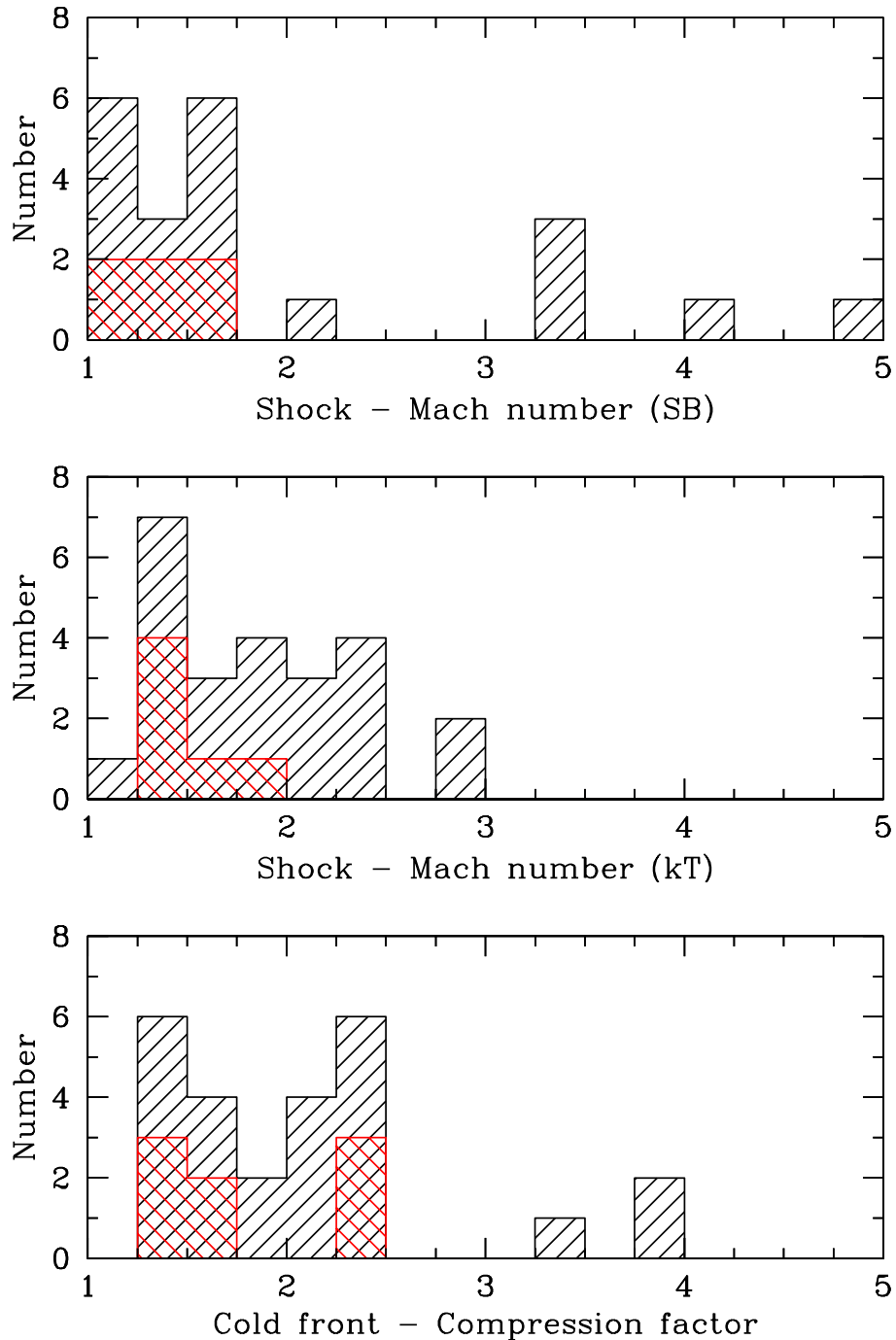


Figure 6.14: Contribution of our work (*red*) on the total number (*black*) of shocks and cold fronts reported in Tab. 6.1. The central values of Mach numbers and compression factors found in literature were used to create the histograms.

6.5.3 Non-detections

Our analysis did not allow us to detect any edge in the following objects: A2813 ($z = 0.292$), A1413 ($z = 0.143$), A1689 ($z = 0.183$) and A3827 ($z = 0.098$). All these systems have a more regular X-ray morphology (Fig. 6.15–6.18) with respect to the other clusters of the sample.

A2813. This cluster has a roundish ICM morphology (Fig. 6.15a), nonetheless its value of $K_0 = 268 \pm 44 \text{ keV cm}^2$ is among the highest in our sample (cf. Tab. 6.1). The core is slightly elongated in the NE-SW direction and has a temperature $\sim 7.7 \text{ keV}$, consistently with the *XMM-Newton* value reported by Finoguenov et al. (2005). The maps shown in Fig. 6.15 were produced using all the ObsIDs listed in Tab. 6.2. We mention that the original target of the ACIS-S datasets (ObsIDs 16366, 16491, 16513) is XMMUJ0044.0-2033; however, A2813 is found to entirely lay on an ACIS-I chip that was kept on during the observations. These data provide the largest amount ($\sim 80\%$) of the total exposure time on A2813 and were used in our analysis although the unavoidable degradation of the instrument spatial resolution due to the ACIS-I chip being off-axis with this observing configuration.

A1413. It has a borderline value of K_0 (cf. Tab. 6.1) from the threshold set in this work. The distribution of cluster gas is somewhat elliptical, elongated in the N-S direction (Fig. 6.16a). Our analysis and previous *Chandra* temperature profiles (Vikhlinin et al. 2005; Baldi et al. 2007) are in contrast with *XMM-Newton* that does not provide evidence of a CC (Pratt & Arnaud 2002). This discrepancy is probably due to the poorer PSF of the latter instrument. A radio mini-halo covering the CC region is also found by Govoni et al. (2009). The region in the NW direction with a possible discontinuity suggested by the GGM filtered images did not show the evidence for an edge with the SB profile fitting (Fig. E.4).

A1689. It represents a massive galaxy cluster deeply studied in the optical band because its weak and strong gravitational lensing (e.g. Broadhurst et al. 2005; Limousin et al. 2007). The X-ray emission is quasi-spherical and centrally peaked (Fig. 6.17a), features that apparently indicate a CC. Nevertheless, optical (Girardi et al. 1997) and *XMM-Newton* observations (Andersson & Madejski 2004) both suggest that the system is undergoing to a head-on merger seen along the line of sight due either to the presence of optical sub-structures or to the asymmetric temperature of the ICM, hotter in the N. Our results confirm the presence of asymmetries in temperature distribution (Fig. 6.17d). The detection of a radio halo (Vacca et al. 2011) supports the dynamically unrelaxed nature of the system.

A3827. It constitutes another cluster studied in detail mainly for its optical properties. Its central galaxy is one of the most massive known found in a cluster center and exhibits strong lensing features (Carrasco et al. 2010). Gravitational lensing also indicates a separation between the stars and the center of mass of the dark matter in the central galaxies (Massey et al. 2015), making A3827 a good candidate to investigate the dark matter self-interactions (Kahlhoefer et al. 2015). On the X-ray side, the cluster emission is roughly spherical (Fig. 6.18a), with an irregular temperature distribution (Fig. 6.18d) and a mean value of $\sim 7 \text{ keV}$ (Leccardi & Molendi 2008). Two regions to the E and W directions suggested by the GGM images did not show any discontinuity with the SB profile fitting (Fig. E.5).

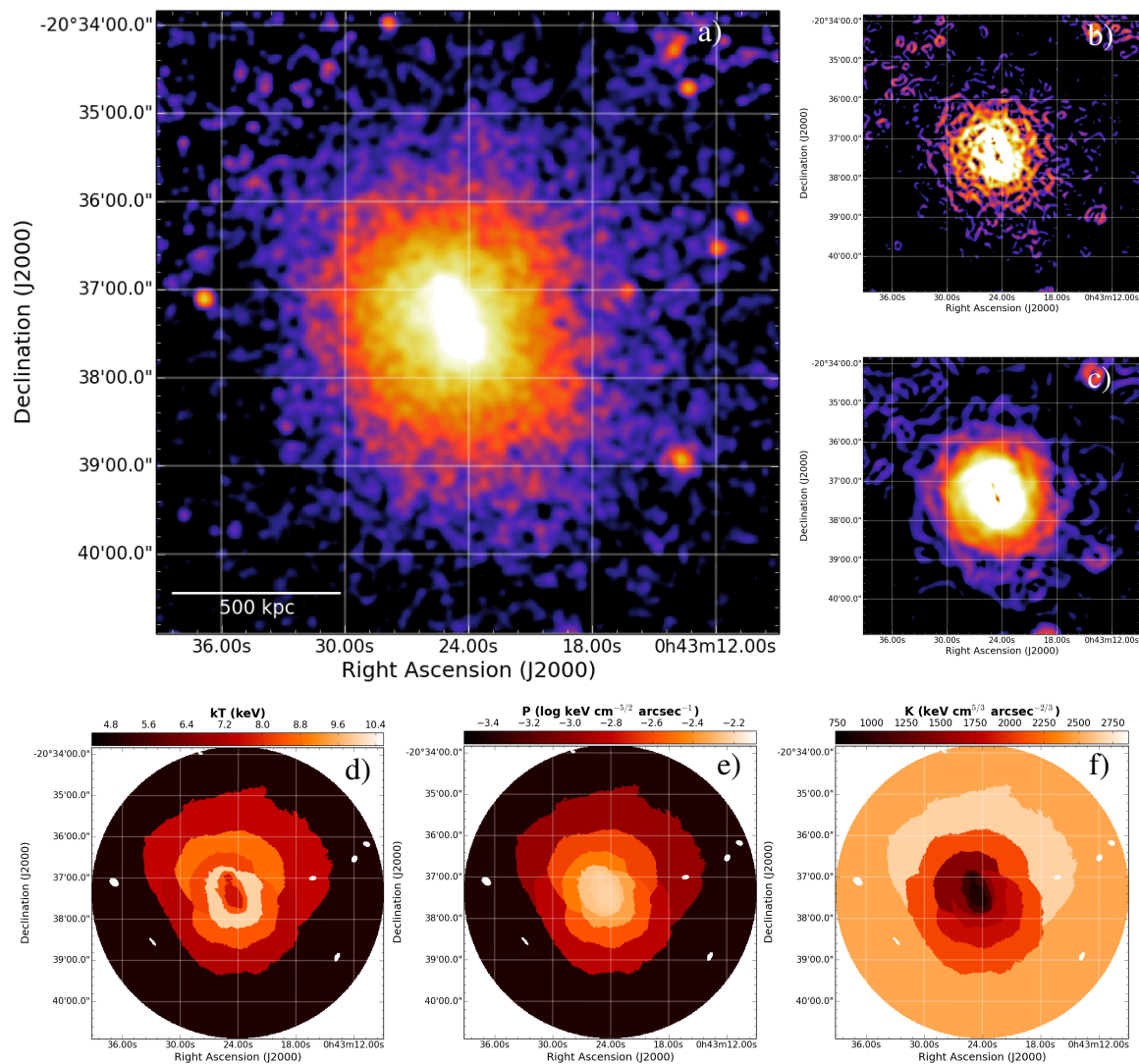


Figure 6.15: A2813. The same as for Fig 6.3. The statistical precision of the fits is reported in Fig. D.11.

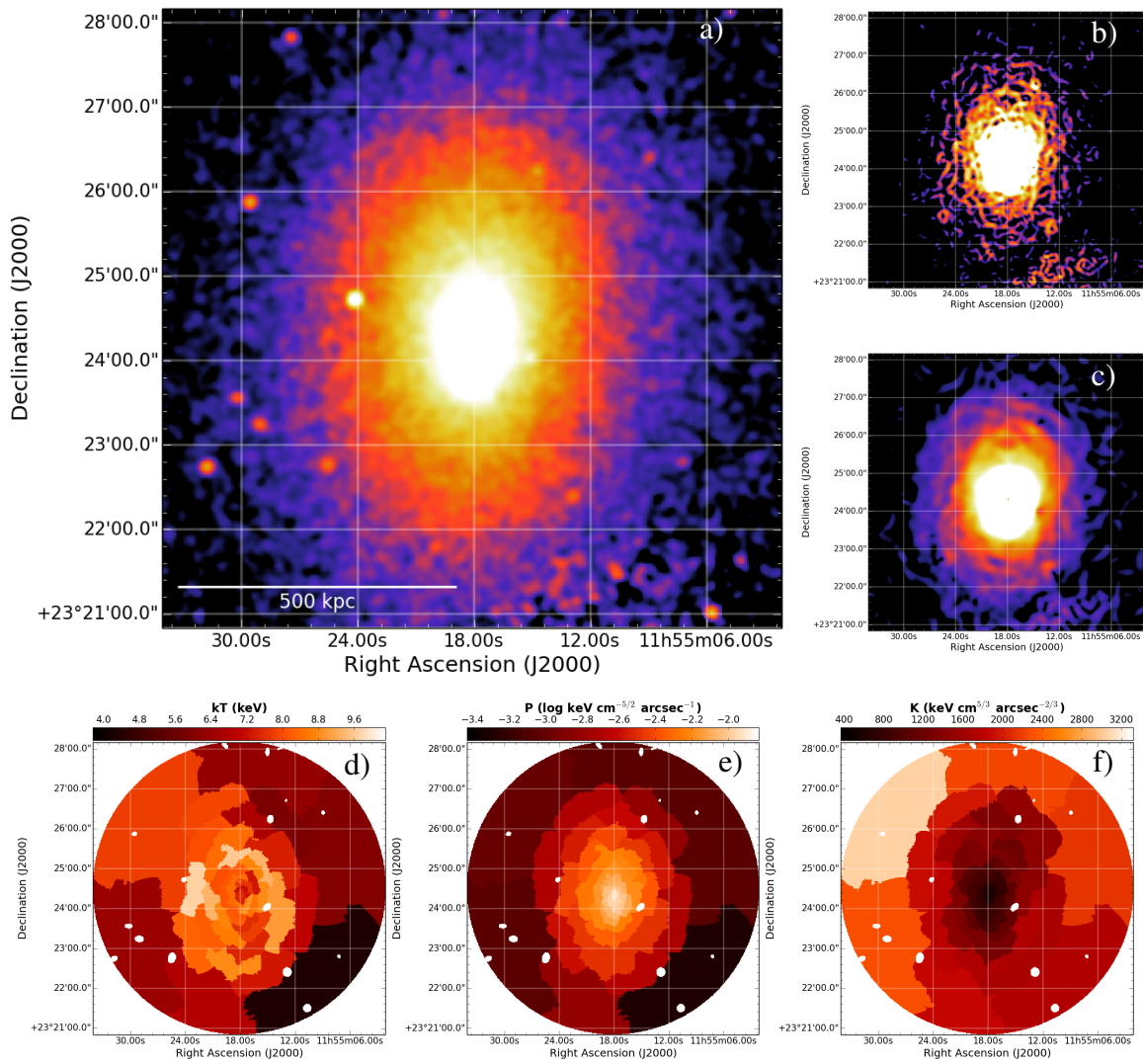


Figure 6.16: A1413. The same as for Fig 6.3. The statistical precision of the fits is reported in Fig. D.12.

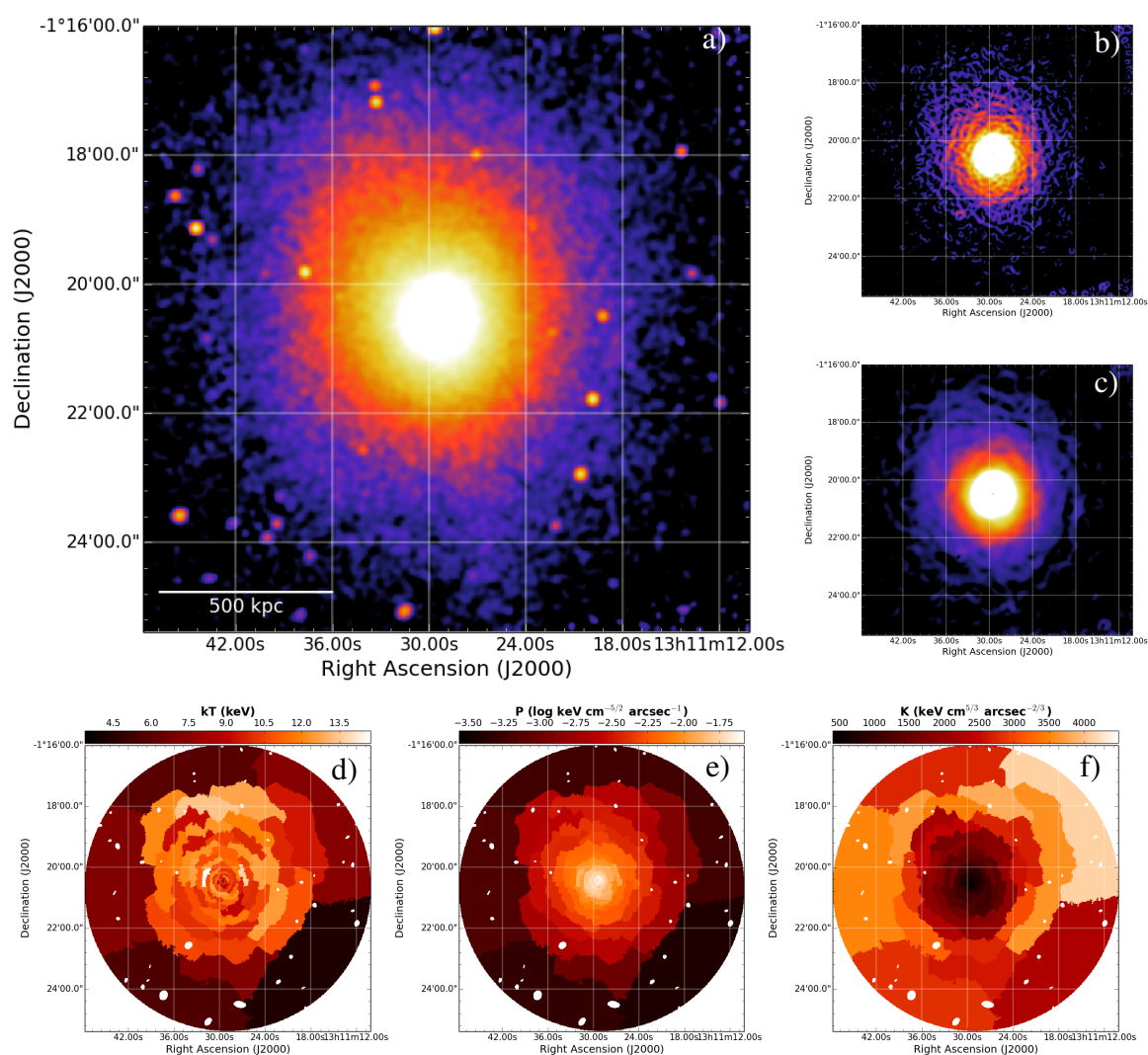


Figure 6.17: A1689. The same as for Fig 6.3. The statistical precision of the fits is reported in Fig. D.13.

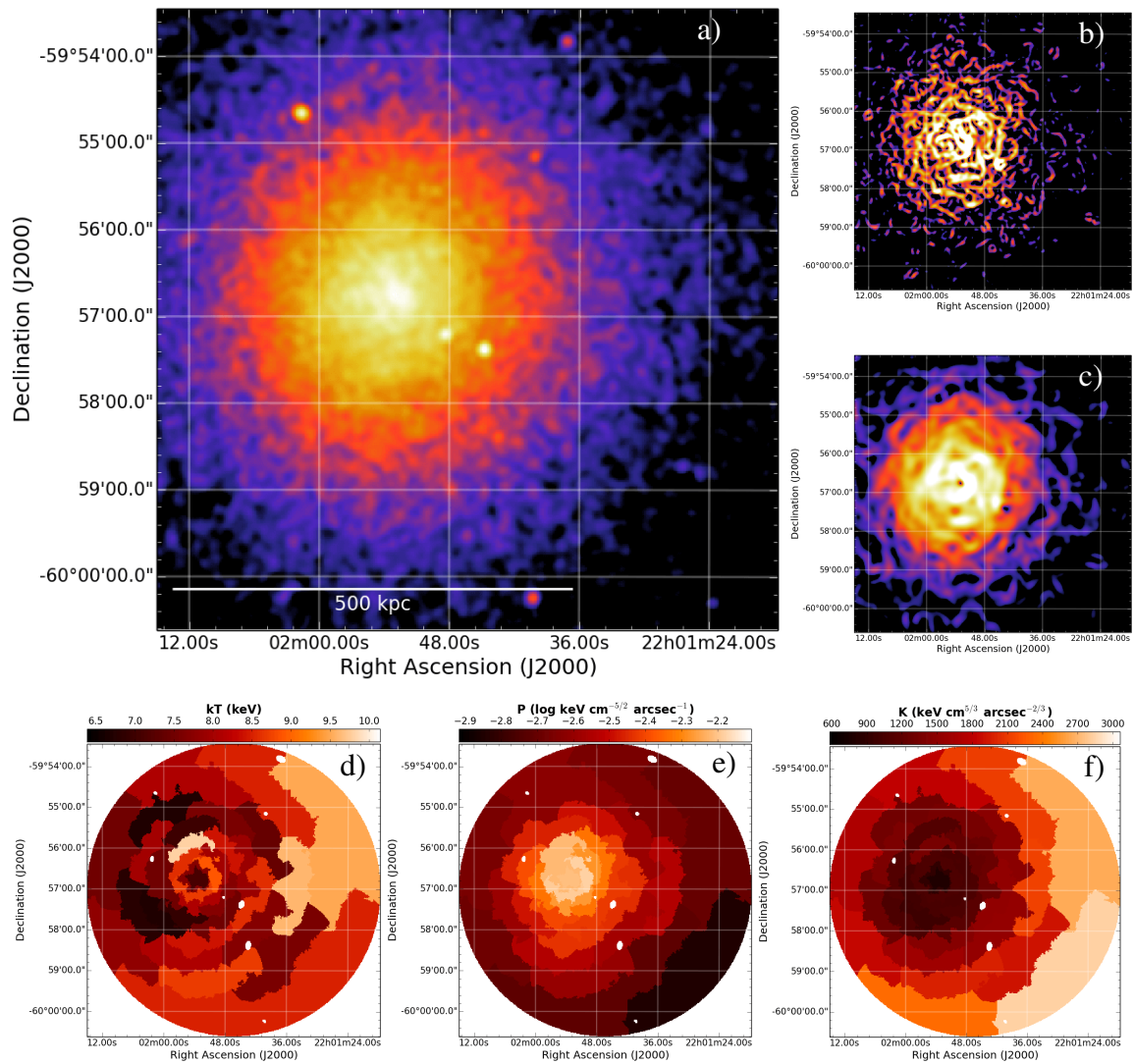


Figure 6.18: A3827. The same as for Fig 6.3. The statistical precision of the fits is reported in Fig. D.14.

6.6 Conclusions

As explained in Section 1.3.2, shocks and cold fronts produced in a collision between galaxy clusters provide information on the dynamics of the merger and can be used to probe the microphysics of the ICM. Nonetheless their detection is challenged by the low number of X-ray counts in cluster outskirts and by possible projection effects that can hide these sharp edges. For this reason, only a few of them have been successfully detected both in SB and in temperature jumps.

In this Chapter, we explored a combination of different analysis approaches of X-ray observations to firmly detect and characterize edges in NCC massive galaxy clusters. Starting from GGM filtered images on different scales and the maps of the ICM thermodynamical quantities of the cluster, one can pinpoint ICM regions displaying significant SB and/or temperature variations. These can be thus investigated with the fitting of SB profiles, whose extracting sectors have to be accurately chosen in order to properly describe the putative shock or cold front. Once that the edge is well located, spectral analysis on dedicated upstream and downstream regions can also be performed in an optimized way. The discontinuity is firmly detected if the jump is observed both in images and in spectra.

We selected 37 massive NCC clusters with adequate X-ray data in the *Chandra* archive to search for new discontinuities driven in the ICM by merger activity. In particular we looked at 15 of these systems for which no claim of edges was published. We were able to characterize at least one SB jump in 11 out of these 15 clusters of the sample. The performed SB analysis relies on the spherical assumption. Among the detected edges, we also constrained the temperature jump for 14 discontinuities, six shocks and eight cold fronts, while for eight edges the classification is still uncertain. As a further check, we also computed the pressure ratios across the edges and verified the presence of the pressure discontinuity in shocks and the absence of a pressure jump in cold fronts.

Our work provides a significant contribution to the search for shocks and cold fronts in merging galaxy clusters (Fig. 6.14) demonstrating the strength of combining diverse techniques aimed to identify edges in the ICM. Indeed, many shocks and cold fronts reported in the literature have been discovered because either they were evident in the unsmoothed cluster images or there were priors suggesting their existence (e.g. merger geometry and/or presence of a radio relic). The usage of edge detection algorithms (as the GGM filter) in particular helps in highlighting also small SB gradients to investigate with SB profile and spectral fitting. Among the small jumps detected we found low Mach numbers ($\mathcal{M} < 2$) shocks; this is a possible consequence of the fact that the central regions of the ICM are crossed by weak shocks while the strongest ones quickly fades in the cluster outskirts, making their observation more difficult (see also discussion in Vazza et al. 2012a on the occurrence of radio relics in clusters as a function of radius).

As discussed in Section 1.5 and shown in Chapter 2, 3 and 5, testing the shock acceleration models in weak shocks (where the energy flux at the shock is smaller) is particularly effective. In this case, the connection between shocks and bright radio relics severely challenges a DSA model where thermal particles are accelerated to relativistic radio bright energies. As a consequence, the radio follow-up of the shocks detected in this work will be useful to study the connection between weak shocks and non-thermal phenomena in the ICM.

Galaxy cluster science with LOFAR

ABSTRACT

LOFAR is an international radio telescope operating in the the frequency range 10 – 240 MHz. It provides a number of unique observing capabilities allowing to achieve unprecedented levels of resolution and sensitivity at low frequencies. The several technical challenges (hardware, data transport, data calibration) faced by LOFAR make this instrument an important pathfinder (actually, the largest one) for the SKA. Non-thermal diffuse emission in galaxy clusters represents an ideal case of study for LOFAR. Surveys with LOFAR are expected to detect many new radio halos and relics, which can be used to increase the statistics and the knowledge of non-thermal phenomena in the ICM.

7.1 The LOw Frequency ARray

LOFAR, the LOw Frequency ARray (van Haarlem et al. 2013), is a new generation interferometer operated by ASTRON and spread all over Europe. It is the largest pathfinder of the SKA¹ at low frequencies, accounting about 8,000 dipole antennas spread over most of the European continent and observing in the frequency range 10 – 240 MHz (corresponding to wavelengths of 30 – 1.2 m). LOFAR exploits this relatively unexplored portion of the electromagnetic spectrum with unprecedented resolution and sensitivity. The longest European baseline permit to reach sub-arcsecond resolution over most of the operating bandpass while the densely populated core allows to recover very extended emission in the sky. The effectively all-sky coverage of the dipoles gives LOFAR a large FoV, essential for surveying purposes. This makes LOFAR a power and versatile instrument with potential breakthroughs in many fields of astrophysics. The science drivers for LOFAR determined the design, development and construction of the facility during its initial and commissioning phase, and have been divided into six Key Science Projects (KSP), as outlined below.

- **Epoch of Reionization:** aims at searching for the redshifted 21 cm line signal that marks the transition between the dark ages and the period after recombination when the Universe became neutral (e.g. Pritchard & Loeb 2012). This process possibly started at $z \sim 20 - 15$ and finished at $z \sim 6$. The redshift ranges $z \sim 30 - 20$ and $z \sim 12 - 6$ can be probed by LOFAR.

¹<https://www.skatelescope.org>

- **Cosmic Rays:** will allow to understand the origin of high-energy CRs at energies between $10^{15} - 10^{20.5}$ eV through the detection of air showers of secondary particles caused by interaction of CRs with the Earth atmosphere. Both the sites and processes for accelerating these energetic particles are still poorly known.
- **Solar Physics and Space Weather:** includes the definition of solar observing modes and the development of the necessary software infrastructure for solar and space weather studies.
- **Transients:** comprises the study of all time-variable astronomical radio sources, including pulsars, gamma-ray bursts, gravitational waves, X-ray binaries, radio supernovae, flare stars, and even exoplanets. Thanks to the all-sky monitoring, LOFAR is expected to detect many new transient events, and to provide alerts to the international community for follow-up observations at other wavelengths.
- **Cosmic Magnetism of the Nearby Universe:** allows to study the polarized radio synchrotron emission to unveil the structure and strength of the magnetic fields of several objects, from the Milky Way, dwarf galaxies, galaxy halos, nearby galaxy clusters, and up to the intergalactic filaments related to the formation of large-scale structures.
- **Surveys:** is one of the LOFAR science drivers since its inception. Due to its nature, the Surveys KSP touches a broad range of astrophysics topics, with possible cross-talks with the other KSPs. Four main science drivers have been identified for the proposed surveys:
 - Formation of massive galaxies, clusters and black holes using $z \gtrsim 6$ radio galaxies as probes.
 - Intra-cluster magnetic fields using diffuse radio emission in galaxy clusters as probes.
 - Star formation processes in the early Universe using starburst galaxies as probes.
 - Exploration of new parameter space for serendipitous discovery.

Since the Surveys KSP is very relevant for this Thesis, in Section 7.4 more details will be given on one of the main ongoing LOFAR survey.

7.1.1 System overview

Currently (October 2018), LOFAR comprises 51 individual stations distributed mainly on the northern part of Europe. The majority of these stations, 38 in total, are located in the Netherlands, and form the LOFAR Dutch array. The remaining 13 stations are built in Germany (6), the UK (1), France (1), Sweden (1), Poland (3) and Ireland (1). The construction of two additional stations in Latvia and Italy has already been planned, further expanding the size of this international facility (Fig. 7.1). The Latvian station will be completed by 2019, whereas a new generation LOFAR 2.0 station in Italy will be installed in 2021 (Section 7.2). An overview of the LOFAR stations and antennas is summarized in Tab. 7.1.

The LOFAR core consists in a strong concentration of 24 stations located within a radius of 2 km near the town of Exloo, in the Netherlands. This area was chosen because of its low population density and relatively low level of RFI. The core station distribution has been optimized to achieve the good instantaneous uv -coverage required by many of the KSPs. At the heart of the core, a 320 m diameter island referred to as “the Superterp” contains six core stations that provide the shortest baselines in the array (Fig. 7.2).

The remaining 14 stations in the Netherlands are called remote stations. They are approximately arranged in a logarithmic spiral distribution over an area roughly 180 km in diameter around Exloo.



Figure 7.1: Current (October 2018) distribution of the European LOFAR stations that have been built in Germany (6), France (1), Ireland (1), Poland (3), Sweden (1) and the UK (1). The stations of Irbene (Latvia) and Medicina (Italy) are planned to be completed by 2019 and 2021, respectively. Credit: ASTRON.



Figure 7.2: The Superterp at the heart of the LOFAR core (August 2011). The large circular island encompasses the six core stations that make up the Superterp. Three additional LOFAR core stations are visible in the upper right and lower left of the image. From van Haarlem et al. (2013).

Table 7.1: Overview of station and antenna. From van Haarlem et al. (2013).

Station configurations	Number of stations	LBA dipoles	HBA tiles	Min. baseline (m)	Max. baseline (km)
Superterp	6	2×48	2×24	68	0.24
NL Core Stations	24	2×48	2×24	68	3.5
NL Remote Stations	15	48	48	68	121
International Stations	13	96	96	68	$\sim 2000^\dagger$

Notes. The 6 stations comprising the central Superterp are a subset of the total 24 core stations. The tabulated baseline lengths represent unprojected values. Both the LBA dipoles and the HBA tiles are dual polarization. [†]The longest baseline length will increase thanks to the addition of the stations in Latvia and Italy.

The 13 international stations have been located according to indications provided by the host countries and institutions that own them. In this respect, the longest baseline distribution has not been designed to achieve optimal uv -coverage but it has been primarily determined by the existing facilities and infrastructures. The operational stations are in Germany: Effelsberg (DE601), Unterweilenbach (near Garching/Munich, DE602), Tautenburg (DE603), Potsdam-Bornim (DE604), Jülich (DE605), Norderstedt (DE609), in the UK: Chilbolton (UK608), in France: Nançay (FR606), in Sweden: Onsala (SE607), in Poland: Borowiec (PL610), Lazy (PL611), Baldy (PL612) and in Ireland: Birr (IE613). The addition of the stations in Irbene (Latvia) and Medicina (Italy), will increase the baseline in the north-south and east-west directions (see Fig. 7.1).

The datastreams from all these stations meet several non-trivial technical challenges. A dedicated high-speed (10 Gbit/s) fiber network infrastructure allows to transport the data collected by LOFAR stations to a central processing (CEP) facility where data from all stations are aligned in time, combined, and processed using a supercomputer offering a peak of processing power of 34 TFlop/s. Raw data products are then written to a storage cluster for additional post-processing. A number of reduction pipelines are available to further process the data (e.g. flagging, averaging, calibration), and are run on a dedicated computer cluster with a total processing power of approximately 10 Tflop/s. Thus, the final scientific data products are transferred to the LOFAR Long Term Archive² (LTA) at rates of 1.5 GB/s for cataloging and distribution to the community. This implies a growth of the stored data of ~ 6 PB/yr. This makes LOFAR one of the first of a number of new astronomical facilities that must deal with the transport, processing, and storage of these large amounts of data. In this sense, LOFAR represents an important technological pathfinder for new astronomical facilities in the coming decade, such as the SKA, approaching “Big data” astronomy.

7.1.2 Antennas

The fundamental receiving elements of LOFAR are two types of small, relatively low-cost antennas that together cover the 10 – 240 MHz operating bandpass. Because the optimized bandwidth of the operating frequency range spans 8 octaves, at least two types of antenna are necessary. The number of antennas included in a LOFAR station depends on its configuration (Tab. 7.1). The resulting properties are summarized in Tab. 7.2. Single antenna elements are connected via coaxial cables to the electronics housed in a cabinet located on the edge of each station, where the hardware used to perform the first data processing stage is located. The datastreams enter the digital electronics section which is mainly responsible for beam-forming. Further processing is done by the remote station processing boards utilizing low-cost, field programmable gate arrays. Following the beam-forming step, the data packets are streamed over the wide-area network to the correlator at the CEP facility.

²<https://lta.lofar.eu/>

Table 7.2: LOFAR effective area (A_{eff}), full-width half-maximum ($FWHM$) and field of view (FOV) at different frequencies and for different station configurations (D is the station diameter). From van Haarlem et al. (2013).

Freq. (MHz)	λ (m)	D (m)	A_{eff} (m ²)	$FWHM$ (deg)	FOV (deg ²)	D (m)	A_{eff} (m ²)	$FWHM$ (deg)	FOV (deg ²)	D (m)	A_{eff} (m ²)	$FWHM$ (deg)	FOV (deg ²)
NL Inner													
15	20.0	32.25	1284.0	39.08	1199.83	81.34	4488.0	15.49	188.62	65.00	3974.0	19.39	295.36
30	10.0	32.25	848.9	19.55	299.96	81.34	1559.0	7.75	47.15	65.00	2516.0	9.70	73.84
45	6.67	32.25	590.2	13.02	133.31	81.34	708.3	5.16	20.96	65.00	1378.0	6.46	32.82
60	5.00	32.25	368.5	9.77	74.99	81.34	399.9	3.88	11.78	65.00	800.0	4.85	18.46
75	4.00	32.25	243.6	7.82	47.99	81.34	256.0	3.10	7.55	65.00	512.0	3.88	11.81
NL Outer													
EU													
NL core													
120	2.50	30.75	600.0	4.75	17.73	41.05	1200.0	3.56	9.95	56.50	2400.0	2.59	5.25
150	2.00	30.75	512.0	3.80	11.35	41.05	1024.0	2.85	6.37	56.50	2048.0	2.07	3.36
180	1.67	30.75	355.6	3.17	7.88	41.05	711.1	2.37	4.42	56.50	1422.0	1.73	2.33
200	1.50	30.75	288.0	2.85	6.38	41.05	576.0	2.13	3.58	56.50	1152.0	1.55	1.89
210	1.43	30.75	261.2	2.71	5.79	41.05	522.5	2.03	3.25	56.50	1045.0	1.48	1.72
240	1.25	30.75	200.0	2.38	4.43	41.05	400.0	1.78	2.49	56.50	800.0	1.29	1.31

Low Band Antenna

The Low Band Antennas (LBA) are designed to operate from the ionospheric cutoff of the radio window near 10 MHz up to the onset of the commercial FM radio band at about 90 MHz. Due to the presence of strong RFI at the lowest frequencies and the proximity of the FM band at the upper end, this range is operationally limited to 30 – 80 MHz by default (Fig. 7.3, right panel). A digital filter is employed to suppress the response outside of this band, with the option of deselecting this filter for observations below 30 MHz.

The LBA units consist of simple dual linear polarization droop dipoles connected to a molded cap on the top of a vertical shaft of PVC pipe. The wires are connected on a ground plane consisting

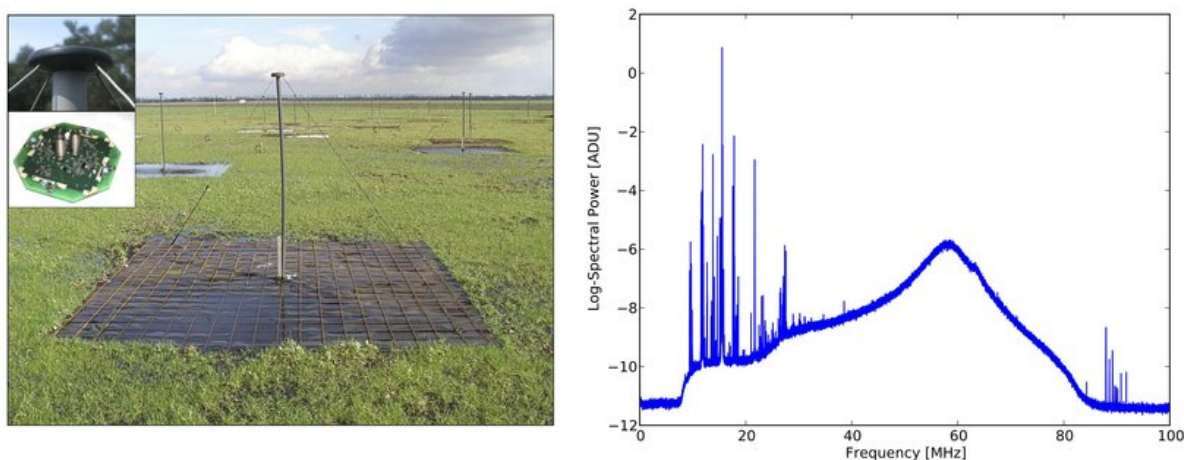


Figure 7.3: LOFAR LBA. *Left:* a single LBA dipole including the ground plane. The inset images show the molded cap containing the electronics and the wires attachment points. *Right:* LBA median response curve for all LBA dipoles of a LOFAR station. The peak of the curve is near 58 MHz. The strong RFI below 30 MHz and above 80 MHz are clearly visible. From van Haarlem et al. (2013).

of a metal mesh located above a foil sheet used to minimize the vegetation growth underneath the antenna. The resulting LBA element is shown in Fig. 7.3 (left panel). Despite this low-cost design, LBA dipoles allow an innovative all-sky covering at the lowest frequency on short timescales, fundamental to study the large scale emission from the Galaxy and for the monitoring of radio transients.

Two configurations are possible with LBA. Each consists of 48 dipoles that are grouped into an inner circle (i.e. the “LBA Inner”) and an outer annulus (i.e. the “LBA Outer”), leading to different instrument responses, as reported in Tab. 7.2.

High Band Antenna

The High Band Antennas (HBA) cover the higher end of the LOFAR spectral response from 110 MHz to 250 MHz. This frequency range is limited to the range 110 – 240 MHz due to the high RFI contamination above 240 MHz. A different (but still low-cost) design was necessary for HBA to minimize the contribution of the electronics to the system noise at this higher frequency. In Fig. 7.4, an image and the spectrum of LOFAR HBA is reported.

The HBA elements are grouped in 16 dual dipole antennas and arranged in a 4×4 grid to form a single HBA “tile”. A single “tile beam” is created by combining the signals from these 16 antenna elements in phase for a given direction on the sky. A polypropylene foil layer shields the contents of the tile by bad weather conditions.

In the core stations, HBA dipoles are distributed over two sub-stations of 24 tiles each that can be used in concert as a single station or independently. The advantage of the latter configuration is to provide more short baselines within the core, hence a significantly more uniform uv -coverage. This is fundamental for the KSPs that make a critical use of the LOFAR core such as the Epoch of Reionization experiment or the search for radio transients. In addition, the dual HBA sub-stations result in the redundancy of many short baselines yielding additional diagnostics for identifying bad phase and gain solutions during the calibration process.

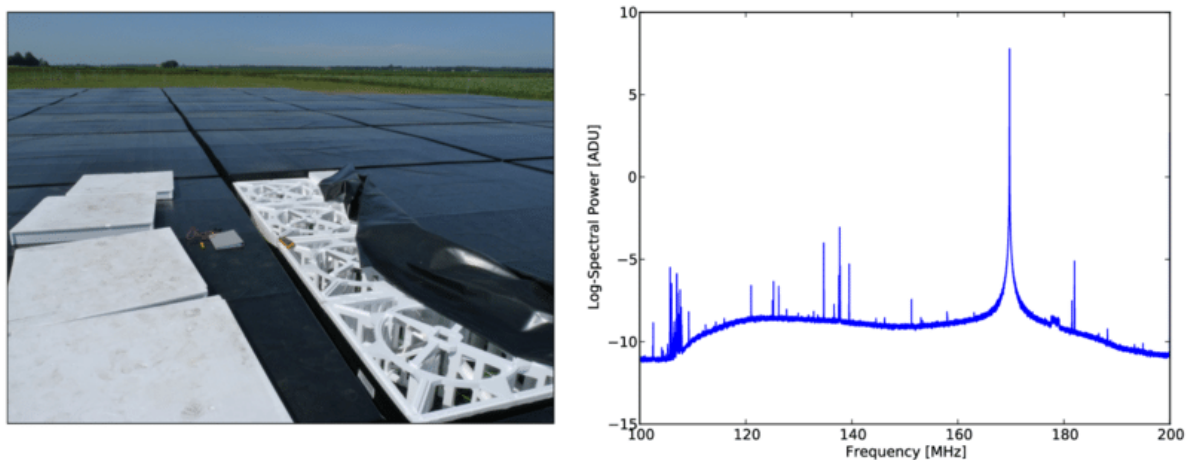


Figure 7.4: LOFAR HBA. *Left:* close-up image of a single HBA tile. The protective covering has been partially removed to expose the actual dipole assembly. *Right:* HBA median response curve for all HBA tiles of a LOFAR station. Various prominent RFI sources are clearly visible distributed across the band including the strong peak near 170 MHz corresponding to an emergency pager signal. From van Haarlem et al. (2013).

7.2 LOFAR 2.0 and LOFAR-IT

The infrastructure of LOFAR is continuously evolving. Recently, the international LOFAR board scheduled a staged expansion of the scientific and technical capabilities of LOFAR. This represents the first significant update of the instrument and it goes under the name of LOFAR 2.0. This operation will lead to the enhancement of the instrument especially in the lowest operative band, enabling an order of magnitude step in effective sensitivity and imaging capabilities in the 10 – 90 MHz. This will secure LOFAR 2.0 preeminence as the world best ultra-low frequency telescope, scientifically complementary and in no way redundant with the first phase of the SKA antennas operating at low radio frequencies, i.e. the SKA1-LOW³.

On June 2017, the Istituto Nazionale di AstroFisica (INAF) started the negotiation with ASTRON with the aim to make Italy join the LOFAR consortium. The agreement ended with the proposal of a roadmap guaranteeing Italy the role of full member of LOFAR with immediate access of INAF personnel to the KSPs. On 16 April 2018, INAF officially joined LOFAR and established the consortium LOFAR-IT⁴. Thanks to the recent involvement, Italy is now already directly involved in the technological development leading the upgrade to LOFAR 2.0. Indeed, a LOFAR 2.0 station will be installed in Medicina, near Bologna, where other radio telescopes, namely the “Croce del Nord” and a 32 m antenna, are maintained (in a radio protected area) by the Istituto di RadioAstronomia (IRA) of INAF (Fig. 7.5). This implies the participation of Italian scientists in Technical Working Groups for commissioning, data calibration, and processing.



Figure 7.5: Aerial view of the Medicina Radio Observatory. The current facilities and the proposed location for the new LOFAR 2.0 station are marked.

³https://astronomers.skatelescope.org/wp-content/uploads/2017/10/SKA-TEL-SK0-0000818-01_SKA1_Science_Perform.pdf

⁴<http://www.lofar.inaf.it> (website in Italian).

The realization of an effective e-infrastructure to support the analysis and archiving of LOFAR data is planned within INAF. Indeed, due to the unprecedented large FoV and frequency coverage/resolution, the large size of a typical LOFAR dataset after data correlation and compression requires specific computers for the data calibration (Section 7.5). Four nodes are planned in Italy: Bologna, Catania, Trieste and Torino (C3S HPC system, University of Torino). IRA has been the first institute in Italy that hosted a LOFAR node and where the analysis of these data was possible. The installation of the specific and complex software infrastructure necessary to calibrate LOFAR observations was one of the activities carried out during the PhD project. The testing of the computing performances of the LOFAR pipelines at IRA was essential before the procurement and installation of the other LOFAR Italian nodes.

7.3 The impact of LOFAR in the study of merging galaxy clusters

It has long been recognized that LOFAR has the potential to make breakthroughs in the field of galaxy cluster science (Röttgering et al. 2006, 2011; Cassano et al. 2010a, 2012; Nuza et al. 2012). Here we focus on the contribution that LOFAR has provided for this Thesis, i.e. the study of diffuse radio emission in merging galaxy clusters (Section 1.4). Complementary cluster science includes the study of starburst galaxies in clusters, the fate and evolution of radio lobes/bubbles, the distribution of the ICM magnetic fields, and the interplay between cluster radio galaxies with the ambient medium.

Radio halos and relics have steep synchrotron spectra, meaning that they are better observed at low frequencies, hence they are ideal targets for LOFAR. The dense core of LOFAR provides excellent SB sensitivity, that coupled with the low observing frequencies allows for sensitive observations. Furthermore, the arcsec resolution allows an excellent determination of the properties and flux densities of the foreground/background and embedded sources projected onto the diffuse emission.

Enßlin & Röttgering (2002) showed that high-sensitivity surveys at low radio frequencies have the potential to provide an unbiased statistical census of the radio halo population in the Universe, which, together with the models of structure formation, represents a powerful tool to constrain the link between cluster merging rate and radio halos at different cosmic epochs and for different cluster masses (Cassano et al. 2016). In addition, according to the turbulent re-acceleration scenario (Section 1.6), USSRHs should be more common in the Universe and these should be preferentially observed at lower radio frequencies (e.g. Cassano et al. 2006). The following five goals have been identified by the clusters working group within the LOFAR Surveys KSP:

1. **Discovery of new halos and relics:** increasing the number of detected halos and relics is necessary to properly analyze the statistical properties of these sources and determine their origin and evolution with cosmic time. Cassano et al. (2010a) and Nuza et al. (2012) estimated that LOFAR has the potential to discover hundreds of new halos (mostly with ultra steep spectrum) and relics up to redshift $z \sim 1$.
2. **Probing the merger–halo/relic connection:** the cross-match between the new halos and relics discovered with LOFAR with information derived by complementary X-ray, optical, and SZ observations will provide a multi-frequency view of the processes involving the formation of diffuse radio emission in galaxy clusters. The connection between non-thermal phenomena in the ICM and merging clusters started with the GMRT radio halo survey (Venturi et al. 2007, 2008, 2013; Kale et al. 2013, 2015) will be extended by LOFAR with the study of halos and relics in higher redshift systems ($z > 0.4$) and in less massive clusters (e.g. Cassano 2010; Nuza et al. 2012).

3. **Studying the spectrum of halos:** extending the frequency range where the spectrum of radio halos is observed is fundamental to understand the mechanisms responsible of particle (re)acceleration in the ICM (e.g. Brunetti 2003; Petrosian & Bykov 2008). The 10 – 240 MHz frequency range of LOFAR allows to study the spectrum of halos in this poorly constrained (to date) spectral window.
4. **Spectral and polarization studies of relics:** whilst the relic–shock connection is nowadays well established, it is still not clear whether the origin of relics is due to shock acceleration of thermal particles or to re-energization of relativistic plasma due to the shock passage (Section 1.5). The models predict different spectral behaviours and polarization properties that can be tested thanks to LOFAR high-sensitive observations at low frequencies that also probe the oldest population of (re)accelerated particles that has been advected downstream the shock.
5. **Spatial distribution of radio emission in the ICM:** the brightness fluctuations (filaments and patches) in the emission of radio halos and relics reflect the underlying distribution of magnetic fields and CRs in the ICM. Resolving scales smaller than the typical coherent scales of magnetic fields and of turbulent eddies in galaxy clusters ($\leq 30 - 50$ kpc) is crucial to probe the magnetic field power spectrum (e.g. Murgia et al. 2004; Vacca et al. 2010, 2012; Govoni et al. 2017), and the CRe acceleration and transport/diffusion processes. LOFAR high-resolution observations make possible this kind of studies.

The results obtained with LOFAR during this Thesis on two galaxy clusters are presented in Chapters 8 and 9. In the following Section, we will discuss the LOFAR survey that represents the most important source of data for cluster science.

7.4 The LOFAR Two-meter Sky Survey

One of the main goals of LOFAR since its inception is to conduct wide and deep surveys. Three surveys were designed during and after the commissioning phase:

- **MSSS** (Multifrequency Snapshot Sky Survey; Heald et al. 2015), is the first shallow survey aimed at covering the northern sky with LOFAR LBA and HBA.
- **LoTSS** (LOFAR Two-meter Sky Survey; Shimwell et al. 2017), is a sensitive, high-resolution survey of the northern sky at the frequency of 144 MHz. The survey is currently ongoing and the first full-quality partial data release incorporating direction-dependent error correction has been recently published in Shimwell et al. (2018).
- **LoLSS** (LOFAR LBA Sky Survey; de Gasperin et al., in preparation), is the ultra-low frequency counterpart of LoTSS and will produce an unprecedented view of the sky at 54 MHz. The survey is currently ongoing.

A three-tier approach to the LOFAR surveys has been adopted: Tier 1 is the widest tier and includes observations across the whole 2π steradians of the northern sky; deeper Tier 2 and Tier 3 observations are focusing on smaller areas with high-quality multi-wavelength datasets. Here we focus on the LoTSS Tier 1 survey (Shimwell et al. 2017). The primary observation objectives of LoTSS are to reach a sensitivity of less than $100 \mu\text{Jy beam}^{-1}$ at an angular resolution of $\sim 5''$ across the whole northern hemisphere by using LOFAR HBA. This can be achieved at optimal declinations with 8 hr dwell times and a frequency coverage of 120 – 168 MHz. A sensitivity of $\sim 100 \mu\text{Jy beam}^{-1}$ at 144 MHz is equivalent to a depth of $\sim 5 \mu\text{Jy beam}^{-1}$ at 1.4 GHz for a typical

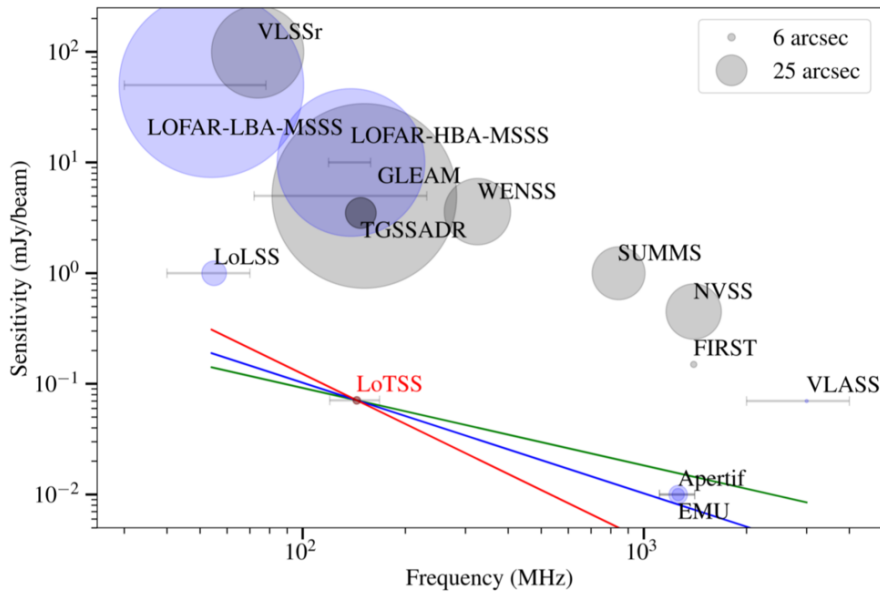


Figure 7.6: The image rms, frequency and angular resolution (linearly proportional to the radius of the markers) of LoTSS in comparison to a selection of existing wide-area completed (*grey*) and upcoming (*blue*) radio surveys. The horizontal lines show the frequency coverage for surveys with large fractional bandwidths. The *green*, *blue* and *red* lines show an equivalent sensitivity to LoTSS for compact radio sources with spectral indexes of 0.7, 1.0 and 1.5 respectively. From Shimwell et al. (2018).

radio halo in a galaxy cluster of spectral index $\alpha \sim 1.3$ (Section 1.4.2). This has not been achieved previously in any wide-area radio survey so far (see Fig. 7.6), making LoTSS at least a factor of 50 – 1000 more sensitive and 5 – 30 times higher in resolution than other recent low-frequency surveys, such as the TIFR GMRT Sky Survey Alternative Data Release (TGSS ADR; Intema et al. 2017), MSSS (Heald et al. 2015), GaLactic and Extragalactic All-sky MWA (GLEAM; Wayth et al. 2015), and the VLA Low-frequency Sky Survey Redux (VLSSr; Lane et al. 2014), as shown in Tab. 7.3.

The preliminary LoTSS images and catalogs covering right ascension from 10h45m00s to 15h30m00s and declination $45^{\circ}00'00''$ to $57^{\circ}00'00''$, i.e. the region of the Hobby-Eberly Telescope Dark Energy Experiment (HETDEX) Spring Field (Hill et al. 2008), were presented in Shimwell et al. (2017). In that release the desired imaging specifications were not achieved, as no attempt was made to correct either for errors in the beam model or for direction-dependent ionospheric distortions, which are severe in these low-frequency datasets. This led to images with a median noise of

Table 7.3: Summary of recent large area low-frequency surveys. From Shimwell et al. (2017).

Survey	Resolution ($''$)	Noise (mJy beam^{-1})	Frequency (MHz)	Area
VLSSr (Lane et al. 2014)	75	100	73 – 74.6	$\delta > -30^{\circ}$
MSSS-LBA (Heald et al. 2015)	150	50	30 – 78	$\delta > 0^{\circ}$
MSSS-HBA (Heald et al. 2015)	120	10	119 – 158	$\delta > 0^{\circ}$
GLEAM (Wayth et al. 2015)	150	5	72 – 231	$\delta < +25^{\circ}$
TGSS ADR (Intema et al. 2017)	25	3.5	140 – 156	$\delta > -53^{\circ}$
LoTSS (ongoing)	5	0.1	120 – 168	$\delta > 0^{\circ}$

Notes. This is an attempt to provide a fair comparison of sensitivities and resolutions, but both the sensitivity and resolution achieved varies within a given survey.

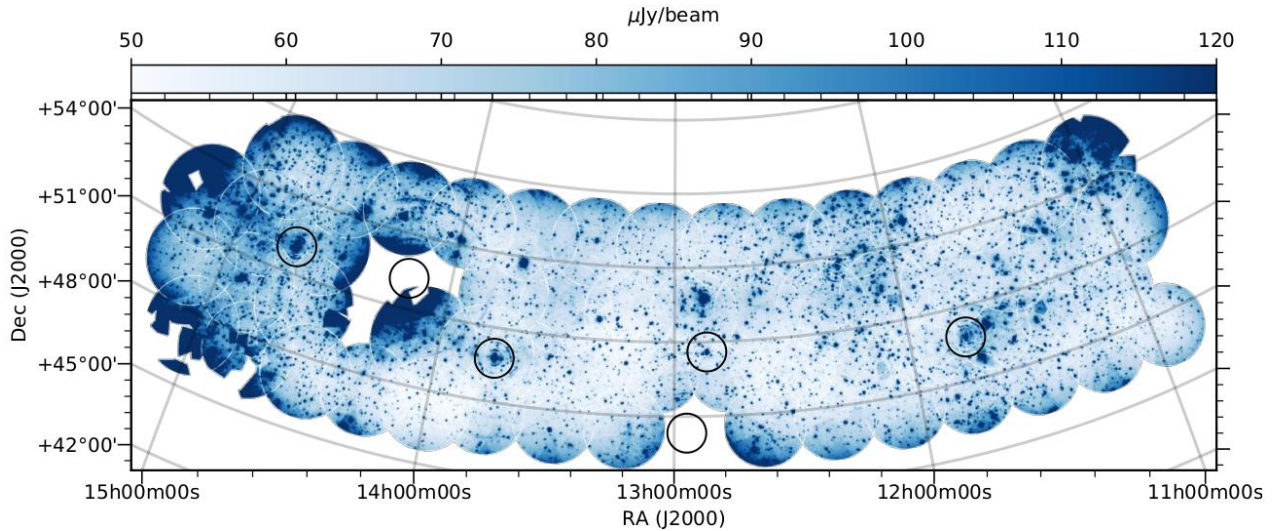


Figure 7.7: A LoTSS noise mosaic where the median noise level is $71 \mu\text{Jy beam}^{-1}$. Many of the regions with high noise levels are caused by dynamic-range limitations. Black circles mark the location of potentially problematic objects from the revised 3C catalog of radio sources (Bennett 1962). From Shimwell et al. (2018).

$500 \mu\text{Jy beam}^{-1}$ at $25''$ resolution. Thanks to the recent progress in improving the quality, speed and robustness of the calibration of direction-dependent effects (e.g. Tasse 2014a; Tasse et al. 2018; Yatawatta 2015; van Weeren et al. 2016b), it has been shown that the desired imaging specifications of LoTSS are feasible (e.g. Hardcastle et al. 2016; Williams et al. 2016). Indeed, we recently published the first full-quality public data release⁵ of the HETDEX Spring Field in Shimwell et al. (2018). In this release, the fully-automated direction-dependent calibration and imaging pipeline developed for LoTSS allowed us to reach a median sensitivity of $71 \mu\text{Jy beam}^{-1}$ (Fig. 7.7). A total of 325,694 sources have been detected with a signal of at least five times the noise in the region of the HETDEX Spring Field, meaning a source density a factor of ~ 10 higher than the most sensitive existing very wide-area radio-continuum surveys. The optical identification of the radio sources with the photometric redshift estimates and host galaxy properties have been presented in Williams et al. (2018) and Duncan et al. (2018). The redshift measurements will be improved in the near future thanks to the multi-object and integral field spectrograph of the WEAVE (Dalton et al. 2012, 2014) as part of the WEAVE-LOFAR survey (Smith et al. 2016).

7.5 LOFAR HBA data calibration

Observations at low radio frequency require advanced calibration and specific processing techniques to obtain deep high-fidelity images.

One of the main calibration challenge is the correction for the delay differences between antenna stations introduced by ionospheric distortions that cause phase errors in the measured visibilities (e.g. Lonsdale 2005; Intema et al. 2009). In the case of a large array such as LOFAR, these corrections must be applied direction-dependently, being related to the free electron column density along each line of sight through the ionosphere. Another challenge is given by the time-varying station beam shape. Indeed, LOFAR stationary antenna units imply that sources are tracked across their motion in the sky by adjusting the delays between the dipole elements. Further errors are due to small differences in the station beam models and shapes. These and the other systematics effects inherent

⁵<http://lofar.strw.leidenuniv.nl>

LOFAR data has been recently reviewed in de Gasperin et al. (2018).

Recent advances in the calibration and imaging techniques allow to fully exploit LOFAR capabilities. In particular, the LoTSS pointings are processed using the novel approaches to estimate direction-dependent effects and to apply these during the images developed in KillMS (kms; Tasse 2014b,a; Smirnov & Tasse 2015) and DDFACET (Tasse et al. 2018), respectively⁶.

The LOFAR data presented in Chapters 8 and 9 have been processed using the facet calibration scheme, i.e. another approach that has been successfully applied to image several galaxy clusters observed with LOFAR HBA. The two main steps of this calibration scheme are outlined below; a full description of the procedure is reported in van Weeren et al. (2016b), Williams et al. (2016) and de Gasperin et al. (2018).

1. In the first step, direction-independent calibration (PREFACTOR⁷ pipeline) is performed. In this step, the flux calibrator data are averaged in time and frequency and bad quality data are flagged. Clock offsets and complex gains for different antenna stations are calibrated off a calibrator model adopting the absolute flux density scale of Scaife & Heald (2012). The amplitude and clock solutions are then transferred to the target data before an initial phase calibration against a sky model generated from the TGSS ADR (Intema et al. 2017) or, alternatively, a Global Sky Model (GSM) for LOFAR⁸ generated from the VLSSr (Lane et al. 2014), the Westerbork Northern Sky Survey (WENSS; Rengelink et al. 1997) and the NRAO VLA Sky Survey (NVSS; Condon et al. 1998). In the second step, wide-field images covering the full LOFAR FoV are made from the products of the first step using WSCLEAN (Offringa et al. 2014). The Python Blob Detector and Source Finder (PYBDSF; Mohan & Rafferty 2015) software is then used to detect sources which are then subtracted from the uv -data using their clean component models. Images are produced at medium ($\sim 40'' \times 30''$) and low resolution ($\sim 120'' \times 100''$) to ensure that both compact and extended sources are subtracted out. The image sizes are about $12^\circ \times 12^\circ$ and $30^\circ \times 30^\circ$ for medium and low resolution, respectively.
2. In the direction-dependent calibration step (FACTOR⁹ pipeline), nearly thermal noise limited images can be produced. It operates by using bright sources in the field to calibrate the phases and amplitudes in a restricted portion of the sky seen by the interferometer, i.e. a “facet”. This is needed as the LOFAR primary beam is large, requiring many different corrections for ionospheric distortions and beam model errors across the FoV. For this reason, the FoV (usually a region within 2.5° from the pointing center) is divided into tens of facets using a Voronoi tessellation scheme (Fig. 7.8). This ensures that each point on the sky lies within the facet of the nearest calibrator source, where the calibration solutions are reasonably similar. Facets are typically processed in order of decreasing flux density of the calibrator source. After a number of self-calibration cycles on the facet calibrator, the fainter sources that were subtracted in the second step are added back into the data and are calibrated using the solutions derived from the facet calibrator. An updated sky model of the region covered by the facet is obtained by subtracting the components of the processed facet from the uv -data. The uv -data used for the calibration of the subsequent facet have smaller systematics due to the source subtraction and the effective noise reduction. This process is iteratively repeated until all the desired directions have been calibrated.

⁶The kms and DDFACET pipelines are available at <https://github.com/saopicc>

⁷<https://github.com/lofar-astron/prefactor>

⁸<https://support.astron.nl/LOFARImagingCookbook>

⁹<https://github.com/lofar-astron/factor>

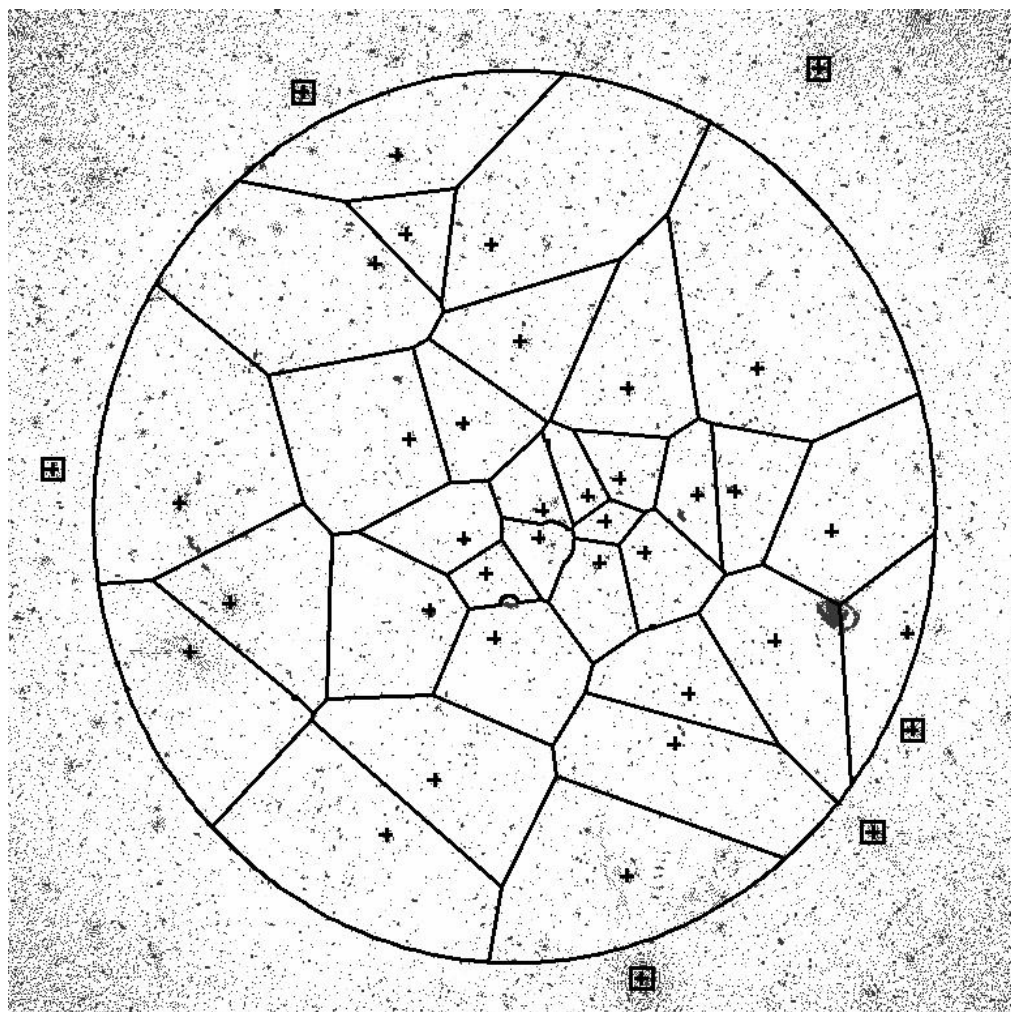


Figure 7.8: A LOFAR pointing tessellated into facets by the FACTOR pipeline. Crosses mark the positions of the facet calibrators. The displayed image is $6^\circ \times 6^\circ$.

It is worth to remark that LOFAR calibration pipelines must deal with large volume datasets¹⁰ and require a considerable amount of computing power and storage. For these reasons, a specific machine with a single 20 core (two 10-core Xeon E5-2640v4 2.4 GHz CPUs), 512 GB of RAM, and 40 TB of local disk storage has been bought at IRA (Section 7.2). Despite this powerful machine, the data reduction requires still several days/weeks of processing time for a single 8 hr observing run.

¹⁰A typical 8 hr LoTSS pointing consists in ~ 16 TB archived data, together with ~ 350 GB for each 10 min calibrator observation.

The spectacular cluster chain Abell 781 as observed with LOFAR, GMRT, and *XMM-Newton*[†]

ABSTRACT

The Abell 781 complex is a spectacular system composed of an apparent chain of clusters on the sky. Its main component is undergoing a merger, and hosts peripheral emission, classified as a candidate radio relic, as well as a disputed radio halo. We use new LOFAR observations at 143 MHz and archival GMRT observations at 325 and 610 MHz to study radio emission from non-thermal components in the ICM of Abell 781. Complementary information comes from *XMM-Newton* data that allow us to investigate the connection with the thermal emission and its complex morphology. We speculate that the peripheral source is related to the interaction between a head tail radio galaxy and shock. However, the current data allow us only to set an upper limit of $\mathcal{M} < 1.4$ on the Mach number of this putative shock. Instead, we successfully characterize the SB and temperature jumps of a shock and two cold fronts in the main cluster component of Abell 781. Their positions suggest that the merger is involving three sub-structures. We do not find any evidence for a radio halo neither at the center of this system nor in the other clusters of the chain. We placed an upper limit on the diffuse radio emission in the main cluster of Abell 781 that is a factor of 2 below the current $P_{1.4} - M_{500}$ relation for giant radio halos.

8.1 Introduction

Abell 781 is a complex system with multiple galaxy cluster components (Wittman et al. 2006, 2014; Abate et al. 2009; Geller et al. 2010; Cook & Dell’Antonio 2012). In the X-rays, it appears as a chain with four prevailing clusters that extends over $\sim 25'$ in the E-W direction (Wittman et al. 2006; Sehgal et al. 2008). Fig. 8.1 shows an *XMM-Newton* image of the system where we have labelled the clusters following Sehgal et al. (2008) and reported the redshifts from Geller et al. (2010). These four clusters lie in two different redshift planes: the “Main” (that hereafter we will refer to simply as A781) and “Middle” are located at $z \sim 0.30$, whereas the “East” and “West” are

[†]Based on Botteon et al. (2018c).

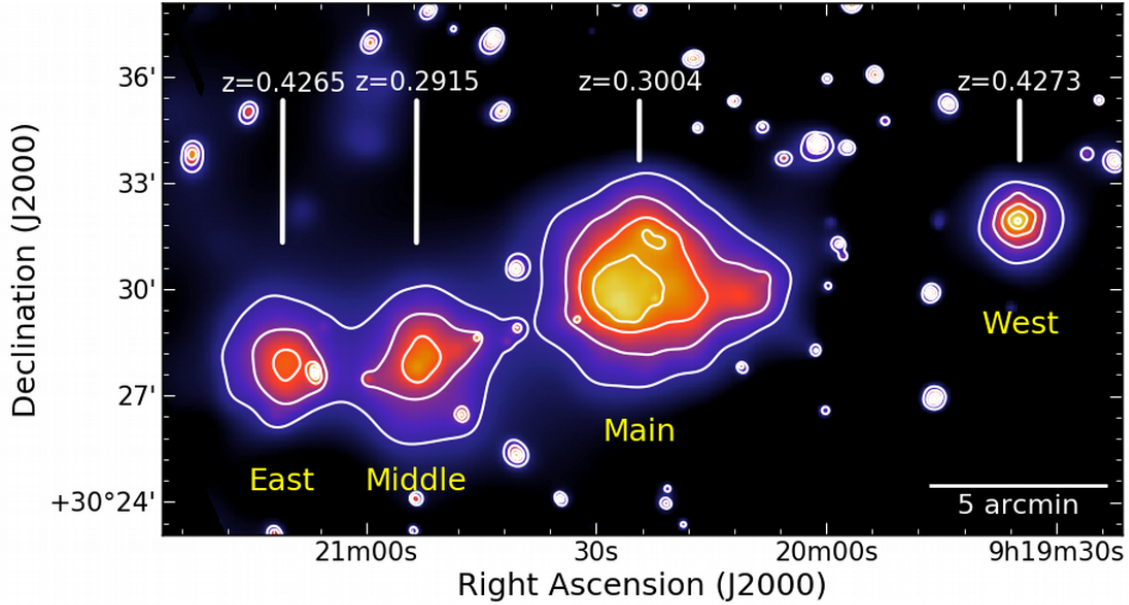


Figure 8.1: Adaptively smoothed, background-subtracted and exposure-corrected *XMM-Newton* mosaic image in the 0.5 – 2.0 keV band of the Abell 781 complex. Contours are spaced by a factor of 2 starting from 3.5×10^{-6} counts s^{-1} pixel $^{-1}$.

located at $z \sim 0.43$ (therefore they are not related to the other two clusters of the system). The mass of the main cluster is $M_{500} = (6.1 \pm 0.5) \times 10^{14} M_{\odot}$, as reported in the second *Planck* catalog of SZ sources (PSZ2; Planck Collaboration XXVII 2016).

Observations taken with the GMRT at 610 MHz revealed the presence of a peripheral source at the boundary of the X-ray thermal emission of A781 that was suggested to be a candidate radio relic by Venturi et al. (2008). Although this interpretation would be in agreement with the location of the emission in the cluster outskirts, the source morphology is puzzling: neither arc-like nor elongated, its morphology changes from 610 to 325 MHz (Venturi et al. 2011). The source is also detected with the VLA at 1.4 GHz (Govoni et al. 2011). The presence of a central radio halo in A781 is also disputed, it was observed at high frequency with the VLA (Govoni et al. 2011) but not at lower frequencies with the GMRT (Venturi et al. 2008, 2011, 2013).

In this Chapter, we present a new LOFAR observation at 120 – 168 MHz and the reanalysis of archival GMRT and *XMM-Newton* observations of the cluster chain Abell 781. In particular, we focus on the main merging cluster of the complex to study the peripheral source and shed light on the presence of the radio halo that has been reported in the literature.

8.2 Observations and data reduction

8.2.1 LOFAR

We analyzed the LoTSS (Shimwell et al. 2017, 2018) pointing closest to A781 (offset by $\sim 1.5^{\circ}$). The observation is 8 hr long and used the Dutch HBA array operating at 120 – 168 MHz (see Tab. 8.1 for more details). The data reduction performed in this work followed the facet calibration scheme developed to analyze LOFAR HBA data outlined in Section 7.5.

The LOFAR images reported in the Chapter were produced with WSCLEAN v2.4 (Offringa et al. 2014) and have a central observing frequency of 143 MHz. The imaging was done using the multi-scale multi-frequency deconvolution algorithm described in Offringa & Smirnov (2017). Data were calibrated (and subsequently imaged) applying an inner uv -cut of 200λ to get rid of some noise

Table 8.1: Summary of the radio observations used in this work.

	LOFAR	GMRT	GMRT
Project code	LC6_015	11TVA01	08RCA01
Observation date	2016 Dec 02	2007 Jan 29	2005 Oct 02
Total on-source time (hr)	8.0	9.2	3.4
Flux calibrator	3C196	3C286	3C48
Total on-calibrator time (min)	10	30	34
Central frequency (MHz)	143	325	610
Bandwidth (MHz)	48	33	33

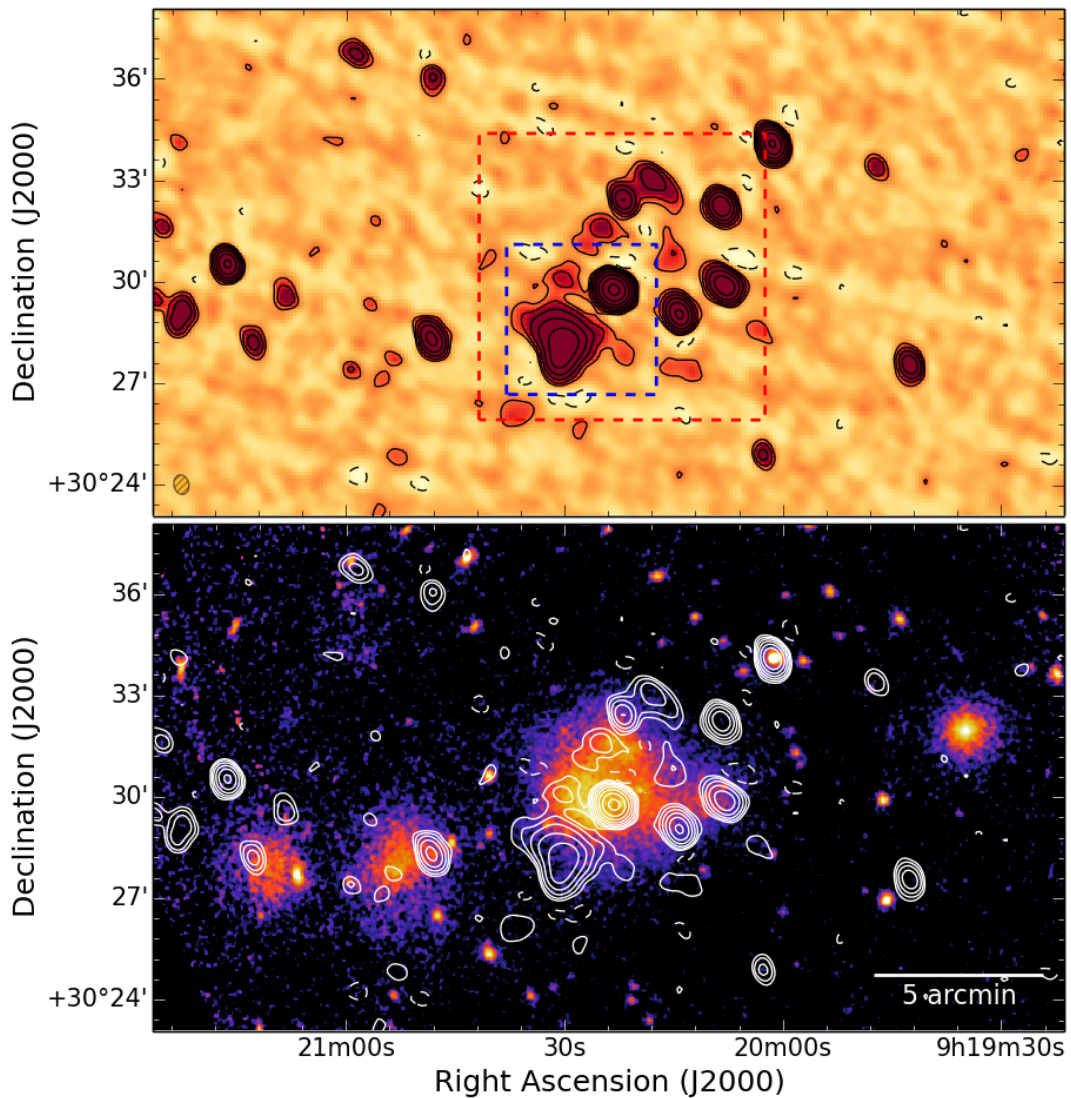


Figure 8.2: *Top:* LOFAR 143 MHz image at a resolution of $34.9'' \times 26.6''$ (the beam is shown in the bottom left corner). Contours are spaced by a factor of 2 starting from 3σ , where $\sigma = 650 \mu\text{Jy beam}^{-1}$. The negative -3σ contours are shown in dashed. Dashed boxes mark the FoV of the other images reported along the Chapter. *Bottom:* XMM-Newton smoothed image with the LOFAR contours overlaid.

coming from RFI on the shortest baselines. The largest angular scale that is possible to recover with this uv -cut is $17.2'$, larger than the separation between each cluster of the chain. The uv -tapering of visibilities and the Briggs weighting scheme (Briggs 1995) with different robust values were used to obtain two images with different resolutions. The low-resolution image of the cluster chain is shown in Fig. 8.2.

It is known that the LOFAR flux density scale can show systematic offsets and needs to be corrected relying on other surveys (e.g. van Weeren et al. 2016b; Hardcastle et al. 2016). In this respect, we cross-matched a catalog of LOFAR point-sources extracted in the facet containing A781 with the WENSS at 325 MHz (Rengelink et al. 1997). We rescaled the WENSS flux densities at 143 MHz assuming a spectral index $\alpha = 0.75$. The adopted correction factor of 0.85 on LOFAR flux densities was derived from the mean flux density ratio LOFAR/WENSS₁₄₃. We conservatively set a systematic uncertainty of 20% on LOFAR flux density measurements.

8.2.2 GMRT

GMRT observations on A781 at 325 MHz and at 610 MHz have been presented in Venturi et al. (2008, 2011). In this work, we reanalyzed these datasets with the SPAM package (Intema et al. 2009) and produced new images of the cluster. The details of the observations are shown in Tab. 8.1. The data reduction with SPAM consists of a standard-automated pipeline that includes data averaging, instrumental calibration, multiple cycles of self-calibration and flagging of bad data. Furthermore, the bright sources within the primary beam are selected and used to perform a direction-dependent calibration, whose solutions are interpolated to build a global ionospheric model to suppress ionospheric phase errors. The calibrated data are then reimaged with WSCLEAN v2.4 (Offringa et al. 2014), as described at the end of Section 8.2.1. For more details on the SPAM pipeline we refer the reader to Intema et al. (2009, 2017). The flux density scale in the images was set by calibration on 3C48 (at 610 MHz) and 3C286 (at 325 MHz) using the models from Scaife & Heald (2012). No flux scale offset (e.g. due to the system temperature, see Sirothia 2009) was found cross-matching a catalog of GMRT sources with the WENSS (Rengelink et al. 1997). Residual amplitude errors are estimated to be 15% at 325 MHz and 10% at 610 MHz, in agreement with other studies (e.g. Chandra et al. 2004).

8.2.3 XMM-Newton

The Abell 781 complex was observed twice with *XMM-Newton* (ObsID: 0150620201 and 0401170101), for a total exposure time of 98.7 ks. Data reduction was performed using the pipeline developed to analyze the observations of the X-COP (Eckert et al. 2017a), fully described in Ghirardini et al. (2019). The pipeline uses the ESAS tools developed within the *XMM-Newton* SAS v14.0.0 to analyze EPIC observations. Briefly, the tasks `mos-filter` and `pn-filter` were used to filter out observation periods affected by soft proton flares. Residual soft proton flare contamination was checked by measuring in a hard band the count rates of the MOS and pn cameras in the exposed and unexposed parts of the detectors FoV (inFoV/outFoV, see Leccardi & Molendi 2008). The results of this procedure are summarized in Tab. 8.2. For MOS cameras, values of inFoV/outFoV below 1.15 indicate absence of residual soft proton flares while values between 1.15 and 1.30 indicate slight contamination of soft proton flares. Single detector count images were then combined to produce the mosaic EPIC background-subtracted and exposure-corrected images in the 0.5 – 2.0 keV band shown in Figs. 8.1 and 8.2. The tasks `ewavelet` and `cheese` were used to detect and exclude point sources before the spectral region extraction and SB profile fitting. The output files of the routines were checked for missed sources and/or false detections; therefore, contaminating point sources were excised.

Table 8.2: Clean exposure time and inFoV/outFoV ratio of each EPIC detector for the two *XMM-Newton* observations used in this work (medium filter, full frame science mode).

	Exposure (ks)	inFoV/outFoV
ObsID	0150620201	
MOS1	14.5	1.157 ± 0.051
MOS2	14.2	1.070 ± 0.044
pn	10.5	1.199 ± 0.055
ObsID	0401170101	
MOS1	58.6	1.106 ± 0.025
MOS2	60.8	1.049 ± 0.022
pn	47.5	1.232 ± 0.026

Spectra of the two ObsIDs were extracted in the same regions and jointly fitted in the 0.5 – 12.0 keV band (MOS detectors) and in the 0.5 – 14.0 keV band (pn detector) with XSPEC v12.9.0o (Arnaud 1996) adopting Cash statistics (Cash 1979). The energy range 1.2 – 1.9 keV was excluded in the fit due to strong instrumental emission lines; for the pn detector, we excluded for the same reason also the range 7.0 – 9.2 keV. The NXB was modeled with a phenomenological model that includes a number of fluorescence lines (see Ghirardini et al. 2019). The local sky background was estimated in a cluster free region adopting a model composed of a CXB component, modeled with an absorbed power-law with photon index $\Gamma = 1.46$ (De Luca & Molendi 2004), and of a Galactic foreground component, modeled with two thermal plasmas (one unabsorbed and the other absorbed) with solar metallicity and temperatures 0.11 keV and 0.28 keV (McCammon et al. 2002). The ICM emission was modeled with an absorbed thermal model with normalization, metallicity and temperature free to vary in the fit. Galactic absorption in the direction of the cluster was set to $N_{\text{H}} = 1.65 \times 10^{20} \text{ cm}^{-2}$ (Kalberla et al. 2005).

SB profiles were extracted and fitted with PROFFIT v1.5 (Eckert et al. 2011) from the EPIC mosaic image in the 0.5 – 2.0 keV band. All the profiles reported in this work were convolved for the *XMM-Newton* PSF, that was modeled with the psf task (for more details, see Appendix C in Eckert et al. 2016b).

8.3 Results

8.3.1 The peripheral emission in A781

The peripheral diffuse radio emission in the SE outskirts of the main cluster (Fig. 8.3) was classified as a candidate radio relic by Venturi et al. (2008). The source has been observed with the GMRT (Venturi et al. 2008, 2011, 2013) and VLA (Govoni et al. 2011); it is also detected in the NVSS (Condon et al. 1998) but not in the Faint Images of the Radio Sky at Twenty-centimeter survey (FIRST; Becker et al. 1995).

In Fig. 8.4, we show our images of the peripheral emission at three frequencies with comparable resolution obtained from the new LOFAR data and from the reanalysis of the archival GMRT observations. The flux densities measured within the LOFAR 3σ contour in these images are $S_{143\text{MHz}} = 267 \pm 53 \text{ mJy}$, $S_{325\text{MHz}} = 94 \pm 14 \text{ mJy}$ and $S_{610\text{MHz}} = 38 \pm 4 \text{ mJy}$, where the quoted errors have been estimated via Eq. 2.1. The source morphology is consistent between 143 MHz and 610 MHz and appears slightly more extended at low frequency, with a largest linear size of ~ 550

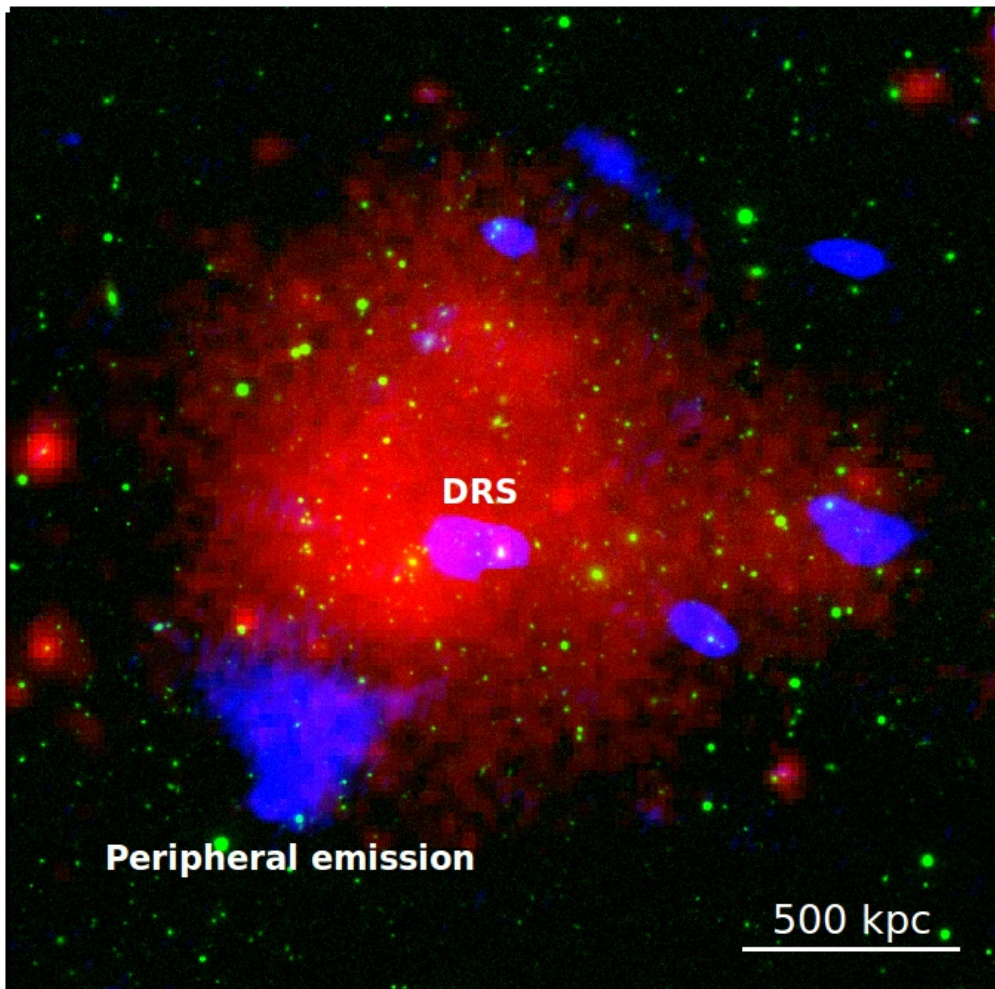


Figure 8.3: Composite multi-wavelength image of A781 (red region of Fig. 8.2). Optical SDSS_{g,r,i} mosaic is shown in *green*. Radio emission at 143 MHz from LOFAR is shown in *blue*. X-ray *XMM-Newton* emission is shown in *red*.

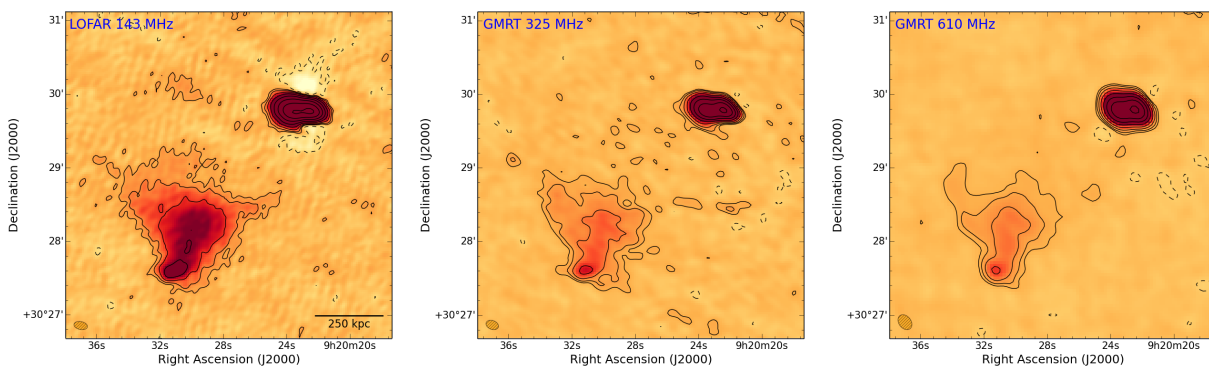


Figure 8.4: The peripheral emission in A781 (blue region of Fig. 8.2) as observed in the radio band with LOFAR at 143 MHz (*left*) and with the GMRT at 325 MHz (*center*) and 610 MHz (*right*). Contours are spaced by a factor of 2 starting from 3σ , where $\sigma_{143} = 270 \mu\text{Jy beam}^{-1}$, $\sigma_{325} = 150 \mu\text{Jy beam}^{-1}$ and $\sigma_{610} = 120 \mu\text{Jy beam}^{-1}$. The negative -3σ contours are shown in dashed. The beam sizes are $11.1'' \times 6.5''$ (143 MHz), $10.6'' \times 7.2''$ (325 MHz) and $13.5'' \times 9.8''$ (610 MHz) and are shown in the bottom left corners.

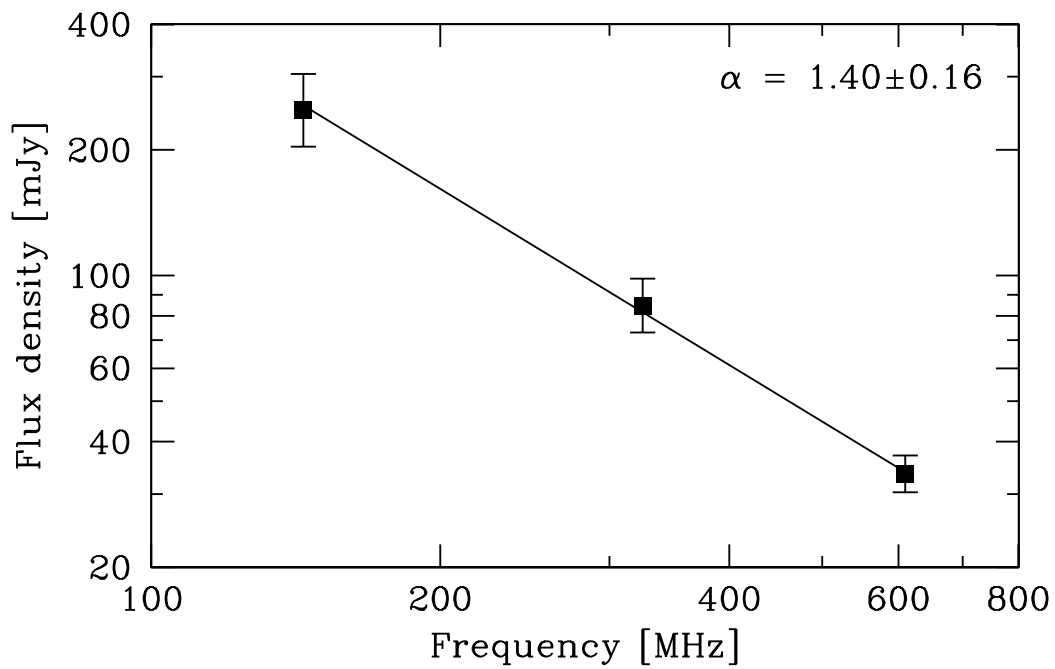


Figure 8.5: Integrated spectrum of the peripheral source in A781.

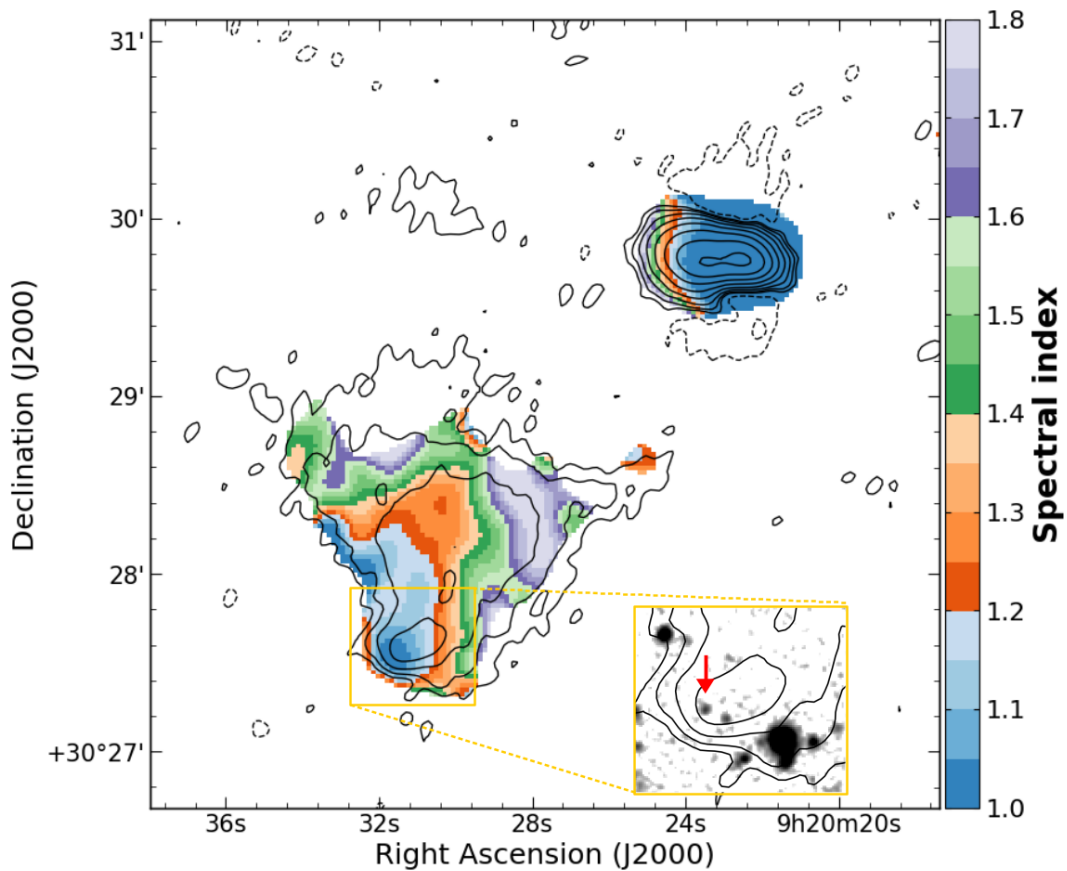


Figure 8.6: Spectral index map of the peripheral emission between 143 MHz and 610 MHz at a resolution of $15'' \times 15''$ overlaid on the LOFAR contours of Fig. 8.4. Pixels with values below 3σ were blanked. The corresponding error map is reported in Fig. F.1. The inset panel shows an SDSS image with two candidate optical counterparts.

kpc. It displays a peculiar wedge shape characterized by a bright knot of emission in the SE which is attached to a high SB spine that is extended NW in the direction of the central double radio source (DRS; cf. Fig. 8.3). The radio emission shows a sharper edge toward the E direction where also the X-ray thermal emission fades away.

We measured the spectral index properties of the source from images produced with a uniform weighting scheme and with matched uv -range. The integrated spectral index computed between the three frequencies is $\alpha = 1.40 \pm 0.16$ (Fig. 8.5), consistent within the errors with that reported by Venturi et al. (2011). The k -corrected and spectral index rescaled radio power of the source at 1.4 GHz is $P_{1.4} \sim 3.5 \times 10^{24} \text{ W Hz}^{-1}$ (Eq. 1.23), assuming that it is located at the cluster redshift $z = 0.3004$. The spectral index map calculated from the 143 MHz and 610 MHz images convolved to the same resolution of $15'' \times 15''$, corrected for any position misalignment, and regridded to identical pixel size, is shown in Fig. 8.6 (the error map is reported in Appendix F). This map shows that the SE bright knot of emission has also a flatter spectral index, possibly arising from the radio emission of an AGN. In the Sloan Digital Sky Survey (SDSS; York et al. 2000), two possible optical counterparts are observed in this position (see inset panel in Fig. 8.6); these will be discussed in Section 8.4.1. The absence of significant compact emission at a level of $0.5 \text{ mJy beam}^{-1}$ in the FIRST data suggests that the AGN is not active anymore. The diffuse source exhibits a hint of spectral index flattening in coincidence with the E edge of the radio emission. The spectral index gradually steepens in the direction of the DRS, where $\alpha \sim 1.8$. A similar spectral trend can be inferred also from Fig. 5 of Govoni et al. (2011), despite the lower resolution ($53'' \times 53''$) of their spectral index map. As a further check, we evaluated the spectral index of the peripheral source in sectors, as shown in Fig. 8.7. This confirms a spectral gradient in both the E-W and S-N directions. As discussed in Section 1.4.1, spectral index steepening toward the cluster center has been observed in a number of radio relics (e.g. Giacintucci et al. 2008; van Weeren et al. 2010; de Gasperin et al. 2015a; Hoang et al. 2018a).

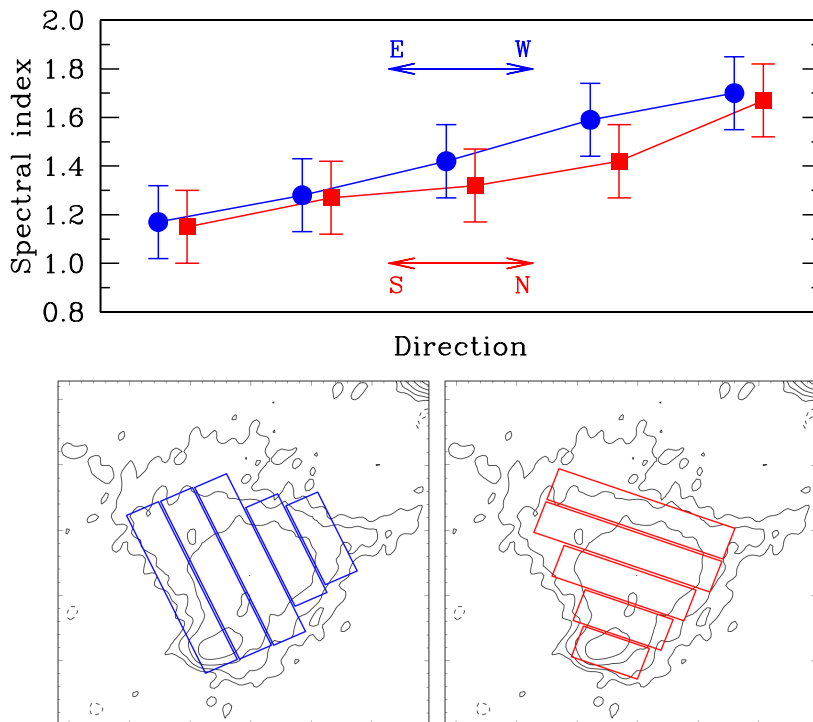


Figure 8.7: Spectral index trend of the peripheral emission toward the E-W (*blue*) and S-N (*red*) directions. The spectral index has been computed between 143 and 610 MHz in the sectors shown in the bottom panels.

8.3.2 X-ray discontinuities in the ICM

The visual inspection of the *XMM-Newton* image in the 0.5 – 2.0 keV band suggests the presence of three SB jumps in A781, toward the SE, NW and W directions, that have not been studied in the literature so far. We investigated the possible features with the fitting of the SB profiles extracted in the sectors highlighted in Fig. 8.8. A broken power-law model (Eq. 1.21) was assumed to fit the data as it generally provides a good description of discontinuities in the ICM, namely shocks and cold fronts (e.g. Markevitch & Vikhlinin 2007; Owers et al. 2009; Botteon et al. 2018a). A single power-law model was also fitted for comparison. The three profiles are shown in Fig. 8.9. The broken-power law models always yield the best description of the data, confirming the existence of drops in SB. The compression ratios between the downstream and upstream density are $\mathcal{C} = 1.9 \pm 0.1$ (SE), $\mathcal{C} = 2.0 \pm 0.2$ (NW) and $\mathcal{C} = 2.2^{+0.4}_{-0.3}$ (W).

In order to determine the nature of the edges (shocks or cold fronts), a careful spectral analysis is necessary. Shocks are characterized by higher temperature and pressure in the downstream region than in the upstream region. Instead, the temperature jump is inverted and the pressure is almost continuous across cold fronts (Section 1.3.2). We extracted and fitted spectra in the downstream and upstream regions delimited by the dashed and solid lines in Fig. 8.8. The pressure jump \mathcal{P} at the discontinuity can be computed as the product between the density and temperature ratios¹ achieved

¹Although this procedure combines a deprojected density jump with a temperature evaluated along the line of sight, previous studies have shown that projection effects do not have a strong impact (e.g. Botteon et al. 2018a).

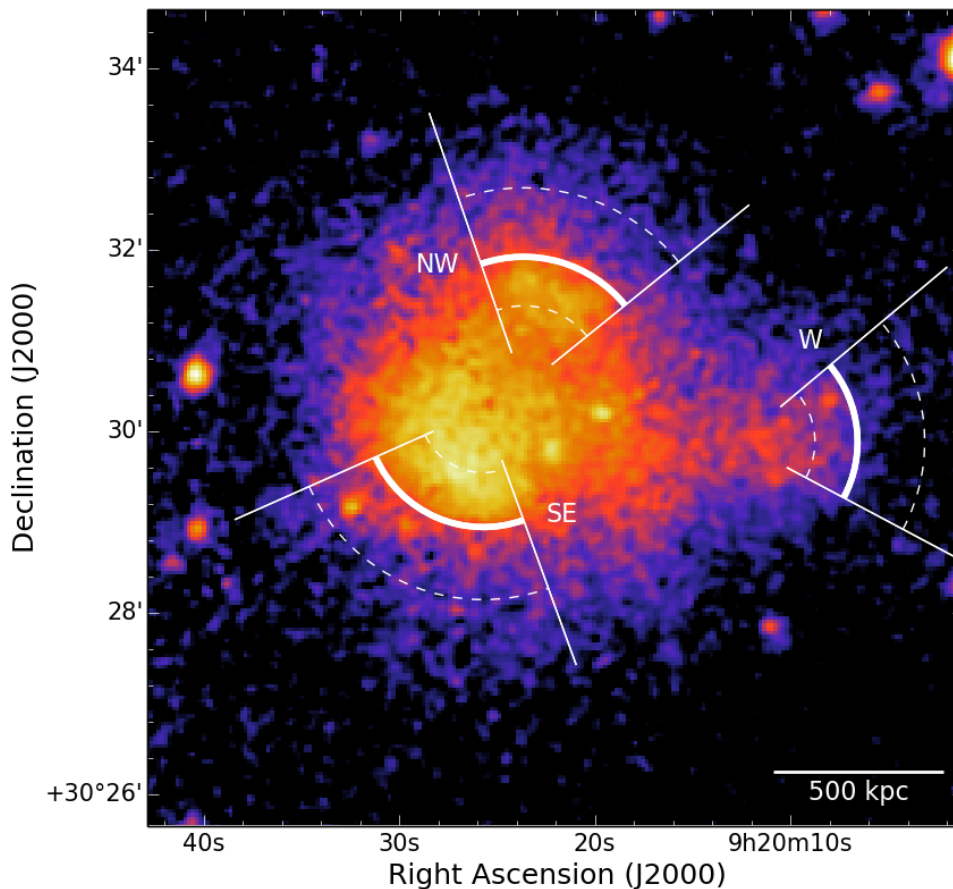


Figure 8.8: *XMM-Newton* smoothed image of A781 (red region of Fig. 8.2) with the sectors used for the spectral and spatial analysis. The positions of the edges are marked by *thick lines* while *dashed lines* limit the regions used for the spectral analysis.

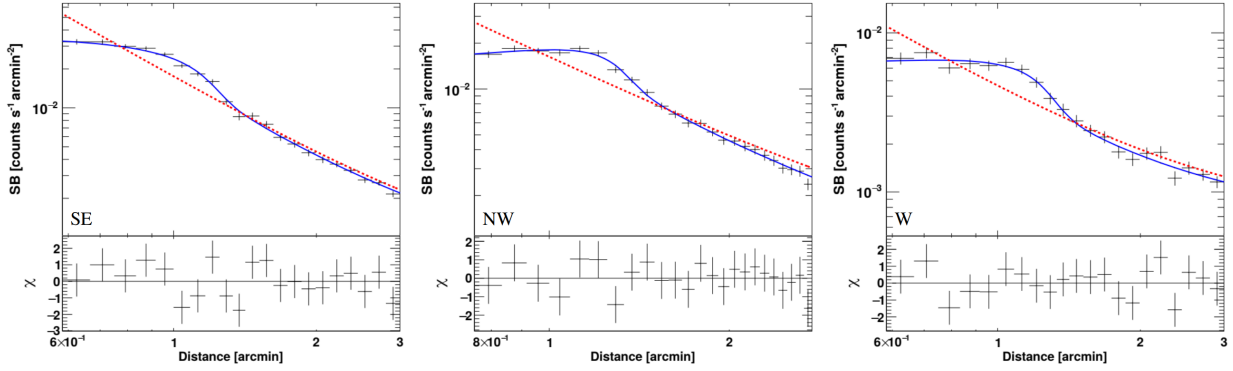


Figure 8.9: *XMM-Newton* SB profiles in the 0.5 – 2.0 keV energy band extracted in the white sectors of Fig. 8.8. The best-fitting broken power-laws with residuals and single power-laws are reported in *solid blue* and *dashed red*, respectively. The residuals at the bottom of the plots refer to the broken power-law fits.

with the spatial and spectral analysis, respectively. Results are summarized in Tab. 8.3. All the SB discontinuities are associated with temperature jumps. For the SE and NW edges, the downstream temperature is lower and the pressure is consistent to be constant across the discontinuities, as expected in the case of cold fronts. For the W edge, the downstream gas is hotter and a pressure jump is observed, revealing the shock nature of the discontinuity. We applied the Rankine-Hugoniot equations (e.g. Landau & Lifshitz 1959) to derive independent constraints of the shock Mach number from the temperature (Eq. 1.17) and density (Eq. 1.18) jumps, leading to consistent values of $\mathcal{M}_{kT} = 1.6 \pm 0.3$ and $\mathcal{M}_{SB} = 1.9^{+0.4}_{-0.3}$, respectively. We note that no diffuse radio emission in form of radio relic is observed at the location of this shock.

Finally, we searched for a possible X-ray discontinuity at the position of the peripheral diffuse radio emission. In particular, a shock could be responsible for the peculiar morphology and the observed spectral index trend of the source (Fig. 8.6). Moreover, a number of merger shocks have been found ahead of cold fronts (e.g. Vikhlinin et al. 2001b; Markevitch et al. 2002; Russell et al. 2010, 2012; Emery et al. 2017), and it is possible that also the SE cold front detected in A781 is following a shock. In this respect, we extracted and fitted a SB profile in a box across the radio edge in the E that shows a hint of spectral index flattening, as shown in Fig. 8.10. However, the current *XMM-Newton* data is not deep enough to characterize this potential feature due to the low count statistics of this region. We used the MULTINEST Bayesian nested sampling algorithm (Feroz et al. 2009) interfaced in PROFFIT to determine an upper limit of $\mathcal{C} < 1.6$ (90% confidence level) on the compression factor by fitting a broken power-law and assuming that the discontinuity is located at the edge of the radio emission. This implies that if a shock exists, it is weak ($\mathcal{M} < 1.4$). Projection effects (if any) should play a small role as the detection of the two diametrically opposite cold fronts in the NW and SE directions suggests that the merger is occurring approximately on the plane of the sky.

Table 8.3: Properties measured across the X-ray SB discontinuities.

	SE	NW	W
kT_d (keV)	$5.4^{+0.4}_{-0.2}$	$4.1^{+0.2}_{-0.2}$	$4.2^{+0.6}_{-0.4}$
kT_u (keV)	$9.5^{+1.6}_{-1.3}$	$7.4^{+1.0}_{-1.0}$	$2.6^{+0.5}_{-0.5}$
\mathcal{C}	$1.9^{+0.1}_{-0.1}$	$2.0^{+0.2}_{-0.2}$	$2.2^{+0.4}_{-0.3}$
\mathcal{P}	$1.0^{+0.1}_{-0.1}$	$1.1^{+0.1}_{-0.1}$	$3.5^{+0.9}_{-0.8}$

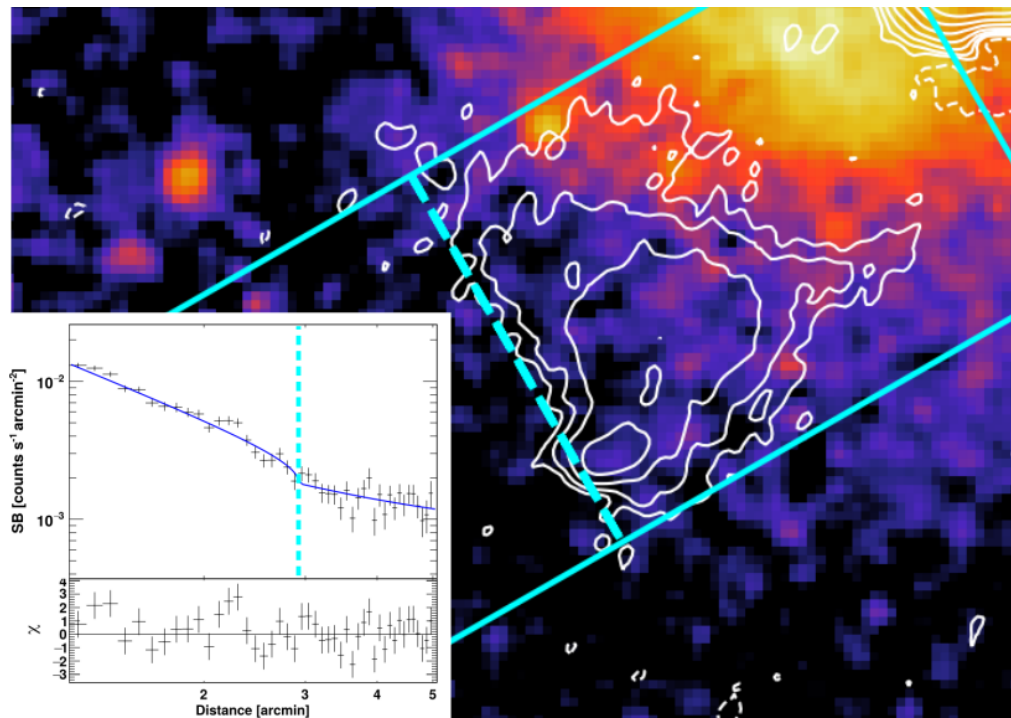


Figure 8.10: The sector used to extract the *XMM-Newton* SB profile across the peripheral source. In the fit, the position of the jump was fixed at the location of the radio edge of emission (*dashed line*).

8.3.3 Constraints on the radio halo emission

The presence of diffuse radio emission at the center of A781 was debated. Originally, A781 was classified as one of the few dynamically disturbed without evidence of a radio halo in the GMRT 610 MHz sample of Venturi et al. (2008). However, Govoni et al. (2011) claimed the presence of a radio halo using VLA observations and reported a flux density $S_{1.4\text{GHz}} = 20 \pm 5$ mJy at 1.4 GHz. Nonetheless, this detection remained debated as Venturi et al. (2011) found only a low level of residuals in the cluster center with the GMRT at 325 MHz (consistent with our reanalysis of the same dataset performed with the SPAM pipeline) that would imply an unusual flat spectrum $\alpha_{325\text{MHz}}^{1.4\text{GHz}} < 0.5$ for a diffuse cluster source when combined with the claim of Govoni et al. (2011). LOFAR has the sensitivity required to shed light on this point: our images have a brightness sensitivity 1.5 – 2.5 times better than the GMRT at 325 MHz and the VLA at 1.4 GHz assuming a typical value of $\alpha = 1.3$ for the radio halo spectrum². With this spectral index and considering the flux density reported with the VLA by Govoni et al. (2011), the flux density expected at 143 MHz is ~ 400 mJy. This should be clearly observable in the LOFAR image. However, a radio halo is not visible and only a low level of residuals is measured in the central region of A781 at 143 MHz. The origin of these residuals is unclear. They may well be patches of emission due to unresolved sources in the cluster or possible contamination of spurious emission due to the central bright DRS ($S_{143\text{MHz}} = 0.5 \pm 0.1$ Jy).

To further quantify the limits of our non-detection, we used the technique of injecting mock radio halos in the dataset to infer an upper limit on the diffuse emission flux density (e.g. Brunetti et al. 2007; Venturi et al. 2008; Kale et al. 2013, 2015; Bonafede et al. 2017; Johnston-Hollitt & Pratley 2017; Cuciti et al. 2018). Specifically, we applied this method to A781 following the procedure

²This estimate is also conservative as it does not account for the fact that the *uv*-coverage at short baselines of LOFAR is much better than those of the GMRT and VLA.

Table 8.4: Expected properties of a radio halo at 1.4 GHz in A781 according to the relation of Cassano et al. (2013). The halo reference radius was calculated as $r_h = 2.6r_e$ (Bonafede et al. 2017).

M_{500} (M_\odot)	$P_{1.4}$ (W Hz^{-1})	$S_{1.4}$ (mJy)	r_h (kpc)	r_e (kpc)
6.1×10^{14}	1.56×10^{24}	5.0	437	168

described in Bonafede et al. (2017). The mock halos were injected in a region close to the cluster center, avoiding bright radio sources and selecting a region with similar noise properties to that within the cluster region. The SB of the mock radio halos is assumed to follow an exponential law in the form $I(r) = I_0 \exp(-r/r_e)$, where I_0 is the central SB and r_e denotes the e -folding radius (e.g. Orrù et al. 2007; Murgia et al. 2009). We first injected a halo with the properties reported in Tab. 8.4, i.e. consistent with that expected from the $P_{1.4} - M_{500}$ relation of Cassano et al. (2013) starting from the value of M_{500} reported in the PSZ2 catalog (Planck Collaboration XXVII 2016). We verified that this mock radio halo was clearly detected by our LOFAR observation at 143 MHz (assuming a spectral index $\alpha = 1.3$, the implied flux density is $S_{143\text{MHz}} = 97$ mJy). We then reduced the flux density of the injected halos until we recovered a flux density that matches the level of residuals measured in the cluster center. This occurred when $S_{143\text{MHz}} < 50$ mJy, and we consider this as the upper limit on the radio halo emission. This converts into a limit of $P_{143\text{MHz}} < 1.6 \times 10^{25} \text{ W Hz}^{-1}$ for the radio halo power at 143 MHz. Whilst the LOFAR brightness sensitivity is much better than that of the GMRT, this limit is similar to that derived by Venturi et al. (2008). Indeed, the residuals due to the contamination from the DRS constrain the depth of our measurement. The upper limit is a factor of 2 below the values expected by the $P_{1.4} - M_{500}$ relation. We note that the *Planck* estimate of M_{500} for A781 could be slightly biased high due to the presence of the “Middle” cluster in the *Planck* beam (see Botteon et al. 2018b, for a similar case).

There is evidence that a fraction of merging clusters do not show radio halos and this fraction is seen to increase at smaller cluster masses (Cuciti et al. 2015). According to current models, a fraction of these low-mass merging clusters should glow up at low radio frequencies and host halos with very steep spectra (e.g. Cassano et al. 2006; Brunetti et al. 2008) that are typically also less luminous in the $P_{1.4} - M_{500}$ plane than radio halos with flatter spectrum (e.g. Cassano 2010; Wilber et al. 2018). Unfortunately, the artifacts around the DRS prevent us to explore the presence of a halo less luminous than one in line with the Cassano et al. (2013) relation.

We also searched our low-resolution LOFAR image for emission from the other clusters in the Abell 781 chain (Fig. 8.2). There are no clear detections toward any of the other clusters but this is to be expected given the low mass of these components (cf. Tab. 1 in Wittman et al. 2014). Due to the expected non-detections we did not determine precise upper limits on the diffuse radio emission.

8.4 Discussion

8.4.1 On the nature of the peripheral radio emission

The most striking feature in the composite image of A781 (Fig. 8.3) is the peculiar peripheral radio source in the SE. Whilst its nature is still uncertain, two possible explanations for its origin can be proposed based on the results coming from the joint radio and X-ray analysis presented in this work.

The first possibility is that the source traces a radio relic, as already hypothesized by Venturi et al. (2008). This scenario is in agreement with the location of the emission in the cluster outskirts and with the overall steepening of the spectral index toward the cluster center (Fig. 8.6 and 8.7). Although the source has an edge that coincides with a region with flatter spectral index as observed

Table 8.5: Photometric redshifts of the source marked with the red arrow in the inset panel in Fig. 8.6 for two different SDSS Data Releases. From Ahn et al. (2014, DR10) and Abolfathi et al. (2018, DR14).

	RF method	KD-tree method
DR10	0.292 ± 0.126	0.241 ± 0.132
DR14	–	0.467 ± 0.124

in almost the totality of radio relics, the global morphology is not recalling the typical arc-shaped structure observed for this class of sources (e.g. van Weeren et al. 2010). In particular, the presence of the high SB spine and of the bright knot of emission with flat spectral index are difficult to explain in the radio relic scenario even assuming strong projection effects (e.g. Slee et al. 2001; Hoeft et al. 2008).

Alternatively, the source could be associated with a radio galaxy just turned off (as suggested by the lack of a bright core in the FIRST). Whilst its morphology does not benefit directly to any of the typical classes of radio galaxies (e.g. Miley 1980), the structure observed in Fig. 8.4 vaguely resembles a head tail source. In this case, it is natural to associate the core emission with the bright knot in the SE that displays a flatter spectral index (Fig. 8.6). Thus, the high SB spine would result from the relativistic plasma trailed behind the host galaxy during its motion toward the cluster outskirts. As a consequence of particle aging, the spectral index gets steeper along the tail; however, in A781, the spectral index shows also a transversal trend (Fig. 8.7). We tentatively interpret this gradient as the signature of a shock passing through the radio galaxies from the W to the E direction compressing and potentially re-accelerating the radio plasma. The interaction between shocks and radio galaxies is very complicated and leads both to the compression of the plasma and to the modification of the source morphology (e.g. Enßlin & Brüggen 2002; Pfrommer & Jones 2011; Jones et al. 2017). In this scenario, the presence of a clear spectral gradient would suggest that the shock has gone through the tail. An external shock can only propagate as a shock inside the tail if the sound speed inside the relativistic plasma is lower than the shock speed in the external medium. This could be explained by entrainment of thermal plasma in the non-thermal plasma and a small volume filling fraction of the non-thermal plasma. Tailored numerical simulation on the source in A781 will test this scenario.

Both interpretations described above assume that a shock is involved in the formation of the peripheral source. Nonetheless, the present *XMM-Newton* observations allowed us to determine only an upper limit on the density jump across the E region of the source that would imply a low Mach number shock. We currently prefer the second scenario as it can be more easily reconciled with the source morphology and spectral index properties. Furthermore, two possible optical counterparts are visible in the SDSS image within the radio knot. Both the sources are detected by the *Spitzer* satellite, possibly indicating infrared emission from AGN. However, only the galaxy marked with the red arrow³ in the inset panel in Fig. 8.6 is in the SDSS catalog. Different estimates⁴ of the photometric redshift for this object are reported in Tab. 8.5. The galaxy is consistent to be a cluster member within 1σ for Ahn et al. (2014) and within 1.4σ for Abolfathi et al. (2018). We mention that the apparent discrepancy between the redshifts reported in the two SDSS Data Releases might be due to changes in the machine learning technique (e.g. in the training sample) between the two releases. Spectroscopic follow-up observations are required to precisely determine the galaxy redshift and nuclear activity.

In conclusion, we point out that the radio relic and radio galaxy–shock interaction scenarios do not necessarily exclude each other. The shock with $\mathcal{M} < 1.4$ inferred from the X-ray analysis, if present, would challenge DSA due to the inefficient particle acceleration at weak cluster shocks (e.g.

³SDSS J092031.54+302733.1

⁴See Csabai et al. (2007) and Carliles et al. (2010) for details on the photometric redshift estimation methods.

Kang et al. 2012; Pinzke et al. 2013). The re-acceleration of a pre-existing population of relativistic electrons injected by nearby radio galaxies is usually invoked to alleviate the high acceleration efficiency required for many relics (e.g. Botteon et al. 2016a; Eckert et al. 2016a; van Weeren et al. 2016a; Hoang et al. 2018a). To date, the clearest example of AGN–relic connection is provided by Abell 3411–3412 (van Weeren et al. 2017a), where a shock was suggested to be responsible of the AGN distorted radio tail and the spectral index flattening at the edge of the relic. The peripheral emission in A781 could resemble this case, provided that future observations will confirm the optical counterpart and shock front. The fact that a radio relic is not observed at the position of the stronger shock toward the W direction further supports the scenario of AGN–shock interaction or the case of particle re-acceleration.

8.4.2 A triple merger in A781

The detection of discontinuities in the thermal ICM requires that the collision is occurring almost exactly in the plane of the sky, as projection effects could hide the sharp SB and temperature jumps. Therefore, the shock and cold fronts observed in A781 can be used to outline the approximate geometry of the merger. We complemented this information with the temperature and entropy maps shown in Fig. 8.11 (the error maps are reported in Appendix F), that are useful diagnostic tools to search for sub-structures in the ICM. Maps were produced by fitting a thermal model to the count rates measured in five energy bands from *XMM-Newton* EPIC Voronoi tessellated images (Cappellari & Copin 2003), and requiring a threshold of 400 counts per bin in the 0.5 – 2.0 keV band (for more details, see Jauzac et al. 2016). Reported quantities are projected along the line of sight.

From the analysis of the *XMM-Newton* observations, we suggest that A781 is undergoing a triple merger, as sketched in Fig. 8.12. Merger cold fronts usually trace the direction of motion of a cluster core (e.g. Markevitch et al. 2002); hence, the two diametrically opposite cold fronts detected in A781 suggest a collision axis along the NW–SE direction. The presence of two sub-structures (clump A and clump B) is supported by the low values of entropy and the X-ray contours in Fig. 8.11 (right panel). The two X-ray clumps seem detached (e.g. Fig. 8.3), with clump B likely tracing a smaller sub-structure moving apart from the dominant clump A. The spatial coincidence between

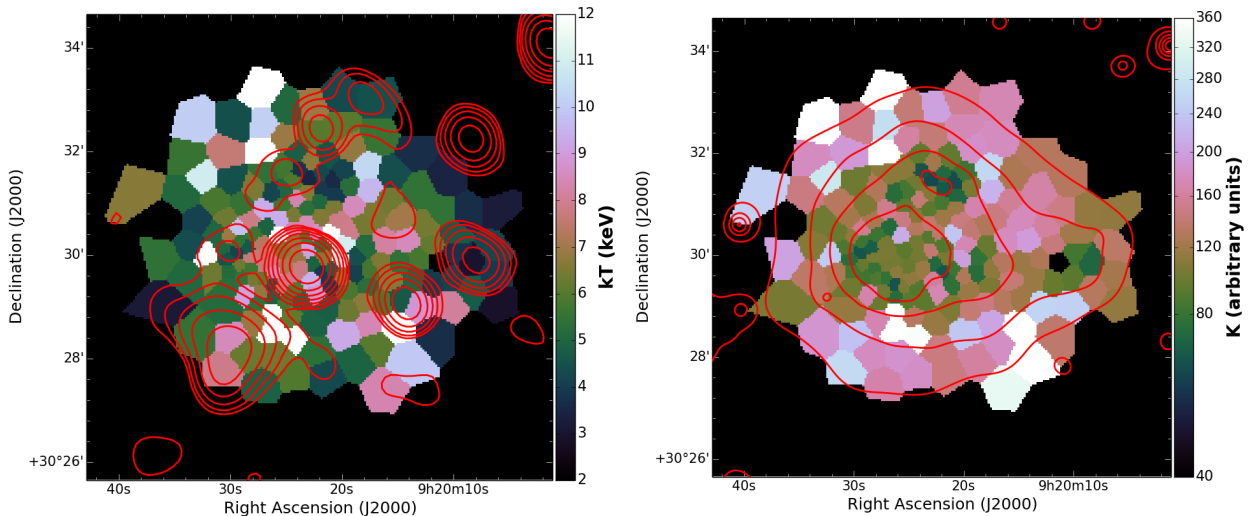


Figure 8.11: Thermodynamical properties of the ICM in A781 projected along the line of sight. *Left:* temperature map with overlaid the LOFAR contours of Fig. 8.2. *Right:* entropy map with overlaid the *XMM-Newton* contours of Fig. 8.1. The corresponding error maps are reported in Fig. F.2.

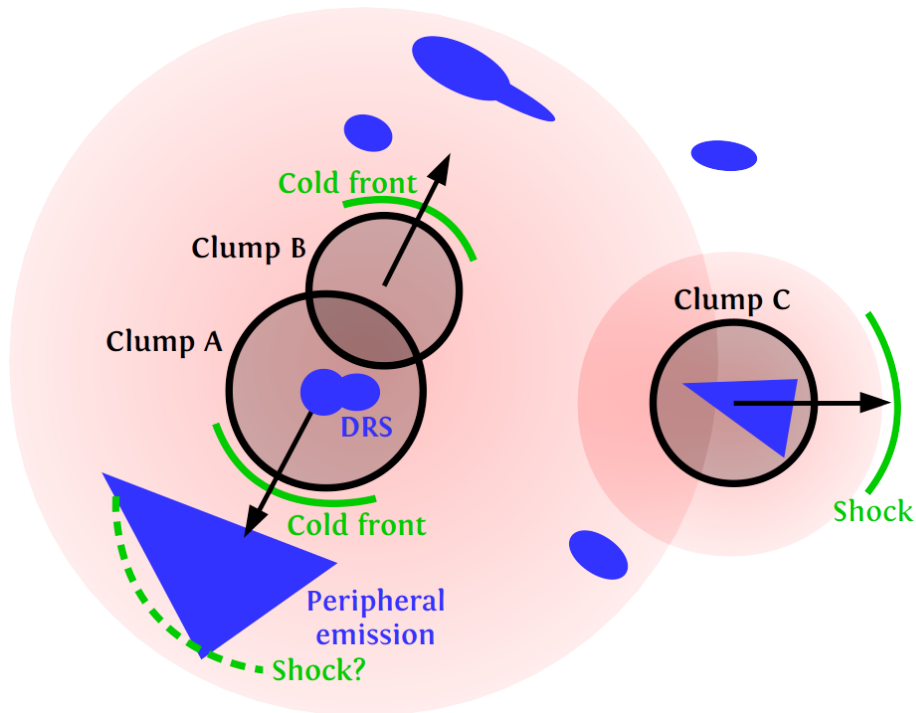


Figure 8.12: Cartoon of the dynamics of the merger in A781 as suggested from the X-ray data; the diffuse radio sources are sketched in *blue* while the thermal ICM emission is reported in *red* (cf. Fig. 8.3).

the peripheral radio emission high SB spine and bins with $kT \sim 9$ keV in Fig. 8.11 (left panel) could indicate a region heated by the passage of the shock invoked in the previous Section to explain the properties of the source observed in the radio band. In addition, the presence of a third sub-cluster (clump C) is highlighted by the X-ray clump of emission to the W and, again, by the low entropy gas in this region (Fig. 8.11, right panel). This sub-cluster is clearly disturbed as it does not show evidence of an X-ray peak (Fig. 8.8). In this respect, we suggest that it is moving toward the W direction and it has already crossed the ICM of clump A+B, rather than infalling into the system. The detection of the shock in the W supports this scenario. This provides an additional merger axis in the E-W direction. Overall, the irregular distribution of temperature with the existence of blobs of hot gas (Fig. 8.11, left panel) is in agreement with a complex merger dynamics as that described above.

The tentative dynamics of the merger outlined above is based on the features observed in the X-rays. Recently, Golovich et al. (2018) presented an optical analysis of A781 that supports the triple merger scenario. As pointed out by these authors, it is worth noting that on larger scales the merger could be even more complex because of the existence of the “Middle” cluster, located at a similar redshift of A781 (Fig. 8.1).

8.5 Conclusions

In this Chapter, we presented a joint radio/X-ray analysis of the cluster chain Abell 781 using new LOFAR data and reanalyzing archival GMRT and *XMM-Newton* observations. We focused on the main merging component of the complex, for which the presence of non-thermal emission in the ICM was already investigated in the literature. Our results can be summarized as follows.

1. The nature of the peripheral radio emission in the SE of A781 remains uncertain. We suggested that this source results from the interaction between a weak shock with $\mathcal{M} < 1.4$ and a

radio galaxy. This scenario could explain its unusual morphology and spectral index steepening toward the cluster center. The non-detection of a radio relic at the position of the stronger shock observed in the W direction further supports the fact that the SE emission, if associated to a shock, represents a case of AGN–shock connection or particle re-acceleration. Future optical follow-up and numerical simulations are required to clarify the origin of the source.

2. We proposed a tentative interpretation of the dynamics of the merger occurring in A781 where three sub-structures are involved. We detected two cold fronts and a shock front; these were used to delineate the motion of the three mass clumps. The two diametrically opposite cold fronts indicate a merger axis in the SE-NW direction, while the presence of a third sub-structure moving toward the W and preceding a shock suggests another merger axis in the E-W direction. Three low entropy clumps are also observed in the entropy map of A781.
3. Our results from the new LOFAR data and the reanalysis of the archival GMRT observations do not find evidence of the radio halo in A781 (in agreement with Venturi et al. 2008, 2011) and in the other clusters of the chain. We placed an upper limit on the diffuse radio emission a factor of 2 below the $P_{1.4} - M_{500}$ relation of Cassano et al. (2013). This limit is not conveniently deep enough due to the presence of artifacts around the bright radio galaxy at the center of A781. The absence of a radio halo in a merging system provides useful information on the mechanisms that generate these sources and on their evolution.

LOFAR discovery of a double radio halo system in Abell 1758 and radio/X-ray study of the cluster pair[†]

ABSTRACT

We present a new LOFAR observation of the double galaxy cluster Abell 1758. This system is composed of A1758N, a massive cluster hosting a known giant radio halo, and A1758S, which is a less massive cluster whose diffuse radio emission is confirmed here for the first time. Our observations have revealed a radio halo and a candidate radio relic in A1758S, and a suggestion of emission along the bridge connecting the two systems which deserves confirmation. We combined the LOFAR data with archival VLA and GMRT observations to constrain the spectral properties of the diffuse emission. We also analyzed a deep archival *Chandra* observation and used this to provide evidence that A1758N and A1758S are in a pre-merger phase. The ICM temperature across the bridge that connects the two systems shows a jump which might indicate the presence of a transversal shock generated in the initial stage of the merger.

9.1 Introduction

Abell 1758 (hereafter A1758) is a galaxy cluster located at $z = 0.279$ that has been intensively studied in the literature. Early ROSAT data (Rizza et al. 1998) revealed that it consists of two components, A1758N (in the north) and A1758S (in the south), separated by a projected distance of ~ 8 arcmin (about 2 Mpc). David & Kempner (2004) estimated virial radii of 2.6 Mpc (for A1758N) and 2.2 Mpc (for A1758S), indicating that each cluster is affected by the potential well of the other and that they are gravitationally bound. Despite this, no signs of significant interaction between A1758N and A1758S were found by *Chandra* and *XMM-Newton* observations (David & Kempner 2004). However, from X-ray and optical studies, it is clear that the two sub-clusters are undergoing their own distinct mergers, with A1758N in a late and A1758S in an early merger state (e.g. David & Kempner 2004; Boschin et al. 2012b). This might also be reflected in the infrared luminosity of the galaxies of A1758N, which is almost two times larger than that of A1758S, suggesting different

[†]Based on Botteon et al. (2018b).

dynamical histories for the two clusters (Haines et al. 2009). Weak lensing studies indicate that A1758N has a bimodal mass distribution, while A1758S represents a single mass clump (Dahle et al. 2002; Okabe & Umetsu 2008; Ragozzine et al. 2012; Monteiro-Oliveira et al. 2017). Individual mergers are possibly occurring near the plane of the sky for A1758N and close to the line of sight for A1758S.

So far, most studies have focused on A1758N, which is more massive and hotter than A1758S (e.g. David & Kempner 2004). The mass of A1758N has been estimated using several methods (e.g. X-ray scaling relations, David & Kempner 2004; weak lensing, Okabe & Umetsu 2008; member galaxy dynamics, Boschini et al. 2012b; hydrostatic equilibrium, Martino et al. 2014), providing a virial mass of $\sim 10^{15} M_{\odot}$, which is split approximately equally between the two sub-components. This is further supported by hydrodynamical simulations, which can reproduce the X-ray morphology of A1758N assuming an off-axis collision of two equal mass ($\sim 5 \times 10^{14} M_{\odot}$) clusters (Machado et al. 2015). A compilation of the different mass estimates reported for A1758N is given in Tab. 1 of Monteiro-Oliveira et al. (2017). Note that the mass of A1758S is more uncertain whilst it appears to be at least a factor of 1.5 smaller than that of A1758N (David & Kempner 2004; Ragozzine et al. 2012; Haines et al. 2018).

In the radio band, A1758N hosts a giant radio halo that was first detected by Kempner & Sarazin (2001) and later investigated at 1.4 GHz with the VLA (Giovannini et al. 2009) and at 325 MHz with the GMRT (Venturi et al. 2013). There are no reports of diffuse radio emission associated with A1758S in the literature.

In this Chapter, we present a new LOFAR observation together with archival GMRT, VLA and *Chandra* data. Using these data we have discovered and characterized the second double radio halo system known to date and we argue that the two clusters that constitute A1758 are in a pre-merger state.

9.2 Observations and data reduction

9.2.1 LOFAR

The LoTSS (Shimwell et al. 2017) observations are typically separated by 2.6° and we have analyzed the LoTSS pointing that is centered closest to A1758 (offset by $\sim 1.1^{\circ}$). The characteristics of this observation are summarized in Tab. 9.1. To calibrate the data we followed the facet calibration scheme described in Section 7.5. This procedure has been successfully applied to image several other galaxy clusters with the LOFAR HBA (e.g. van Weeren et al. 2016a; de Gasperin et al. 2017; Hoang et al. 2017; Wilber et al. 2018).

Table 9.1: Summary of the radio observations used in this work.

	LOFAR	GMRT	VLA	
			Array C	Array D
Project code	LC2_038	11TVA01	AG639	
Pointing center (RA, DEC)	13h37m30s +49°44'53"	13h32m32s +50°30'37"	13h32m32s +50°30'36"	
Observation date	2014 Jun 1	2007 Mar 30/31	2004 May 6	2003 Mar 11
Total on-source time (hr)	8.0	8.0	2.5	2.5
Flux calibrator	3C196	3C147	3C286	
Total on-calibrator time (min)	10	26	10	9
Central frequency (MHz)	144	325	1425	
Bandwidth (MHz)	48	33	50	

Table 9.2: Imaging parameters for the radio images shown in the Chapter. The beam position angle (PA) is measured from north to east.

Fig.	Instrument	Frequency (MHz)	Robust	Taper ($''$)	Resolution ($'' \times ''$)	PA ($^\circ$)	rms ($\mu\text{Jy beam}^{-1}$)
1	LOFAR	144	+0.5	0	34×23	45	230
1	GMRT	325	0.0	35	43×29	29	400
1	VLA	1425	0.0	35	43×38	50	70
3	LOFAR	144	0.0	40	60×51	69	390
4	LOFAR	144	-0.5	10	16×11	88	140

All LOFAR images in the Chapter are reported at the central observing frequency of 144 MHz and were produced with CASA v4.7 (McMullin et al. 2007). The imaging was done using the multi-scale multi-frequency deconvolution algorithm (MS-MFS; Rau & Cornwell 2011), with second order Taylor terms ($n_{\text{terms}} = 2$), and W-projection (Cornwell et al. 2005). For the facet containing A1758, an image size of $5120'' \times 5120''$ was adopted to ensure that all of the sources in the vicinity of the cluster were adequately deconvolved. An inner uv -cut of 80λ (corresponding to an angular scale of $43'$) was also applied on the data to reduce sensitivity to very large scale emission from the Galaxy. Different resolution images were created using various different Briggs weightings (Briggs 1995) and by applying an uv -taper, as reported in Tab. 9.2. Primary beam correction was performed with AWIMAGER (Tasse et al. 2013). Uncertainties in the flux scale that are caused by inaccuracies in the LOFAR HBA beam model (see van Weeren et al. 2016b; Hardcastle et al. 2016) were corrected by cross-matching a number of compact sources extracted from the LOFAR image with the TGSS ADR (Intema et al. 2017). Throughout the Chapter, we have applied correction factor that was computed from the mean LOFAR/TGSS integrated flux density ratio of 1.08 and a calibration error of 15% on LOFAR flux densities, which is in agreement with other LOFAR HBA studies (e.g. Shimwell et al. 2016; Savini et al. 2018c).

9.2.2 GMRT

We analyzed an 8 hr archival GMRT 325 MHz observation of A1758 (details in Tab. 9.1). Data were reduced with the SPAM package (Intema et al. 2009), which is an automated pipeline to process GMRT observations based on AIPS. Here we outline the main steps of the SPAM data reduction, for more details the reader is referred to Intema et al. (2009, 2017). First, the dataset is averaged in time and frequency to reduce the data processing time whilst keeping enough resolution in both time and frequency to avoid smearing. Bad data due to corrupted baselines, non-working antennas, and RFI were also excised. The bandpass and absolute flux density scale were calibrated using the primary flux calibrator 3C147 and adopting the Scaife & Heald (2012) flux scale. An initial phase-only calibration using a sky model generated from the VLSSr (Lane et al. 2014), the WENSS (Rengelink et al. 1997) and the NVSS (Condon et al. 1998) was followed by a number of loops of self-calibration, wide-field imaging and additional flagging of bad data. Then the bright sources in the primary beam are used to perform a direction-dependent calibration and ionospheric modeling aiming to mitigate the phase errors introduced by the ionosphere. The final calibrated data were then imaged with CASA v4.7, as described at the end of Section 9.2.1. In our analysis we did not consider the effect of variation in system temperature (see Sirothia 2009). Instead, we adopted a similar approach to that described in Section 9.2.1, cross-matching a number of sources extracted from the GMRT image with the WENSS (Rengelink et al. 1997) and applying a correction factor of 0.73 on the GMRT flux densities with a systematic uncertainty of 15% (see Chandra et al. 2004).

9.2.3 VLA

We analyzed archival VLA observations of A1758 at 1.4 GHz in configurations C and D. The details of the observations are reported in Tab. 9.1. Data reduction was performed with AIPS where the two datasets were edited, calibrated and imaged separately. Thus, the uv -data were combined to produce a single image of the cluster. The flux calibrator of VLA observations was 3C286 (model from Perley & Butler 2013). The final imaging was performed with CASA v4.7 as described in Section 9.2.1. The absolute flux scale calibration errors were conservatively set to 5% on VLA flux densities.

9.2.4 Integrated synchrotron spectra and source subtraction

Given the different uv -coverage of the LOFAR, GMRT and VLA observations, it was necessary to match the uv -sample of the different interferometers as closely as possible to provide an accurate comparison between the flux densities measured at different frequencies, and to compute the diffuse emission spectra.

As a first step, we removed the discrete sources from each datasets. This procedure was performed by applying an inner uv -cut of $2.0 \text{ k}\lambda$ (corresponding to an angular scale of $103''$, i.e. about 440 kpc at $z = 0.279$) to the data to image only the compact sources in the field whose clean components were subsequently subtracted from the visibilities. To image the diffuse emission after the source subtraction, for each dataset we used the an inner uv -cut of 170λ and uniform weighting. A Gaussian uv -taper of $35''$ was also used to enhance diffuse emission and to produce images with comparable beams. Errors on flux densities were estimated via Eq. 2.1.

In Fig. 9.1 we present the LOFAR image (left panel) along with the point-source-subtracted images from the GMRT (central panel) and VLA (right panel). This choice has been made since the diffuse emission is best visible.

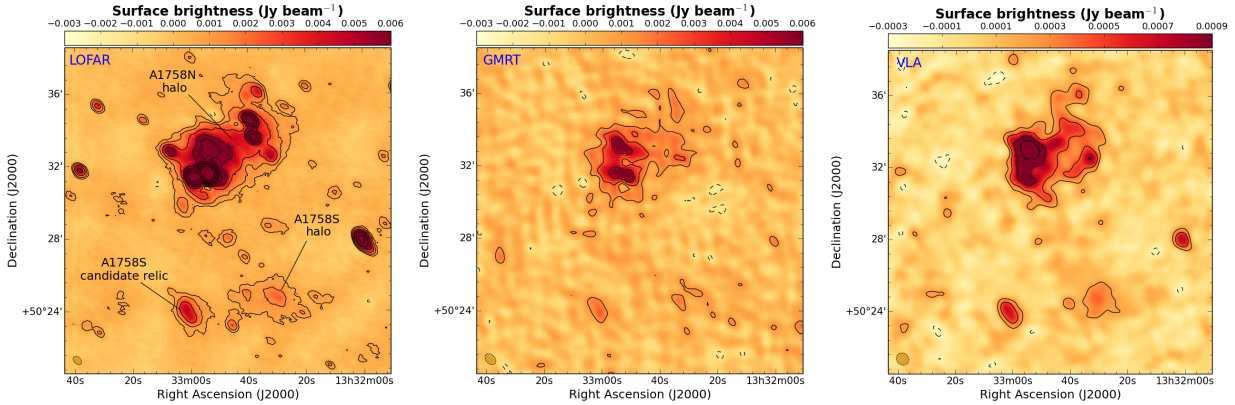


Figure 9.1: The cluster A1758 as observed in the radio band with LOFAR (*left*), GMRT (*center*) and VLA (*right*). The point-sources were subtracted in the GMRT and VLA images. Contours are spaced by a factor of 2 starting from 3σ , where $\sigma_{\text{LOFAR}} = 230 \mu\text{Jy beam}^{-1}$, $\sigma_{\text{GMRT}} = 400 \mu\text{Jy beam}^{-1}$ and $\sigma_{\text{VLA}} = 70 \mu\text{Jy beam}^{-1}$. The negative -3σ contours are shown in dashed. The beam sizes are $34'' \times 23''$ (LOFAR), $43'' \times 29''$ (GMRT) and $43'' \times 38''$ (VLA) and are shown in the bottom left corners. More details on the images are reported in Tab. 9.2.

9.2.5 *Chandra*

We retrieved three ACIS-I observations (ObsID: 13997, 15538, 15540) on A1758 from the *Chandra* data archive¹ for a total exposure time of 150 ks. We mention that two other *Chandra* pointings on A1758 also exist; however, they are composed of an ACIS-S observation where only A1758N is in the FoV (ObsID 2213) and by a short (7 ks) observation (ObsID 7710) whose exposure time is negligible with respect to the total integration time. For these reasons, they were not considered in our analysis.

Data reduction was performed with CIAO v4.9 and *Chandra* CALDB v4.7.3. Time periods affected by soft proton flares were removed by inspecting the light curves in the 0.5 – 7.0 keV band extracted for each ObsID from the S2 chip with the `lc_clean` routine. After this step, the resulting clean exposure time is 137 ks. We used `merge_obs` to add together the three datasets and produce the final cluster image in the 0.5 – 2.0 keV band shown in Fig. 9.2. An exposure-corrected PSF map with minimum size was created from the combination of the PSF and exposure maps of the three ObsIDs. This was used to detect discrete sources with the `wavdetect` task, which were later confirmed by eye and excluded in the further analysis.

Spectra were extracted in the same regions from all the ObsIDs and simultaneously fitted in the 0.5 – 10.0 keV band with XSPEC v12.9.0o (Arnaud 1996). The background was carefully treated with a model that included both astrophysical and instrumental emission components, as shown in Fig. 9.3. The former is described by two main components due to: the Galactic emission, modeled with two thermal plasmas with $kT_1 = 0.14$ keV and $kT_2 = 0.25$ keV, and the CXB, described with an absorbed power-law with photon index $\Gamma = 1.4$. For the latter we followed Bartalucci et al.

¹<http://cda.harvard.edu/chaser/>

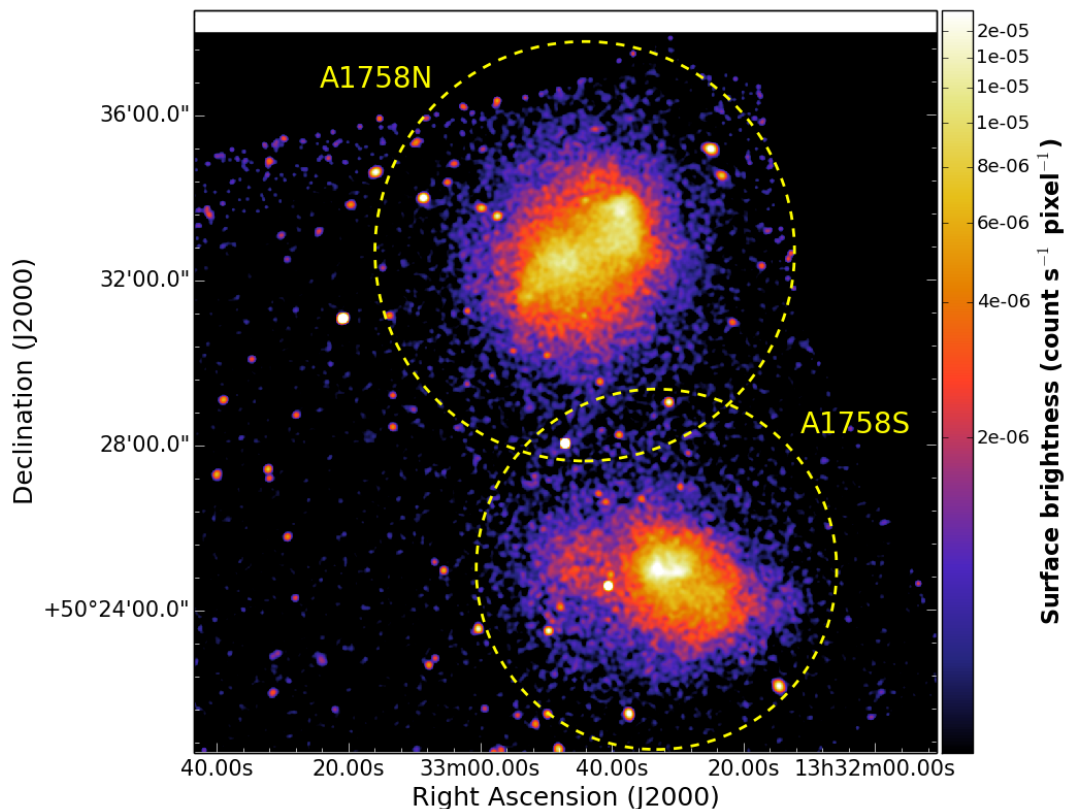


Figure 9.2: *Chandra* exposure-corrected image in the 0.5 – 2.0 keV band of A1758 smoothed to a resolution of $\sim 3''$. Yellow circles indicate the approximate location of r_{500} for each cluster.

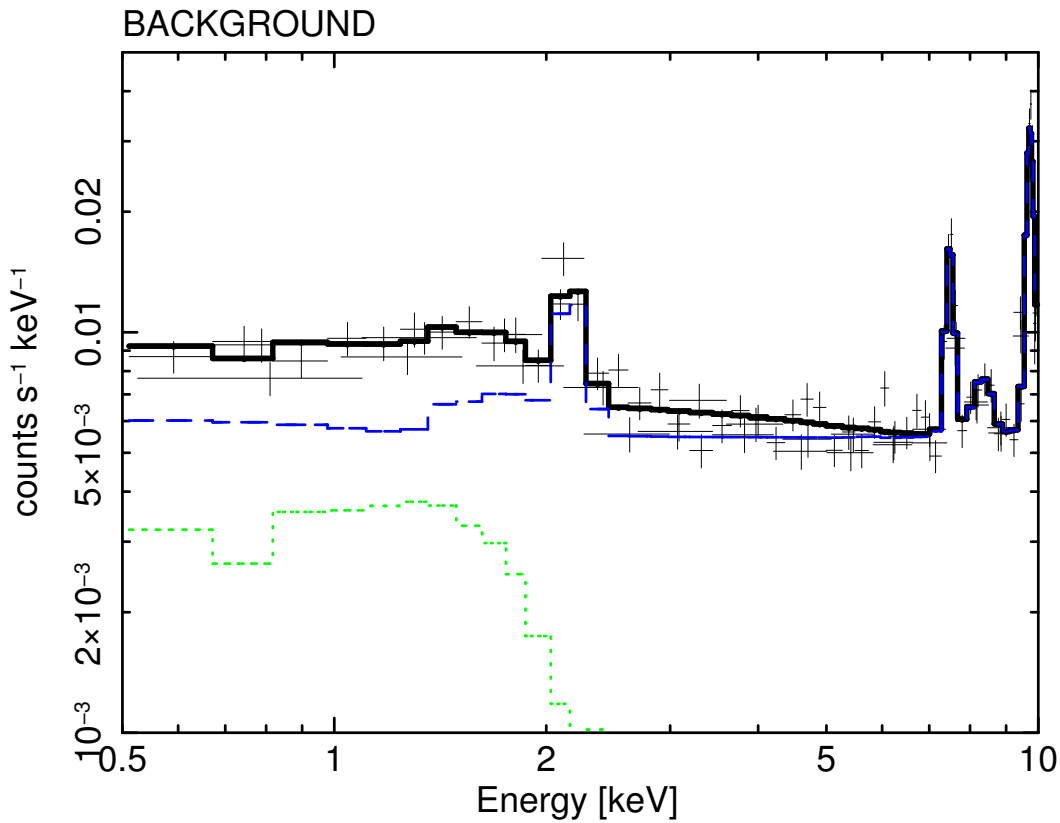


Figure 9.3: Spectrum of the *Chandra* background. Data points are shown in *black* together with the best-fitting model. The astrophysical and instrumental backgrounds are shown in *dotted green* and *dashed blue*, respectively. Whilst the three ObsID spectra were simultaneously fitted, the models for only one observation were reported in order to avoid confusion in the plot. The c-stat/d.o.f. of the fit is 406/386.

(2014) which provided an analytical model for the ACIS-I particle background. Spectra were fitted adopting Cash statistics (Cash 1979) and an absorbed thermal model for the ICM with metallicity fixed at $0.3 Z_{\odot}$ (solar abundance table by Anders & Grevesse 1989) and hydrogen column density $N_{\text{H}} = 1.03 \times 10^{20} \text{ cm}^{-2}$ computed from the Leiden/Argentine/Bonn Survey of Galactic HI (Kalberla et al. 2005).

We used CONTBIN v1.4 (Sanders 2006) to compute the thermodynamical properties of the ICM in A1758. A S/N of 50 for the net counts in the 0.5 – 2.0 keV band was set to delineate the regions where spectra were extracted and fitted as written above. For more details on the computation of the maps of the ICM thermodynamical quantities and generally on the *Chandra* data analysis we refer the reader to Botteon et al. (2018a) in which the same procedures adopted in this Chapter have been more thoroughly described.

9.3 Results

9.3.1 A1758N radio halo

Diffuse emission in A1758N is visible both from the NVSS and the WENSS surveys (Kempner & Sarazin 2001). The observations taken with the VLA at 1.4 GHz (Giovannini et al. 2009) and with the GMRT at 325 MHz (Venturi et al. 2013) confirmed the presence of a giant radio halo which is elongated in the NW-SE direction and only partially covers the X-ray emission of the cluster. The spectral index reported between these two frequencies is $\alpha = 1.31 \pm 0.16$ (Venturi et al. 2013).

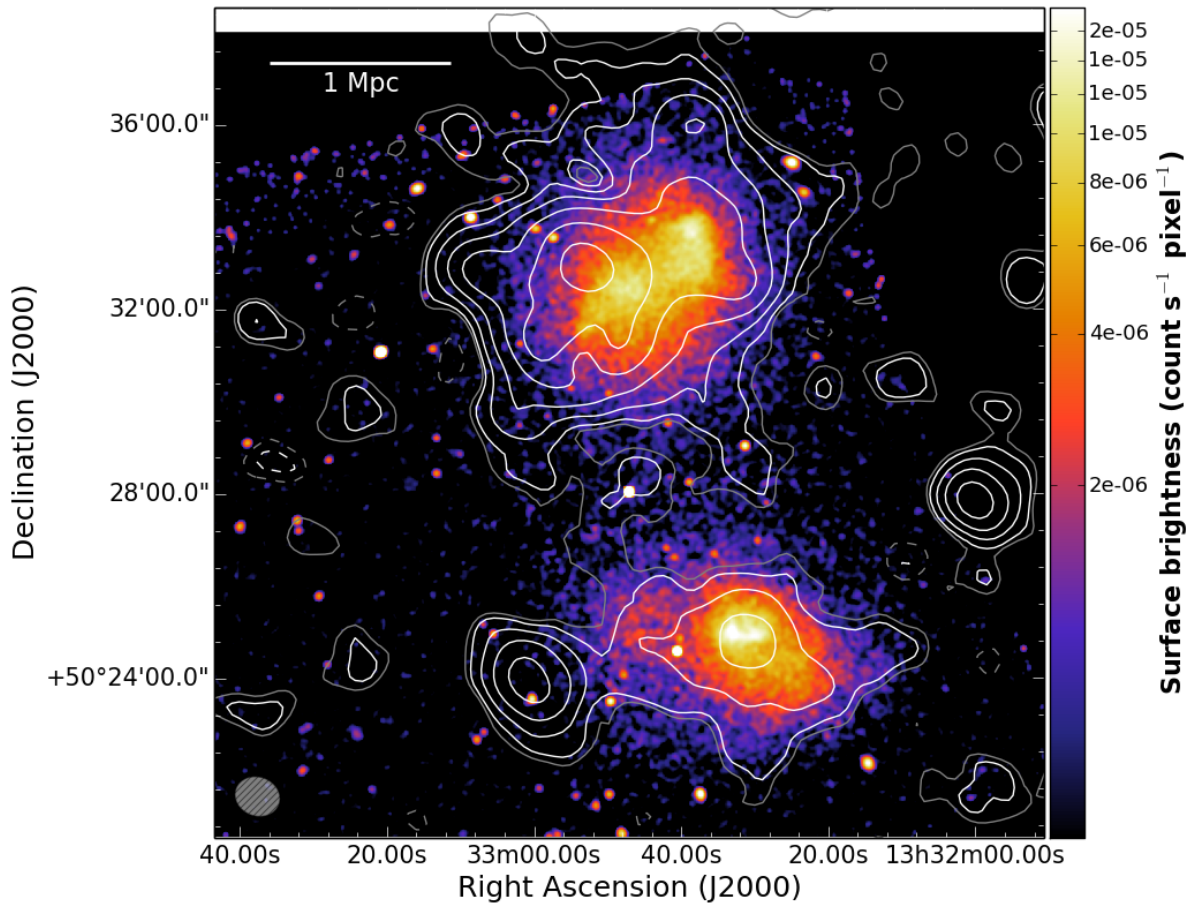


Figure 9.4: LOFAR radio contours with point-sources subtracted of A1758 overlaid on the *Chandra* color image of Fig. 9.2. The LOFAR white contours are spaced by a factor of 2 starting from 3σ , where $\sigma_{\text{LOFAR}} = 390 \mu\text{Jy beam}^{-1}$. The negative -3σ contours are shown in dashed. Gray contours correspond to the $\pm 2\sigma$ level. The beam size is $60'' \times 51''$ and is shown in the bottom left corner. More details on the LOFAR image are reported in Tab. 9.2.

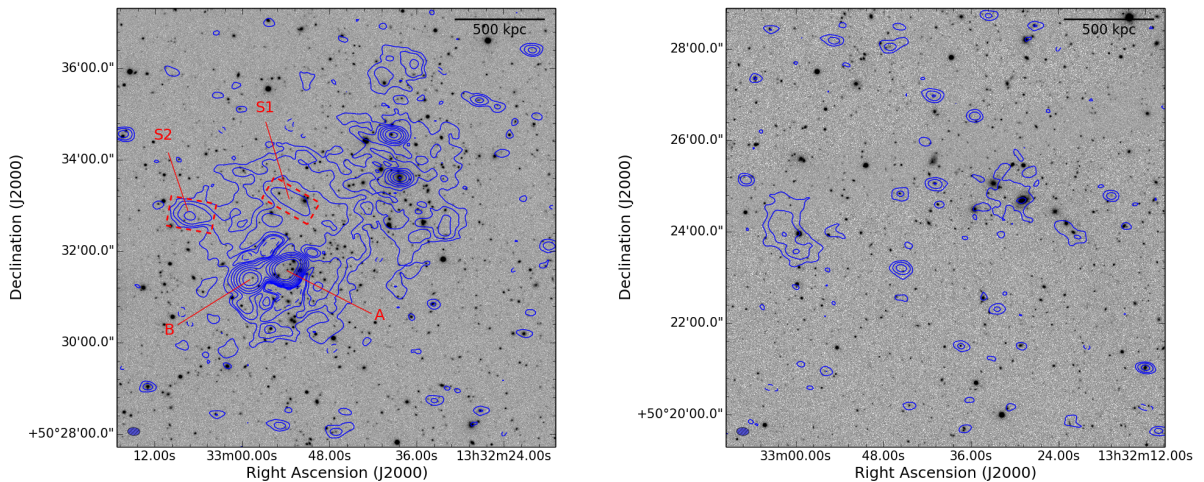


Figure 9.5: Mosaic SDSSg,r,i images of A1758N (*left*) and A1758S (*right*) overlaid with the LOFAR contours spaced by a factor of 2 starting from 3σ , where $\sigma_{\text{LOFAR}} = 140 \mu\text{Jy beam}^{-1}$. The negative -3σ contours are shown in dashed. The beam size is $16'' \times 11''$ and is shown in the bottom left corners. At this resolution the radio halo in A1758S is marginally visible. More details on the LOFAR image are reported in Tab. 9.2.

LOFAR detects the extended radio halo flux in A1758N at higher significance and the recovered morphology appears consistent with the GMRT and VLA maps, as demonstrated in Fig. 9.1. We measure a largest linear size of the emission of ~ 2.2 Mpc. The low-resolution point-source-subtracted LOFAR contours displayed in Fig. 9.4 suggest that the non-thermal radio emission in A1758N covers the X-ray bright region of the cluster. At higher resolution (Fig. 9.5, left panel), only the brightest part of the radio halo is visible; in particular, LOFAR shows two bright and straight structures (labeled as S1 and S2 in Fig. 9.5, left panel) apparently not associated with any optical galaxy. They might indicate regions where the plasma has been somehow locally compressed or re-accelerated (e.g. Shimwell et al. 2016; de Gasperin et al. 2017). The feature S1 is also detected with the GMRT and VLA (Fig. 9.1). In the southeast, A1758N also hosts two prominent narrow angle tailed radio galaxies labeled as A and B in Fig. 9.5 (left panel). The former (also identified as 1330 + 507) was studied at high resolution with the VLA by O’Dea & Owen (1985).

The presence of resolved radio galaxies embedded in the halo (e.g. source A and B in Fig. 9.5, left panel) makes it difficult to disentangle their contribution from that of the halo. We repeated the subtraction by adopting inner uv -cuts in the range $1.0 - 3.5$ $k\lambda$, corresponding to linear sizes of $873 - 249$ kpc at the cluster redshift, to assess the uncertainties in our source subtraction on the LOFAR dataset, in addition to the procedure described in Section 9.2.4. In Fig. 9.6 we show how the flux density measurement of the northern radio halo varies with the uv -cut, ranging from 415 to 483 mJy (the mean value is 440 mJy). This indicates that the choice of the uv -cut has an impact on the halo in A1758N. In contrast, the integrated flux density of the diffuse sources in A1758S (see Sections below) is essentially independent on the uv -cut used (Fig. 9.6), indicating that the subtraction is less problematic which is expected as there are just a few weak discrete sources without significant extended emission (cf. Fig. 9.5, right panel).

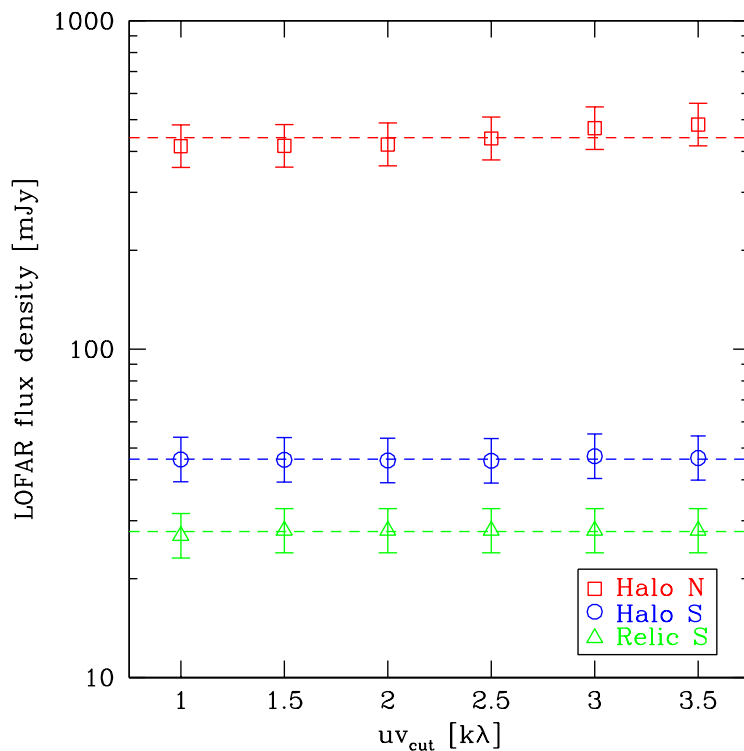


Figure 9.6: The flux densities of the diffuse emission in A1758 measured with LOFAR versus the inner uv -cuts adopted to subtract the point-sources. Dashed horizontal lines show the mean values of the measurements.

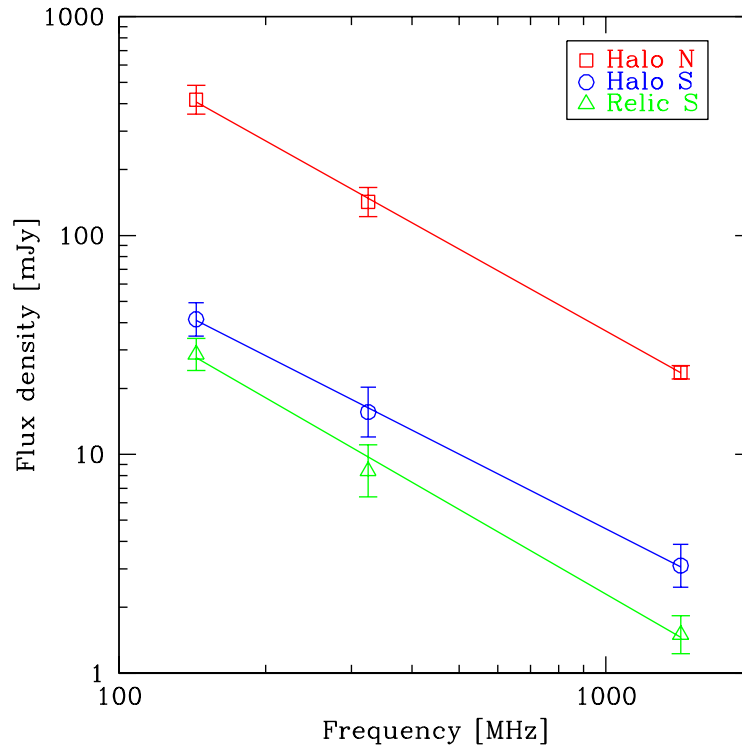


Figure 9.7: Integrated spectra of the diffuse radio emissions in A1758. The spectral index values are reported in Tab. 9.3.

In Tab. 9.3 and Fig. 9.7 we report the flux density measurements at three frequencies and the spectra, respectively, of the diffuse emission in A1758. The spectral index between 144 MHz and 1.4 GHz is $\alpha = 1.2 \pm 0.1$ for the halo in A1758N, consistent with that of $\alpha = 1.31 \pm 0.16$ computed by Venturi et al. (2013). The flux densities measured in our GMRT and VLA images agree to that reported in Venturi et al. (2013) within 1σ . The emission from the potential relic and the halo in A1758S have not been previously reported.

Table 9.3: Flux densities of the diffuse emission in A1758. The spectral indexes were computed adopting the procedure described in Section 9.2.4.

ν [MHz]	S_ν [mJy]		
	Halo N	Halo S	Relic S
144	420 ± 63	45.8 ± 7.1	28.0 ± 4.3
325	134 ± 20	16.8 ± 3.5	8.9 ± 2.0
1425	$24.7 \pm 1.7^\dagger$	$3.1 \pm 0.7^\dagger$	1.5 ± 0.3
α	1.2 ± 0.1	1.1 ± 0.1	1.3 ± 0.1

Notes. [†]The error takes into account also the uncertainties of the source subtraction.

9.3.2 A1758S radio halo

We discovered a diffuse radio sources in A1758S with LOFAR. The characteristics of the emission recovered by LOFAR (Fig. 9.4) are typical for a radio halo, i.e. low SB, similar morphology with respect to the ICM thermal emission and a largest linear size of ~ 1.6 Mpc. The halo in A1758S

is barely visible with the GMRT and it is detected at low significance with the VLA (Fig. 9.1). Indication of the presence of a radio halo in A1758S has also been found in the Westerbork Synthesis Radio Telescope (WSRT) data at 367 MHz (Drabent 2017). However, the available observation is not suitable to study in detail the diffuse emission due to its inadequate angular resolution which makes the point-source subtraction unreliable. It is worth noting that the merger axis of A1758S is likely close to the line of sight (e.g. Monteiro-Oliveira et al. 2017), hence we can not fully discard the possibility that the radio emission traces a radio relic observed face-on, although this is unlikely because the remarkable similarity between the radio and the X-ray emission (Fig. 9.4). Future studies on the source polarization level will definitely clarify this point.

The integrated flux density measured with LOFAR within the 3σ contour from the low-resolution image of Fig. 9.4 (excluding the peripheral emission to the east, see Section below) is 45.8 ± 7.1 mJy, i.e. one order of magnitude lower than that of the halo in A1758N. The spectral index computed between 144 MHz and 1.4 GHz within a region traced by the LOFAR emission is $\alpha = 1.1 \pm 0.1$ (see Tab. 9.3) and the fit is shown in Fig. 9.7. We also determined the halo spectral index considering a region defined by the VLA 3σ contour. In this case, the flux densities evaluated in the LOFAR and VLA images are ~ 12.5 mJy and ~ 1.2 mJy, respectively, and the spectral index is consistent with that reported above.

9.3.3 A1758S candidate radio relic

To the east of A1758S, an extended radio source at the boundaries of the X-ray emission is observed with LOFAR, GMRT and VLA (Fig. 9.1). In the LOFAR low-resolution contours of Fig. 9.4, the 3σ contour of this emission is connected with that of the radio halo. In Tab. 9.3 we report the flux density measurements at various frequencies. We estimated a spectral index between 144 MHz and 1.4 GHz of $\alpha = 1.3 \pm 0.1$ for this source (Fig. 9.7). We tentatively classify this emission as a radio relic based on the following characteristics: (i) its elongated morphology roughly arc-shaped and perpendicular to the thermal cluster emission, (ii) its largest linear size > 500 kpc, (iii) its peripheral location in the same direction of the ICM elongation, (iv) its steep spectrum, and (v) the absence of a clear optical counterpart² and/or bright compact radio emission (Fig. 9.5, right panel). All these properties are commonly observed in radio relics but can also be seen in other objects, such as dead radio galaxies (e.g. Brienza et al. 2016, and references therein). A definitive claim would require either the study of the spectral index gradient toward the cluster center, measurements of the source polarization or the detection in the X-rays of an underlying shock front. Unfortunately, none of these measurements can be carried out with the present data.

9.3.4 X-ray properties of A1758N and A1758S

The deep *Chandra* observation of A1758 allowed us to derive the projected maps of the ICM thermodynamical quantities shown in Fig. 9.8. The temperature map displays overall higher values in A1758N than in A1758S. These values are within the ranges 8.0 – 9.9 keV, for A1758N, and 6.0 – 6.7 keV, for A1758S, that were reported by David & Kempner (2004) who made measurements within 1 Mpc radius aperture centered on the centroid of each cluster. Shock heated regions toward the NW and SE of the northern cluster are suggested by high values of temperature and pressure (Fig. 9.8, see also Fig. G.2). This is in agreement with the late merger scenario (David & Kempner 2004) where the shocks have already crossed the central region of the ICM and are moving

²Note that the source roughly at the center of the diffuse radio emission in the optical image of Fig. 9.5 (right panel) is a star. No redshift has been reported for the X-ray point source (identified as SDSS J133300.32+502332.2) embedded in the candidate relic that is visible in the *Chandra* image of Fig. 9.4. With the current data we can not conclude whether it is associated with the radio emission.

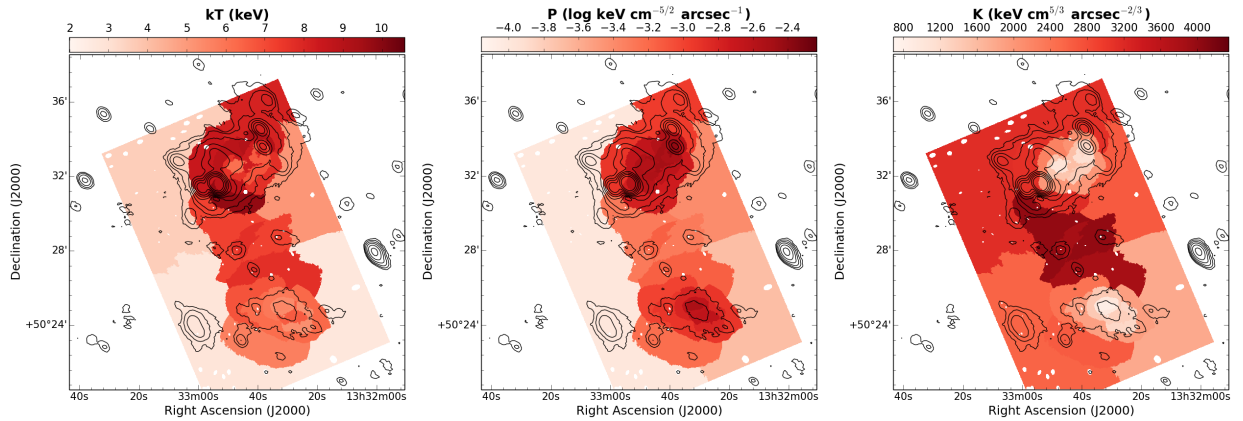


Figure 9.8: Thermodynamical properties of the ICM in A1758 with overlaid the LOFAR contours of Fig. 9.1. Images depict projected values of temperature (*left*), pressure (*center*) and entropy (*right*). The temperature error map and a lower S/N temperature map are reported in Appendix G.

outwards with high Mach numbers (Machado et al. 2015). Our entropy map of Fig. 9.8 (right panel) highlights the presence of the two cores in A1758N and the single core in A1758S, characterized by the lowest values of entropy in the map. This is in line with the bimodal (A1758N) and single clump (A1758S) mass distribution already inferred from optical studies (Dahle et al. 2002; Okabe & Umetsu 2008; Ragozzine et al. 2012; Monteiro-Oliveira et al. 2017).

9.3.5 The bridge between A1758N and A1758S

The maps of the ICM thermodynamical quantities shown in Fig. 9.8 show a complex thermodynamics in the region between A1758N and A1758S, suggesting that the two clusters are in early interaction. At this stage of the interaction the gas between them is compressed and heated, somewhat explaining the observed high values of temperature (~ 7.5 keV) and pressure in the region between the cluster pair. Moreover, the entropy map (Fig. 9.8, right panel) displays the largest values in such a region, further indicating an unrelaxed state of the clusters outskirts.

In these situations it is possible that a fraction of the energy dissipated in gas heating is channeled into non-thermal components via shocks, turbulence or other mechanisms activated by ICM microphysics. The LOFAR low-resolution contours of Fig. 9.4 give a tantalizing hint of a low SB bridge connecting A1758N and A1758S. This emission is detected at the 2σ level toward the eastern edge of the region between the two clusters. On the western edge of this region, a protuberance of the A1758N halo extends toward A1758S. Although particular care was devoted in the subtraction of the point-sources between the clusters, the blending of low level residual emission due to faint and unresolved sources, combined with the large synthesized beam of the image and with the non-uniform distribution of the noise, could mimic the filamentary structure. All this, together with the low significance level of the emission, does not allow us to make a firm statement about its presence. Nonetheless, filaments connecting galaxy clusters are expected to be observed in the radio band even on larger scales (e.g. Keshet et al. 2004; Araya-Melo et al. 2012; Vazza et al. 2015b). We note that a hint of a SZ signal connecting A1758N and A1758S was reported also in AMI Consortium: Rodríguez-González et al. (2012).

Given the possible evidence of a radio bridge, we searched for possible shocks or regions of gas compression in the X-rays. We analyzed the thermal properties of the X-ray emission between A1758N and A1758S, visible by smoothing to a resolution of $\sim 15''$ the *Chandra* 0.5 – 2.0 keV image (Fig. 9.9, left panel). We extracted spectra from five regions enclosing ~ 1000 counts each in the 0.5 – 2.0 keV band that were fitted as described in Section 9.2.5. The best-fitting spectra are re-

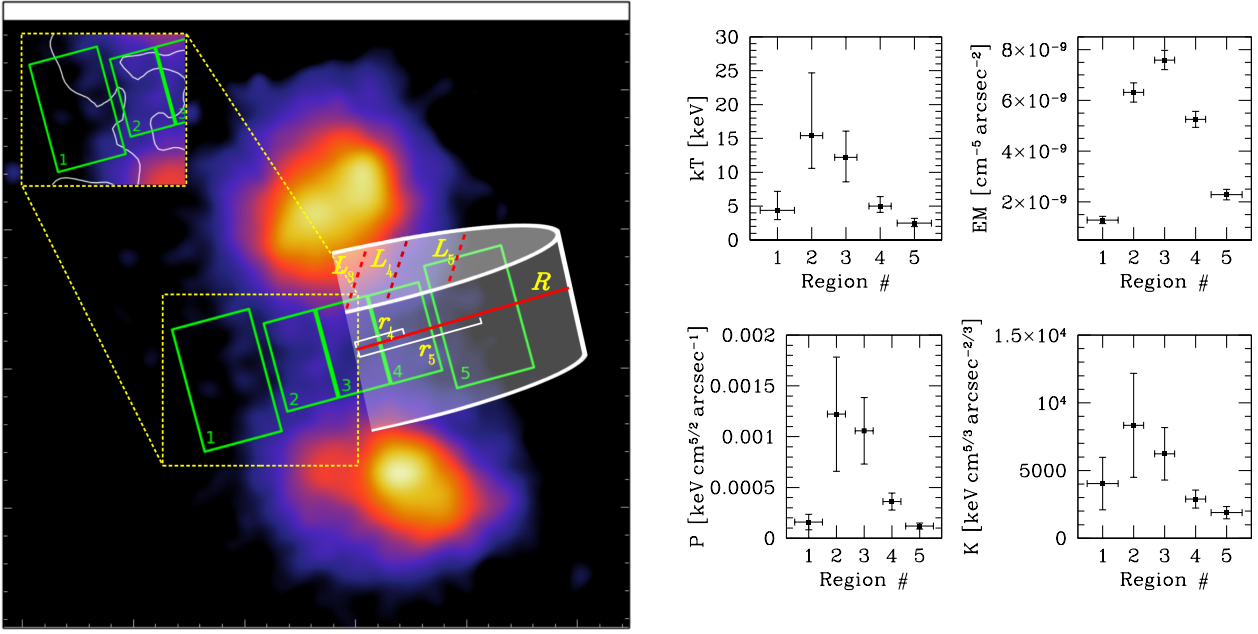


Figure 9.9: *Left panel:* same *Chandra* image of Fig. 9.2 but with point-sources subtracted and smoothed to a resolution of $\sim 15''$ to highlight the X-ray channel between the clusters. The spectral extracting regions are overlaid in green. The inset panel shows the spatial coincidence between the tentative radio bridge and the putative post-shock region. The cylindrical model assumed to assess the effects of projection is also sketched. The line of sight across the i -region is $L_i \sim 2\sqrt{R^2 - r_i^2}$. *Right panels:* projected values of temperature (kT), emission measure (EM), pressure (P) and entropy (K) of the X-ray channel.

ported in Appendix H. These were used to compute the temperature profile shown in Fig. 9.9 (right panel). We measure high kT values inside the X-ray channel that drop by a factor of ~ 3 between regions 2 and 1 (see Appendix G for the apparent discrepancy between the values of the temperature map and profile shown in Fig. 9.9); if projection effects play a role, the temperature drop would be even larger. Unfortunately, the count statistics does not allow us to increase spatial resolution to firmly understand if this is a sharp drop or a gradual decrement. If we assume that this is a jump due to a shock and we apply the Rankine-Hugoniot jump conditions (e.g. Landau & Lifshitz 1959), the derived Mach number³ would be $\mathcal{M}_{kT} = 3.0_{-1.0}^{+1.4}$ (Eq. 1.17). We notice that this putative shock is co-located with the 2σ level emission observed by LOFAR (Fig. 9.9, inset in the left panel). This is tantalizing and deserves future follow-ups as it might suggest a connection between the shock and the possible radio bridge. Its uncommonly high Mach number and unusual transversal location are in agreement with the recent work of Ha et al. (2018), where these kind of shocks are referred to as “equatorial”. Alternatively, the high kT values of the X-ray channel could be due to the adiabatic compression of the gas in the filament connecting A1758N and A1758S during the initial stage of the merger.

As a complementary information, the five spectra were used to compute the profiles of emission measure, pressure and entropy shown in Fig. 9.9 (right panel). These quantities are also observed to jump from the external to internal regions. We urge caution when interpreting these measurements as they were derived from the normalization of the cluster thermal model, that is $\propto n^2 L$, and are projected along the line of sight L (n is the density of the medium). For this reason, they are usually referred to as “pseudo” quantities (e.g. Mazzotta et al. 2004). We can assess the effects of projection

³Although also the SB drops outside the X-ray channel, we did not attempt the “canonical” broken power-law density profile fit (e.g. Markevitch & Vikhlinin 2007) to search for the edge due to the complex geometrical problem at this location (overlap of the outskirts of two galaxy clusters).

assuming a cylindrical shape for the X-ray channel (Fig. 9.9, left panel) and using the dependencies on the line of sight of the emission measure ($\propto L^{-1}$), pressure ($\propto L^{-1/2}$) and entropy ($\propto L^{1/3}$). For example, the ratio between the quantities measured at center and r_5 ($\equiv r_1$), i.e. the distance of the outermost region, changes by $< 16\%$ (or $< 34\%$) for emission measure, $< 8\%$ (or $< 16\%$) for pressure and $< 4\%$ (or $< 10\%$) for entropy for cylinder radii $R > 2r_5$ (or $> 1.5r_5$).

9.4 Discussion

A1758 is an ideal object to study the merger processes between galaxy clusters and the impact of these events on their environment. Indeed, this system is composed of two main components, A1758N and A1758S, in different evolutionary stages (see Section 9.1).

The diffuse radio emission in A1758 follows the X-ray emission of the ICM (Fig. 9.4), suggesting a relation between the thermal and non-thermal components. The double cluster A1758N and A1758S represents the second system known to date to host two radio halos. The first discovered is the pair A399-A401 (Murgia et al. 2010), located at $z = 0.07$. Both A1758 and A399-A401 show the presence of an X-ray channel between the cluster pair and some evidence for a lateral shock (Akamatsu et al. 2017b). The bridge connecting A399 and A401 is more clear and indeed it has been also observed via the SZ effect by the *Planck* satellite (Planck Collaboration VIII 2013); a hint of SZ signal is also found between A1758N and A1758S (AMI Consortium: Rodríguez-González et al. 2012).

9.4.1 The radio halos in the A1758 complex

It is known that giant radio halos follow a relation between their radio power at 1.4 GHz and the mass of the hosting cluster (e.g. Cassano et al. 2013). We used the values reported in Tab. 9.3 to calculate the k -corrected 1.4 GHz radio power (Eq. 1.23) for the two halos in A1758N and A1758S, corresponding to $P_{1.4}^N = (6.3 \pm 0.4) \times 10^{24} \text{ W Hz}^{-1}$ and $P_{1.4}^S = (7.7 \pm 1.8) \times 10^{23} \text{ W Hz}^{-1}$, respectively.

The $P_{1.4} - M_{500}$ relation reported in Cassano et al. (2013) was obtained using the masses derived from the *Planck* satellite via SZ effect, which is known to be a robust indicator of the cluster mass (e.g. Motl et al. 2005; Nagai 2006). However, the accuracy of the mass estimate for A1758N and A1758S with *Planck* is hindered by the difficulty of properly separating the two SZ components. Although the mass for A1758N has been estimated with different techniques, it is still uncertain and there is a large scatter in the values reported in the literature (see Tab. 1 in Monteiro-Oliveira et al. 2017). The mass of A1758S is even more uncertain due to the lack of literature studies focused on this sub-cluster. In this respect, we adopted the $M - T$ relation reported in Arnaud et al. (2005) to estimate M_{500} . We used the temperatures reported in David & Kempner (2004), and derived $M_{500}^N = 8.0_{-0.8}^{+1.8} \times 10^{14} M_{\odot}$ and $M_{500}^S = (5.1 \pm 0.4) \times 10^{14} M_{\odot}$ for A1758N and A1758S, respectively. We assumed these values being aware of the possible biases introduced in the scaling relation due to the ongoing mergers in A1758N and A1758S. However, we note that the masses estimated in such a way are within the values reported in the literature.

In Fig. 9.10 we compare our results with the $P_{1.4} - M_{500}$ relation reported in Cassano et al. (2013). The two radio halos in the A1758 complex lie very close to the best-fitting curve. Our results are in agreement with the fact that the most powerful radio halos are found in the most massive clusters.

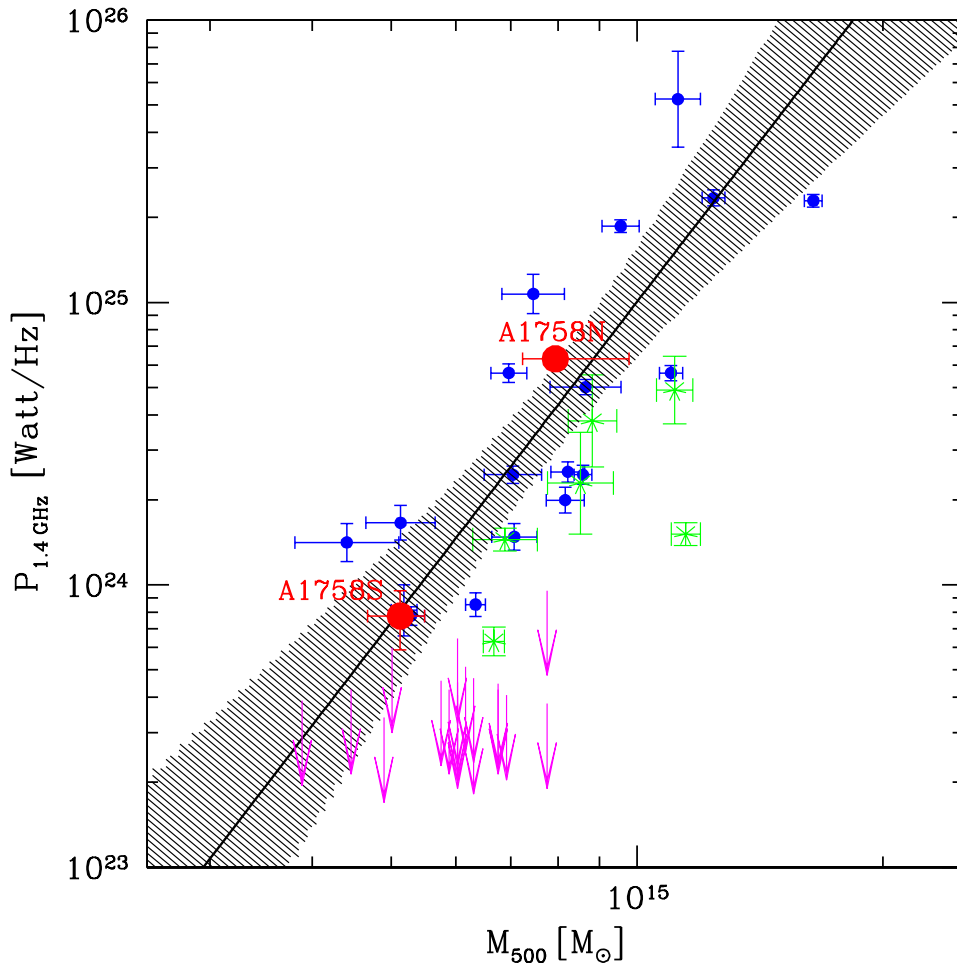


Figure 9.10: The $P_{1.4} - M_{500}$ relation for giant radio halos. Different colors indicate: giant radio halos (*blue*), ultra steep spectrum radio halos (*green*), upper limits from Venturi et al. (2008) (*magenta*) and the radio halos in A1758N and A1758S (*red*). Errors on $P_{1.4}^N$ are smaller than the point size. The best-fitting relation for giant radio halos and its 95% confidence level are shown. Adapted from Cassano et al. (2013).

9.4.2 Merger scenario between A1758N and A1758S

David & Kempner (2004) did not find any excess emission in the *XMM-Newton* data in the region between A1758N and A1758S above that expected from a projection of the two systems. This suggested that the two components are not interacting because numerical simulations of merging clusters predict a SB enhancement in the X-rays in the region of interaction (e.g. Roettiger et al. 1997; Ricker & Sarazin 2001; Ritchie & Thomas 2002). However, our observations provide new insights on the merger scenario between A1758N and A1758S.

Thanks to the new and deep *Chandra* observations, we were able to produce maps of the ICM thermodynamical quantities of all the A1758 complex (Fig. 9.8). They highlight the presence of high temperature and high entropy plasma in the region between the clusters, suggesting the existence of shock heated gas. This has been observed in a number of binary X-ray clusters in an early merging phase (e.g. A98, Paterno-Mahler et al. 2014; A115, Gutierrez & Krawczynski 2005; A141, Caglar 2018; A399-A401, Akamatsu et al. 2017b; A1750, Belsole et al. 2004; A3395, Lakhchaura et al. 2011; A3653, Caglar & Hudaverdi 2017; 1E2216.0-0401 and 1E2215.7-0404, Akamatsu et al. 2016; CIZA J1358.9-4750, Kato et al. 2015) and it is in agreement with predictions by numerical simulations (e.g. Takizawa 1999; Akahori & Yoshikawa 2010). In contrast, the temperature en-

hancement is typically not observed when the separation of the pair exceeds their combined virial radii (e.g. A2467 Wegner et al. 2017; A3528, Gastaldello et al. 2003; A3556-A3558, Mitsuishi et al. 2012; A3716, Andrade-Santos et al. 2015). Further indication of compressed gas in A1758 is given by the transversal profiles of Fig. 9.9 that also pinpoint a drop of the computed quantities outside the X-ray channel, toward the east direction. We speculated that this region traces a transversal shock. Reasons for this include the high Mach number inferred from the temperature jump ($\mathcal{M}_{\text{KT}} = 3.0_{-1.0}^{+1.4}$) and its position resembling that of the “equatorial” shocks recently studied by Ha et al. (2018). These shocks are the first to form during the merger phase and have high velocities and high Mach numbers since they propagate in very low density regions, contrary to those found in between the cluster pairs that are weaker due to the high temperature of the central medium (e.g. Belsole et al. 2004; Paterno-Mahler et al. 2014; Kato et al. 2015; Akamatsu et al. 2016, 2017b; Caglar 2018).

The 2σ level radio emission connecting A1758N and A1758S observed with LOFAR (Fig. 9.4) needs further confirmation. If real, it could have been generated as a consequence of the encounter between the two clusters. This may indicate that part of the gravitational energy is dissipated into non-thermal components during the early phase of the merger. We find intriguing its collocation with the possible transversal shock suggested by the temperature profile in Fig. 9.9 (see also Fig. G.2). A shock could indeed power the radio emission similarly to the case of radio relics, whilst equatorial shocks are less energetic due to the lower density of the upstream gas⁴ (Ha et al. 2018).

In conclusion, the results coming from our radio/X-ray analysis are consistent with a scenario where A1758N and A1758S are in a pre-merger phase, where the clusters are approaching, the gas between them is compressed and heated and the first shocks are launched. The application of a two-body dynamical model (e.g. Beers et al. 1982) to test the gravitational binding of the clusters would be of great interest to probe the merging scenario. Due to the overall complex dynamics of the merger (collision between clusters that are undergoing their own mergers), tailored numerical simulations would be useful to determine the impact velocities of the components in combination with multi-wavelength data (see e.g. Molnar et al. 2013 for the A1750 case).

9.5 Conclusions

In this Chapter, we presented new LOFAR HBA observations of the double galaxy cluster A1758. In combination with archival VLA and GMRT data, we constrained the spectral properties of the diffuse radio emission in the ICM. We also analyzed a deep archival *Chandra* observation on the system. Here, we summarize our main results.

1. The radio halo in A1758N is well known in the literature. LOFAR allowed us to recover diffuse radio emission from the ICM on a largest linear scale of ~ 2.2 Mpc. The integrated spectral index computed from 144 MHz to 1.4 GHz is $\alpha = 1.2 \pm 0.1$. The radio power of this halo is $P_{1.4}^{\text{N}} = (6.3 \pm 0.4) \times 10^{24} \text{ W Hz}^{-1}$.
2. Using LOFAR we discovered a new, faint, radio halo in A1758S, which was not previously identified in studies at higher frequencies with the GMRT and VLA observations. Our reanalysis of these datasets revealed its elusive nature and constrained its spectral index between 144 MHz and 1.4 GHz to $\alpha = 1.1 \pm 0.1$. The radio power of this halo is $P_{1.4}^{\text{S}} = (7.7 \pm 1.8) \times 10^{23} \text{ W Hz}^{-1}$.

⁴The energy dissipated by shocks is $\propto n_u V_{sh}^3$, where n_u is the upstream density and V_{sh} is the shock speed.

3. Peripheral emission in the eastern outskirts of A1758S is also observed with LOFAR, GMRT and VLA. We tentatively classified this source as a radio relic ($\alpha = 1.3 \pm 0.1$). Although the relic origin is suggested by a number of observational properties (e.g. morphology, location, linear extension), further observations are required to firmly determine its nature.
4. The two radio halos in A1758N and A1758S lie within the 95% confidence region of the best-fitting $P_{1.4} - M_{500}$ relation reported by Cassano et al. (2013).
5. The maps of the ICM thermodynamical quantities computed from the deep *Chandra* observation indicate that the region between A1758N and A1758S is unrelaxed. In this respect, we suggested that the two sub-clusters are in a pre-merger phase.
6. A possible bridge of radio emission connecting A1758N and A1758S is suggested by the low-resolution LOFAR image. The ICM temperature across this bridge shows a drop possibly indicating the presence of a compressed region or a transversal shock generated in the initial stage of the merger that could play a role in the formation of this diffuse emission.

CLUSTER MERGERS and the energy dissipated during these events play a central role in determining the observed properties of galaxy clusters and the physics of the ICM on different scales. A large fraction of the energy involved in these cosmic collisions is dissipated through shocks and turbulence in the ICM, where it can be channeled also into non-thermal phenomena. Whilst the knowledge of diffuse synchrotron sources in clusters, namely radio relics and halos, has significantly improved in the past decades, many questions concerning their origin, evolution and connection with the ICM physics remain still open.

In this Thesis, we aimed at deriving constraints on the generation mechanisms of non-thermal emission in merging clusters using X-ray and radio data. The PhD work included the exploitation of observations performed with LOFAR, a new generation instrument that is providing a revolutionary view of clusters at low frequencies. The data analysis carried out during the Thesis is state of the art and routinely made use of the joint radio/X-ray analysis. We obtained efficient constraints on the mechanisms at the origin of radio relics and their connection with cluster merger shocks. Furthermore, we entered in the exploration of non-thermal phenomena from dynamically complex cluster mergers with multiple components and obtained also first hints of a radio bridge of emission connecting two clusters in a pre-merging phase. Some of the most important outcomes of the Thesis are summarized below.

I. Relic–shock connection and particle acceleration mechanisms

Particle acceleration in Abell 115 and El Gordo

Deep *Chandra* observations of the clusters Abell 115 (Chapter 2) and El Gordo (Chapter 3) allowed us to clearly detect two shocks co-spatially located with two radio relics. This is a striking point favoring the relic–shock connection that only recently found observational support with the increasing number of detections in the X-rays of shocks underlying relics. Two models are proposed for the origin of relics: direct acceleration of electrons from the thermal pool via DSA and re-acceleration of a pre-existing population of relativistic seed electrons within clouds of relativistic plasma. The detection of shocks in Abell 115 and El Gordo, in combination with the re-analysis of VLA and GMRT data, allowed us to test the two formation scenarios. In particular, for the weak shock in Abell 115 we ruled out the DSA of thermal particles in favor of re-acceleration of seed electrons; this finding is in line with the picture emerging from the latest observations (Bonafede et al. 2014a; Shimwell et al. 2015; Eckert et al. 2016a; van Weeren et al. 2017a; Hoang et al. 2018a).

Conversely, for the strong shock in El Gordo we found that shock acceleration from the thermal pool is still a viable possibility.

Analysis of particle acceleration efficiency in a sample of radio relics

We extended the analysis done in Abell 115 and El Gordo to a sample of radio relics with underlying shocks detected with *Chandra* and/or *XMM-Newton* (Chapter 5). This is the first attempt to measure the shock acceleration efficiency in a physically motivated way for a sample of relics. We found that DSA can not explain the observed bolometric luminosity of relics if particles are accelerated from the thermal pool. This is basically due to the fact that shocks in cluster mergers are too weak to inject enough particles from the thermal pool in order to match the observed radio luminosity of radio relics. This strongly support that other mechanisms, such as shock re-acceleration, are involved in the formation of this kind of sources. The only exception is El Gordo; as discussed in Chapter 3, this represent a peculiar case as its NW relic is associated with strongest shock detected underlying a radio relic.

Discovery of new shocks (and cold fronts)

Based on the results presented in Chapters 2, 3 and 5, weak shocks are particularly important to understand the physics of particle acceleration in galaxy clusters because acceleration and re-acceleration models provide different expectations for these shocks. Although weak shocks should be, in principle, common in the ICM, they are very difficult to observe in the X-rays and their detection requires advanced techniques of data analysis. For this reason, we searched for new X-ray discontinuities in a sample of 15 merging galaxy clusters observed with *Chandra* (Chapter 6). Thus, we combined different approaches of data reduction to firmly claim the presence of the edges both via temperature and density jumps. The analysis was fruitful, and we were able to discover 22 new X-ray discontinuities in the ICM: 6 shocks, 8 cold fronts and 8 edges with uncertain origin. This work increased the statistics of detected edges in clusters and provided the discovery of new, weak, shocks to study the mechanisms of particle acceleration in cluster outskirts. The detection of cold fronts is an interesting by-product that, in combination with the ICM temperature, entropy, and pressure maps obtained during the analysis, will serve as a legacy for future studies of the clusters of the sample. For example, the maps of the ICM thermodynamical quantities and the presence of discontinuities in the ICM can be used to determine the dynamics of the merger, as we did for Abell 781 (Chapter 8) and Abell 1758 (Chapter 9). Remarkably, in the latter system we possibly found evidence for a transversal shock between the two cluster components. This would be the second case after the cluster pair Abell 399-401 (Akamatsu et al. 2017b) where a shock has been detected in a such peculiar location.

II. Non-thermal phenomena in dynamically complex mergers

The study of complex cluster chains and pairs in pre-merging phase is important to address the evolution of diffuse radio sources in the ICM and to use large scale emission to probe the dissipation of kinetic energy into non-thermal components on very large scales. For this reason, we analyzed radio and X-ray observations on the spectacular cluster chain Abell 781 (Chapter 8) and on the cluster pair Abell 1758 (Chapter 9). The research was anchored to the analysis of LOFAR data provided by the LOFAR Surveys KSP.

Radio halos in Abell 781 and Abell 1758

We solved a debate in the literature about the presence of a radio halo in Abell 781 (Chapter 8). Our LOFAR images have a brightness sensitivity to steep spectrum emission which is better than any other observation currently available on this target. We did not find any evidence for a radio halo in the main cluster of the chain and put a limit on the diffuse emission at its center. The absence of a radio halo in a merging system provides useful information on the mechanisms responsible of the origin of these sources. We speculated that the combination of mass and merger ratio of the system is too small to generate a radio halo, in agreement with model expectations that indeed predict a statistical decrement of the fraction of halos in merging systems with masses below $6 - 7 \times 10^{14} M_{\odot}$. It is possible that a faint halo or USSRH could be present but not visible in our observations due the presence of artifacts around the bright radio galaxy at the center of the cluster.

One of the contributions that LOFAR is expected to provide in galaxy cluster science is the detection of new radio halos and relics. This was the case of the double galaxy cluster Abell 1758, where we discovered a radio halo and a candidate radio relic in the southern system (Chapter 9). The new radio halo is barely visible from our re-analysis of GMRT and VLA data, but the evidence on these single observations alone is not compelling. Indeed, “classic” interferometers are typically able to detect very luminous radio halos, i.e. those harbored in massive clusters (as implied by the $P_{1.4} - M_{500}$ relation). Instead, the high sensitivity to low SB emission of LOFAR combined with its operative low frequencies range made possible a clear detection of diffuse emission even in A1758S, i.e. one of the less massive systems known so far to host a giant radio halo. Our results probes that LOFAR is enabling the detection of a population of low-power radio halos that were missed by previous instruments. This class of objects is important for the models of radio halo formation. The fact that we detected a halo in A1758S but not in Abell 781 suggests that the energetics of the two mergers is different and/or that they are in a different dynamical state.

AGN–shock connection in Abell 781

An interesting outcome of the radio/X-ray analysis of the cluster Abell 781 is the revision of the nature of its peripheral emission (Chapter 8). This source was previously classified as a candidate radio relic. The scenario emerging from the new LOFAR observations and the re-analysis of archival GMRT data is that this emission is more likely due to a giant radio galaxy distorted by the interaction with a shock crossing the ICM. The presence of a candidate optical counterpart and the bright knot of radio emission at the tip of the source strongly supports this hypothesis. However, the spectral index trend of the source is not typical of a head tail radio galaxy: the gradient observed shows a spectral steepening from the straight, outer, edge of emission toward the cluster center, which is common for radio relics. Therefore, we speculated that we are witnessing an intermediate stage between the destruction of a radio galaxy and the formation of a radio relic. This is an important result as the AGN–shock connection could explain the origin of some radio relics, including the eastern region of the relic in Abell 115 that may well be related to the radio galaxy 0056 + 26 B (Chapter 2), and the relic in Abell 3411-3412, which provides the most clear case of AGN–relic–shock connection observed so far (van Weeren et al. 2017a). In this scenario, the seed electrons to re-accelerate would be naturally provided by the nearby AGN. The currently available *XMM-Newton* observation on Abell 781 did not allow us to detect the putative shock and we were able to set an upper limit on the shock Mach number. Following the results presented in Chapter 5, the weak shock inferred from the present data, if present, would emphasize the problem of high acceleration efficiency implied by DSA from the thermal pool.

Bridge of radio emission between A1758N and A1758S

Another noteworthy result obtained thanks to high-sensitivity LOFAR observations on Abell 1758 is the tentative detection of a bridge of radio emission connecting the two clusters (Chapter 9). The bridge has a projected linear size of ~ 2 Mpc. In this region, the thermal gas displays high value of temperature, pressure, and entropy, suggesting that the two clusters are in a pre-merging state. Currently, it is not clear whether the gas kinetic energy can be dissipated into non-thermal components already at this stage. Our results provides, for the first time, a direct observational support to the possibility that diffuse radio emission could be triggered even in the early phase of interaction. A candidate shock suggested by *Chandra* data and co-located with the radio emission could be responsible of the observed feature. The existence of bridges of radio emission between interacting clusters is a new observational field. For this reason, we proposed to observe other binary clusters with LOFAR. Data analysis is in progress but not included in this Thesis.

III. Magnetic field in cluster outskirts

If confirmed, the detection of the radio bridge in Abell 1758 would suggest that magnetic fields between interacting systems can be amplified and compressed up to reach μG levels. In general, the knowledge of the magnetic field amplification in cluster outskirts is still limited. This is relevant for the origin of radio relics and to calculate the shock particle acceleration efficiency at cluster shocks (Chapter 5). The detection of IC emission from a radio relic has the potential to constrain the downstream magnetic field strength, hence the acceleration efficiency of the underlying shock (Chapter 4). We showed that El Gordo cluster is the best target to perform this search and that a clear detection of IC from its NW relic would rule out DSA also in the case of the strongest merger shocks. However, the achievement of this goal would require a major time investment with the current instruments, even for an exceptional target such as El Gordo.

Final remarks

The results obtained in this PhD Thesis are at the cutting edge of galaxy cluster science. Increasing the number of shocks and radio relics will be critical to determine in a definitive way the acceleration efficiency at cluster merger shocks and the related problem of the formation of diffuse synchrotron sources in cluster outskirts. A longer term perspective in the study of particle acceleration and magnetic field amplification at cluster shocks is the detection of IC emission from radio relics. This is a challenging result that is feasible only by coupling the *Chandra*-like high angular resolution to a large effective area. In the future, the study of the interplay between thermal and non-thermal components in the ICM will benefit of the new generation of X-ray and radio instruments, in particular *Athena* and the SKA (and its pathfinders). During the PhD project we exploited the unique capabilities of LOFAR, the largest pathfinder of SKA-LOW. LOFAR is entering into unexplored territories for non-thermal phenomena in clusters and large scale structure of the Universe, including the investigation of diffuse radio emission from less massive systems and that from pre-merging systems. Studies at low frequencies with LOFAR and MWA will shortly provide fundamental information on the physics of non-thermal components in these environments.

A SB jump across the Sausage?

Whilst the single power-law fit shown in Fig. 5.13 provides a fair description of the SB across the Sausage, some data points are in excess with respect to the model at $r \sim 7'$, i.e. at the position of the radio relic. If this excess is a real astrophysical signal, it may indicate the presence of IC emission from the relic or the suggestion of a SB jump (or a combination of the two). We exclude that we missed to excise any point source during the analysis. Here we focus on the second possibility because, as shown in Chapter 4, the level of SB due to IC is expected to be low for the Sausage.

If we use the same sector shown in Fig. 5.13 and rebin the data to reach a minimum S/N of 5 (instead of 7), a broken power-law model (Eq. 1.21) appears to be in excellent agreement with SB profile (Fig. A.1). The position of the density jump is well constrained and coincides with the leading edge of the radio relic. Assuming that this discontinuity traces a shock, the corresponding Mach number is $\mathcal{M}_{\text{SB}} = 2.0_{-0.5}^{+2.7}$, where the large errors are due to the low count statistics. This is tantalizing as it could confirm the claim of a shock based on the temperature jump observed with *Suzaku* by Akamatsu et al. (2015). The profile shown in Fig. A.1 must be considered only as a hint of discontinuity, as the fit becomes unstable if systematic uncertainties are considered (e.g. different choice of the extracting sector). Deeper *Chandra* observations will clarify this point.

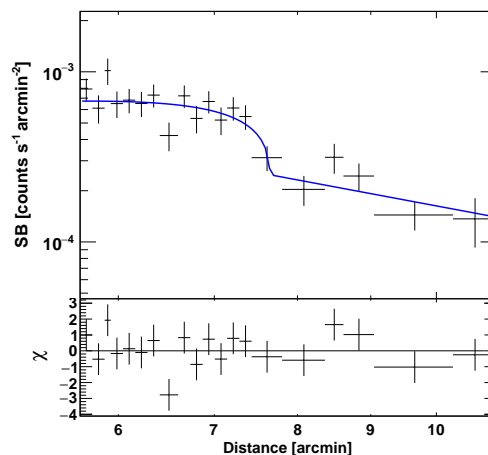


Figure A.1: SB profile across the Sausage relic. Data were extracted in the same sector shown in Fig. 5.13 and were rebinned to reach a minimum S/N of 5. A broken power-law model suggests the presence of a discontinuity at the location of the outer edge of the relic.

Galactic absorption

From Fig. 6.1 it seems that for five clusters of our sample (A399, A401, AS592, A2104 and Triangulum Australis) the molecular component of the hydrogen density column can not be neglected. Here we want to compare the density column values as derived from the Leiden/Argentine/Bonn survey of H_I (Kalberla et al. 2005), the Willingale et al. (2013) work (where the molecular hydrogen density column was derived using a function depending on the product between N_{H_I} and the dust extinction), the fits in Cavagnolo et al. (2009) and ours, obtained by fitting *Chandra* spectra extracted in central regions of the above-mentioned clusters and keeping the density column parameter free to vary. Values are compared in Tab. B.1 and the results of our fits can be summarized as follows.

- A399 and A401 are in line with the values reported from Kalberla et al. (2005) and Cavagnolo et al. (2009), indicating lower values with respect to Willingale et al. (2013).
- AS592 is in line with Willingale et al. (2013) while Kalberla et al. (2005) and Cavagnolo et al. (2009) suggest lower column densities. However, the discrepancy is $\lesssim 25\%$.
- A2104 appears to be in a direction with a higher density column with respect to that expected from H_I (Kalberla et al. 2005), in agreement with Willingale et al. (2013) and Cavagnolo et al. (2009).
- *Triangulum Australis* is known lay in a region with high absorption, our density column is more in line with Willingale et al. (2013) than with Kalberla et al. (2005).

We carried out the analysis that led to the results presented in Section 6.5 adopting the density column values achieved in our fits (Tab. B.1) for these five clusters.

Table B.1: Density columns reported from Kalberla et al. (2005) (K05), Willingale et al. (2013) (W13) and Cavagnolo et al. (2009) (C09) compared with the results of our fits. Values are reported in units of 10^{20} cm^{-2} .

Cluster name	K05	W13	C09	Fit
A399	10.6	17.1	11.5	9.8 ± 1.1
A401	9.88	15.2	12.5	10.8 ± 0.4
AS592	6.07	8.30	6.41	8.0 ± 0.5
A2104	8.37	14.5	14.9	15.8 ± 0.7
Triangulum Australis	11.5	17.0	...	18.4 ± 0.8

The NXB spectrum is different for the ACIS-I and ACIS-S detectors¹ (Eq. 6.2) and its continuum part can be rewritten as

$$C(E) = \mathcal{K}_1 e^{-A_1 E} + \mathcal{K}_2 E^{-A_2} \quad (\text{C.1})$$

for ACIS-I and as

$$C(E) = \mathcal{K}_1 e^{-A_1 E} + \begin{cases} \mathcal{K}_2 E^{-\Gamma_1} & \text{if } E \leq E_b \\ \mathcal{K}_2 E_b^{\Gamma_2 - \Gamma_1} \left(\frac{E}{1 \text{ keV}}\right)^{-\Gamma_2} & \text{if } E > E_b \end{cases} \quad (\text{C.2})$$

for ACIS-S, where the parameters \mathcal{K}_1 and \mathcal{K}_2 represent the normalizations, A_1 and A_2 are dimensionless factors and E_b is the break point for the energy of the broken power-law described by the two photon indexes Γ_1 and Γ_2 .

The ACIS-I NXB was investigated by Bartalucci et al. (2014), they performed a detailed analysis of the stowed VFAINT ACIS-I event files to create an analytical model of background. We adopted the values reported in Tab. 1 of Bartalucci et al. (2014) for the parameters of Eq. C.1. To model the ACIS-S NXB we used a similar approach and extracted spectra from the S3 chip (used for the imaging of the target) of the stowed ACIS-S event files taken in the closer epoch to the observation. Our best-fitting values are reported in Tab. C.1 for both FAINT and VFAINT observing mode. The NXB models for ACIS-I and ACIS-S are shown in Fig. C.1.

Once that the shape of the NXB has been modeled on the stowed files, the total (astrophysical+instrumental) background of Eq. 6.1 was fitted in a peripheral region of the target observation, where the cluster emission is almost negligible, letting the normalizations free to vary and then it was rescaled in the region of interest. In the fitting of ACIS-S spectral regions we found that for $E > E_b$ the spectrum can not be described by a single value of Γ_2 that, for this reason, was also let free to vary in the fits. This possibly indicates a spatial variation with respect to the chip coordinates of the second photon index of the broken power-law. A deeper investigation of the ACIS-S NXB (as the one performed by Bartalucci et al. 2014 for ACIS-I) would be of great interest and certainly desirable.

¹<http://cxc.cfa.harvard.edu/contrib/maxim/stowed/>

Table C.1: Best-fit parameters of Eq. C.2. The normalization values \mathcal{K}_1 and \mathcal{K}_2 are given in XSPEC units, the break energy E_b is in keV.

Parameter	ACIS-S	
	FAINT	VFAINT
\mathcal{K}_1	0.0257	0.0167
A_1	0.52	0.40
\mathcal{K}_2	0.0025	0.0028
Γ_1	-0.73	-0.52
Γ_2	-5.19	-5.57
E_b	6.48	6.42

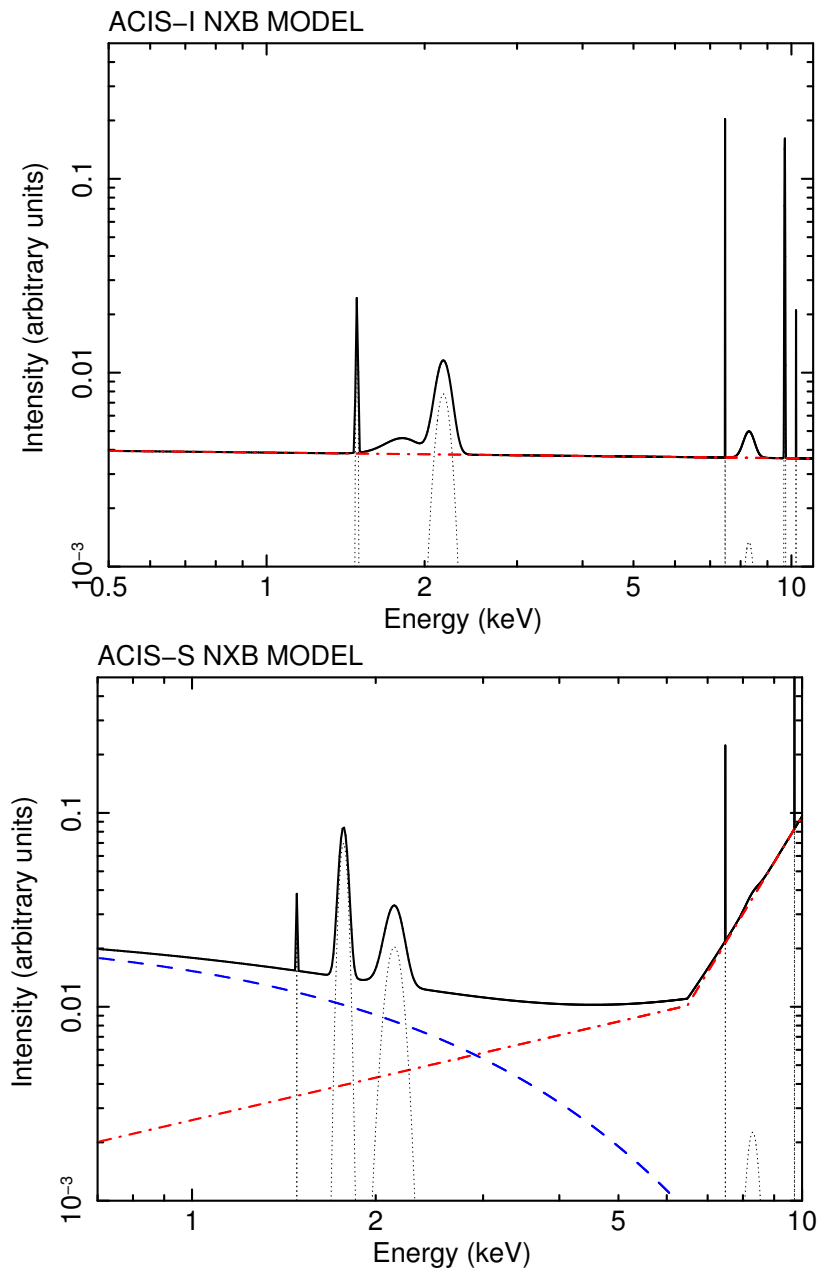


Figure C.1: ACIS-I (top) and ACIS-S (bottom) NXB models. Gaussian lines are reported in *dotted black*, the exponential decay in *dashed blue* (not visible for ACIS-I) and the (broken) power-law in *dot-dashed red*.

Statistical precision of the fits

In Fig. D.1–D.14 we report the c -stat/d.o.f. and the fractional error on the determination of the temperature for each spectral region shown in Fig. 6.3–6.12 and 6.15–6.18. Pressure and entropy uncertainties are dominated by the errors on the temperature (see Eq. 6.6 and 6.7) as the errors on the emission measure are only at a level of a few percent. The χ^2 /d.o.f. of the broken power-law fits is close to unity in the majority of SB profiles.

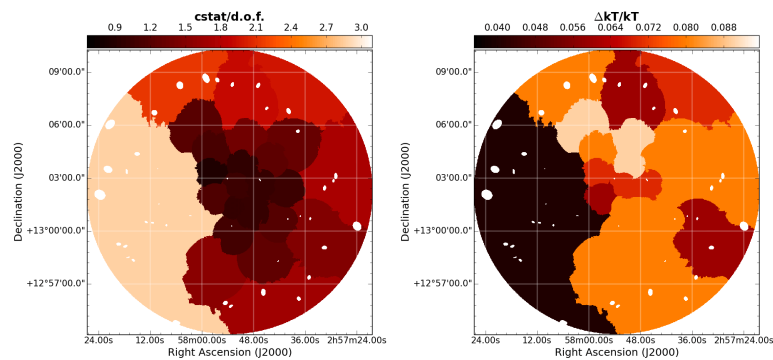


Figure D.1: Values of c -stat/d.o.f. (*left*) and error map on kT (*right*) for A399 (cf. Fig. 6.3).

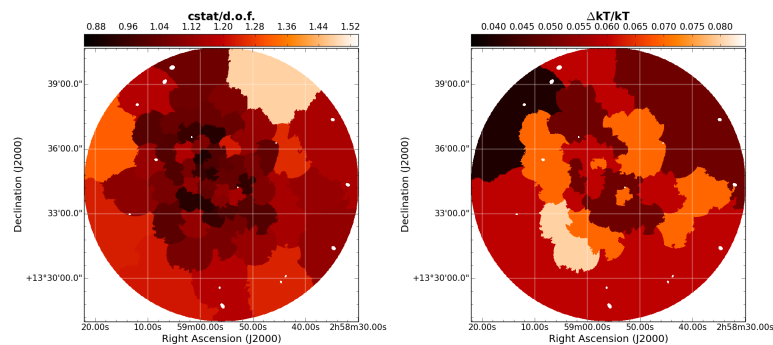


Figure D.2: The same as Fig. D.1 but for A401 (cf. Fig. 6.4).

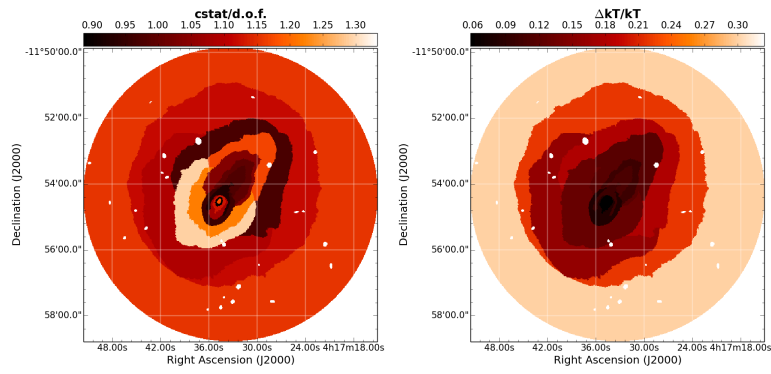


Figure D.3: The same as Fig. D.1 but for MACSJ0417 (cf. Fig. 6.5).

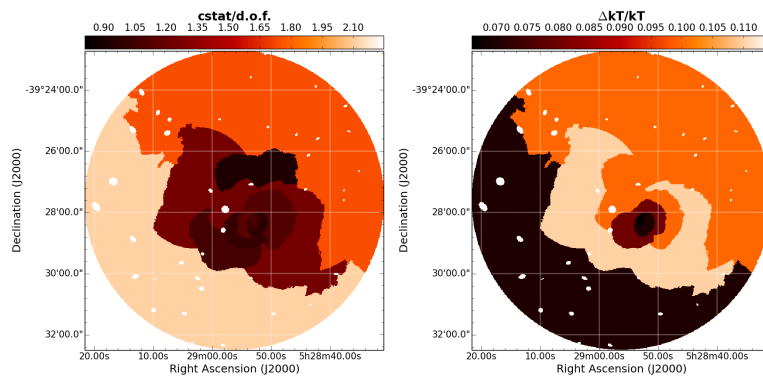


Figure D.4: The same as Fig. D.1 but for RXCJ0528 (cf. Fig. 6.6).

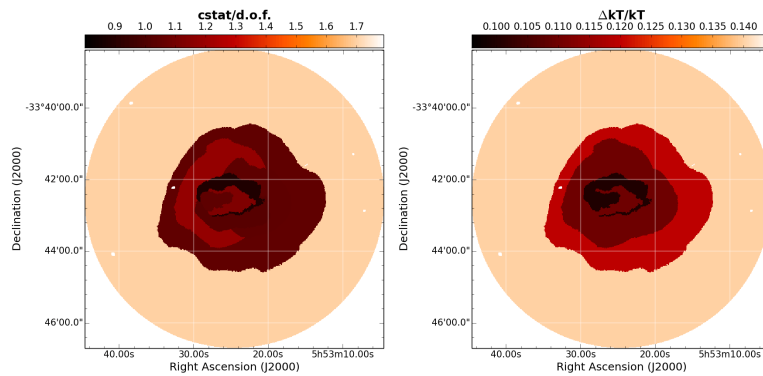


Figure D.5: The same as Fig. D.1 but for MACSJ0553 (cf. Fig. 6.7).

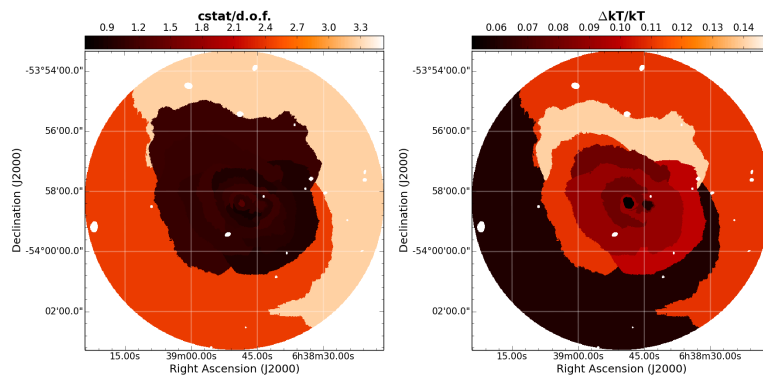


Figure D.6: The same as Fig. D.1 but for AS592 (cf. Fig. 6.8).

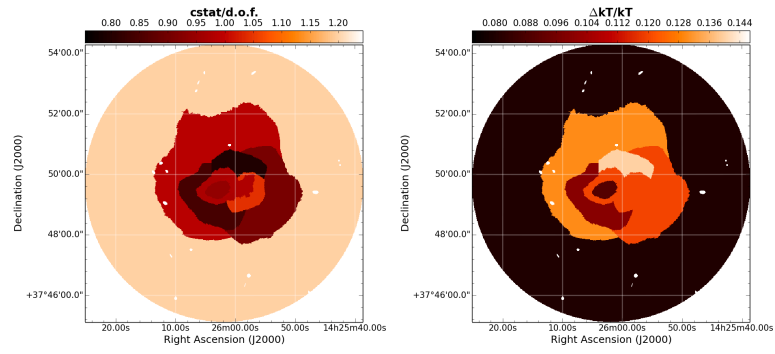


Figure D.7: The same as Fig. D.1 but for A1914 (cf. Fig. 6.9).

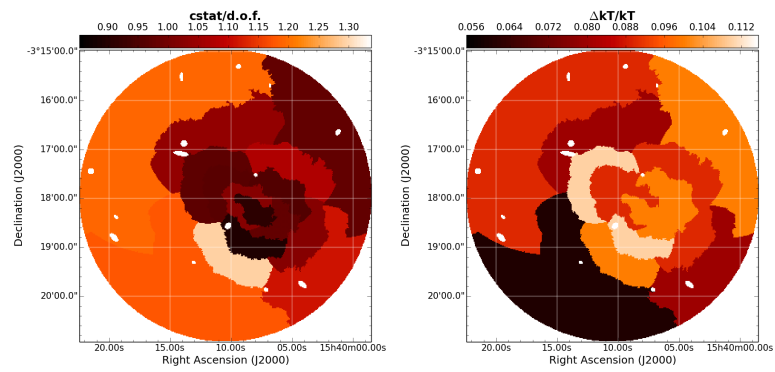


Figure D.8: The same as Fig. D.1 but for A2104 (cf. Fig. 6.10).

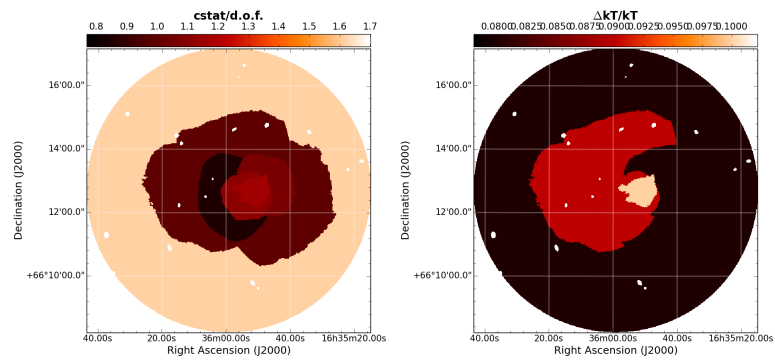


Figure D.9: The same as Fig. D.1 but for A2218 (cf. Fig. 6.11).

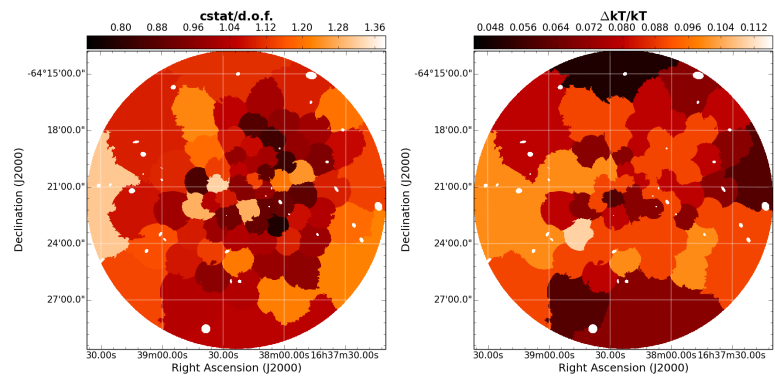


Figure D.10: The same as Fig. D.1 but for Triangulum Australis (cf. Fig. 6.12).

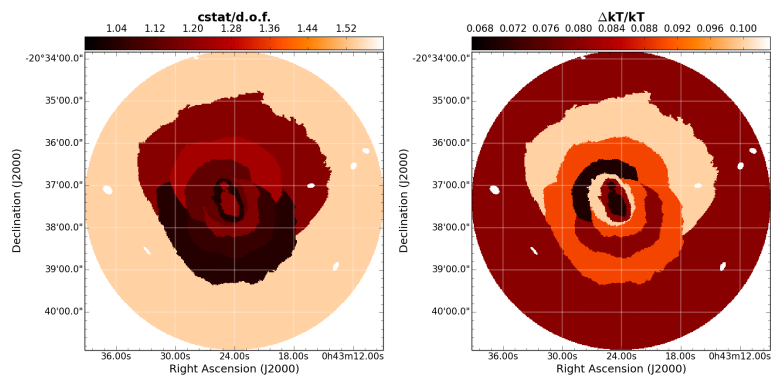


Figure D.11: The same as Fig. D.1 but for A2813 (cf. Fig. 6.15).

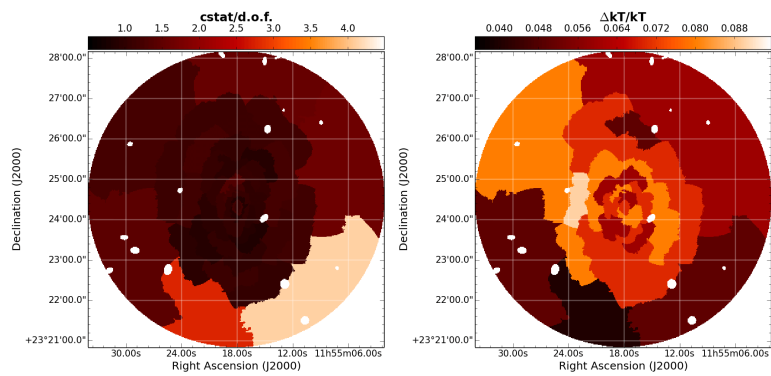


Figure D.12: The same as Fig. D.1 but for A1413 (cf. Fig. 6.16).

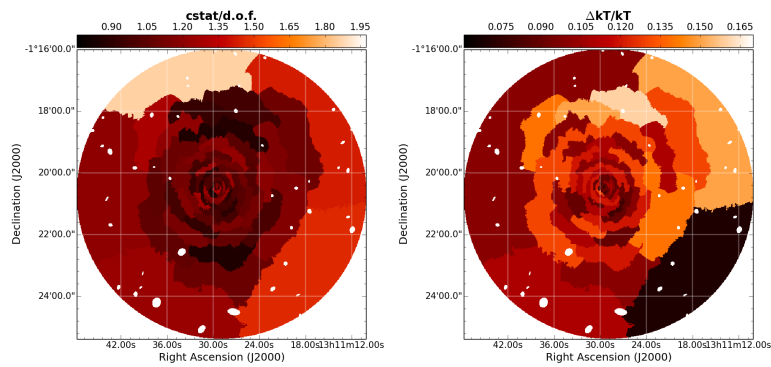


Figure D.13: The same as Fig. D.1 but for A1689 (cf. Fig. 6.17).

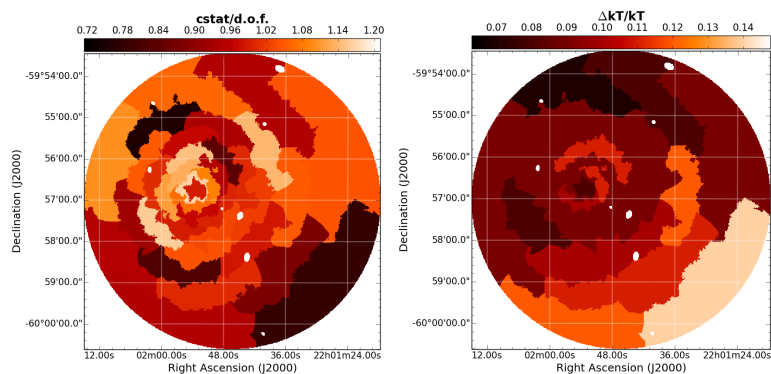


Figure D.14: The same as Fig. D.1 but for A3827 (cf. Fig. 6.18).

Null results

Here we report seven cases where the presence of a SB gradient was suggested by the GGM filters but the fitting of the SB profile did not evidence any sharp edge. In Fig. E.1–E.5 we show the GGM images with $\sigma = 8$ pixels with overlaid the sectors used to extract the SB profiles of the candidate edges together with the corresponding broken power-law model (Eq. 1.21) fits.

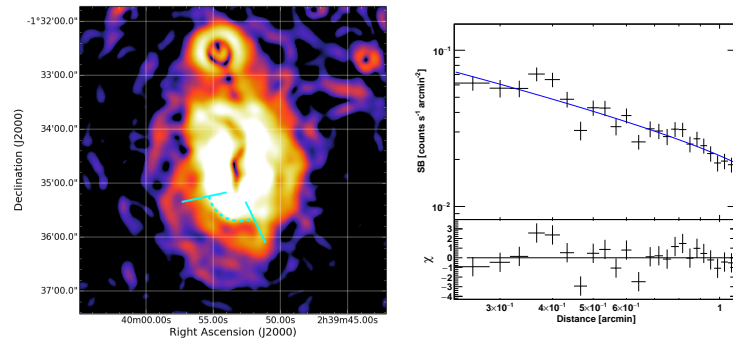


Figure E.1: GGM filtered image of A370 (the same as Fig. 6.2c) marked with the region used to extract the SB profile (*left*) and corresponding fit (*right*). The putative edge is at $r \sim 0.6'$.

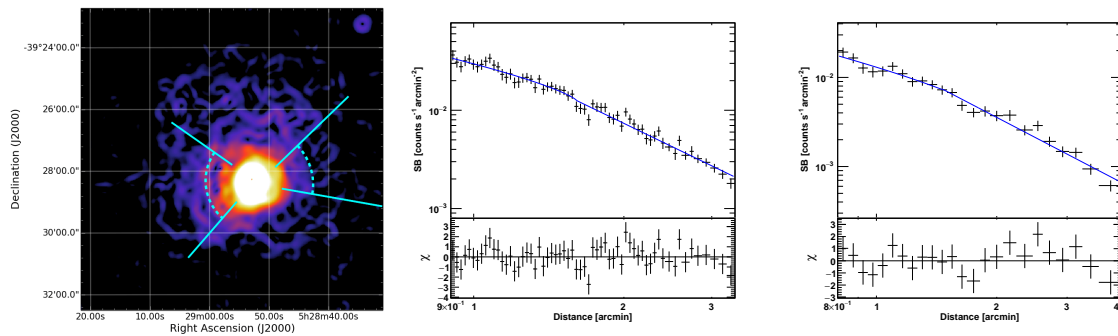


Figure E.2: GGM filtered image of RXCJ0528 (the same as Fig. 6.6c) marked with the regions used to extract the SB profiles (*left*) and corresponding fits. The putative edge in the E sector is at $r \sim 1.6'$ (*center*) whereas in the W sector is at $r \sim 1.8'$ (*right*).

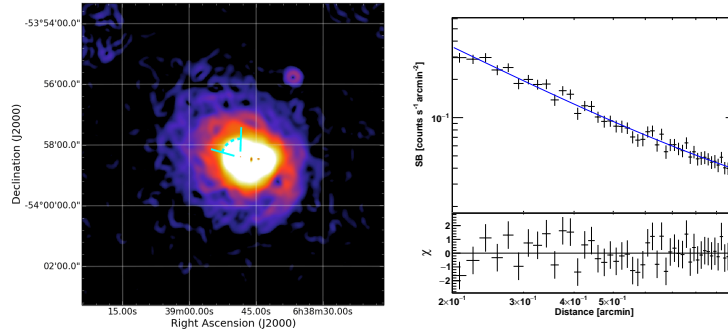


Figure E.3: GGM filtered image of AS592 (the same as Fig. 6.8c) marked with the region used to extract the SB profile (*left*) and corresponding fit (*right*). The putative edge is at $r \sim 0.6'$

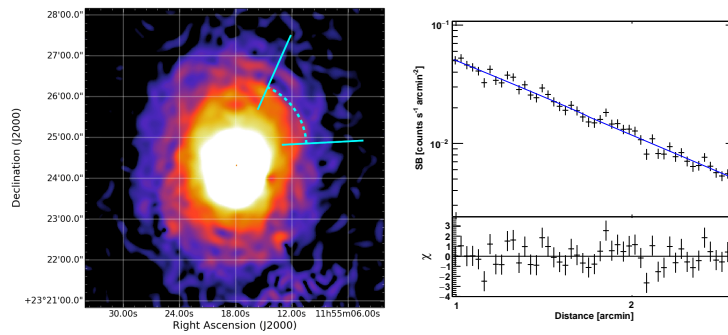


Figure E.4: GGM filtered image of A1413 (the same as Fig. 6.16c) marked with the region used to extract the SB profile (*left*) and corresponding fit (*right*). The putative edge is at $r \sim 1.6'$

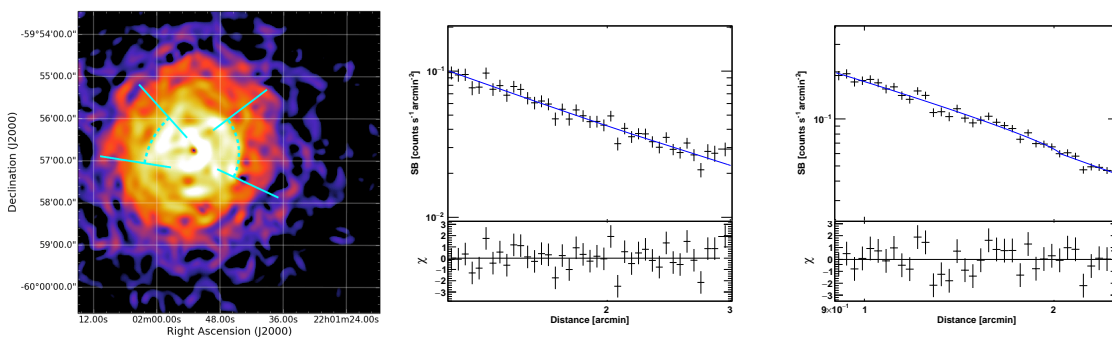


Figure E.5: GGM filtered image of A3827 (the same as Fig. 6.18c) marked with the regions used to extract the SB profiles (*left*) and corresponding fits. The putative edge in the E sector is at $r \sim 1.8'$ (*center*) whereas in the W sector is at $r \sim 1.3'$ (*right*).

Error maps for the spectral index (Fig. F.1), temperature and entropy (Fig. F.2).

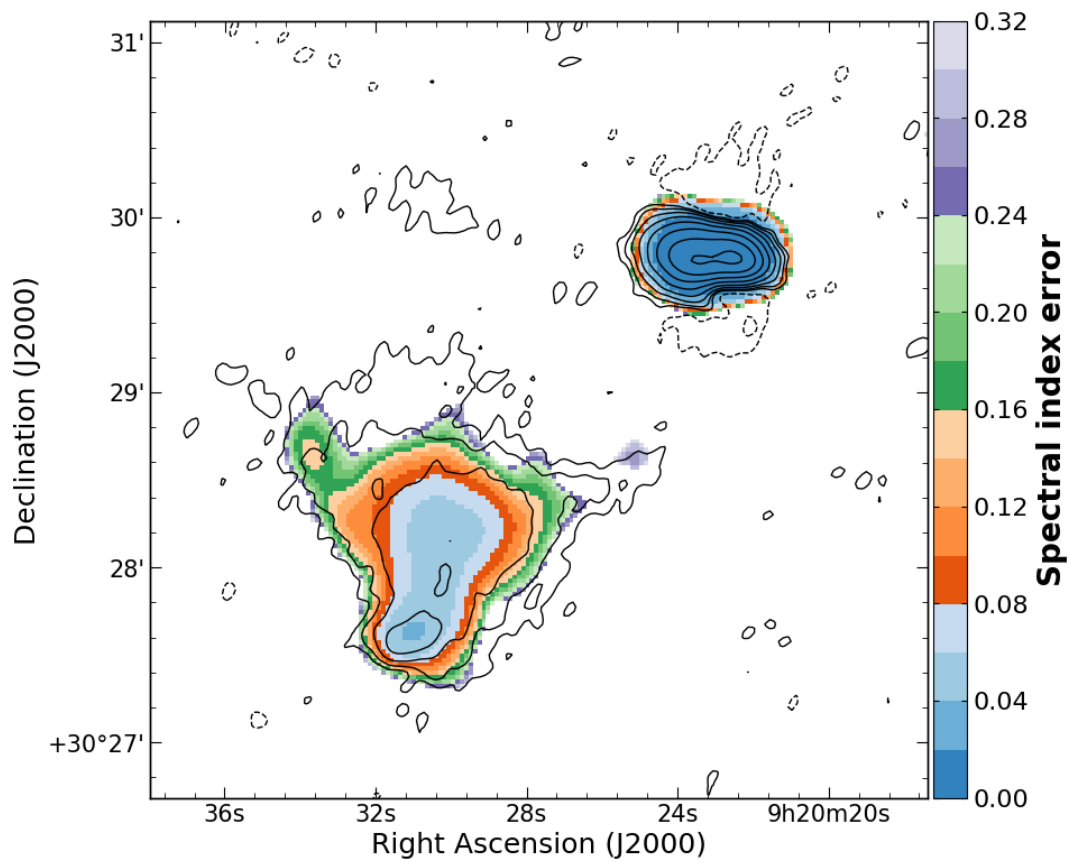


Figure F.1: Spectral index error map corresponding to Fig. 8.6.

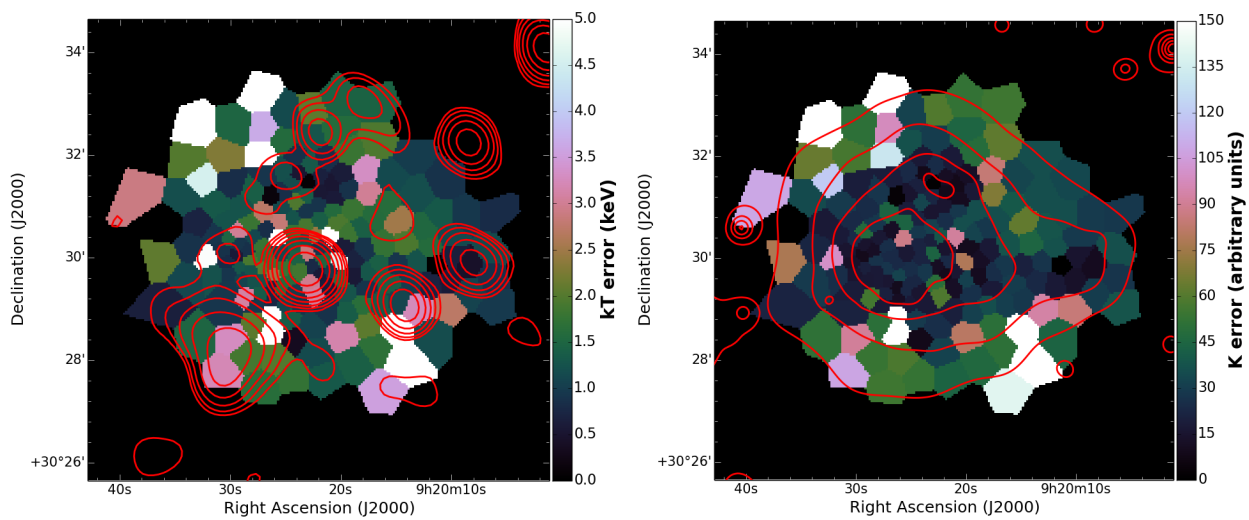


Figure F.2: Temperature (*left*) and entropy (*right*) error maps corresponding to Fig. 8.11.

Temperature map

The fractional errors on the temperature map of Fig 9.8 are reported in Fig. G.1. Projected pressure and entropy have similar fractional errors due to their linear dependence on the temperature and to the general small error on the emission measure.

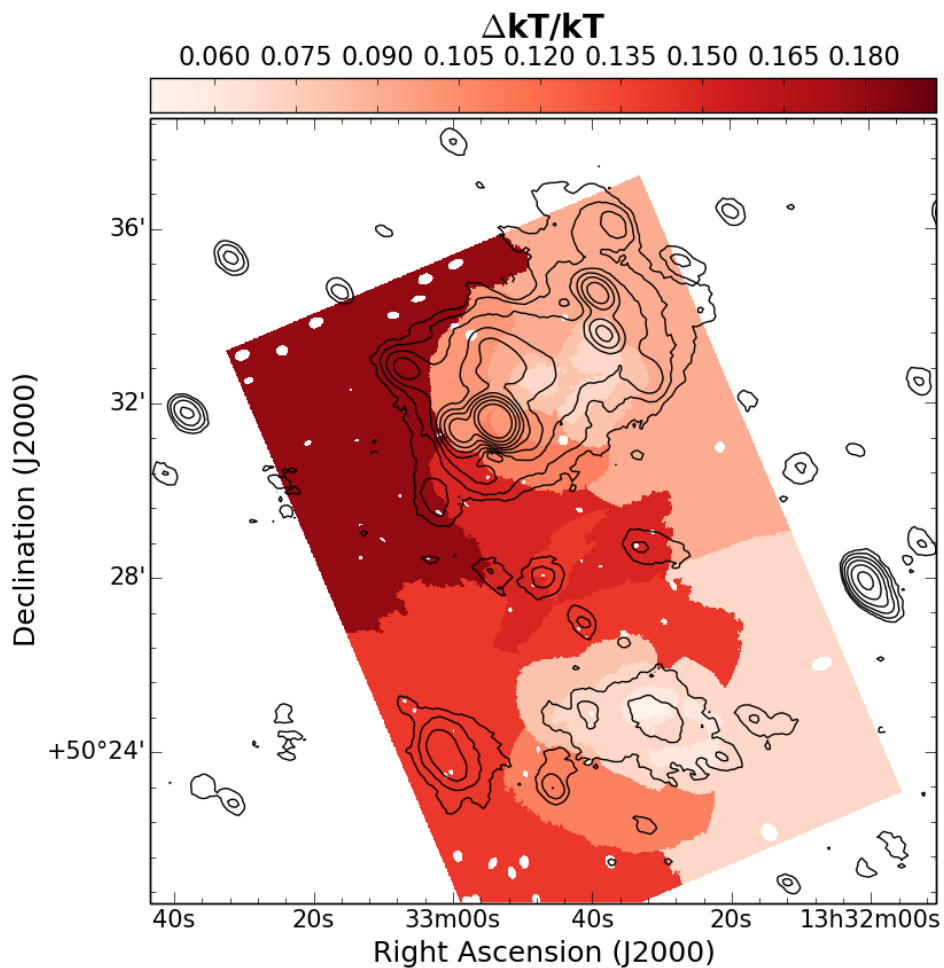


Figure G.1: Temperature error map of A1758 (cf. with Fig 9.8).

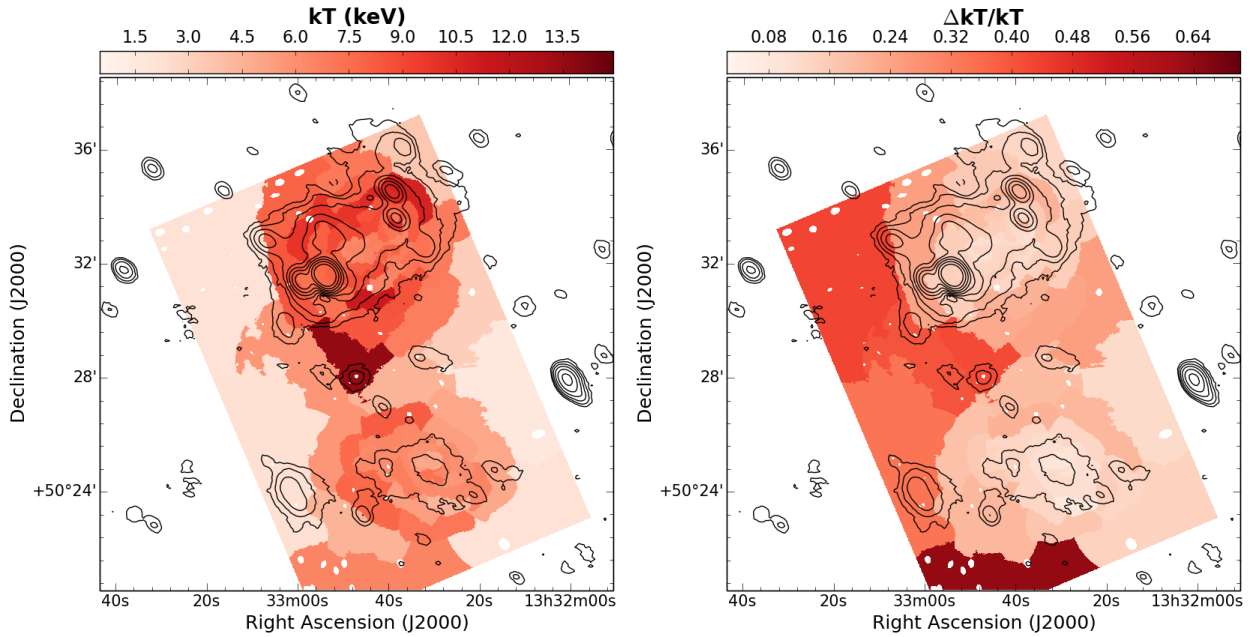


Figure G.2: Low S/N temperature map (*left*) and relative error map (*right*) of A1758.

The high value of temperature in the putative post-shock region of Fig. 9.9 can not be identified in the temperature map of Fig. 9.8 (left panel) likely due to the fact that the spectral extracting sectors are large, hence they might contain a mix of plasma with different temperatures. In Fig. G.2 we show that if the required S/N per region is reduced to 30, the CONTBIN algorithm is able to draw a smaller sector similar in size and position to region 2 in Fig. 9.9 where the spectral fit provides again $kT \sim 15$ keV, canceling the apparent tension between the two results.

X-ray channel spectra

The best-fitting spectra of the five regions shown in Fig. 9.9 are reported in Fig. H.1. The spectral model components are depicted with different colors in the plots. To assess the impact of the systematic uncertainties of the background modeling to the estimates of the ICM temperature, we re-performed the spectral fits varying within $\pm 1\sigma$ the normalization levels first of the instrumental background alone, and later of both the instrumental and astrophysical backgrounds. The results are summarized in Tab. H.1 and are consistent within 1σ with that reported in Fig. 9.9 (right panel). Finally, we mention that the drop of the *Chandra* effective area above 5 keV makes the estimation of high temperatures critical with this instrument. In this respect, the errors on the high temperatures reported in Tab. H.1 may not reflect entirely the real range of statistical and systematic uncertainties.

Table H.1: Impact of the systematic uncertainties of the background modeling on the temperature estimates reported in Fig. 9.9 (right panel). Tests were performed varying within $\pm 1\sigma$ the normalization level of the instrumental background (“NXB”) and of the astrophysical background (“sky”). Temperatures are reported in keV units.

Region	Best fit	NXB		NXB + Sky	
		+1 σ	-1 σ	+1 σ	-1 σ
1	4.4 ^{+2.8} _{-1.4}	3.7 ^{+2.1} _{-1.0}	5.4 ^{+4.1} _{-1.9}	3.5 ^{+4.1} _{-1.5}	5.1 ^{+3.4} _{-1.1}
2	15.4 ^{+9.3} _{-4.8}	14.1 ^{+7.7} _{-3.8}	17.1 ^{+12.5} _{-5.1}	15.4 ^{+9.8} _{-5.1}	16.7 ^{+10.0} _{-5.1}
3	12.2 ^{+3.9} _{-3.6}	10.2 ^{+4.5} _{-2.3}	13.6 ^{+3.5} _{-3.9}	11.8 ^{+4.1} _{-3.4}	13.2 ^{+3.5} _{-3.7}
4	5.0 ^{+1.4} _{-0.9}	4.5 ^{+1.2} _{-0.7}	5.4 ^{+1.5} _{-1.1}	4.8 ^{+1.4} _{-0.9}	5.3 ^{+1.5} _{-1.0}
5	2.5 ^{+0.7} _{-0.5}	2.2 ^{+0.6} _{-0.3}	2.7 ^{+0.9} _{-0.5}	2.3 ^{+0.7} _{-0.4}	2.8 ^{+0.8} _{-0.6}

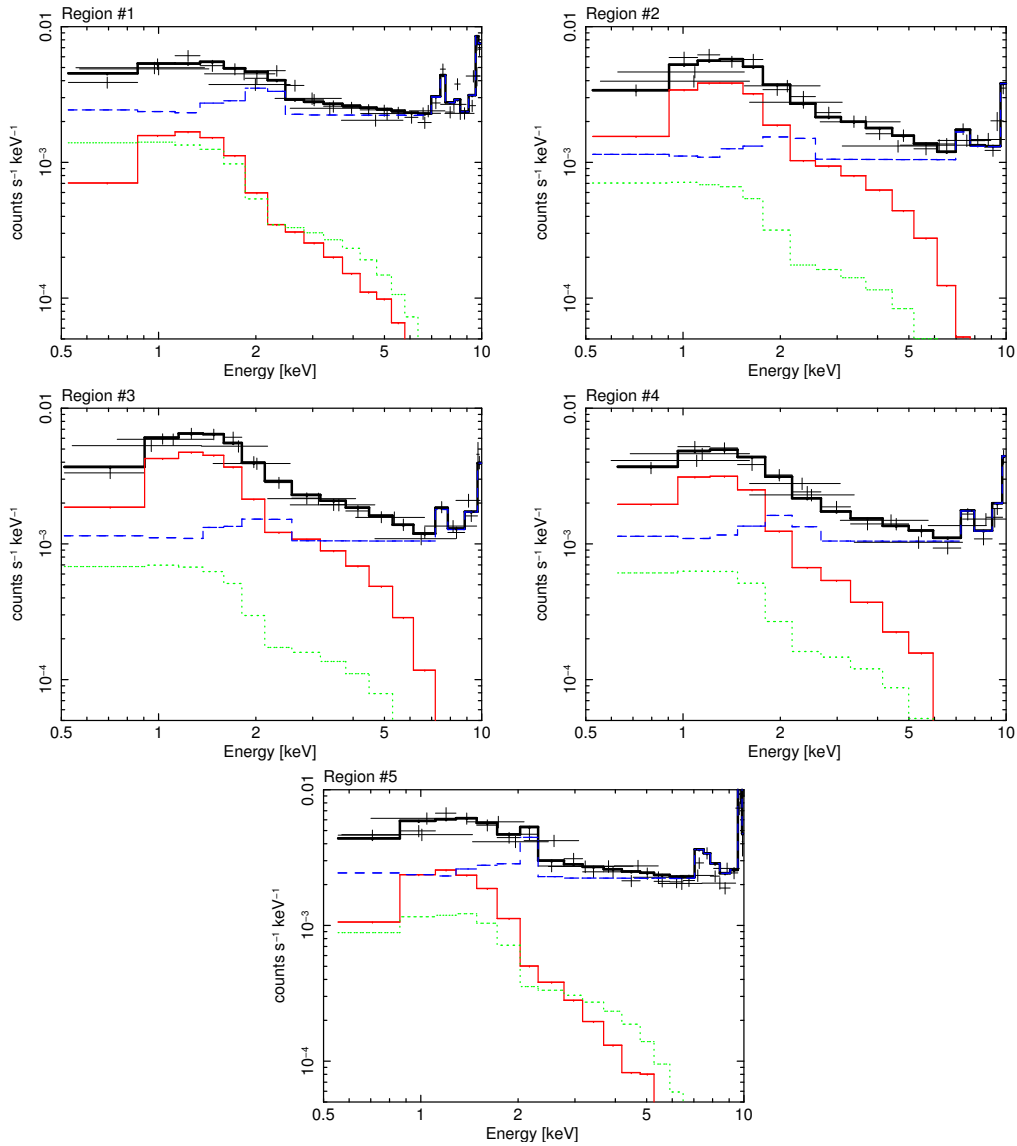


Figure H.1: Spectral fitting results for the five regions shown in Fig. 9.9 (left panel). Data points are shown in black together with the best-fitting model. Different colors denote the components of the spectral model; i.e., the cluster emission (*solid red*), the astrophysical background (*dotted green*) and the instrumental background (*dashed blue*). Whilst the three ObsID spectra were simultaneously fitted, the models for only one observation were reported in order to avoid confusion in the plot. The c -stat/d.o.f. of the fits from region 1 to 5 are: 232/184, 135/127, 114/132, 115/113 and 224/182.

- Abate, A., et al. 2009, *ApJ*, 702, 603
- Abell, G., et al. 1989, *ApJS*, 70, 1
- Abolfathi, B., et al. 2018, *ApJS*, 235, 42
- Ackermann, M., et al. 2010, *ApJ*, 717, L71
- Ackermann, M., et al. 2014, *ApJ*, 787, 18
- Ackermann, M., et al. 2016, *ApJ*, 819, 149
- Adam, R., et al. 2016, *A&A*, 586, A122
- Adam, R., et al. 2017a, *A&A*, 606, A64
- Adam, R., et al. 2017b, *A&A*, 598, A115
- Adam, R., et al. 2018a, *A&A*, 609, A115
- Adam, R., et al. 2018b, *A&A*, 614, A118
- Ahn, C., et al. 2014, *ApJS*, 211, 17
- Akahori, T., & Yoshikawa, K. 2010, *PASJ*, 62, 335
- Akamatsu, H., et al. 2013, *PASJ*, 65, 89
- Akamatsu, H., & Kawahara, H. 2013, *PASJ*, 65, 16
- Akamatsu, H., et al. 2012, *PASJ*, 64, 67
- Akamatsu, H., et al. 2015, *A&A*, 582, A87
- Akamatsu, H., et al. 2016, *A&A*, 593, L7
- Akamatsu, H., et al. 2017a, *A&A*, 600, A100
- Akamatsu, H., et al. 2017b, *A&A*, 606, A1

- Allen, S., et al. 2001, MNRAS, 324, 842
- AMI Consortium: Rodríguez-González, C., et al. 2012, MNRAS, 425, 162
- Anders, E., & Grevesse, N. 1989, Geochim. Cosmochim. Acta, 53, 197
- Andersson, K., & Madejski, G. 2004, ApJ, 607, 190
- Andrade-Santos, F., et al. 2015, ApJ, 803, 108
- Angulo, R., et al. 2012, MNRAS, 426, 2046
- Araya-Melo, P., et al. 2012, MNRAS, 423, 2325
- Arnaud, K. 1996, in Astronomical Society of the Pacific Conference Series, Vol. 101, Astronomical Data Analysis Software and Systems V, ed. G. Jacoby & J. Barnes, 17
- Arnaud, M. 2009, A&A, 500, 103
- Arnaud, M., et al. 2000, A&A, 355, 461
- Arnaud, M., et al. 2005, A&A, 441, 893
- Bacchi, M., et al. 2003, A&A, 400, 465
- Bagchi, J., et al. 2006, Science, 314, 791
- Baldi, A., et al. 2007, ApJ, 666, 835
- Barrena, R., et al. 2007, A&A, 469, 861
- Barrena, R., et al. 2013, MNRAS, 430, 3453
- Barrena, R., et al. 2009, A&A, 503, 357
- Barrena, R., et al. 2014, MNRAS, 442, 2216
- Bartalucci, I., et al. 2014, A&A, 566, A25
- Bartelmann, M. 2010, Classical Quantum Gravity, 27, 233001
- Bartelmann, M., & Schneider, P. 2001, Phys. Rep., 340, 291
- Basu, K., et al. 2016, ApJ, 829, L23
- Becker, R., et al. 1995, ApJ, 450, 559
- Beers, T., et al. 1982, ApJ, 257, 23
- Bell, A. 1978a, MNRAS, 182, 147
- Bell, A. 1978b, MNRAS, 182, 443
- Bell, A. 2013, Astropart. Phys., 43, 56
- Bell, A. 2014, Braz. J. Phys., 44, 415
- Belsole, E., et al. 2004, A&A, 415, 821

- Bennett, A. 1962, *MmRAS*, 68, 163
- Bennett, C., et al. 1996, *ApJ*, 464, L1
- Benson, B., et al. 2017, *ApJ*, 841, 7
- Beresnyak, A., et al. 2013, *ApJ*, 771, 131
- Berezhko, E., et al. 2009, *A&A*, 505, 169
- Berezinsky, V., et al. 1997, *ApJ*, 487, 529
- Bernardi, G., et al. 2016, *MNRAS*, 456, 1259
- Birkinshaw, M. 1999, *Phys. Rep.*, 310, 97
- Blandford, R., & Eichler, D. 1987, *Phys. Rep.*, 154, 1
- Blasi, P. 2004, *JKAS*, 37, 483
- Blasi, P., & Colafrancesco, S. 1999, *Astropart. Phys.*, 12, 169
- Blasi, P., et al. 2007, *IJMPA*, 22, 681
- Blumenthal, G., et al. 1984, *Nature*, 311, 517
- Blumenthal, G., & Gould, R. 1970, *Rev. Mod. Phys.*, 42, 237
- Böhringer, H., et al. 1994, *Nature*, 368, 828
- Böhringer, H., & Werner, N. 2010, *ARA&A*, 18, 127
- Böhringer, H., et al. 2000, *ApJS*, 129, 435
- Böhringer, H., et al. 2004, *A&A*, 425, 367
- Bonafede, A., et al. 2010, *A&A*, 513, A30
- Bonafede, A., et al. 2009, *A&A*, 494, 429
- Bonafede, A., et al. 2014a, *ApJ*, 785, 1
- Bonafede, A., et al. 2013, *MNRAS*, 433, 3208
- Bonafede, A., et al. 2012, *MNRAS*, 426, 40
- Bonafede, A., et al. 2014b, *MNRAS*, 444, L44
- Bonafede, A., et al. 2017, *MNRAS*, 470, 3465
- Bonafede, A., et al. 2018, *MNRAS*, 478, 2927
- Boschin, W., et al. 2009, *A&A*, 495, 15
- Boschin, W., & Girardi, M. 2018, *MNRAS*, 480, 1187
- Boschin, W., et al. 2012a, *A&A*, 547, A44

- Boschin, W., et al. 2013, MNRAS, 434, 772
- Boschin, W., et al. 2012b, A&A, 540, A43
- Boschin, W., et al. 2006, A&A, 449, 461
- Botteon, A., et al. 2015, in *The Many Facets of Extragalactic Radio Surveys: Towards New Scientific Challenges*, 46
- Botteon, A., et al. 2018a, MNRAS, 476, 5591
- Botteon, A., et al. 2016a, MNRAS, 460, L84
- Botteon, A., et al. 2016b, *Galaxies*, 4, 68
- Botteon, A., et al. 2016c, MNRAS, 463, 1534
- Botteon, A., et al. 2018b, MNRAS, 478, 885
- Botteon, A., et al. 2018c, ArXiv e-prints, arXiv:1811.07930
- Bourdin, H., & Mazzotta, P. 2008, A&A, 479, 307
- Bourdin, H., et al. 2013, ApJ, 764, 82
- Bourdin, H., et al. 2004, A&A, 414, 429
- Bourne, M., & Sijacki, D. 2017, MNRAS, 472, 4707
- Boylan-Kolchin, M., et al. 2009, MNRAS, 398, 1150
- Braginskii, S. 1965, *Rev. Plasma Phys.*, 1, 205
- Briel, U., et al. 1991, A&A, 246, L10
- Brienza, M., et al. 2016, A&A, 585, A29
- Briggs, D. 1995, in *Bulletin of the American Astronomical Society*, Vol. 27, American Astronomical Society Meeting Abstracts, 1444
- Broadhurst, T., et al. 2005, ApJ, 621, 53
- Brown, S., & Rudnick, L. 2011, MNRAS, 412, 2
- Brüggen, M., et al. 2012a, *Space Sci. Rev.*, 166, 187
- Brüggen, M., et al. 2005, ApJ, 631, L21
- Brüggen, M., et al. 2012b, MNRAS, 425, L76
- Brüggen, M., et al. 2018, MNRAS, 477, 3461
- Brunetti, G. 2003, in *Astronomical Society of the Pacific Conference Series*, Vol. 301, *Matter and Energy in Clusters of Galaxies*, ed. S. Bowyer & C.-Y. Hwang, 349
- Brunetti, G. 2004, JKAS, 37, 493

- Brunetti, G. 2016, *Plasma Phys. Control. Fusion*, 58, 14011
- Brunetti, G., et al. 2004, *MNRAS*, 350, 1174
- Brunetti, G., et al. 2012, *MNRAS*, 426, 956
- Brunetti, G., et al. 2009, *A&A*, 507, 661
- Brunetti, G., & Jones, T. 2014, *IJMPD*, 23, 30007
- Brunetti, G., & Lazarian, A. 2007, *MNRAS*, 378, 245
- Brunetti, G., & Lazarian, A. 2011a, *MNRAS*, 412, 817
- Brunetti, G., & Lazarian, A. 2011b, *MNRAS*, 410, 127
- Brunetti, G., & Lazarian, A. 2016, *MNRAS*, 458, 2584
- Brunetti, G., et al. 2013, *A&A*, 558, A52
- Brunetti, G., et al. 2001, *MNRAS*, 320, 365
- Brunetti, G., et al. 2007, *ApJ*, 670, L5
- Brunetti, G., et al. 2017, *MNRAS*, 472, 1506
- Brunetti, G., et al. 2008, *Nature*, 455, 944
- Buote, D. 2001, *ApJ*, 553, L15
- Burns, J. 1998, *Science*, 280, 400
- Bykov, A. 2001, *Space Sci. Rev.*, 99, 317
- Caglar, T. 2018, *MNRAS*, 475, 2870
- Caglar, T., & Hudaverdi, M. 2017, *MNRAS*, 472, 2633
- Canning, R., et al. 2017, *MNRAS*, 464, 2896
- Cappellari, M., & Copin, Y. 2003, *MNRAS*, 342, 345
- Caprioli, D., & Spitkovsky, A. 2014, *ApJ*, 783, 91
- Caprioli, D., & Zhang, H. 2018, *J. Plasma Phys.*, 84, 715840301
- Carilli, C., & Taylor, G. 2002, *ARA&A*, 40, 319
- Carliles, S., et al. 2010, *ApJ*, 712, 511
- Carlstrom, J., et al. 2002, *ARA&A*, 40, 643
- Carrasco, E., et al. 2010, *ApJ*, 715, L160
- Cash, W. 1979, *ApJ*, 228, 939
- Cassano, R. 2010, *A&A*, 517, A10

- Cassano, R., & Brunetti, G. 2005, *MNRAS*, 357, 1313
- Cassano, R., et al. 2016, *A&A*, 593, A81
- Cassano, R., et al. 2012, *A&A*, 548, A100
- Cassano, R., et al. 2010a, *A&A*, 509, A68
- Cassano, R., et al. 2006, *MNRAS*, 369, 1577
- Cassano, R., et al. 2010b, *ApJ*, 721, L82
- Cassano, R., et al. 2013, *ApJ*, 777, 141
- Cavagnolo, K., et al. 2009, *ApJS*, 182, 12
- Cavaliere, A., & Fusco-Femiano, R. 1976, *A&A*, 49, 137
- Cavaliere, A., & Fusco-Femiano, R. 1978, *A&A*, 70, 677
- Chandra, P., et al. 2004, *ApJ*, 612, 974
- Chiu, I.-N., et al. 2018, *ApJ*, 860, 126
- Churazov, E., et al. 2003, *ApJ*, 590, 225
- Churazov, E., et al. 2004, *MNRAS*, 347, 29
- Churazov, E., et al. 2012, *MNRAS*, 421, 1123
- Clarke, T., et al. 2001, *ApJ*, 547, L111
- Coles, P., & Lucchin, F. 1995, *Cosmology. The origin and evolution of cosmic structure*
- Coles, P., & Lucchin, F. 2002, *Cosmology: The Origin and Evolution of Cosmic Structure, Second Edition*
- Condon, J., et al. 1998, *AJ*, 115, 1693
- Cook, R., & Dell'Antonio, I. 2012, *ApJ*, 750, 153
- Cornwell, T., et al. 2005, in *Astronomical Society of the Pacific Conference Series, Vol. 347, Astronomical Data Analysis Software and Systems XIV*, ed. P. Shopbell, M. Britton, & R. Ebert, 86
- Csabai, I., et al. 2007, *Astron. Nachrichten*, 328, 852
- Cuciti, V., et al. 2018, *A&A*, 609, A61
- Cuciti, V., et al. 2015, *A&A*, 580, A97
- Dahle, H., et al. 2002, *ApJS*, 139, 313
- Dallacasa, D., et al. 2009, *ApJ*, 699, 1288
- Dalton, G., et al. 2012, in *Proceedings of SPIE, Vol. 8446, Ground-based and Airborne Instrumentation for Astronomy IV*, 84460P

- Dalton, G., et al. 2014, in Proceedings of SPIE, Vol. 9147, Ground-based and Airborne Instrumentation for Astronomy V, 91470L
- Dasadia, S., et al. 2016, ApJ, 820, L20
- David, L., & Kempner, J. 2004, ApJ, 613, 831
- De Filippis, E., et al. 2004, ApJ, 611, 164
- de Gasperin, F., et al. 2015a, MNRAS, 453, 3483
- de Gasperin, F., et al. 2015b, MNRAS, 448, 2197
- de Gasperin, F., et al. 2014, MNRAS, 444, 3130
- de Gasperin, F., et al. 2017, Science Adv., 3, e1701634
- de Gasperin, F., et al. 2018, ArXiv e-prints, arXiv:1811.07954
- De Luca, A., & Molendi, S. 2004, A&A, 419, 837
- Deiss, B., et al. 1997, A&A, 321, 55
- Dennison, B. 1980, ApJ, 239, L93
- Dermer, C. 1986, A&A, 157, 223
- Dicker, S., et al. 2014, in Proceedings of SPIE, Vol. 9153, Millimeter, Submillimeter, and Far-Infrared Detectors and Instrumentation for Astronomy VII, 91530J
- Diehl, S., & Statler, T. 2006, MNRAS, 368, 497
- Dolag, K., et al. 2008, Space Sci. Rev., 134, 311
- Dolag, K., & Enßlin, T. 2000, A&A, 362, 151
- Dolag, K., et al. 2001, A&A, 378, 777
- Dolag, K., et al. 2005, MNRAS, 364, 753
- Donnelly, R., et al. 1999, ApJ, 513, 690
- Donnelly, R., et al. 1998, ApJ, 500, 138
- Donnert, J. 2014, MNRAS, 438, 1971
- Donnert, J., et al. 2017, MNRAS, 471, 4587
- Donnert, J., et al. 2013, MNRAS, 429, 3564
- Donnert, J., et al. 2010a, MNRAS, 401, 47
- Donnert, J., et al. 2010b, MNRAS, 407, 1565
- Donnert, J., et al. 2009, MNRAS, 392, 1008
- Donnert, J., et al. 2016, MNRAS, 462, 2014

- Donnert, J., et al. 2018, *Space Sci. Rev.*, 214, 122
- Doré, O., et al. 2001, *A&A*, 375, 14
- Drabent, A. 2017, PhD thesis, Friedrich-Schiller-Universität Jena
- Drury, L. 1983, *Rep. Prog. Phys.*, 46, 973
- Duchesne, S., et al. 2017, ArXiv e-prints, arXiv:1707.03517
- Duncan, K., et al. 2018, ArXiv e-prints, arXiv:1811.07928
- Dwarakanath, K., et al. 2011, *J. Astrophys. Astron.*, 32, 529
- Ebeling, H., et al. 2007, *ApJ*, 661, L33
- Ebeling, H., et al. 2000, *MNRAS*, 318, 333
- Ebeling, H., et al. 1998, *MNRAS*, 301, 881
- Ebeling, H., et al. 2010, *MNRAS*, 407, 83
- Ebeling, H., et al. 2017, *MNRAS*, 471, 3305
- Eckert, D., et al. 2017a, *Astron. Nachrichten*, 338, 293
- Eckert, D., et al. 2017b, *ApJ*, 843, L29
- Eckert, D., et al. 2016a, *MNRAS*, 461, 1302
- Eckert, D., et al. 2011, *A&A*, 526, A79
- Eckert, D., et al. 2015, *Nature*, 528, 105
- Eckert, D., et al. 2016b, *A&A*, 592, A12
- Ellison, D., et al. 2010, *ApJ*, 712, 287
- Emery, D., et al. 2017, *ApJ*, 834, 159
- Enßlin, T. 1999, in *Diffuse Thermal and Relativistic Plasma in Galaxy Clusters*, ed. H. Boehringer, L. Feretti, & P. Schuecker, 275
- Enßlin, T., et al. 1998, *A&A*, 332, 395
- Enßlin, T., et al. 1997, *ApJ*, 477, 560
- Enßlin, T., & Brüggen, M. 2002, *MNRAS*, 331, 1011
- Enßlin, T., & Gopal-Krishna. 2001, *A&A*, 366, 26
- Enßlin, T., et al. 2011, *A&A*, 527, A99
- Enßlin, T., & Röttgering, H. 2002, *A&A*, 396, 83
- Erlar, J., et al. 2015, *MNRAS*, 447, 2497
- Ettori, S. 2000, *MNRAS*, 311, 313

- Ettori, S., et al. 2013, *Space Sci. Rev.*, 177, 119
- Ettori, S., & Molendi, S. 2011, *MmSAI*, 17, 47
- Evrard, A., et al. 1996, *ApJ*, 469, 494
- Feretti, L., et al. 2012, *A&A Rev.*, 20, 54
- Feretti, L., et al. 2005, *A&A*, 444, 157
- Fermi, E. 1949, *Phys. Rev.*, 75, 1169
- Feroz, F., et al. 2009, *MNRAS*, 398, 1601
- Ferrari, C., et al. 2006, *A&A*, 446, 417
- Ferrari, C., et al. 2008, *Space Sci. Rev.*, 134, 93
- Ferrari, C., et al. 2003, *A&A*, 399, 813
- Finoguenov, A., et al. 2005, *A&A*, 442, 827
- Finoguenov, A., et al. 2010, *ApJ*, 715, 1143
- Forman, W., et al. 1981, *ApJ*, 243, L133
- Fox, D., & Pen, U.-L. 2002, *ApJ*, 574, 38
- Fujita, Y., et al. 2016, *PASJ*, 68, 34
- Fujita, Y., et al. 1996, *PASJ*, 48, 191
- Fujita, Y., et al. 2003, *ApJ*, 584, 190
- Fujita, Y., et al. 2015, *ApJ*, 815, 116
- Fukui, Y., et al. 2012, *ApJ*, 746, 82
- Furlanetto, S., & Loeb, A. 2001, *ApJ*, 556, 619
- Fusco-Femiano, R., et al. 1999, *ApJ*, 513, L21
- Fusco-Femiano, R., et al. 2001, *ApJ*, 552, L97
- Fusco-Femiano, R., et al. 2005, *ApJ*, 624, L69
- Fusco-Femiano, R., et al. 2007, *ApJ*, 654, L9
- Fusco-Femiano, R., et al. 2003, *A&A*, 398, 441
- Fusco-Femiano, R., et al. 2000, *ApJ*, 534, L7
- Gaskin, J., et al. 2017, in *Society of Photo-Optical Instrumentation Engineers (SPIE) Conference Series*, Vol. 10397, *Society of Photo-Optical Instrumentation Engineers (SPIE) Conference Series*, 103970S
- Gaspari, M., & Churazov, E. 2013, *A&A*, 559, A78

- Gaspari, M., et al. 2014, *A&A*, 569, A67
- Gastaldello, F., et al. 2003, *A&A*, 411, 21
- Gastaldello, F., & Molendi, S. 2004, *ApJ*, 600, 670
- Gastaldello, F., et al. 2015, *ApJ*, 800, 139
- Gavazzi, R. 2005, *A&A*, 443, 793
- Geller, M., et al. 2010, *ApJ*, 709, 832
- George, L., et al. 2015, *MNRAS*, 451, 4207
- George, L., et al. 2017, *MNRAS*, 467, 936
- Ghirardini, V., et al. 2019, *A&A*, 621, A41
- Ghizzardi, S., et al. 2010, *A&A*, 516, A32
- Giacintucci, S., et al. 2017, *ApJ*, 841, 71
- Giacintucci, S., et al. 2008, *A&A*, 486, 347
- Gieseler, U., et al. 2000, *A&A*, 364, 911
- Giovannini, G., et al. 2009, *A&A*, 507, 1257
- Giovannini, G., & Feretti, L. 2000, *New Astron.*, 5, 335
- Giovannini, G., et al. 1991, *A&A*, 252, 528
- Giovannini, G., et al. 1993, *ApJ*, 406, 399
- Girardi, M., & Biviano, A. 2002, in *Astrophysics and Space Science Library*, Vol. 272, *Merging Processes in Galaxy Clusters*, ed. L. Feretti, I. Gioia, & G. Giovannini, 39–77
- Girardi, M., et al. 1997, *ApJ*, 490, 56
- Girardi, M., et al. 2016, *MNRAS*, 456, 2829
- Golovich, N., et al. 2016, *ApJ*, 831, 110
- Golovich, N., et al. 2017, *ApJ*, 838, 110
- Golovich, N., et al. 2018, *ArXiv e-prints*, arXiv:1806.10619
- Govoni, F., et al. 2001a, *A&A*, 369, 441
- Govoni, F., & Feretti, L. 2004, *IJMPD*, 13, 1549
- Govoni, F., et al. 2001b, *A&A*, 376, 803
- Govoni, F., et al. 2004, *ApJ*, 605, 695
- Govoni, F., et al. 2011, *A&A*, 529, A69
- Govoni, F., et al. 2009, *A&A*, 499, 371

- Govoni, F., et al. 2017, *A&A*, 603, A122
- Grasso, D., & Rubinstein, H. 2001, *Phys. Rep.*, 348, 163
- Gu, L., et al. 2009, *ApJ*, 700, 1161
- Guo, X., et al. 2014a, *ApJ*, 794, 153
- Guo, X., et al. 2014b, *ApJ*, 797, 47
- Gutierrez, K., & Krawczynski, H. 2005, *ApJ*, 619, 161
- Ha, J.-H., et al. 2018, *ApJ*, 857, 26
- Haines, C., et al. 2009, *MNRAS*, 396, 1297
- Haines, C., et al. 2018, *MNRAS*, 477, 4931
- Hallman, E., et al. 2018, *ApJ*, 859, 44
- Hardcastle, M., et al. 2016, *MNRAS*, 462, 1910
- Harris, D., & Grindlay, J. 1979, *MNRAS*, 188, 25
- Harwood, J., et al. 2015, *MNRAS*, 454, 3403
- Heald, G., et al. 2015, *A&A*, 582, A123
- Helder, E., et al. 2012, *Space Sci. Rev.*, 173, 369
- Henriksen, M., et al. 2000, *ApJ*, 529, 692
- Henriksen, M., & Markevitch, M. 1996, *ApJ*, 466, L79
- Henry, J., & Briel, U. 1991, *A&A*, 246, L14
- Henry, J., & Briel, U. 1995, *ApJ*, 443, L9
- Hill, G., et al. 2008, in *Astronomical Society of the Pacific Conference Series*, Vol. 399, *Panoramic Views of Galaxy Formation and Evolution*, ed. T. Kodama, T. Yamada, & K. Aoki, 115
- Hillel, S., & Soker, N. 2017, *MNRAS*, 466, L39
- Hindson, L., et al. 2014, *MNRAS*, 445, 330
- Hitomi Collaboration. 2016, *Nature*, 535, 117
- Hlavacek-Larrondo, J., et al. 2018, *MNRAS*, 475, 2743
- Hoang, D., et al. 2017, *MNRAS*, 471, 1107
- Hoang, D., et al. 2018a, *MNRAS*, 478, 2218
- Hoang, D., et al. 2018b, *ArXiv e-prints*, arXiv:1811.09713
- Hoang, D., et al. 2018c, *ArXiv e-prints*, arXiv:1811.09708
- Hoeft, M., & Brüggen, M. 2007, *MNRAS*, 375, 77

- Hoefl, M., et al. 2008, MNRAS, 391, 1511
- Hong, S., et al. 2015, ApJ, 812, 49
- Hughes, J., et al. 2014, in AAS 223rd Meeting, abstract 106.07
- Hunstead, R., & SUMSS Team. 1999, in Diffuse Thermal and Relativistic Plasma in Galaxy Clusters, ed. H. Boehringer, L. Feretti, & P. Schuecker, 19
- Iapichino, L., & Brüggén, M. 2012, MNRAS, 423, 2781
- Iapichino, L., et al. 2017, MNRAS, 469, 3641
- Iapichino, L., & Niemeyer, J. 2008, MNRAS, 388, 1089
- Iapichino, L., et al. 2011, MNRAS, 414, 2297
- Inogamov, N., & Sunyaev, R. 2003, Astron. Lett., 29, 791
- Intema, H., et al. 2017, A&A, 598, A78
- Intema, H., et al. 2009, A&A, 501, 1185
- Itahana, M., et al. 2015, PASJ, 67, 113
- Jaffe, W. 1977, ApJ, 212, 1
- Jauzac, M., et al. 2016, MNRAS, 463, 3876
- Jeltema, T., & Profumo, S. 2011, ApJ, 728, 53
- Ji, S., et al. 2016, MNRAS, 463, 3989
- Johnston-Hollitt, M. 2003, PhD thesis, University of Adelaide
- Johnston-Hollitt, M. 2004, in The Riddle of Cooling Flows in Galaxies and Clusters of galaxies, ed. T. Reiprich, J. Kempner, & N. Soker
- Johnston-Hollitt, M., & Pratley, L. 2017, ArXiv e-prints, arXiv:1706.04930
- Jones, C., & Forman, W. 1984, ApJ, 276, 38
- Jones, F., & Ellison, D. 1991, Space Sci. Rev., 58, 259
- Jones, T., et al. 2017, Phys. Plasmas, 24, 41402
- Kahlhoefer, F., et al. 2015, MNRAS, 452, L54
- Kaiser, N. 1984, ApJ, 284, L9
- Kaiser, N. 1986, MNRAS, 222, 323
- Kalberla, P., et al. 2005, A&A, 440, 775
- Kale, R., & Dwarakanath, K. 2012, ApJ, 744, 46
- Kale, R., et al. 2012, MNRAS, 426, 1204

- Kale, R., et al. 2018, MNRAS, 480, 5352
- Kale, R., et al. 2013, A&A, 557, A99
- Kale, R., et al. 2015, A&A, 579, A92
- Kang, H., & Jones, T. 2005, ApJ, 620, 44
- Kang, H., et al. 2014, ApJ, 788, 142
- Kang, H., & Ryu, D. 2011, ApJ, 734, 18
- Kang, H., & Ryu, D. 2013, ApJ, 764, 95
- Kang, H., & Ryu, D. 2016, ApJ, 823, 13
- Kang, H., & Ryu, D. 2018, ApJ, 856, 33
- Kang, H., et al. 1996, ApJ, 456, 422
- Kang, H., et al. 2012, ApJ, 756, 97
- Kato, Y., et al. 2015, PASJ, 67, 71
- Kempner, J., & David, L. 2004, MNRAS, 349, 385
- Kempner, J., & Sarazin, C. 2001, ApJ, 548, 639
- Keshet, U., et al. 2004, ApJ, 617, 281
- Kim, K.-T., et al. 1990, ApJ, 355, 29
- Kim, K.-T., et al. 1991, ApJ, 379, 80
- Kitayama, T., et al. 2004, PASJ, 56, 17
- Kneib, J., et al. 1993, A&A, 273, 367
- Kneib, J.-P., et al. 1996, ApJ, 471, 643
- Korngut, P., et al. 2011, ApJ, 734, 10
- Kravtsov, A., & Borgani, S. 2012, ARA&A, 50, 353
- Kronberg, P., et al. 1999, ApJ, 511, 56
- Krymskii, G. 1977, Dokl. Akad. Nauk SSSR, 234, 1306
- Kuntz, K., & Snowden, S. 2000, ApJ, 543, 195
- Kuo, P.-H., et al. 2004, ApJ, 604, 108
- Lakhchaura, K., et al. 2011, ApJ, 743, 78
- Landau, L., & Lifshitz, E. 1959, Fluid mechanics
- Lane, W., et al. 2014, MNRAS, 440, 327

- Large, M., et al. 1959, *Nature*, 183, 1663
- Lau, E., et al. 2017, *ApJ*, 849, 54
- Lazarian, A., & Beresnyak, A. 2006, *MNRAS*, 373, 1195
- Lazarian, A., & Brunetti, G. 2011, *MmSAI*, 82, 636
- Leccardi, A., & Molendi, S. 2008, *A&A*, 486, 359
- Leccardi, A., et al. 2010, *A&A*, 510, A82
- Levinson, A., & Eichler, D. 1992, *ApJ*, 387, 212
- Liang, H., et al. 2000, *ApJ*, 544, 686
- Limousin, M., et al. 2007, *ApJ*, 668, 643
- Lin, Y.-T., et al. 2003, *ApJ*, 591, 749
- Lindner, R., et al. 2014, *ApJ*, 786, 49
- Loi, F., et al. 2017, *MNRAS*, 472, 3605
- Lonsdale, C. 2005, in *Astronomical Society of the Pacific Conference Series*, Vol. 345, *From Clark Lake to the Long Wavelength Array: Bill Erickson's Radio Science*, ed. N. Kassim, M. Perez, W. Junor, & P. Henning, 399
- Lumb, D., et al. 2002, *A&A*, 389, 93
- Macario, G., et al. 2011, *ApJ*, 728, 82
- Macario, G., et al. 2010, *A&A*, 517, A43
- Macario, G., et al. 2013, *A&A*, 551, A141
- Machacek, M., et al. 2002, *ApJ*, 567, 188
- Machado, R., & Lima Neto, G. 2013, *MNRAS*, 430, 3249
- Machado, R., & Lima Neto, G. 2015, *MNRAS*, 447, 2915
- Machado, R., et al. 2015, *MNRAS*, 451, 3309
- Mahdavi, A., & Chang, W. 2011, *ApJ*, 735, L4
- Malkov, M., & Drury, L. 2001, *Rep. Prog. Phys.*, 64, 429
- Mandal, S., et al. 2018, *ArXiv e-prints*, arXiv:1811.08430
- Mann, A., & Ebeling, H. 2012, *MNRAS*, 420, 2120
- Mantz, A., et al. 2010, *MNRAS*, 406, 1773
- Markevitch, M. 2006, in *ESA Special Publication*, Vol. 604, *The X-ray Universe 2005*, ed. A. Wilson, 723

- Markevitch, M. 2010, ArXiv e-prints, arXiv:1010.3660
- Markevitch, M., et al. 1998, *ApJ*, 503, 77
- Markevitch, M., et al. 2002, *ApJ*, 567, L27
- Markevitch, M., et al. 2005, *ApJ*, 627, 733
- Markevitch, M., et al. 1996a, *ApJ*, 456, 437
- Markevitch, M., et al. 1996b, *ApJ*, 472, L17
- Markevitch, M., et al. 1999, *ApJ*, 521, 526
- Markevitch, M., & Vikhlinin, A. 2007, *Phys. Rep.*, 443, 1
- Markevitch, M., et al. 2000, *ApJ*, 541, 542
- Marriage, T., et al. 2011, *ApJ*, 737, 61
- Martino, R., et al. 2014, *MNRAS*, 443, 2342
- Massey, R., et al. 2015, *MNRAS*, 449, 3393
- Mastropietro, C., & Burkert, A. 2008, *MNRAS*, 389, 967
- Mauch, T., et al. 2003, *MNRAS*, 342, 1117
- Maurogordato, S., et al. 2000, *A&A*, 355, 848
- Maurogordato, S., et al. 2011, *A&A*, 525, A79
- Mazzotta, P., et al. 2011, *MmSAI*, 82, 495
- Mazzotta, P., et al. 2004, *MNRAS*, 354, 10
- McCammon, D., et al. 2002, *ApJ*, 576, 188
- McCarthy, I., et al. 2007, *MNRAS*, 376, 497
- McMullin, J., et al. 2007, in *Astronomical Society of the Pacific Conference Series*, Vol. 376, *Astronomical Data Analysis Software and Systems XVI*, ed. R. Shaw, F. Hill, & D. Bell, 127
- Menanteau, F., et al. 2010, *ApJ*, 723, 1523
- Menanteau, F., et al. 2012, *ApJ*, 748, 7
- Meneghetti, M., et al. 2010, *A&A*, 514, A93
- Miley, G. 1980, *ARA&A*, 18, 165
- Million, E., & Allen, S. 2009, *MNRAS*, 399, 1307
- Miniati, F. 2014, *ApJ*, 782, 21
- Miniati, F. 2015, *ApJ*, 800, 60
- Miniati, F., et al. 2001, *ApJ*, 562, 233

- Mitsuishi, I., et al. 2012, PASJ, 64, 18
- Mohan, N., & Rafferty, D. 2015, PyBDSF: Python Blob Detection and Source Finder, Astrophysics Source Code Library, ,
- Molendi, S., & Pizzolato, F. 2001, ApJ, 560, 194
- Molnar, S. 2015, FrASS, 2, 7
- Molnar, S., & Broadhurst, T. 2015, ApJ, 800, 37
- Molnar, S., & Broadhurst, T. 2017, ApJ, 841, 46
- Molnar, S., & Broadhurst, T. 2018, ApJ, 862, 112
- Molnar, S., et al. 2013, ApJ, 779, 63
- Monteiro-Oliveira, R., et al. 2017, MNRAS, 466, 2614
- Morandi, A., et al. 2012, MNRAS, 425, 2069
- Morlino, G., et al. 2009, MNRAS, 392, 240
- Morlino, G., & Caprioli, D. 2012, A&A, 538, A81
- Motl, P., et al. 2005, ApJ, 623, L63
- Murgia, M., et al. 2010, A&A, 509, A86
- Murgia, M., et al. 2004, A&A, 424, 429
- Murgia, M., et al. 2009, A&A, 499, 679
- Mushotzky, R. 2018, in Society of Photo-Optical Instrumentation Engineers (SPIE) Conference Series, Vol. 10699, Society of Photo-Optical Instrumentation Engineers (SPIE) Conference Series., 1069929
- Nagai, D. 2006, ApJ, 650, 538
- Nascimento, R., et al. 2016, MNRAS, 460, 2193
- Ng, K., et al. 2015, MNRAS, 453, 1531
- Norman, C., et al. 1995, ApJ, 454, 60
- Norman, M., & Bryan, G. 1999, in Lecture Notes in Physics, Berlin Springer Verlag, Vol. 530, The Radio Galaxy Messier 87, ed. H.-J. Röser & K. Meisenheimer, 106
- Nuza, S., et al. 2017, MNRAS, 470, 240
- Nuza, S., et al. 2012, MNRAS, 420, 2006
- O’Dea, C., & Owen, F. 1985, AJ, 90, 927
- Offringa, A., & Smirnov, O. 2017, MNRAS, 471, 301
- Offringa, A., et al. 2014, MNRAS, 444, 606

- Ogrean, G., & Brüggén, M. 2013, *MNRAS*, 433, 1701
- Ogrean, G., et al. 2013a, *MNRAS*, 429, 2617
- Ogrean, G., et al. 2013b, *MNRAS*, 433, 812
- Ogrean, G., et al. 2014, *MNRAS*, 440, 3416
- Ogrean, G., et al. 2016, *ApJ*, 819, 113
- Oguri, M., et al. 2005, *ApJ*, 632, 841
- O'Hara, T., et al. 2004, *ApJ*, 604, 604
- Okabe, N., & Umetsu, K. 2008, *PASJ*, 60, 345
- Orrù, E., et al. 2007, *A&A*, 467, 943
- Ota, N., et al. 2014, *A&A*, 562, A60
- Owers, M., et al. 2009, *ApJ*, 704, 1349
- Owers, M., et al. 2011, *ApJ*, 728, 27
- Pandge, M., et al. 2017, *MNRAS*, 472, 2042
- Parekh, V., et al. 2017, *MNRAS*, 464, 2752
- Park, J., et al. 2015, *Phys. Rev. Lett.*, 114, 85003
- Paterno-Mahler, R., et al. 2014, *ApJ*, 791, 104
- Paul, S., et al. 2011, *ApJ*, 726, 17
- Pearce, C., et al. 2017, *ApJ*, 845, 81
- Peebles, P. 1980, *The large-scale structure of the universe*
- Peebles, P. 1993, *Principles of Physical Cosmology*
- Perley, R., & Butler, B. 2013, *ApJS*, 204, 19
- Perley, R., & Taylor, G. 1991, *AJ*, 101, 1623
- Peterson, J., & Fabian, A. 2006, *Phys. Rep.*, 427, 1
- Peterson, J., et al. 2004, *ApJ*, 615, 545
- Petrosian, V. 2001, *ApJ*, 557, 560
- Petrosian, V., & Bykov, A. 2008, *Space Sci. Rev.*, 134, 207
- Pfrommer, C., et al. 2008, *MNRAS*, 385, 1211
- Pfrommer, C., & Jones, T. 2011, *ApJ*, 730, 22
- Pierre, M., et al. 1994, *A&A*, 289, L37

- Pinzke, A., et al. 2013, MNRAS, 435, 1061
- Pinzke, A., et al. 2017, MNRAS, 465, 4800
- Pistinner, S., et al. 1996, ApJ, 467, 162
- Planck Collaboration I. 2011, A&A, 536, A1
- Planck Collaboration VIII. 2011, A&A, 536, A8
- Planck Collaboration VIII. 2013, A&A, 550, A134
- Planck Collaboration X. 2013, A&A, 554, A140
- Planck Collaboration XXIX. 2014, A&A, 571, A29
- Planck Collaboration XXVII. 2016, A&A, 594, A27
- Poole, G., et al. 2006, MNRAS, 373, 881
- Pratt, G., & Arnaud, M. 2002, A&A, 394, 375
- Pratt, G., et al. 2005, A&A, 433, 777
- Pratt, G., et al. 2009, A&A, 498, 361
- Press, W., & Schechter, P. 1974, ApJ, 187, 425
- Pritchard, J., & Loeb, A. 2012, Rep. Prog. Phys., 75, 86901
- Puchwein, E., & Bartelmann, M. 2006, A&A, 455, 791
- Ragozzine, B., et al. 2012, ApJ, 744, 94
- Rajpurohit, K., et al. 2018, ApJ, 852, 65
- Rasia, E., et al. 2006, MNRAS, 369, 2013
- Rasia, E., et al. 2012, New J. Phys., 14, 55018
- Rau, U., & Cornwell, T. 2011, A&A, 532, A71
- Reblinsky, K. 2000, A&A, 364, 377
- Refregier, A. 2003, ARA&A, 41, 645
- Rengelink, R., et al. 1997, A&AS, 124
- Rephaeli, Y. 1979, ApJ, 227, 364
- Rephaeli, Y., & Gruber, D. 2002, ApJ, 579, 587
- Rephaeli, Y., et al. 1999, ApJ, 511, L21
- Rephaeli, Y., et al. 2008, Space Sci. Rev., 134, 71
- Ricker, P., & Sarazin, C. 2001, ApJ, 561, 621

- Riseley, C., et al. 2015, MNRAS, 447, 1895
- Ritchie, B., & Thomas, P. 2002, MNRAS, 329, 675
- Rizza, E., et al. 1998, MNRAS, 301, 328
- Roettiger, K., et al. 1996, ApJ, 473, 651
- Roettiger, K., et al. 1999a, ApJ, 518, 603
- Roettiger, K., et al. 1997, A&AS, 109, 307
- Roettiger, K., et al. 1999b, ApJ, 518, 594
- Roland, J., et al. 1985, A&A, 148, 323
- Roncarelli, M., et al. 2018, A&A, 618, A39
- Rossetti, M., et al. 2013, A&A, 556, A44
- Rossetti, M., & Molendi, S. 2004, A&A, 414, L41
- Rossetti, M., & Molendi, S. 2010, A&A, 510, A83
- Röttgering, H., et al. 1997, MNRAS, 290, 577
- Röttgering, H., et al. 2006, ArXiv e-prints, arXiv:astro-ph/0610596
- Röttgering, H., et al. 2011, J. Astrophys. Astron., 32, 557
- Rudnick, L., & Lemmerman, J. 2009, ApJ, 697, 1341
- Russell, H., et al. 2010, MNRAS, 406, 1721
- Russell, H., et al. 2011, MNRAS, 417, L1
- Russell, H., et al. 2012, MNRAS, 423, 236
- Ryu, D., et al. 2008, Science, 320, 909
- Ryu, D., et al. 2003, ApJ, 593, 599
- Ryu, D., et al. 2012, Space Sci. Rev., 166, 1
- Sakelliou, I., & Ponman, T. 2004, MNRAS, 351, 1439
- Sanders, J. 2006, MNRAS, 371, 829
- Sanders, J., et al. 2004, MNRAS, 349, 952
- Sanders, J., et al. 2016a, MNRAS, 460, 1898
- Sanders, J., et al. 2016b, MNRAS, 457, 82
- Santos-Lima, R., et al. 2017, MNRAS, 465, 4866
- Santos-Lima, R., et al. 2014, ApJ, 781, 84

- Sarazin, C. 1986, *Rev. Mod. Phys.*, 58, 1
- Sarazin, C. 1999, *ApJ*, 520, 529
- Sarazin, C. 2002, in *Astrophysics and Space Science Library*, Vol. 272, *Merging Processes in Galaxy Clusters*, ed. L. Feretti, I. Gioia, & G. Giovannini, 1–38
- Sarazin, C., et al. 2016, *ArXiv e-prints*, arXiv:1606.07433
- Savini, F., et al. 2018a, *MNRAS*, 478, 2234
- Savini, F., et al. 2018b, *ArXiv e-prints*, arXiv:1811.08410
- Savini, F., et al. 2018c, *MNRAS*, 474, 5023
- Scaife, A., & Heald, G. 2012, *MNRAS*, 423, L30
- Scaife, A., et al. 2015, *MNRAS*, 451, 4021
- Schekochihin, A., & Cowley, S. 2006, *Phys. Plasmas*, 13, 56501
- Schekochihin, A., et al. 2010, *MNRAS*, 405, 291
- Schindler, S. 1996, *A&A*, 305, 756
- Schindler, S., & Mueller, E. 1993, *A&A*, 272, 137
- Schlickeiser, R. 2002, *Cosmic Ray Astrophysics*
- Schlickeiser, R., et al. 1987, *A&A*, 182, 21
- Schmidt, W., et al. 2016, *MNRAS*, 459, 701
- Schmidt, W., et al. 2014, *MNRAS*, 440, 3051
- Schneider, P. 2005, *ArXiv e-prints*
- Schuecker, P., et al. 2004, *A&A*, 426, 387
- Sehgal, N., et al. 2008, *ApJ*, 673, 163
- Sereno, M., et al. 2017, *MNRAS*, 467, 3801
- Sereno, M., & Zitrin, A. 2012, *MNRAS*, 419, 3280
- Shibata, R., et al. 1999, *ApJ*, 524, 603
- Shimwell, T., et al. 2014, *MNRAS*, 440, 2901
- Shimwell, T., et al. 2015, *MNRAS*, 449, 1486
- Shimwell, T., et al. 2016, *MNRAS*, 459, 277
- Shimwell, T., et al. 2017, *A&A*, 598, A104
- Shimwell, T., et al. 2018, *ArXiv e-prints*, arXiv:1811.07926
- Sirothia, S. 2009, *MNRAS*, 398, 853

- Skillman, S., et al. 2013, *ApJ*, 765, 21
- Slee, O., et al. 2001, *AJ*, 122, 1172
- Smirnov, O., & Tasse, C. 2015, *MNRAS*, 449, 2668
- Smith, D., et al. 2016, in *SF2A-2016: Proceedings of the Annual meeting of the French Society of Astronomy and Astrophysics*, ed. C. Reyl  , J. Richard, L. Cambr  sy, M. Deleuil, E. P  contal, L. Tresse, & I. Vauglin, 271–280
- Smith, R., et al. 2001, *ApJ*, 556, L91
- Soucail, G., et al. 1987, *A&A*, 172, L14
- Spitzer, L. 1956, *Physics of Fully Ionized Gases*
- Springel, V., et al. 2006, *Nature*, 440, 1137
- Springel, V., et al. 2005, *Nature*, 435, 629
- Storm, E., et al. 2018, *MNRAS*, 479, 553
- Stroe, A., et al. 2013, *A&A*, 555, A110
- Stroe, A., et al. 2014, *MNRAS*, 441, L41
- Stroe, A., et al. 2016, *MNRAS*, 455, 2402
- Subramanian, K. 2016, *Rep. Prog. Phys.*, 79, 76901
- Subramanian, K., et al. 2006, *MNRAS*, 366, 1437
- Sun, M., et al. 2002, *ApJ*, 565, 867
- Sunyaev, R., et al. 2003, *Astron. Lett.*, 29, 783
- Sunyaev, R., & Zeldovich, I. 1980, *MNRAS*, 190, 413
- Sunyaev, R., & Zel’dovich, Y. 1972, *CoASP*, 4, 173
- Takizawa, M. 1999, *ApJ*, 520, 514
- Tasse, C. 2014a, *ArXiv e-prints*, arXiv:1410.8706
- Tasse, C. 2014b, *A&A*, 566, A127
- Tasse, C., et al. 2013, *A&A*, 553, A105
- Tasse, C., et al. 2018, *A&A*, 611, A87
- Taylor, G., & Perley, R. 1993, *ApJ*, 416, 554
- Tchernin, C., et al. 2018, *A&A*, 614, A38
- Thierbach, M., et al. 2003, *A&A*, 397, 53
- Trasatti, M., et al. 2015, *A&A*, 575, A45

- Treu, T. 2010, *ARA&A*, 48, 87
- Umetsu, K., et al. 2018, *ApJ*, 860, 104
- Urdampilleta, I., et al. 2018, *A&A*, 618, A74
- Vacca, V., et al. 2011, *A&A*, 535, A82
- Vacca, V., et al. 2010, *A&A*, 514, A71
- Vacca, V., et al. 2012, *A&A*, 540, A38
- van Haarlem, M., et al. 2013, *A&A*, 556, A2
- van Weeren, R., et al. 2012a, *MNRAS*, 425, L36
- van Weeren, R., et al. 2011a, *MNRAS*, 418, 230
- van Weeren, R., et al. 2019, *Space Sci. Rev.*, 215, 16
- van Weeren, R., et al. 2011b, *A&A*, 528, A38
- van Weeren, R., et al. 2009, *A&A*, 508, 75
- van Weeren, R., et al. 2010, *Science*, 330, 347
- van Weeren, R., et al. 2012b, *A&A*, 546, A124
- van Weeren, R., et al. 2016a, *ApJ*, 818, 204
- van Weeren, R., et al. 2016b, *ApJS*, 223, 2
- van Weeren, R., et al. 2017a, *Nature Astron.*, 1, 5
- van Weeren, R., et al. 2017b, *ApJ*, 835, 197
- Vanderlinde, K., et al. 2010, *ApJ*, 722, 1180
- Vazza, F., et al. 2018a, *MNRAS*, 481, L120
- Vazza, F., & Brüggén, M. 2014, *MNRAS*, 437, 2291
- Vazza, F., et al. 2017a, *Classical Quantum Gravity*, 34, 234001
- Vazza, F., et al. 2014, *MNRAS*, 445, 3706
- Vazza, F., et al. 2012a, *MNRAS*, 421, 1868
- Vazza, F., et al. 2016, *MNRAS*, 459, 70
- Vazza, F., et al. 2018b, *MNRAS*, 474, 1672
- Vazza, F., et al. 2009a, *MNRAS*, 395, 1333
- Vazza, F., et al. 2011, *A&A*, 529, A17
- Vazza, F., et al. 2009b, *A&A*, 504, 33

- Vazza, F., et al. 2015a, MNRAS, 451, 2198
- Vazza, F., et al. 2015b, A&A, 580, A119
- Vazza, F., et al. 2017b, MNRAS, 464, 210
- Vazza, F., et al. 2012b, A&A, 544, A103
- Vazza, F., et al. 2006, MNRAS, 369, L14
- Venturi, T., et al. 2007, A&A, 463, 937
- Venturi, T., et al. 2011, MNRAS, 414, L65
- Venturi, T., et al. 2008, A&A, 484, 327
- Venturi, T., et al. 2013, A&A, 551, A24
- Vikhlinin, A., et al. 1999, ApJ, 525, 47
- Vikhlinin, A., et al. 2006, ApJ, 640, 691
- Vikhlinin, A., et al. 2001a, ApJ, 549, L47
- Vikhlinin, A., et al. 2001b, ApJ, 551, 160
- Vikhlinin, A., et al. 2005, ApJ, 628, 655
- Vogelsberger, M., et al. 2014, MNRAS, 444, 1518
- Voit, G. 2005, Rev. Mod. Phys., 77, 207
- Völk, H., et al. 1996, Space Sci. Rev., 75, 279
- Völk, H., & Atoyan, A. 2000, ApJ, 541, 88
- Völk, H., et al. 2005, A&A, 433, 229
- Walker, S., et al. 2016, MNRAS, 461, 684
- Walker, S., et al. 2019, Space Sci. Rev., 215, 7
- Wang, Q., et al. 2018, ApJ, 856, 162
- Wang, Q., et al. 2016, ApJ, 833, 99
- Wayth, R., et al. 2015, PASA, 32, e025
- Wegner, G., et al. 2017, ApJ, 844, 67
- Werner, N., et al. 2013, Nature, 502, 656
- White, J., et al. 2015, MNRAS, 453, 2718
- Widrow, L., et al. 2012, Space Sci. Rev., 166, 37
- Wik, D., et al. 2011, ApJ, 727, 119

- Wik, D., et al. 2014, *ApJ*, 792, 48
- Wilber, A., et al. 2018, *MNRAS*, 473, 3536
- Williams, W., et al. 2016, *MNRAS*, 460, 2385
- Williams, W., et al. 2018, *ArXiv e-prints*, arXiv:1811.07927
- Willingale, R., et al. 2013, *MNRAS*, 431, 394
- Willson, M. 1970, *MNRAS*, 151, 1
- Wittman, D., et al. 2014, *MNRAS*, 437, 3578
- Wittman, D., et al. 2006, *ApJ*, 643, 128
- Wittor, D., et al. 2017, *MNRAS*, 464, 4448
- Xu, H., et al. 2009, *ApJ*, 698, L14
- Yan, H., & Lazarian, A. 2011, *ApJ*, 731, 35
- Yatawatta, S. 2015, *MNRAS*, 449, 4506
- York, D., et al. 2000, *AJ*, 120, 1579
- Young, A., et al. 2015, *ApJ*, 809, 185
- Yuan, Z., et al. 2015, *ApJ*, 813, 77
- Zaroubi, S., et al. 1998, *ApJ*, 500, L87
- Zhang, C., et al. 2015, *ApJ*, 813, 129
- Zhang, C., et al. 2018, *ApJ*, 855, 36
- Zhuravleva, I., et al. 2013, *MNRAS*, 435, 3111
- Zhuravleva, I., et al. 2014, *Nature*, 515, 85
- Zimbardo, G., & Perri, S. 2018, *MNRAS*, 478, 4922
- ZuHone, J., et al. 2010, *ApJ*, 717, 908
- ZuHone, J., & Roediger, E. 2016, *J. Plasma Phys.*, 82, 535820301

Acknowledgments

THIS THESIS would not have been possible without Daniele D., Gianfranco B., and Fabio G.. I consider myself extremely lucky to have been supervised and formed by them in the past three years. They are not only distinguished scientists, but also patient, motivating, and helpful mentors. Working with these guys was a lot of fun and they deserve my biggest “thank you”.

It was my pleasure to collaborate with many great researchers in the last years. I would like to thank Annalisa B., Dominique E., Franco V., Gianni B., Huib I., Julius D., Reinout vW., Rossella C., Ruta K., Tim S., and Tiziana V. for discussions and support during the data analysis and interpretation. Kudos to Tim in particular for his training in Leiden and for being always available on Skype despite his infinite duties.

Thanks also to my “younger” colleagues (past and new) at IRA and in Leiden both for useful and useless discussions. A special mention goes to my office mate Virginia C. for the several chats in which we shared our doubts and suggestions (despite that e.i.w.) and for the daily laughs and breaks in the last three years.

I honor the system managers at IRA for their technical support and especially Francesco B. for struggling with me to install the LOFAR software.

Last but not least, I would like to thank my parents for their support (and courage) for letting me study whatever I liked. In return, I always tried to give my best.